Imperial College London
Department of Aeronautics

Meshless methods for shear-deformable beams and plates based on mixed weak forms

Jack Samuel Brand Hale

August 8, 2013

Submitted in part fulfilment of the requirements for the degree of Doctor of Philosophy of Imperial College London and the Diploma of Imperial College London

To my family

Declaration

I declare that the work presented in this thesis is my own and that all else is appropriately referenced.

Acknowledgements

Above all I would like to thank Dr. Pedro M. Baiz Villafranca for his supervision throughout the three years I have spent at Imperial College. As his first PhD student I know that he has placed a great deal of faith in me and I hope that I have met his high expectations. I cannot remember a point during my PhD studies where he couldn't find the time to sit down and discuss yet another problem I was having with my research. His help has always set me back on the right track.

I would also like to thank the Department of Aeronautics for providing financial support via the EPSRC DTA throughout my time at Imperial College. Further thanks goes to the Royal Aeronautical Society and the Imperial College Trust for their financial support to travel to various conferences.

I would like to thank all of the academics who have taken time to reply to my emails or give me a little bit of their time at conferences. My apologies to anyone who I have forgotten; Prof. Sukumar, Dr. Hardesty, Prof. Lovadina, Prof. J. S. Chen, Prof. Arnold, Dr. Rognes, Dr. Wells, Dr. Martinelli, Dr. Castellazzi and Dr. Augarde, thank you.

A special thanks however is reserved for Dr. Alejandro Ortiz. Just one email that I sent mid-way through my studies concerning the computational implementation of the volume-averaged nodal pressure procedure resulted in a trip to Chile and a series of fruitful on-going collaborations.

Finally I would like to thank all of the wonderful people that I have met at Imperial over the past few years, in particular my girlfriend Konstanze. Her love and support has been invaluable.

Abstract

Thin structural theories such as the shear-deformable Timoshenko beam and Reissner-Mindlin plate theories have seen wide use throughout engineering practice to simulate the response of structures with planar dimensions far larger than their thickness dimension. Meshless methods have been applied to construct numerical methods to solve the shear deformable theories.

Similarly to the finite element method, meshless methods must be carefully designed to overcome the well-known shear-locking problem. Many successful treatments of shear-locking in the finite element literature are constructed through the application of a mixed weak form. In the mixed weak form the shear stresses are treated as an independent variational quantity in addition to the usual displacement variables.

We introduce a novel hybrid meshless-finite element formulation for the Timoshenko beam problem that converges to the stable first-order/zero-order finite element method in the local limit when using maximum entropy meshless basis functions. The resulting formulation is free from the effects shear-locking.

We then consider the Reissner-Mindlin plate problem. The shear stresses can be identified as a vector field belonging to the Sobelov space with square integrable rotation, suggesting the use of rotated Raviart-Thomas-Nedelec elements of lowest-order for discretising the shear stress field. This novel formulation is again free from the effects of shear-locking.

Finally we consider the construction of a generalised displacement method where the shear stresses are eliminated prior to the solution of the final linear system of equations. We implement an existing technique in the literature for the Stokes problem called the nodal volume averaging technique. To ensure stability we split the shear energy between a part calculated using the displacement variables and the mixed variables resulting in a stabilised weak form. The method then satisfies the stability conditions resulting in a formulation that is free from the effects of shear-locking.

Contents

Figures

Tables

List of frequently used nomenclature

$(u, v)_{\mathcal{V}}$ Inner product between u and v on space $\mathcal{V}$

$|u|_c$ Semi-norm of u induced by a bilinear form c

α_ρ Scaling factor for calculating support size

$\bar{\Omega}$ Closure of Ω

$\bar{t}$ Normalised plate thickness $\bar{t} = t/L$

δ_{ij} Kronecker-delta function

$\dim(\mathcal{V}_h)$ Dimension of space $\mathcal{V}_h$

ε Small parameter in Timoshenko beam problem

η Rotation (test)

Γ Problem boundary

Γ_0 Boundary of mid-surface of plate

Γ_D Subset of boundary with prescribed Dirichlet boundary conditions

Γ_N Subset of boundary with prescribed Neumann boundary conditions

$\hat{K}$ Reference triangular element

κ Shear correction factor = 5/6

λ	Plate shear modulus = $E\kappa/(2(1+\nu))$
$\{\}_h$	Discrete counterpart of continuous variable eg. $\mathcal{V}_{3h}$ and $\mathcal{V}_3$
$\boldsymbol{\varepsilon}$	Small strain tensor
$\boldsymbol{\varepsilon}(\cdot)$	Small strain operator
$\boldsymbol{\eta}$	Rotation vector (test)
$\boldsymbol{\gamma}$	Shear stress vector (trial)
$\boldsymbol{\varphi}$	Partition of unity basis function vector
$\boldsymbol{\psi}$	Shear stress vector (test)
$\boldsymbol{\sigma}$	Stress tensor
$\boldsymbol{\theta}$	Rotation vector (trial)
$\boldsymbol{I}$	Identity tensor
$\boldsymbol{L}[\cdot]$	Bending stress operator
$\boldsymbol{N}$	Finite element basis functions vector
$\boldsymbol{n}$	Unit normal on Γ
$\boldsymbol{u}$	Displacement vector
γ	Shear stress (trial)
$\mathcal{L}$	Operator of partial derivatives
$\mathcal{N}_h$	Node set
$O(f)$	Varies on the order of some function f (Big-O notation)
$\mathcal{R}$	Function space for rotations $\boldsymbol{\theta}$
S	Function space for shear stress
S_h	Connectivity set

$\mathcal{T}_h$	Triangulation with standard definition
$\mathcal{V}^T$	Function space for Timoshenko beam problem
$\mathcal{V}_0^T$	Function space of pure bending displacements for Timoshenko beam problem
$\mathcal{V}_3$	Function space for transverse displacements z_3
$\mathcal{V}_3^0$	Function space for Bernoulli beam problem
$\mathcal{Z}$	Kernel function space
$\|u\|_{\mathcal{V}}$	Norm of u on space $\mathcal{V}$
ν	Poisson's ratio
Ω	Problem domain
ω	Support domain set
Ω_0	Thin structure mid-surface domain
φ_i	Partition of unity basis function associated with degree of freedom i
Π_h	General projection operator
Π_h^p	Local patch projection operator
ψ	Shear stress (test)
ρ	Slope of e vs $\dim(\mathcal{U}_h)$ convergence plot
ρ	Support radius set
rot	Rotation operator
θ	Rotation (trial)
θ_1	Rotation around x_2 axis
θ_2	Rotation around x_1 axis
$\tilde{m}$	Scaled moment in Timoshenko beam problem

$\tilde{p}$ Scaled load in Timoshenko beam problem

$\tilde{P}_k(\Sigma)$ Space of homogeneous polynomials of order p defined on geometrical entity Σ

$a_b(\boldsymbol{\theta}; \boldsymbol{\eta})$ Bilinear form relating to bending energy

$a_s(\boldsymbol{\theta}, z_3; \boldsymbol{\eta}, y_3)$ Bilinear form relating to shear energy

$CG_p(\Omega; \mathcal{T}_h)$ Space of continuous Lagrangian finite elements of order p

D Bending modulus = $E/12(1 - \nu^2)$

$d\Gamma$ Surface measure

$d\Omega$ Volume measure

$DG_p(\Omega; \mathcal{T}_h)$ Space of discontinuous Lagrangian finite elements of order p

E Young's modulus

e Error

$e(u)_V$ Error of variable u calculated in norm of space $\mathcal{V}$

e_i Edges of reference element

F Push-forward from reference element to general element in mesh

F_K Push-forward between general triangular element to general element in mesh

G Beam shear modulus

$g(y_3)$ Linear form relating to transverse loading

h Cell size

$H(\text{rot}; \Omega)$ Sobolev space of square integrable functions with square integrable rotation

$H^1(\Omega)$ Sobolev space of square-integrable functions with square-integrable weak derivatives

$H^{-1}(\text{div}; \Omega)$ Sobolev space defined as the dual space of $H(\text{rot}; \Omega)$

I Second moment of inertia of the cross section

K General triangular element

L Characterisic in-plane dimension of thin structure

$L^2(\Omega)$ Space of square-integrable functions

$ME(\Omega; \mathcal{N}_h, \rho)$ Space of maximum-entropy basis functions

$MLS_p(\Omega; \mathcal{N}_h, \rho)$ Space of MLS basis functions of polynomial order p

N_i Finite element basis functions associated with degree of freedom i

$NED_p(\Omega; \mathcal{T}_h)$ Space of rotated Raviart–Thomas-Nédélec finite elements of order p

p Polynomial order

p_3 Transverse loading function

$P_k(\Sigma)$ Space of polynomials of order p defined on geometrical entity Σ

r Constraint ratio

R_h MITC reduction operator

$RPIM_p(\Omega; \mathcal{N}_h, \rho)$ Space of RPIM basis functions of polynomial order p

T General element

t Thickness of thin structure in x_3 direction

w_i Weight function associated with node i

$x^1, x^2, \ldots$ Nodes in node set

x_1, x_2 Coordinates on mid-surface of plate or beam

x_3 Coordinate through thickness of plate or beam

y_1, y_2, y_3 Generalised displacements along coordinates x_1, x_2, x_3 (test)

z_1, z_2, z_3 Generalised displacements along coordinates x_1, x_2, x_3 (trial)

1 Introduction

1.1 General

Many physical problems can be described by a set of partial differential equations (PDEs) that contain a mathematical description of the underlying physical phenomenon. Usually it is impossible to obtain a classical analytical solution to such problems, except in specific cases with simple domain geometries and boundary conditions. Therefore numerical methods are required to find approximate solutions to these PDEs.

The physical problems we study in this thesis are the mechanical deformation of beam and plate structures. The PDEs that describe these physical phenomenon are known as beam and plate theories, and are a specific subset of a more general class of PDEs known as shell theories which describe the mechanical deformation of shell structures. Simply put, shells are curved three-dimensional bodies that are thin in one dimension and long in the other two. Plates can then be viewed as shells without curvature, and beams are just plates with one long dimension instead of two. We will refer to beams, plates and shells collectively as thin structures and the PDEs that describe their behaviour as thin structural theories.

The reason that shell structures are so important is that they are extremely efficient; they can carry huge applied loads over vast areas using very little material. They are found abundantly in the natural world precisely because of the evolutionary advantages afforded by these efficiencies. Humans also recognise the utility of shell structures. They can be found in all sorts of fields of human endeavour, including civil and naval architecture, mechanical engineering, aerospace engineering and the automotive industry. In many cases shell structures can be remarkably beautiful as well as practical, such as the Great Court roof at the British Museum shown in fig. 1.1.

Because of the wide use of thin structures in modern engineering practice, designers require robust and effective numerical methods for the solution of thin structural theories. A great deal of research effort has been expended on the development of the finite element method for the numerical solution of these theories. Because of the asymptotic behaviours of thin struc-

Figure 1.1: Great Court roof at the British Museum, London. Source: Andrew Dunn/Wikimedia Commons, CC BY-SA 2.0.

tural theories it turns out that this task is somewhat difficult. Particularly in the case of shear-deformable shell theories this task is very complex due to the multiple asymptotic behaviours that arise which are dependent on the geometry, loading and boundary conditions of the particular shell problem at hand. For a numerical method to be effective it must be able to reproduce *all* of the asymptotic behaviours present in the structural theory. It is only relatively recently that finite element methods have become available that are capable of reproducing all of the complicated asymptotic behaviours of the shear-deformable shell theories. The unified analytical proof that these shell finite element methods work in all of these asymptotic cases is still not available, and the evidence of their efficacy is primarily numerical. Nonetheless, in many ways these finite element methods represent one of the pinnacles of modern numerical mathematics.

Despite these successes, finite element methods are not without disadvantages, primarily due to their reliance on constructing the basis functions for the numerical solution of the PDE using a mesh of the problem domain. A relatively recent development in the field of numerical methods, meshless methods, construct the basis functions for the solution of the PDE using just the specification of nodal locations and support sizes in the domain. This lack of mesh bestows meshless numerical methods with various advantages over the finite element method.

Because of these advantages it is natural to want to develop meshless numerical methods capable of solving the thin structural theories. This thesis is concerned with the development of novel meshless numerical methods for the simulation of beam and plate structures described using the shear-deformable beam and plate theories. The shear-deformable beam and plate theories contain one asymptotic behaviour of the shear-deformable shell theory, which is the bending-dominated asymptotic behaviour. If a numerical method fails to be able to represent this bending-dominated asymptotic behaviour the common problem of numerical shear-locking will occur, which leads to entirely erroneous results. The bending-dominated asymptotic behaviour is one of the most commonly encountered behaviours in thin structural theories. Therefore the development of effective meshless numerical methods for the shear-deformable beam and plate theories that are free from shear-locking is a key step towards tackling the more complicated asymptotic behaviour of the shear-deformable shell theory.

The outline of this introductory chapter is as follows. In the next section we will give a historical overview of the development of meshless numerical methods. We will then discuss the development of plate and shell theories before turning our attention to the problem of shear-locking. In particular, we will discuss existing solutions in the meshless literature to the problem of shear-locking. We will then outline the structure of this thesis and the unique contributions that this thesis makes to the field.

1.2 Meshless methods

There is little doubt that the finite element method (FEM) has grown to be the pre-eminent numerical method for the numerical solution of partial differential equations in the physical sciences and engineering. The FEM is a mature and well understood technology and it will undoubtedly continue to attract a huge amount of research effort across a wide range of academic disciplines.

In contrast, meshless methods are a relatively recent development in the field of numerical methods. It is only recently that meshless methods have become available in commercial computational simulation software, and to most practicing engineers they are still viewed as being somewhat exotic and different to the FEM. However, in the context of numerical methods constructed via the application of a weak or variational form, meshless methods in fact have a great deal in common with the FEM. These commonalities were first formalised in the seminal work of Babuška and Melenk as the partition of unity method (PUM) [1]. Simply put, finite element

methods and meshless methods can be viewed as different approaches for the construction of a partition of unity (PU). A partition of unity is any set of basis functions φ that are constructed with the following property everywhere in the problem domain [1]:

$$\sum_i \varphi_i = 1 \tag{1.1}$$

It is this fundamental property which links many seemingly disparate numerical techniques including finite element methods and meshless methods.

In the FEM the problem domain upon which the PDE is posed is divided into a finite number of non-overlapping subdivisions known as elements, see fig. 1.2. These subdivisions are connected together using a topological map known as a mesh. A suitable basis is then constructed on a reference element before being pushed forward to the elements in the mesh via a suitable map, see fig. 1.3. The resulting basis forms a partition of unity. The solution of the entire system is then assembled from the contribution from each finite element in the mesh. This approach is not without limitations; due to the mesh-based interpolation, heavily distorted or low-quality meshes can frequently lead to numerical errors requiring expensive re-meshing operations. Furthermore, the task of meshing is also expensive in terms of human time for the engineer or scientist tasked with the computational simulation of the physical phenomenon of interest. Simulation of moving discontinuities such as cracks and inclusions also requires constant re-meshing as the discontinuity evolves with time.

Meshless or meshfree methods were conceived with the objective of relieving some of the difficulties associated with using a mesh to construct the approximation space for the solution of the partial differential equations. In meshless methods the approximation space is built only from the specification of the position of the nodes in the problem domain and a support domain associated with each node, see fig. 1.4. The basis functions are usually constructed in the global coordinate system, so there is no push-forward as in the finite element method. The resulting meshless basis forms a partition of unity. We expand on the construction of meshless basis functions in chapter 2.

In the following paragraphs, rather than focus on papers that use meshless methods for a particular physical application, we will primarily concentrate on papers concerned with the development of fundamental contributions to the field of meshless numerical methods. For readers interested in a more general overview excellent treatments are given in review papers by V. P. Nguyen et al. [2] and Fries and Matthies [3]. The book by G. R. Liu [4] also gives a

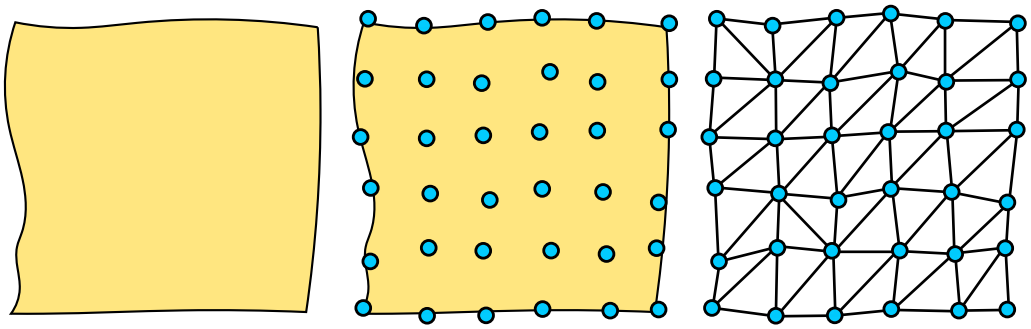

(a) Problem domain Ω described in CAD program

(b) Problem domain seeded with nodes.

(c) Algorithm meshes the nodes.

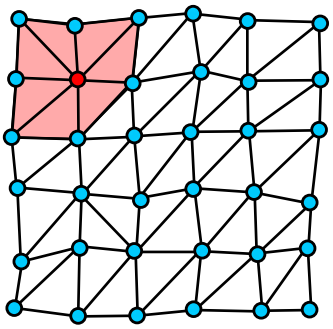

(d) The support and connectivity of each basis function is directly linked to the underlying mesh.

Figure 1.2: Mesh-based partition of unity construction paradigm.

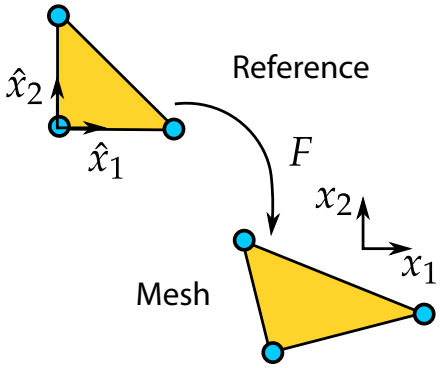

Figure 1.3: In the finite element method basis functions are posed on the reference element then pushed forward with a suitable mapping F to a general element in the mesh.

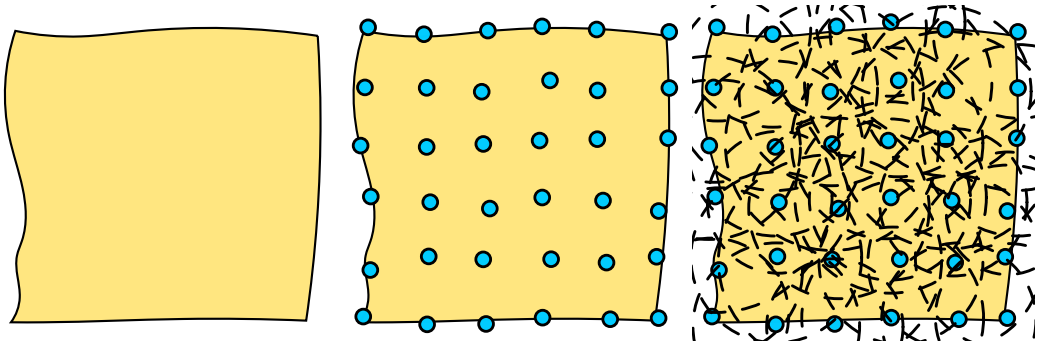

(a) Problem domain Ω described in CAD program.

(b) Problem domain seeded with nodes.

(c) Every node is given a support domain.

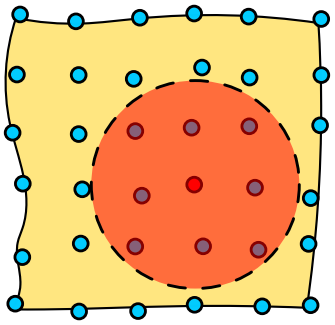

(d) The support and connectivity of each basis function is a natural consequence of the node positions and support domains.

Figure 1.4: Meshless partition of unity construction paradigm.

complete overview of meshless methods. The book by G. R. Liu and Gu [5] gives a complete description of the computer programming aspects of meshless method.

The first widely recognised meshless numerical method is the smoothed particle hydrodynamics (SPH) method introduced by Lucy [6] and Gingold and Monaghan [7]. The initial application of the SPH method was modelling astrophysics phenomenon. Because of its speed and simplicity the SPH method has become popular for numerical simulation of high velocity impact [8] and metal forming [9] problems. Two major issues with the SPH method are the tendency for spurious instabilities to develop and the inconsistent nature of the approximation field, see Swegle et al. [10] and Belytschko et al. [11] for an in-depth discussion. There has been a great deal of theoretical and practical study into solving these stability problems. Liu. et al. introduced a corrected kernel function in the reproducing kernel particle method (RKPM) [12] which helps solve many of the outstanding issues with SPH. The resulting approximation scheme is identical to the moving least-squares approximation scheme of Lancaster and Salkausus [13]. An excellent overview of the SPH method and its modern variants is given in the book by G. R. Liu and M. B. Liu [14].

SPH methods are based upon the strong form of the PDE. Another class of meshless methods, and the one that is the focus of this thesis, are based upon the weak form of the PDE much like the finite element method. Nayroles et al. [15] introduced the diffuse element method (DEM) which used the moving least-squares (MLS) approximations of Lancaster and Salkauskas [13] as the basis functions in a weak form of the PDE. Nayroles et al. [15] omitted certain terms in the derivatives of the MLS basis functions. By including the terms omitted by Nayroles et al. [15], Belytschko et al. [16] proposed the element-free Galerkin method (EFG). In the EFG method integration is carried out using background cells typically constructed using a Delaunay triangulation of the nodal positions. The EFG method has been applied to the many areas of engineering science, including the problem of thin shells and plates by Belytschko and Krysl [17, 18] and dynamic fracture by Belytschko et al. [19].

The EFG method is considered by many to be the archetypal meshless method. There are many other meshless methods in the same vein as the EFG method. The primary variation is using a different meshless basis function construction, such as the point interpolation method (PIM) [20], maximum-entropy method (MaxEnt) [21], radial point interpolation method (RPIM) [22] and moving kriging interpolation [23]. We give an overview of some of these methods in chapter 2. The meshless methods developed in this thesis can be considered descendants of the element-free Galerkin method of Belytschko et al. [19].

Another distinct approach was developed by Atluri et al. [24] based upon local weak forms

called the meshless local Petrov-Galerkin method (MLPG). As the name suggests the resulting methods are of the Petrov-Galerkin type because different function spaces are chosen for the trial and test functions. This is in contrast with most finite element and meshless methods where the same function spaces are chosen for the trial and test functions resulting in methods of the Bubnov-Galerkin type. The MLPG method results in a weak form that is integrated over the local subdomains attached to each node, meaning that no background mesh is required for integration as in the EFG method.

Another class of meshless numerical methods rely heavily upon the partition of unity concept of Babuška and Melenk [1]. Instead of using a basis which is intrinsically consistent like standard Lagrangian finite element or MLS basis functions this family of methods can use any suitable partition of unity satisfying the mathematical properties outlined in [1]. To reach the required order of consistency dictated by the weak form of the PDE the partition of unity is extrinsically enriched. The flexibility of PU methods comes at the expense of additional degrees of freedom associated with the extrinsic enrichment in the final linear system as well as problems with ill-conditioning. The partition of unity finite element method (PUFEM) of Babuška and Melenk [1] uses polynomial finite elements with PU enrichment. The generalised finite element method (GFEM) of Strouboulis et al. [25] includes enrichments allowing the FEM mesh to not conform to the boundary of the problem domain. This allows the inclusion of corners, voids and other singularities in the problem without any modification of the mesh.

As the GFEM and PUFEM use a mesh based partition of unity they can be considered close relatives of the more widely used extended finite element method (XFEM) [26]. There are also partition of unity methods which use meshless PUs. The *hp*-cloud method of Oden et al. [27] uses partition of unity concepts to enrich zero-order consistent Shepard functions. The particle-partition of unity method of Griebel and Schweitzer [28] also uses partition of unity concepts to enrich zero-order consistent Shepard functions [29]. Griebel and Schweitzer study parabolic and hyperbolic PDEs as well as the more common elliptic problems. Oh and Jeong [30] use the flat-top partition of unity method to ease ill-conditioning problem and simplify the issue of integration of the weak form. Oh et. al extend the flat-top construction to three dimensions in [31]. Some of the major advantages of meshless methods can be summarised as follows; the basis functions are particularly good at handing problems with moving discontinuities, large deformations, phase transformations and evolving boundaries; nodes can be easily added, equivalent to an *h*-adaptivity process in finite elements; the basis functions can reach arbitrary order of consistency via intrinsic or extrinsic enrichment; the basis functions have high continuity and compact support resulting in a sparse linear system and meshless methods

can provide more accurate approximations for problems with complex domain geometries.

We take this moment to emphasise our view that meshless methods are not intended to be a replacement for the finite element method, rather that they are complementary in the sense that meshless methods can be used when the inherent limitations of constructing a partition of unity using a mesh become too great. Meshless methods should be viewed as an additional tool which can be used to simulate complex PDEs. Because it is possible to couple regions of the problem domain discretised with meshless methods to regions discretised with finite elements they can even be used in the same computational simulation. In our view it is unlikely that meshless methods will ever surpass the speed and ease of implementation of the FEM. Nonetheless, it is clear that via theoretical developments born from the study of meshless methods that the existing finite element method can be improved to handle new problems. The extended finite element method and the more recent smoothed finite element method (SFEM) are excellent examples of this cross-pollination between meshless methods and finite element methods [26].

We give an in-depth discussion of the construction and mathematical properties of various meshless basis functions in chapter 2.

1.3 Plate theories

A plate is a structure with two in-plane dimensions much larger than its thickness. Typically, the thickness is no greater than 1/10th of the smallest in-plane dimension [32]. Because of the small relative size of the thickness dimension there is no need to model the plate using the full three-dimensional equations of elasticity. Instead, it is possible to pose a simplified two-dimensional theory which can accurately predict the behaviour of the three-dimensional elastic body.

Plate theories have traditionally been formulated by making informed assumptions about the functional form of the displacement field based on the behaviour of an elastic body with constrained geometry [32]. By making differing hypothesis about the form of the displacements we can come up with differing plate theories of varying accuracy with respect to the full three-dimensional equations of elasticity. However, this method of engineering intuition is not the only way of deriving thin-structural theories, and in answering the question of exactly how the thin-structural theory converges to the full three-dimensional elastic body more advanced techniques such as variational methods are required. We do not discuss this topic any further, and refer the reader to S. Zhang [33] for further details.

In chapter 3 we will discuss two of the most widely used plate theories which are the subject of the thesis. The first plate theory is the Kirchhoff-Love or classical plate model. The Kirchhoff-Love model was originally formulated by Love [34] based upon the kinematical assumptions of Kirchhoff [35]. The second plate theory is a first-order relaxation of the Kirchhoff-Love model which is known as the Reissner-Mindlin, or first-order shear deformable plate model. The Reissner-Mindlin plate model was originally formulated by Reissner [36, 37] and Mindlin [38]. Of course, these are by no means the only plate theories available, but they are amongst some of the most widely used in practice. Higher-order shear-deformable theories such as the third-order shear deformable theory of Reddy [39] give an even better approximation than the Reissner-Mindlin theory, at the expense of additional unknowns. In this thesis we restrict our discussion to the Kirchhoff-Love and Reissner-Mindlin models which are the most widely used in practice.

1.4 Shear-locking

A common problem encountered in numerical formulations of the displacement weak form of the Reissner-Mindlin plate problem is the phenomenon of shear-locking. This problem manifests itself as an overly stiff system as the plate thickness $\bar{t} \to 0$ and can be attributed to the inability of the numerical approximation functions to be able to represent the Kirchhoff asymptotic limit [40]. Ultimately, the problem of shear-locking in a numerical formulation leads to entirely erroneous results.

Physically speaking, it is intuitive that given the Kirchhoff model and the Reissner-Mindlin model purport to model the same phenomenon, namely a three-dimensional elastic plate under mechanical load, that both models should coincide with each other when placed under the same kinematical restrictions. This kinematical restriction is known as the Kirchhoff limit or constraint. Indeed, it is relatively straightforward to show that the Reissner-Mindlin problem coincides with the Kirchhoff-Love problem as the thickness of the plate approaches zero. Unfortunately, when we discretise the displacement weak form of the Reissner-Mindlin problem using simple numerical schemes such as the standard Lagrangian finite element method and enforce the Kirchhoff limit by letting $\bar{t} \to 0$ the numerical solution will fail to coincide with that given by the Kirchhoff-Love problem. This failure manifests itself as totally incorrect numerical solutions and is commonly referred to as the shear-locking problem. Shear-locking is the inability of the constructed basis functions to be able to richly represent the Kirchhoff limit. It is

the construction of meshless numerical methods that are free from this shear-locking problem that is the subject of this thesis.

The shear-locking problem was first studied extensively in the context of the FEM. It is well known that using low-order Lagrangian elements for all of the displacement fields will result in shear-locking in the Kirchhoff limit [40]. A huge number of remedies have been introduced in the FEM literature to overcome this problem, including, but not limited to; selective reduced integration methods [41], the assumed natural strain (ANS) or mixed interpolation of tensorial components (MITC) method eg. [42–44], the enhanced assumed strains (EAS) method eg. [45, 46], and the discrete shear gap method eg. [47, 48]. A modern and relatively comprehensive mathematical overview of the finite element analysis of Reissner-Mindlin plates is given by Falk [49]. The underlying mathematical reasoning for these methods can in most cases be found in analysis via mixed weak forms [50] where some combination of stresses, strains and displacements are treated as independent variational quantities. Simo et al. [46] give a mixed analysis of EAS-type methods and Chapelle and Bathe [40] give a mixed analysis of ANS/MITC-type methods.

It is well-known that upon moving to a mixed variational formulation that stability of a numerical method is no longer guaranteed and that a great deal of care must be taken in the design of such methods. The seminal work of Babuška on finite elements with Lagrange multipliers [51] and the later developments of Brezzi [52] describe in general terms the conditions needed for stability of numerical methods based upon mixed weak forms. A contemporary paper by Bathe and Brezzi [53] gives an overview of the stability conditions of mixed finite elements using linear algebra concepts before shifting across to a more rigorous functional analysis approach. Another paper by Arnold [50] covers similar ground but assumes some knowledge of functional analysis.

In the meshless literature various distinct procedures have been introduced to overcome the shear-locking problem. We will also discuss a few approaches in the meshless literature to the problem of volumetric locking which arises in incompressible elasticity problems, as it is related to the problem of shear-locking. We note that this is not an exhaustive review of papers which simulate shell or plate structures with meshless numerical methods, but an overview of those with a particular focus on novel methods for alleviating the shear-locking problem. The review paper by Tiago and Leitão [54] gives an in-depth overview of shear-locking in meshless numerical methods. A recent review paper with particular emphasis on the application of meshless methods to the simulation of laminated and functionally graded plates is given by Liew et al. [55].

One of the simplest methods for curing the shear-locking problem is increasing the polynomial consistency of the approximation. This method is equivalent to p-refinement in the FEM. Increasing the consistency of the approximating functions means that the Kirchhoff mode can be better represented and thus locking is partially alleviated. However, spurious oscillations can occur in the shear strains and the convergence rate is usually non-optimal [56]. Furthermore, high-order consistency meshless basis functions are more computationally expensive. This is due to the larger number of nodes that must be in the nodal support to ensure a well-posed basis function problem. This increase in support size then leads to an increase in the bandwidth of the assembled stiffness matrix [56]. Works using this approach in the hp-cloud context include those by Garcia et al. [57] for shear-deformable plates and Mendonça et al. [58] for shear-deformable beams. In the context of the element-free Galerkin (EFG) method this approach has also been used by Choi and Kim [59]. The p-refinement method has also seen widespread use in the isogeometric method, see eg. Benson et. al [60] for the Reissner-Mindlin (née Naghdi) shell model.

Another popular remedy is the matching fields method. In this approach the Kirchhoff mode is matched exactly by approximating the rotations using the derivatives of the basis functions used to approximate the transverse displacement. This idea was originally introduced by Donning and Liu [61] using cardinal spline approximation and later in the context of the EFG method by Kanok-Nukulchai et al. [56]. More recently the matching fields approach has been used by Bui et al. [62, 63]. However, as shown by Tiago and Leitão [64] using either the m-consistency condition II of Liu et al. [65] or the Partition of Unity concept of Babuška and Melenk [1], the resulting system of linear equations are always nearly singular because of a linear dependency in the basis functions for the rotations. This is because the basis functions for the rotations do not form a partition of unity [64]. A more elegant approach, and one without the drawbacks of the method of Kanok-Nukulchai et al. [56] has recently been introduced for the isogeometric method by Martinelli et. al [66]. In this approach the basis functions for the rotations and displacements are constructed using polynomial spline spaces such that they satisfy the Kirchhoff constraint exactly.

Nodal integration schemes integrate the weak form using points at the nodal positions of the meshless approximation. These schemes essentially work along the same lines as the reduced integration approach in finite elements. Beissel and Belytschko [67] showed that meshless reduced integration techniques can suffer from spurious modes, similar to their FE counterparts. Some form of stabilisation is required to neutralise these problems. Wang and Chen [68] introduced smoothed conforming nodal integration method (SCNI), a form of curvature smooth-

ing, to alleviate locking.

Some authors have modified the underlying plate model to bypass the problem of shear-locking entirely. This approach is called the change of variables approach. In the analysis of Timoshenko beams Cho and Atluri [69] use a change of dependent variables, from transverse displacement and rotation to transverse displacement and shear stress to bypass the problem of shear-locking. This approach has been extended to plates by Tiago and Leitão [64]. We note that the exact relationship between the plate model written with the displacement and shear stresses as primary variables and the standard Reissner-Mindlin model has not been studied in much depth at this point.

Another approach, and the one we use in this thesis, is to use a mixed formulation where fields such as stresses, strains and pressures, as well as the usual displacement fields, are treated as independent quantities in the weak form. In the field of meshless numerical methods this approach has primarily been applied to the problem of volumetric locking in nearly-incompressible elasticity problems. Vidal et al. [70] used diffuse derivatives to construct pseudo-divergence-free approximation for the displacement that would satisfy the incompressibility constraint a priori. González et al. enriched the displacement approximation in a Natural Element Method formulation [71]. The B-bar method from the FE literature [72] was introduced into the EFG method by Recio et al. [73]. Sorić and Jarak apply a mixed formulation in a three-dimensional solid shell formulation [74]. Recently Ortiz et al. [75, 76] constructed a method where the pressure variables are eliminated by calculating volume-averaged pressures across domains attached to a node to formulate a generalised displacement method. In this thesis we develop a generalisation of the volume-averaging technique of Ortiz et al. which we call the local-patch projection (LPP) procedure. We then use the LPP procedure to construct a generalised displacement method for the Reissner-Mindlin plate problem that is free from shear-locking.

1.5 Outline of this thesis

The aim of this thesis is to develop novel meshless numerical methods for the simulation of shear-deformable beam and plate structures that are free from the adverse effects of shear-locking. To do this we apply the canonical method used by many authors in the finite element method of using a mixed weak form where the shear stresses are treated as an independent variational quantity.

The remaining chapters of this thesis are structured as follows:

Chapter 2: An overview of meshless methods. In this chapter we give an overview of meshless methods, meshless basis function construction and imposing Dirichlet boundary conditions in meshless methods. Because they are a relatively new innovation in the field of meshless methods we give a particularly thorough overview of the maximum-entropy basis functions which are used throughout this thesis.

Chapter 3: A study of the shear-locking problem in the Timoshenko beam problem with meshless methods. In this chapter we study the Timoshenko beam problem which is the one-dimensional analogue of the Reissner-Mindlin plate problem. We perform numerical experiments showing the behaviour of meshless and finite element methods with respect to h and p refinement, and additionally in meshless methods the role of the support width. These fundamental experiments clearly identify the shear-locking behaviour of meshless numerical methods with respect to the meshless discretisation parameters.

Chapter 4: Meshless methods for the shear-deformable beam problem based on a mixed weak form. In this chapter we examine the ability of a mixed weak form to produce numerical methods for the Timoshenko beam problem that are free from the effects of shear-locking. We move from the primal or displacement form of the Timoshenko beam problem to a mixed form where the shear stresses are treated as independent variational quantities in the weak form. The proposed scheme is free from the effects of shear-locking.

Chapter 5: Meshless methods for the shear-deformable plate problem based on a mixed weak form. In this chapter we examine the ability of a mixed weak form to produce numerical methods for the Reissner-Mindlin plate problem that are free from the effects of shear-locking. To construct a conforming approximation of the shear stresses we use the lowest-order rotated Raviart–Thomas-Nédélec finite elements. Meshless maximum-entropy basis functions are used to discretise the displacements.

Chapter 6: Generalised displacement meshless methods for the shear-deformable plate problem. In this chapter we examine the use of a stabilised mixed weak form to construct a generalised displacement meshless method for the Reissner-Mindlin problem that is free from the effects of shear-locking.

At the end of the thesis we give some conclusions and suggest ideas for future research topics.

1.6 Published work

1.6.1 International journals

Hale, J. & Baiz, P. A locking-free meshfree method for the simulation of shear-deformable plates based on a mixed variational formulation. *Computer Methods in Applied Mechanics and Engineering* **241–244,** 311–322 (2012)
Hale, J. & Baiz, P. Mixed and generalised displacement meshfree methods for the simulation of shear-deformable beams. *(In preparation)*
Hale, J. & Baiz, P. A comparative study of the shear-locking behaviour of the displacement-based finite element and meshfree methods. *(In preparation)*
Ortiz, A. & Hale, J. Meshfree volume-averaged projection methods for nearly incompressible elasticity. *(In preparation)*

1.6.2 Conference papers and presentations

Hale, J. & Baiz, P. A meshless method for the Reissner-Mindlin plate equations based on a stabilized mixed weak form using maximum-entropy basis functions. *Proceedings of the European Congress on Computational Methods in Applied Sciences and Engineering* (Sept. 2012)
Hale, J. & Baiz, P. Maximum-entropy meshfree method for the Reissner-Mindlin plate problem based on a stabilised mixed weak form. *Proceedings of the Annual ACME UK Conference* (Mar. 2012) *First place, Best PhD Student Paper and Presentation Competition*
Hale, J. & Baiz, P. Simulation of shear deformable plates using meshless maximum entropy basis functions. *Proceedings of ECCOMAS Thematic Conference on the Extended Finite Element Method (XFEM)* (June 2011) *Second place, Best PhD Student Paper and Presentation Competition*

2 An overview of meshless methods

2.1 Introduction

In this chapter we give an overview of the construction of meshless numerical methods via the application of a weak or variational form. The distinct properties of different meshless basis functions, such as continuity, consistency and computational complexity greatly affect the performance of the resulting numerical method. We give a full treatment of these different properties and the mathematical construction of various common meshless basis functions.

2.2 Galerkin methods

2.2.1 Strong form to weak form

Consider a domain $\Omega \subset \mathbb{R}^d$ bounded by a surface Γ forming the closed region $\bar{\Omega}$. We can define a boundary value problem (BVP) as the problem of finding an unknown function $u : \bar{\Omega} \to \mathbb{R}$ such that [84]:

$$\mathcal{L}[u] = f \qquad \forall x \in \Omega \tag{2.1a}$$

$$u = \bar{u} \qquad \forall x \in \Gamma_D \tag{2.1b}$$

$$\frac{\partial u}{\partial n} = \bar{g} \qquad \forall x \in \Gamma_N \tag{2.1c}$$

where $\mathcal{L}$ is an operator of partial derivatives with respect to x and $f : \bar{\Omega} \to \mathbb{R}$ is a specified right hand side. Γ_D and Γ_N correspond to the portions of the boundary where Dirichlet and Neumann boundary conditions are applied respectively, such that $\Gamma_D \cup \Gamma_N = \Gamma$. n is the unit normal on the boundary Γ. We denote $d\Omega$ the volume measure in Ω and $d\Gamma$ the surface measure on Γ.

We now define a corresponding weak or variational form of the BVP by forming the inner

product of the PDE with an arbitrary test function v [84]:

$$\int_{\Omega} \left\{ \mathcal{L}[u] - f \right\} v \, d\Omega = 0 \tag{2.2}$$

Roughly speaking, we are requiring that the differential equation holds in an average sense across the domain Ω by using the test function v to weight the average and requiring the residual be equal to zero. This is why the method is often called the method of weighted residuals.

At this stage it is instructive to restrict our discussion to a specific BVP, in this case the well known elliptic Poisson equation where the differential operator $\mathcal{L}$ is defined as [84]:

$$\mathcal{L} := \Delta = \nabla^2 := \sum_{i=1}^{n} \frac{\partial^2 u}{\partial x_i^2} \tag{2.3}$$

Furthermore we assume homogeneous Dirichlet boundary conditions $\bar{u} = 0$ on all of the boundary $\Gamma_D = \Gamma$. Substituting $\mathcal{L}$ into the weak form gives [84]:

$$\int_{\Omega} \nabla^2 u \; v \, d\Omega = \int_{\Omega} f v \, d\Omega \tag{2.4}$$

Using the well known Green's identity (divergence theorem) we can show that the weak form of our BVP is: Find $u \in V$ such that:

$$\int_{\Omega} \nabla u \cdot \nabla v \, d\Omega = \int_{\Omega} f v \, d\Omega \; \forall v \in V \tag{2.5}$$

2.2.2 Sobolev spaces

In loose terms a function space qualifies certain classes of functions into groups called function spaces. A familiar function space for most engineers is the space of continuous functions denoted by $C^k(\Omega)$ which is the set of functions that are k times continuously differentiable in Ω. In the classical variational formulation solutions to the variational formulation are constructed in these $C^k(\Omega)$ spaces. This approach has numerous issues and the $C^k(\Omega)$ spaces are usually abandoned in favour of a more general definition of function spaces known as Sobolev spaces [84].

For a non-negative integer m the Sobolev space $H^m(\Omega)$ is defined as [84]:

$$H^m(\Omega) = \{v \in L^2(\Omega) \mid D^\alpha v \in L^2(\Omega), \forall\ |\alpha| \leq m\} \tag{2.6a}$$

$$D^\alpha = \frac{\partial^{|\alpha|}}{\partial x_1^{\alpha_1} \dots \partial x_d^{\alpha_d}} \tag{2.6b}$$

where α is a multi-index of order m and $L^2(\Omega)$ is the set of functions with bounded or finite square integral on Ω [84]:

$$L^2(\Omega) = \left\{ v \mid \int_\Omega |v|^2 d\Omega < \infty \right\} \tag{2.7}$$

In other words the Sobolev spaces are composed of functions and their weak derivatives up to order m that are finite or bounded. We can also define an inner product for the space $H^m(\Omega)$ [84]:

$$(u, v)_{H^m(\Omega)} = \sum_{|\alpha| \leq m} \int_\Omega (D^\alpha u) \cdot (D^\alpha v)\ d\Omega \tag{2.8}$$

which induces the following norm:

$$\|u\|_{H^m(\Omega)} = (u, u)^{1/2}_{H^m(\Omega)} = \sum_{|\alpha| \leq m} \left(\int_\Omega |(D^\alpha u)|^2\ d\Omega \right)^{1/2} \tag{2.9}$$

This requirement that the integrals of the functions be finite is intuitive given that most PDEs model physical behaviour where the energy integral must be bounded for the PDE to make sense [84].

For the specific weak form in section 2.2.2 to be well-posed we require that $V = H^1(\Omega)$, which means that any function in the space and its weak first derivatives are square integrable [84]:

$$H^1(\Omega) = \left\{ v \mid v \in L^2(\Omega), \frac{\partial v}{\partial x^i} \in L^2(\Omega), i = 1, \dots, n \right\} \tag{2.10}$$

with inner product:

$$(u, v)_{H^1(\Omega)} = \int_\Omega (uv + \nabla u \cdot \nabla v)\, d\Omega \tag{2.11}$$

which induces the norm:

$$\|u\|_{H^1(\Omega)} = \left(\int_\Omega |u|^2 + |\nabla u|^2\ d\Omega \right)^{1/2} \tag{2.12}$$

Furthermore because we have specified Dirichlet boundary conditions on the entire boundary Γ we can define the subset $H_0^1(\Omega) \subset H^1(\Omega)$ as [84]:

$$H_0^1(\Omega) = \{v \in H^1(\Omega) \mid v = 0 \ \forall x \in \Gamma\} \tag{2.13}$$

So after this brief discussion of Sobolev spaces we can write the variational problem in eq. (2.5) as: Find $u \in H_0^1(\Omega)$ such that [84]:

$$\int_\Omega \nabla u \cdot \nabla v \, d\Omega = \int_\Omega f v \, d\Omega \quad \forall v \in H_0^1(\Omega) \tag{2.14}$$

Comparing the strong formulation with the weak or variational formulation in eq. (2.14) we can see that the requirement that $u \in C^2(\Omega)$ has been weakened to that of $u \in H^1(\Omega)$. This makes the solution of the variational form easier than that of the strong form since it is less demanding on the regularity of the solution u [84].

Finally we re-write eq. (2.14) in the following standard form: Find $u \in H_0^1(\Omega)$ such that [84]:

$$a(u, v) = f(v) \ \ \forall v \in H_0^1(\Omega) \tag{2.15}$$

where $a(u, v)$ is a bilinear form and $f(v)$ is a linear form defined by:

$$a(u, v) = \int_\Omega \nabla u \cdot \nabla v \, d\Omega \tag{2.16a}$$

$$f(v) = \int_\Omega f v \, d\Omega \tag{2.16b}$$

2.2.3 Constructing a Galerkin numerical method

In the framework of Galerkin methods, we can split the construction of a numerical method into the following five steps:

1. Transfer the strong form of the PDE and boundary conditions into a weak or variational form.

   Problem 1 (Infinite dimensional weak form)**.** *Find $u \in \mathcal{U}$ such that:*

   $$a(u, v) = f(v) \quad \forall v \in \mathcal{V} \tag{2.17}$$

   where $\mathcal{U}$ and $\mathcal{V}$ are infinite dimensional function spaces.

2. Construct an appropriate basis φ_i and ψ_i such that $\mathcal{U}_h = \text{span}\{\varphi_i\}_{i=1}^N \subset \mathcal{U}$ and $\mathcal{V}_h = \text{span}\{\psi_i\}_{i=1}^M \subset \mathcal{V}$ respectively, allowing us to write u_h and v in the form:

$$u_h = \sum_{i=1}^{N} \varphi_i u_i \tag{2.18a}$$

$$v = \sum_{i=1}^{M} \psi_i \tag{2.18b}$$

Again, specific choices of how to construct this basis give rise to a huge number of numerical methods, such as finite element methods, discontinuous Galerkin methods, meshless methods, natural element methods, collocation methods and so on. Also note that the trial space $\mathcal{U}_h$ is not necessarily the same the test space $\mathcal{V}_h$, and these choices give rise to a whole host of numerical methods, such as Petrov-Galerkin methods, Bubnov-Galerkin methods, Rayleigh-Ritz methods, boundary element methods and so on.

3. Transfer the infinite dimensional problem to a finite dimensional one by introducing the subspaces $\mathcal{U}_h \subset \mathcal{U}$ and $\mathcal{V}_h \subset \mathcal{V}$. We can write the same variational formulation as before, but replacing the infinite spaces with these new finite dimensional subspaces:

Problem 2 (Finite dimensional weak form)**.** *Find $u_h \in U_h$ such that:*

$$a(u_h, v) = f(v) \quad \forall v \in \mathcal{V}_h \tag{2.19}$$

where $\mathcal{U}_h \subset \mathcal{U}$ and $\mathcal{V}_h \subset \mathcal{V}$ are finite dimensional function spaces with size $\dim(\mathcal{U}_h) = N$ *and* $\dim(\mathcal{V}_h) = M$.

The subscript h is used frequently in the Finite Element literature to denote the dependence of the vector spaces on the characteristic element size of the mesh. Note that it is also possible to make the choice $\mathcal{U}_h \not\subset \mathcal{U}$ or $\mathcal{V}_h \not\subset \mathcal{V}$ resulting in a non-conforming numerical method.

4. Substitute the basis into the finite dimensional weak form resulting in a linear system of equations. For the Bubnov-Galerkin type method where $\mathcal{U}_h = \mathcal{V}_h$:

$$\sum_{j=1}^{N} a(\varphi_j, \varphi_i) = f(\varphi_i), \quad i = 1, 2, \dots, N \tag{2.20}$$

or alternatively:

$$\boldsymbol{K}\boldsymbol{u} = \boldsymbol{f} \tag{2.21}$$

where $\boldsymbol{K}$ is sometimes called the stiffness matrix, $\boldsymbol{u}$ is the solution vector and $\boldsymbol{f}$ is the force vector.

5. Solve the linear system of equations to find the vector of unknowns $\boldsymbol{u}$.

Now that we have discussed how to construct a Galerkin numerical method in a general sense we move on to the problem of constructing the finite dimensional subspace $\mathcal{U}_h$ using meshless methods.

2.3 Constructing a meshless basis

The construction of a meshless basis typically begin by discretising the domain into a set $\mathcal{N}_h$ of N nodes or points located at positions x^i in the domain $\bar{\Omega}$, where $\bar{\Omega}$ is the closure of the domain $\Omega \subset \mathbb{R}^n$ for $n = 1, 2, 3$:

$$\mathcal{N}_h = \{x^1,\ x^2,\ x^3,\ \ \dots,\ x^N\}, \quad x^i \in \overline{\Omega} \tag{2.22}$$

We mimic the tradition from the finite element literature of subscripting with h to denote some form of characteristic length which describes the node set. We associate each node in the set $\mathcal{N}_h$ with a region ω_i in the neighbourhood of x^i which we call the support domain:

$$\omega = \{\omega_1,\ \omega_2,\ \omega_3,\ \ \dots,\ \omega_N\}, \quad \omega_i \subset \bar{\Omega} \tag{2.23}$$

The support domains ω must form a covering of the domain $\bar{\Omega}$:

$$\bar{\Omega} \subseteq \bigcup_{i=1}^{N} \omega_i \tag{2.24}$$

Note that there is no requirement that the union of the support domains exactly cover the original domain.

Throughout this work we use circular support domains which can be uniquely described by a radius of support. Therefore instead of associating each node in the node set with a support domain, we explicitly associate each node in the node set with a support radius ρ_i:

$$\rho = \{\rho_1,\ \rho_2,\ \rho_3,\ \ \dots,\ \rho_N\}, \quad \rho_i \in \mathbb{R}^+ \tag{2.25}$$

Basis	Kronecker delta	Continuity	Compact support	Consistency	Pass patch test
MLS	No	$\boldsymbol{p} \in C^k(\Omega),\ w_i \in C^l(\Omega) \therefore \varphi \in C^{\min(k,l)}(\Omega)$	Yes	Yes, trivial to C^k	Yes
MaxEnt	Yes, weak	C^∞	Yes	first-order	Yes
RBF	Yes	Dependent on RBF $\psi \in C^l(\Omega)$	No	No	No
CSRBF	Yes	Dependent on CSRBF $\psi \in C^l(\Omega)$	Yes	No	No
RPIM	Yes	C^{-1}	Yes	Yes	No

Table 2.1: Summary of properties of various meshless basis functions

Then for any general point in the domain $x \in \bar{\Omega}$ we can define the connectivity set S_h as a subset of the overall node set $\mathcal{N}_h$:

$$S_h = \left\{ \mathcal{N}_h \mid \left\| x - x^i \right\| \leq \rho_i \right\} \tag{2.26}$$

With this notation established we can now use a multitude of methods to define a meshless basis constructed from the pairing of the node set $\mathcal{N}_h$ and associated support radius vector ρ.

2.4 Mathematical properties of meshless basis functions

Before continuing to discuss specific methods for constructing meshless basis functions we will outline some of the general mathematical properties of meshless basis functions. In table 2.1 we give a summary of these properties for specific methods. In the following sections we will discuss the construction and properties of different methods in detail.

Kronecker-delta property

The basis functions φ_i are said to verify the Kronecker-delta property if the following holds [85]:

$$\varphi_i(x^j) = \delta_{ij} \quad \forall\ i, j \tag{2.27}$$

$$\delta_{ij} = \begin{cases} 1 & i = j \\ 0 & i \neq j \end{cases} \tag{2.28}$$

Futhermore if the basis functions do satisfy the Kronecker-delta property then:

$$u_h(x^j) = \sum_{i \in S_h} \varphi_i(x^j) u_i \tag{2.29}$$

$$= \sum_{i \in S_h} \delta_{ij} u_i \tag{2.30}$$

$$= u_j \tag{2.31}$$

Meshless basis functions do not always satisfy the Kronecker-delta property. Therefore we find that $u_h(x^i) \neq u_i$ and imposing essential boundary conditions is not as trivial as in the finite element method. We will explain why this is the case now.

Let $\mathcal{B}$ be the set of all of the indices of the nodes that lie on the boundary Γ_D with prescribed Dirichlet boundary conditions [85]:

$$\mathcal{B} = \left\{ \mathcal{N}_h \mid x^i \in \Gamma_D \right\} \tag{2.32}$$

We now let φ_i be basis functions that do satisfy the Kronecker-delta property. We can write our function approximation for any $x \in \bar{\Omega}$ by splitting the summation between the nodes that are on the boundary $j \in \mathcal{B}$ and those that are not $i \notin \mathcal{B}$ [85]:

$$u_h(x) = \sum_{i \in S_h} \varphi_i(x) u_i = \sum_{i \notin \mathcal{B}} \varphi_i(x) u_i + \sum_{j \in \mathcal{B}} \varphi_j(x) \bar{u}(x^j) \tag{2.33}$$

Due to the Kronecker-delta property for all of the nodes not on the boundary $i \notin \mathcal{B}$ we know that $\varphi_i \in H_0^1(\Omega)\ \forall i \notin \mathcal{B}$. Thus the approximation written above gives $u = \bar{u}$ at the nodes on the boundary Γ_D if and only if the approximation satisfies the Kronecker-delta property [85]. If the approximation does not satisfy the Kronecker-delta property then imposing $u = \bar{u}$ and $v(x) = 0$ on Γ_D is not as straightforward, and the standard bilinear weak form in eq. (2.19) cannot be used [85]. There are various modified variational forms that can overcome this problem and these are discussed in section 2.11.

Continuity

Continuity defines the smoothness of the approximation. A function is called $C^n(\Omega)$ continuous if all j of its derivatives $0 \leq j \leq n$ exist and are continuous in the entire domain Ω [86].

Consistency

Consistency is the capability of an approximation scheme to exactly reproduce a polynomial function of certain order locally within the elements or cells that make up the entire problem domain [4]. A certain minimum level of consistency is required to solve a particular PDE. For a PDE of order $2k$, weakened using the standard Garlerkin technique, we require that the approximation is at least k consistent. If an approximation is called k-order complete then it is consistent from zero to k.

An absolute requirement for any approximation scheme is that it can reproduce constant functions exactly:

$$\sum_{i \in S_h} \varphi_i(x) \cdot 1 = 1 \quad \forall x \tag{2.34}$$

If an approximation can fulfil this requirement then it is called zero-order consistent. This property is also called the partition of unity property.

Furthermore we might require the approximation to be first and second order consistent:

$$\sum_{i \in S_h} \varphi_I(x) \cdot x = x \quad \forall x \tag{2.35}$$

$$\sum_{i \in S_h} \varphi_I(x) \cdot x^2 = x^2 \quad \forall x \tag{2.36}$$

Second-order consistency is particularly desirable in the solution of the fourth-order PDEs found in plate and beam theories where partial derivatives of 2nd order appear in the variational or weak form.

Interpolation or approximation

This difference between interpolation and approximation is a subtle distinction and it is common to see these terms used interchangeably. Given a function $w \in \mathcal{V}$ where $\mathcal{V}$ is a function space, an interpolant $\mathcal{I}_h$ creates a function that lives in a finite subspace $\mathcal{V}_h \subset \mathcal{V}$ with N dimensions, such that $\mathcal{I}_h w \in \mathcal{V}_h$ [4]:

$$\mathcal{I}_h w(x) = \sum_{i=1}^{N} \varphi_i(x) w(x^i) \tag{2.37}$$

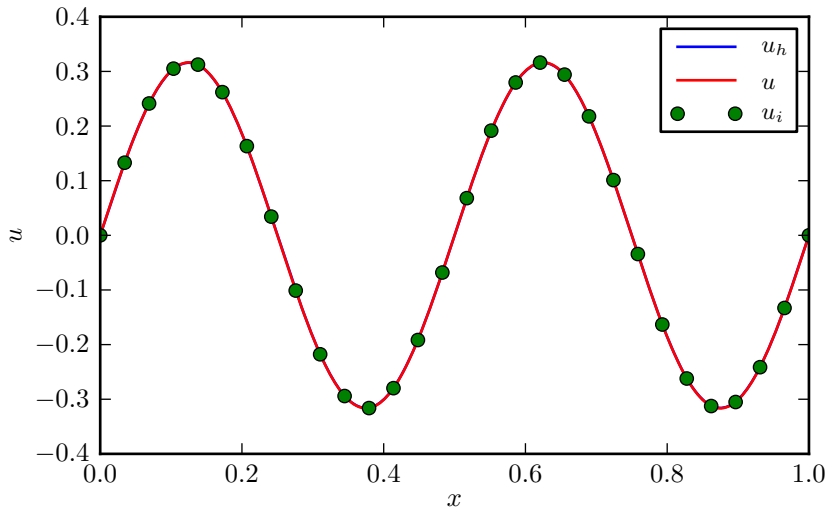

Figure 2.1: Oscillatory function u interpolated using RPIM basis functions on unit interval with $N = 30$ nodes and constant support size $\rho = 0.1$. The interpolated function u_h is nearly indistinguishable from the function u in this plot. The values of the unknown vector are equal to the approximated function itself, ie. $u_i = u_h(x^i)$.

and satisfies the following interpolation condition:

$$\mathcal{I}_h w(x^i) = w(x^i) \quad i = 1, 2, \dots, N \tag{2.38}$$

In other words, an interpolant creates a function w_h that passes through the nodal values of w exactly. Conversely, an approximate creates a new function that does not pass through the nodal values exactly. It should be clear that to satisfy eq. (2.38) we require that the interpolant $\mathcal{I}_h$ has the Kronecker-delta property. In fig. 2.1 we show a meshless interpolation of an oscillating function, and in fig. 2.2 we show a meshless approximation of the same oscillating function.

Computational cost

Every computational algorithm has an associated computational cost. We can expect that each method of constructing meshless basis functions will use varying amounts of resources, and thus speed and memory usage might be a factor in choosing the meshless basis function. Little information in the literature is available comparing different construction methods. Producing accurate, and most importantly fair, measurements can be difficult.

However, we can say a few things with some certainty. Firstly, meshless basis functions gen-

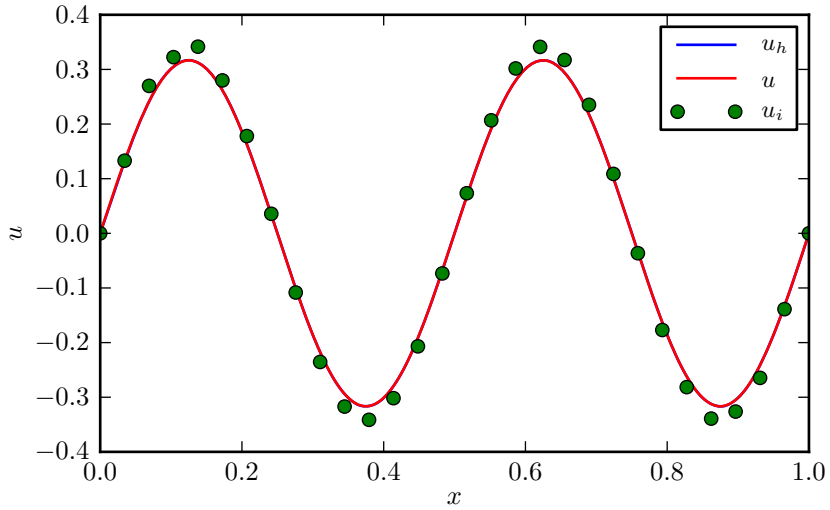

Figure 2.2: Oscillatory function u approximated using MaxEnt basis functions on unit interval with $N = 30$ nodes and constant support size $\rho = 0.1$. The approximated function u_h is nearly indistinguishable from the function u in this plot. The values of the unknown vector are not equal to the approximated function itself, ie. $u_i \neq u_h(x^i)$.

erally involve some computationally intensive process, such as matrix inversion or optimisation in multiple variables, which must be carried out at every integration point in the domain. This means that meshless basis functions are almost always more expensive to compute per evaluation than finite element basis functions which are usually pre-calculated on the reference element $\hat{K}$. The primary cost is then the push-forward from the reference element to the global element in the mesh.

Second of all, the total computational time of all of the meshless basis function evaluations scales linearly with the number of integration points in the domain, that is, with n integration points the complexity of the algorithm is of $O(n)$. The solution of a linear system with n nodes scales at anywhere between $O(n \log n)$ and $O(n^3)$ depending on the properties of the linear system to be solved and the algorithm used. Thus we can say with some certainty that as problem size increases the assembly and solution of the linear system begins to dominate the total amount of computational resources used for the computation of the basis functions. Finally, the evaluation of the basis functions at all the integration points is relatively trivial to parallelise across multiple computing cores, so if we need to speed up the shape function construction we can expect to see roughly linear scaling with the number of computing nodes.

All these factors mean that as long as the algorithms used to construct meshless basis func-

tions are comparable on speed to roughly the same order of magnitude, the mathematical properties mentioned above should probably dominate the selection criteria.

2.5 Moving least-squares

The Moving Least-Squares (MLS) method has its origins in scattered data approximation. A zero-order complete MLS method was introduced by Shepard [29], before being generalized to m-th order consistency by Lancaster and Salkauskas [13]. Shepard's method [29] is a specific case of the more general method presented by Lancaster and Salkauskas [13]. The MLS approximation scheme is used in the Element Free Galerkin (EFG) method [16] as well as many other meshless and particle methods.

Construction

We can define a local approximation $u_h \colon \Omega \to \mathbb{R}^d$ of the function $u \colon \Omega \to \mathbb{R}^d$ at a point $x \in \Omega$ as:

$$u_h(x) = \boldsymbol{p}^T(x) \cdot \boldsymbol{a}(x) \tag{2.39}$$

where $\boldsymbol{p}^T(x)$ is a complete vector of polynomials of order m. For example, in $\mathbb{R}^2$ where $x = \{x_1, x_2\}$ the complete second order polynomial vector is:

$$\boldsymbol{p}^T(x) = \begin{bmatrix} 1 & x_1 & x_2 & x_1 x_2 & x_1^2 & x_2^2 \end{bmatrix} \tag{2.40}$$

The vector $\boldsymbol{a}(x)$ contains non-constant coefficients that depend on x:

$$\boldsymbol{a}^T(x) = \begin{bmatrix} a_0(x) & a_1(x) & a_2(x) & a_3(x) & \dots & a_m(x) \end{bmatrix} \tag{2.41}$$

The key thing to note about eq. (2.39) is that the coefficients $\boldsymbol{a}(x)$ are a function of x and therefore vary throughout the domain Ω. It is this property that gives the prefix moving to the standard least-squares minimisation procedure from elementary statistics.

We now define a weighting function $w(x - x^i)$ centred at each node. This gives nodes nearest to x the highest influence, whilst those further away have little or even no influence.

We now proceed to find the coefficients $\boldsymbol{a}(x)$ by posing a minimisation of the weighted least-

squares function J:

$$J(x) = \sum_{i \in S_h} w_i(x - x^i) \left[u_h(x^i, x) - u_i\right]^2 \tag{2.42}$$

$$= \sum_{i \in S_h} w_i(x - x^i) \left[\boldsymbol{p}^T(x) \cdot \boldsymbol{a}(x) - u_i\right]^2 \tag{2.43}$$

The minimisation problem we are trying to solve is to find the coefficients $\boldsymbol{a}^*(x)$ such that:

$$\boldsymbol{a}^*(x) = \arg\min_{\boldsymbol{a}} J(x) \tag{2.44}$$

We will show that this minimisation problem has a semi-analytical solution.

Weighting Function

It is the weighting function at each node i $w_i(x - x^i)$ that makes the MLS approximation a local approximation scheme. More specifically, we define a function for each node $w_i \colon \Omega \mapsto \mathbb{R}$ with the following properties:

$$w_i(x - x^i) = \begin{cases} 1 & x = x^i \\ 0 & x - x^i \geq \boldsymbol{\rho}_i \end{cases} \tag{2.45a}$$

$$\frac{\mathrm{d}w_i}{\mathrm{d}x}(x - x^i = 0) = \frac{\mathrm{d}w_i}{\mathrm{d}x}(x - x^i = \rho_i) = 0 \tag{2.45b}$$

$$w_i(b) < w_i(a) \quad \forall \{a, b \in [x^i, \rho_i] \mid b > a\} \tag{2.45c}$$

$$\lim_{\rho \to 0} w_i(x - x^i) \to \delta(x - x^i) \tag{2.45d}$$

$$C^k \text{ continuous} \qquad k \geq 0 \tag{2.45e}$$

where $\boldsymbol{\rho}_i$ defines the support size of node i. eq. (2.45c) states that the function must be monotonically decreasing. An example of a weighting function, commonly used in the EFG literature,

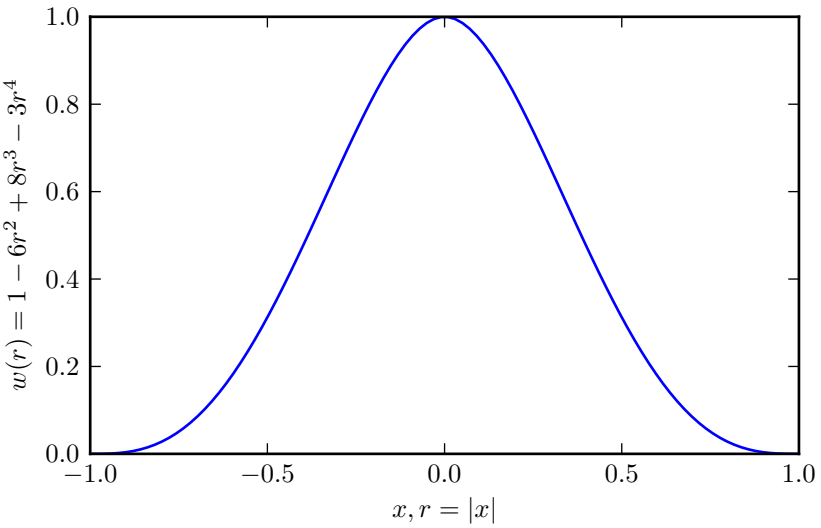

Figure 2.3: Quartic spline weight function

is the quartic spline with circular support centred at x^i, as shown in fig. 2.3:

$$w_i(r) = \begin{cases} 1 - 6r^2 + 8r^3 - 3r^4 & r \leq 1 \\ 0 & r > 1 \end{cases} \tag{2.46a}$$

$$r = \frac{\|x - x^i\|}{\rho_i} \tag{2.46b}$$

From the definition of the weight function we can now define the connectivity set S_h at a general point $x \in \bar{\Omega}$ as a subset of the overall node set $\mathcal{N}_h$ associated with a non-zero weight function w_i at x:

$$S_h = \{\mathcal{N}_h \mid w_i(x - x^i) \neq 0\} \tag{2.47}$$

and we can then define the number of nodes n that contribute to the approximation at point x as:

$$n = |S_h| \tag{2.48}$$

Solution

We can now write the summation in eq. (2.43) in an equivalent matrix form where:

$$J = \frac{1}{2}\left(\boldsymbol{P}\boldsymbol{a} - \boldsymbol{u}\right)^T \boldsymbol{W}\left(\boldsymbol{P}\boldsymbol{a} - \boldsymbol{u}\right) \tag{2.49a}$$

$$\boldsymbol{P} = \begin{bmatrix} p_1(x^1) & p_2(x^1) & \dots & p_m(x^1) \\ p_1(x^2) & p_2(x^2) & \dots & p_m(x^2) \\ \vdots & \vdots & \ddots & \vdots \\ p_1(x^n) & p_2(x^n) & \dots & p_m(x^n) \end{bmatrix} \tag{2.49b}$$

$$\boldsymbol{W} = \begin{bmatrix} w_1(x - x^1) & & & 0 \\ & w_2(x - x^2) & & \\ & & \ddots & \\ 0 & & & w_n(x - x^n) \end{bmatrix} \tag{2.49c}$$

$$\boldsymbol{u}^T = \begin{bmatrix} u_0(x) & u_1(x) & u_2(x) & u_3(x) & \dots & u_n(x) \end{bmatrix} \tag{2.49d}$$

$$\boldsymbol{a}^T = \begin{bmatrix} a_0(x) & a_1(x) & a_2(x) & a_3(x) & \dots & a_m(x) \end{bmatrix} \tag{2.49e}$$

We now find the minimum of function J with respect to the unknown approximation coefficients $\boldsymbol{a}$:

$$\begin{aligned} \frac{\partial J}{\partial \boldsymbol{a}} &= (\boldsymbol{P}\boldsymbol{a} - \boldsymbol{u})^T \boldsymbol{W}\boldsymbol{P} = \boldsymbol{0} \\ &\Rightarrow \boldsymbol{P}^T\boldsymbol{W}\boldsymbol{P}\boldsymbol{a} = \boldsymbol{P}^T\boldsymbol{W}\boldsymbol{u} \end{aligned} \tag{2.50}$$

We now define:

$$\boldsymbol{A} = \boldsymbol{P}^T\boldsymbol{W}\boldsymbol{P} \tag{2.51a}$$

$$\boldsymbol{B} = \boldsymbol{P}^T\boldsymbol{W} \tag{2.51b}$$

And therefore the solution for the coefficients $\boldsymbol{a}(x)$ is:

$$\boldsymbol{a} = \boldsymbol{A}^{-1}\boldsymbol{B}\boldsymbol{u} \tag{2.52}$$

Substituting back into the original approximation eq. (2.39) gives the final approximation as:

$$u_h(x) = \boldsymbol{p}^T(x) \cdot \boldsymbol{A}^{-1}(x)\boldsymbol{B}(x)\boldsymbol{u} \tag{2.53}$$

We can write this in the more familiar form:

$$u_h(x) = \sum_{i \in S_h} \varphi_i(x) u_i \tag{2.54a}$$

$$\boldsymbol{\varphi}(x) = \boldsymbol{p}^T(x) \boldsymbol{A}^{-1}(x) \boldsymbol{B}(x) \tag{2.54b}$$

Derivatives of the basis functions can be found by repeated application of the chain rule to eq. (2.54b):

$$\boldsymbol{\varphi}^T_{,k} = \boldsymbol{p}^T_{,k} \boldsymbol{A}^{-1} \boldsymbol{B} + \boldsymbol{p}^T \boldsymbol{A}^{-1}_{,k} \boldsymbol{B} + \boldsymbol{p}^T \boldsymbol{A}^{-1} \boldsymbol{B}_{,k} \tag{2.55a}$$

$$\boldsymbol{A}^{-1}_{,k} = -\boldsymbol{A}^{-1} \boldsymbol{A}_{,k} \boldsymbol{A}^{-1} \tag{2.55b}$$

$$\boldsymbol{A}_{,k} = \boldsymbol{P}^T \boldsymbol{W}_{,k} \boldsymbol{P} \tag{2.55c}$$

$$\boldsymbol{B}_{,k} = \boldsymbol{P}^T \boldsymbol{W}_{,k} \tag{2.55d}$$

where $_{,k}$ refers to partial differentiation in direction k:

$$_{,k} = \frac{\partial}{\partial x_k} \tag{2.56}$$

In fig. 2.4 we show the basis functions constructed using the MLS method outlined above. For comparison in fig. 2.5 we show the standard linear Lagrangian finite element basis functions constructed on the triangulation of the same node set.

In this thesis we will refer to an approximation space constructed using the above moving least-squares method eq. (2.54b) of order p on a specified node set $\mathcal{N}_h$ with N nodes in the problem domain Ω with associated support radius vector ρ as:

$$MLS_p(\Omega; \mathcal{N}_h, \rho) := \text{span} \{\varphi_i\}_{i=1}^N \tag{2.57}$$

Consistency

One of the primary advantages of the MLS approximation is that it is trivial to build approximations of very high order consistency simply by increasing the order of the polynomial basis $\boldsymbol{p}(x)$ and the weight function w_I. This is particularly attractive in the context of plate and shell systems as building basis functions with C^1 continuity that also fulfil second order consistency

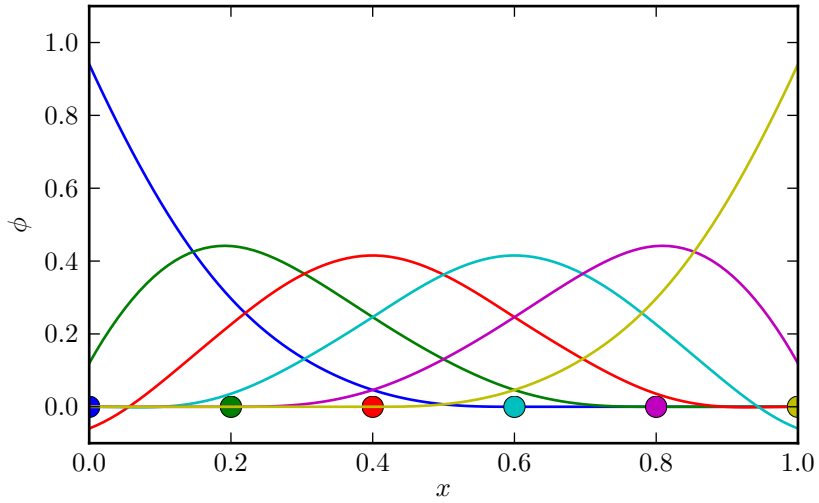

Figure 2.4: Basis functions constructed using first-order MLS method on unit interval with 6 evenly spaced nodes and uniform support size. Note the lack of Kronecker-delta property and the non-vanishing contributions of the basis functions associated with the internal nodes on the boundary of the domain.

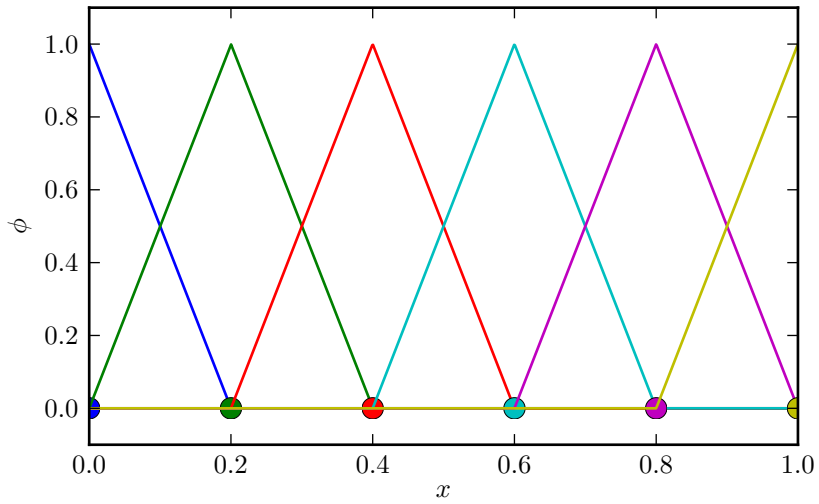

Figure 2.5: Basis functions constructed using P_1 finite element method on unit interval with 6 evenly spaced nodes (5 elements). This basis has the Kronecker-delta property both on the boundary and on the inside of the domain.

is straightforward.

Continuity

It has been shown [13] that if $\boldsymbol{p} \in C^k(\Omega)$ and $w_I \in C^l(\Omega)$ then the basis functions are $\varphi \in C^{\min(k,l)}(\Omega)$. For example, if we are using the fourth order spline $w_I \in C^2(\Omega)$ and a first order polynomial basis $\boldsymbol{p}(x) = [1 \quad x^1]$ and $x = [x^1]$, which implies that $\boldsymbol{p} \in C^1(\Omega)$, our final MLS approximant will be $\boldsymbol{\varphi} \in C^1(\Omega)$.

Kronecker-delta property

The MLS approximants do not satisfy the Kronecker-delta property, meaning that in general:

$$u^h(x^i) \neq u_i \quad \forall i \tag{2.58}$$

Therefore we need to use special methods for imposing the essential boundary conditions on Γ_D when using the standard MLS approximants in a Galerkin formulation.

However, by using a singular weighting function $\lim_{x \to x^I} w_I \to \infty$ Lancaster and Saulskus [13] showed that the Kronecker-delta property could be obtained with MLS-based approximants. A singular weight function is used successfully in [87] and [88] as the basis for an EFG formulation. However Most and Bucher [89] state that using a singular weighting function produces highly singular coefficient matrices $\boldsymbol{A}$ at the nodes x^I. Their solution is to introduce a regularized weighting function in [90] that allows very close approximation of the Kronecker Delta property.

Computational complexity

To efficiently compute the MLS basis functions the formulas used above should not be used directly as they require large numbers of matrix-matrix multiplications and the direct computation of the matrix inverse of $\boldsymbol{A}$. Belytschko et al. [91] demonstrate a method for the efficient computation of MLS basis functions that utilises a single LU decomposition and repeated back substitution with matrix-vector multiplication to find the derivatives of the basis functions.

2.6 Shepard functions

Shepard functions are the zero-order consistent variant of the MLS approximation. If we let:

$$p(x) = 1 \tag{2.59}$$

then the resulting Shepard basis functions are given by:

$$\varphi_i(x) = \frac{w_i(x - x^i)}{\sum_j^N w_j(x - x^j)} \tag{2.60}$$

The primary advantage of Shepard's method is that no matrix inversion is required and therefore the computational complexity compared to a p-order consistent MLS approximation with $p \geq 1$ is far lower. However, the zero-order consistency means that the Shepard functions are not able to solve even a second order BVP. One solution to this problem is to extrinsically enrich the Shepard functions to the required consistency using the partition of unity approach [1].

2.7 Maximum-Entropy method

Background

Shannon's [92] measure of informational entropy was postulated by Jaynes [93] as a means of least-biased statistical inference when insufficient information about a probability distribution is available. The Shannon entropy H of a discrete probability distribution $\boldsymbol{p} = \{p_1, p_2, \dots, p_n\}$ associated with N events $\boldsymbol{x} = \left\{x^1, x^2, \dots, x^N\right\}$ is defined by:

$$H(\boldsymbol{p}) = E(-\ln \boldsymbol{p}) = -\sum_{i=1}^{N} p_i \ln p_i \tag{2.61}$$

where E is the usual expectation function. Jaynes proposed that in the case when insufficient information is available, the least-biased probability distribution $\boldsymbol{p}$ is the one that maximises Shannon's measure of entropy $H(\boldsymbol{p})$ subject to the known prior information about the distribution [93]. Shannon originally introduced his measure of uncertainty in the context of communication theory [92], and it has been widely applied in fields as diverse as biology [94] and machine learning [95].

The maximum-entropy postulate is best explained using a few simple examples from elementary probability. Consider a situation where we have no prior information about a particular pdf $\boldsymbol{p}$ with n possible outcomes. In this case it would seem logical to propose that each outcome is equally likely ($p_i = 1/n$) given that we have no information that would suggest otherwise. And indeed the maximum informational entropy, $\max[S(\boldsymbol{p})]$, occurs when $p_i = 1/n$.

A more interesting example occurs when we do have some testable information. The Brandeis dice problem was introduced by Jaynes during his 1962 lecture series on the maximum-entropy principle [96]. Consider an unfair 6-sided die with $n = 6$ outcomes $x = \{1, 2, 3, 4, 5, 6\}$ associated with the unknown discrete pdf $\boldsymbol{p} = \{p_1, p_2, p_3, p_4, p_5, p_6\}$. We wish to find the most likely pdf $\boldsymbol{p}$ given the information I that the expected value of the probability distribution is 4.5:

$$I = E[x] = \sum_{i=1}^{N} x^i p_i = 4.5 \tag{2.62}$$

This type of problem has a general solution originally proposed by Gibbs in the context of statistical mechanics. Given constraints that consist of specifying the mean values F_k of m functions $\{f_1(x), f_2(x), \dots, f_m(x)\}$:

$$\sum_{i=1}^{n} p_i f_k(x^i) = F_k \qquad k = 1, \dots, m \tag{2.63}$$

the solution can be found using the method of Lagrange multipliers $\{\lambda_1, \dots, \lambda_m\}$:

$$P_i = \frac{1}{Z(\lambda_1, \dots, \lambda_m)} \exp\left[-\lambda_1 f_1(x^i) + \dots + -\lambda_m f_m(x^i)\right] \tag{2.64}$$

where $Z(\lambda_1, \dots, \lambda_m)$ is called the partition function and is defined by:

$$Z(\lambda_1, \dots, \lambda_m) = \sum_{i=1}^{N} \exp\left[\lambda_1 f_1(x^i) + \dots + \lambda_m f_m(x^i)\right] \tag{2.65}$$

and the Lagrange multipliers can be determined via a system of m simultaneous equations:

$$\frac{\partial}{\partial \lambda_k} Z(\lambda_1, \dots, \lambda_m) = F_k \qquad k = 1, \dots, m \tag{2.66}$$

We can apply this general framework to the Brandeis dice problem by letting $m = 1$, $N = 6$,

$f_1 = \{1, 2, 3, 4, 5, 6\}$ and $\sum_{i=1}^{N} p_i f_1(x^i) = 4.5$. Our partition function, $Z(\lambda)$ is [96]:

$$Z(\lambda) = \sum_{i=1}^{6} \exp(-i\lambda) \tag{2.67}$$

$$= x + x^2 + x^3 + x^4 + x^5 + x^6 \tag{2.68}$$

$$= x\frac{1 - x^6}{1 - x} \tag{2.69}$$

where $x = \exp(-\lambda)$ and the final form was found using the geometric series expansion. We now proceed to find the value of λ [96]:

$$-\frac{\partial}{\partial\lambda} \ln Z = -\frac{\partial}{\partial\lambda} \ln\left[x \cdot \frac{1 - x^6}{1 - x}\right] \tag{2.70}$$

$$= \frac{1 - 7x^6 + 6x^7}{(1 - x)(1 - x^6)} \tag{2.71}$$

$$= 4.5 \tag{2.72}$$

This results in the equation [96]:

$$3x^7 - 5x^6 + 9x - 7 = 0 \tag{2.73}$$

with solution $x = 1.44925$ giving $Z = 26.66365,\ \lambda = -0.37105$. The final least-biased probability distribution according to Jaynes' maximum-entropy principle that also satisfies the constraints can therefore be calculated by [96]:

$$p_i = \frac{1}{Z} \exp(-\lambda f_i) \tag{2.74}$$

$$\boldsymbol{p} = \{0.05435, 0.07877, 0.11416, 0.16545, 0.23977, 0.34749\} \tag{2.75}$$

Jaynes states that this distribution "represents a state of knowledge in which one has only (1) the enumeration of the six possibilities; and (2) the mean value constraint; and no other information. The distribution is maximally non-commital with respect to all other matters; it is as uniform (by the criterion of the Shannon information measure) as it can get without violating the given constraint" [96].

In the first paper by Sukumar [97] the principle of maximum-entropy was used to generate interpolants on polygonal convex domains. In the context of constructing a meshless approx-

imation scheme, Sukumar [97] established that the basis functions φ_i could be identified as discrete probabilities p_i associated with the nodes located at x^i. In the words of Sukumar et al. [98]: "the basis function value φ_i is viewed as the probability of influence of a node i located at a point x^i." With this identification made, Sukumar [97] employed Jaynes' principle of maximum-entropy inference to generate a least-biased meshless basis.

Arroyo and Ortiz [21] then introduced a modified entropy functional of the form:

$$H(\boldsymbol{\varphi}, x) = -\sum_{i=1}^{N} \varphi_i(x) \ln \varphi_i(x) - \beta(x) \sum_{i=1}^{N} \varphi_i(x) \left\| x^i - x \right\|^2 \tag{2.76}$$

where $\beta(x) \in \mathbb{R}$ is a parameter that can be varied to adjust the support width of the meshless basis functions. When $\beta \to \infty$ the Delaunay (linear finite element) interpolant is obtained, and for $\beta \to 0$ Shannon's standard measure of entropy is recovered. Adjustment of the parameter $\beta(x)$ across the domain can allow for seamless transition between regions discretised using finite elements and regions discretised with meshless basis functions.

Later, in the most general approach, Sukumar and Wright [99] proposed the use of a relative entropy functional which allows the choice of any sufficiently smooth prior weight function w_i associated with each node i:

$$H(\boldsymbol{\varphi}, \boldsymbol{w}) = -\sum_{i=1}^{N} \varphi_i(x) \ln \left(\frac{\varphi_i(x)}{w_i(x)} \right) \tag{2.77}$$

It can easily be shown that for the choice of a Gaussian Radial Basis Function (RBF) for the prior weight function $w_i(x) = \exp(-\beta(x) \left\| x^i - x \right\|^2)$ the modified entropy functional eq. (2.76) of Arroyo and Ortiz may be recovered [99]. In this thesis we use the C^2 quartic spline as our prior weight function:

$$w_i(r) = \begin{cases} 1 - 6r^2 + 8r^3 - 3r^4, & 0 \leq r \leq 1 \\ 0, & r > 1 \end{cases} \tag{2.78}$$

where $r = \left\| x^i - x \right\| / \rho_i$ and ρ_i is the support radius of node i.

Construction

We follow the approach of Sukumar and Wright [99] to construct the basis functions, and a brief overview is given here. The maximum-entropy basis functions φ_i may be found from the solution of a convex optimisation problem of the form [99]:

$$\min_{\varphi \in \mathbb{R}^n_+} \sum_{i=1}^{N} \varphi_i(x) \ln\left(\frac{\varphi_i(x)}{w_i(x)}\right) \tag{2.79a}$$

subject to the constraints [99]:

$$\sum_{i=1}^{N} \varphi_i(x) = 1 \tag{2.79b}$$

$$\sum_{i=1}^{N} \varphi_i(x) x^i = x \tag{2.79c}$$

$$\varphi_i(x) \geq 0 \quad \forall i, x \tag{2.79d}$$

Constraint eq. (2.79b) is the same as the condition of partition of unity and constraint eq. (2.79d) is required to ensure that the basis functions can be interpreted as probabilities in the context of Shannon's entropy functional. Constraint eq. (2.79c) ensures that the basis functions can exactly reproduce linear polynomials.

The resulting convex optimisation problem is solved numerically using standard techniques from the convex optimisation literature by considering the dual formulation, see eg. Boyd and Vandenberghe [100]. The solution is [99]:

$$\varphi_i(x) = \frac{Z_i(x;\boldsymbol{\lambda})}{Z(x;\boldsymbol{\lambda})} \tag{2.80a}$$

$$Z_i(x,\boldsymbol{\lambda}) = w_i(x) \exp\left(-\boldsymbol{\lambda} \cdot (x - x^i)\right) \tag{2.80b}$$

$$Z(x;\boldsymbol{\lambda}) = \sum_{i=1}^{N} Z_i(x,\boldsymbol{\lambda}) \tag{2.80c}$$

where $\boldsymbol{\lambda} = [\lambda_1, \lambda_2, \ldots, \lambda_d]^T$ is a vector of Lagrange multipliers and d is the dimensionality of the domain. The solution for the Lagrange multipliers $\boldsymbol{\lambda}^*$ can be found from the following optimisation problem:

$$\boldsymbol{\lambda}^* = \arg\min \ \ln Z(\boldsymbol{\lambda}) \tag{2.81}$$

Denoting $\boldsymbol{\varphi}^*$ as the basis function solution corresponding to the Lagrange multipliers $\boldsymbol{\lambda}^*$ calculated at a particular point x we can then write the basis functions as:

$$\varphi_i^*(x) = \frac{Z_i(x;\boldsymbol{\lambda}^*)}{Z(x;\boldsymbol{\lambda}^*)} \tag{2.82}$$

and the basis function spatial derivatives as:

$$\begin{aligned}\nabla\varphi_i^*(x) = \varphi_i\Bigg[(x-x^i)\cdot\left(\boldsymbol{H}^{-1} - \boldsymbol{H}^{-1}\cdot\boldsymbol{A}\right) \\ + \frac{\nabla w_i}{w_i} - \sum_{j=1}^{n}\varphi_j\frac{\nabla w_j}{w_j}\Bigg]\end{aligned} \tag{2.83}$$

where:

$$\boldsymbol{A} = \sum_{j=1}^{N}\varphi_j\,(x-x^i)\otimes\frac{\nabla w_j}{w_j} \tag{2.84}$$

and $\boldsymbol{H}$ is the Hessian matrix calculated with respect to the Lagrange multipliers:

$$\boldsymbol{H} = \sum_{j=1}^{N}\varphi_j\,(x-x^i)\otimes(x-x^i) \tag{2.85}$$

The above equations for the shape function derivatives $\nabla\varphi_i^*(x)$ simplify significantly when the Gaussian prior weight function is used [99]:

$$\nabla\varphi_i^*(x) = \varphi_i\boldsymbol{H}^{-1}\cdot(x-x^i) \tag{2.86}$$

In this thesis we will refer to an approximation space constructed using the above maximum-entropy method eq. (2.79) on a specified node set $\mathcal{N}_h$ with N nodes in the problem domain Ω with associated support radius vector ρ as:

$$ME(\Omega;\mathcal{N}_h,\rho) := \operatorname{span}\{\varphi_i\}_{i=1}^{N} \tag{2.87}$$

In fig. 2.6 we show the basis functions constructed using the MaxEnt method outlined above.

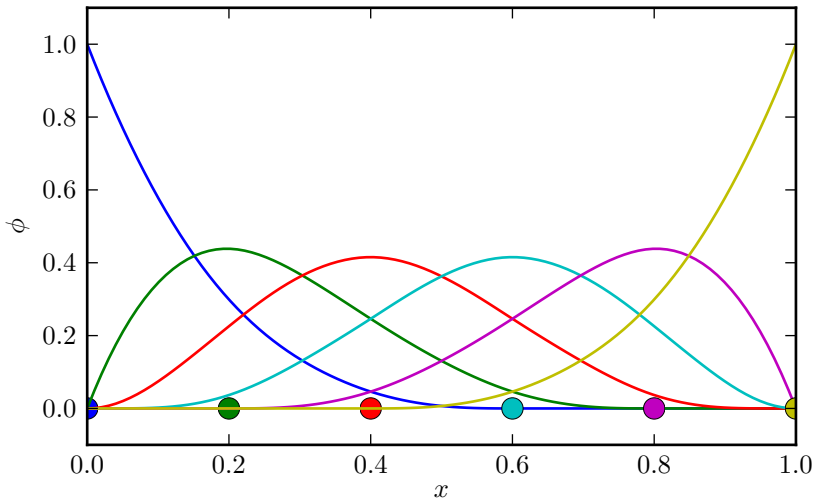

Figure 2.6: Basis functions constructed using maximum-entropy method on unit interval with 6 evenly spaced nodes and uniform support size. Note that whilst the basis lacks the Kronecker-delta property inside the domain, the basis has the Kronecker-delta property on the boundary of the domain. All basis functions associated with the internal nodes vanish on the boundary of the domain. This is the so-called `weak' Kronecker-delta property.

Maximum-entropy basis functions have various advantageous properties over the more commonly used MLS basis functions which have seen wide application in the EFG method [16]. These properties include [21]; variation diminishing property (roughly speaking, the approximation is not more oscillatory than the data that it approximates), C^0 continuity [101] derived using variational methods, C^∞ continuity derived using the inverse function theorem [21], positivity $\varphi_i \geq 0$ which leads to a positive mass matrix, and a `weak' Kronecker-delta property.

We will expand on the weak Kronecker-delta property here. It is well-known that the MLS basis functions do not satisfy the Kronecker-delta property and therefore the trial and test function spaces cannot be built to satisfy the Dirichlet (essential) boundary conditions a priori [85]. We discuss special methods which solve this problem in section 2.11.

For maximum-entropy basis functions there is no need to resort to any special methods to enforce Dirichlet boundary conditions. Arroyo and Ortiz [21] prove that for a node set $\mathcal{N}_h$ with convex hull conv $\mathcal{N}_h$ that the basis functions φ_i corresponding to nodes on the interior of the convex domain vanish on the boundary. Furthermore, if a node is an extreme point of conv $\mathcal{N}_h$ then the basis functions will have the Kronecker-delta property $\varphi_j(x^i) = \delta_{ji}$. These ideas are illustrated in figs. 2.7 to 2.11.The outcome of this is that imposing essential boundary

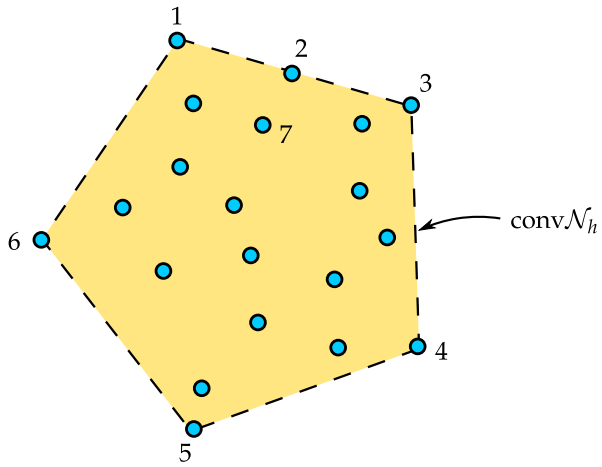

Figure 2.7: A node set $\mathcal{N}_h$ and its (weakly) convex hull conv $\mathcal{N}_h$ shown by the yellow shaded region. Nodes $\{1, 3, 4, 5, 6\}$ have the Kronecker-delta property (interpolatory), whilst node 2 has the 'weak' Kronecker-delta property. All internal nodes (eg. node 7) are non-interpolatory in a similar way to basis functions constructed with MLS. All basis functions associated with the internal nodes (eg. node 7) vanish on the convex hull $\mathcal{N}_h$.

conditions is as simple as in the FEM, greatly easing the implementation of meshless methods based on maximum-entropy basis functions. For this reason maximum-entropy basis functions are used widely in this thesis, although the developed mixed methods are generally applicable to any type of meshless basis function construction.

Some other applications of maximum-entropy approximants include extension to second-order consistency [102, 103], variational optimisation of the support width parameter β [104], constructing smooth manifolds on scattered data points [105] and co-rotational elasticity [106].

2.8 Radial basis functions

We can trace the routes of radial basis functions (RBFs) back to scattered data approximation problems in areas such as geophysics, mapping and meteorology [107]. Hardy [108] introduced the class of RBFs known as multiquadrics in 1971, primarily for the purpose of interpolation in mapping. Since then RBFs have become a popular choice in many applications that require data interpolation on irregular grids of points in high dimensional space.

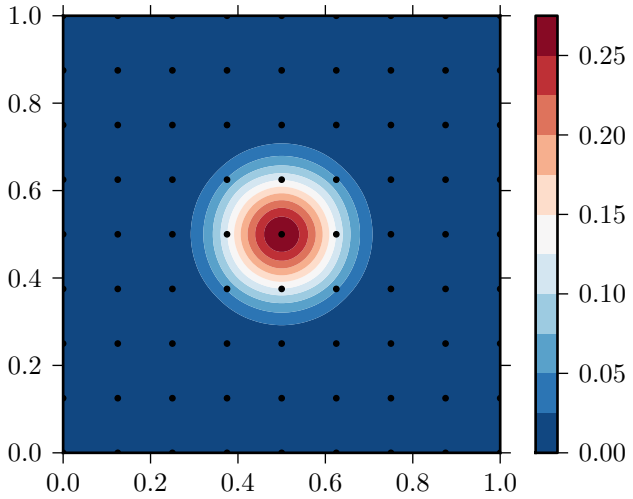

Figure 2.8: MaxEnt basis function associated with the central node on a uniform 9×9 grid of nodes.

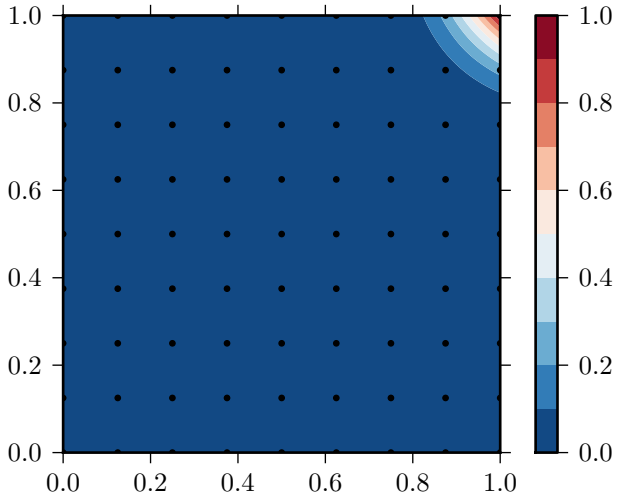

Figure 2.9: MaxEnt basis functions associated with the upper-right corner node on a uniform 9×9 grid of nodes. As the corner node is an extreme point of the convex hull of the node set the basis function associated with the corner node has the Kronecker-delta property.

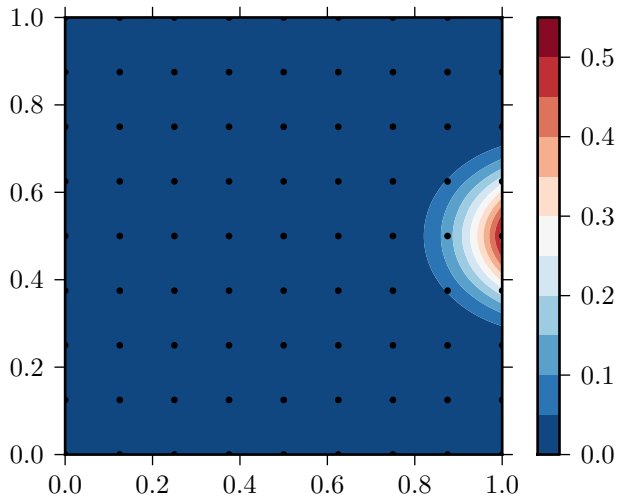

Figure 2.10: MaxEnt basis function associated with a mid-side node on a uniform 9×9 grid of nodes. As the side node is on the convex hull of the grid of nodes it has the weak Kronecker-delta property. Unlike the corner node, the value of the shape function at the node does not equal one, but all interior basis functions vanish. An example of a vanishing basis function is shown in the figure below.

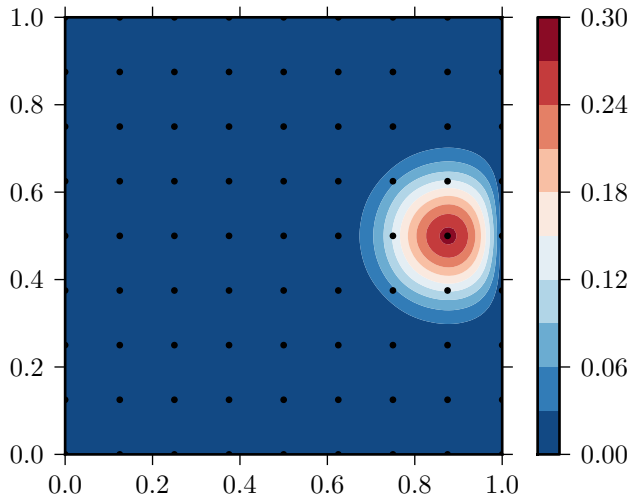

Figure 2.11: MaxEnt basis function associated with a node near the convex hull on a uniform 9×9 grid of nodes. The basis function associated with this node vanishes on the convex hull.

Construction

We begin with a set of nodes $\mathcal{N}_h$ with locations x^i. We can define the Radial Basis Function interpolation as [107]:

$$u_h(x) = \sum_i^N c_i \phi(||x - x^i||_2) \tag{2.88}$$

where c_i are coefficients to be found, ϕ is a radial basis function, and $||\cdot||_2$ denotes the euclidean norm in $\mathbb{R}^d$.

We require that the approximation exactly interpolates the function at the nodes i giving the condition at every node x^j [107]:

$$u_h(x^j) = \sum_{i=1}^N c_i \phi(||x^j - x^i||_2) \tag{2.89}$$

$$= c_1 \phi(||x^j - x^1||_2) + \cdots + c_I \phi(||x^j - x^N||_2) = u_j \tag{2.90}$$

Therefore for every node j we have one interpolating condition equation, resulting in a set of linear equations of the form [107]:

$$\begin{bmatrix} \phi(||x^1 - x^1||_2) & \phi(||x^1 - x^2||_2) & \dots & \phi(||x^1 - x^N||_2) \\ \phi(||x^2 - x^1||_2) & \phi(||x^2 - x^2||_2) & \dots & \phi(||x^2 - x^N||_2) \\ \vdots & \vdots & \ddots & \vdots \\ \phi(||x^N - x^1||_2) & \phi(||x^N - x^2||_2) & \dots & \phi(||x^N - x^N||_2) \end{bmatrix} \begin{bmatrix} c_1 \\ c_2 \\ \vdots \\ c_N \end{bmatrix} = \begin{bmatrix} u_1 \\ u_2 \\ \vdots \\ u_N \end{bmatrix} \tag{2.91}$$

$$\boldsymbol{A}\boldsymbol{c} = \boldsymbol{u} \tag{2.92}$$

By solving the above system of linear equations for $\boldsymbol{c}$ we have found a solution for the scattered data interpolation problem with RBFs.

Choice of RBF

From linear algebra we know that the system of linear equations will have a unique solution if the matrix $\boldsymbol{A}$ is non-singular. The matrix $\boldsymbol{A}$ is non-singular if and only if its determinant $|\boldsymbol{A}| \neq 0$. Currently there is no way of finding a class of radial basis functions that produce a non-singular matrix $\boldsymbol{A}$ for any set of nodes $\mathcal{N}_h$ [107]. However, if we restrict the discussion to positive definite matrices (which are always non-singular) then we can find classes of RBFs

Radial basis function	φ	Parameters	Continuity
Polyharmonic splines	r^ν	$\nu > 0, \nu \notin 2\mathbb{N}$	$m = \nu/2$
	$r^{2k}\log(r)$	$k \in \mathbb{N}$	$m = k + 1$
Gaussians	$\exp(-r^2)$	None	$m = 0$
Multiquadrics	$(1 + r^2)^\nu$	$\nu > 0, \nu \notin \mathbb{N}$	$m = \nu$
Inverse multiquadrics	$(1 + r^2)^\nu$	$\nu < 0$	$m = 0$

Table 2.2: Commonly used radial basis functions [111].

$\phi(||x||)$ called positive definite radial functions that always produce a positive-definite $\boldsymbol{A}$.

A real symmetric matrix $\boldsymbol{A}$ is positive definite if:

$$\boldsymbol{c}\boldsymbol{A}\boldsymbol{c}^T > 0 \quad \forall \boldsymbol{c} = [c_1, \dots, c_N]^T \in \mathbb{R}^N \tag{2.93}$$

If the matrix $\boldsymbol{A}$ is positive definite then all of its eigenvalues are positive and therefore a positive definite matrix is always non-singular:

$$\det \boldsymbol{A} \neq 0 \quad \text{if } \boldsymbol{c}\boldsymbol{A}\boldsymbol{c}^T > 0 \quad \forall \boldsymbol{c} = [c_1, \dots, c_N]^T \in \mathbb{R}^N \tag{2.94}$$

A function $\Phi\colon \mathbb{R}^d \mapsto \mathbb{R}$ is called a positive definite function on $\mathbb{R}^d$ if and only if [109]:

$$\boldsymbol{c}\boldsymbol{A}\boldsymbol{c}^T > 0 \quad \forall \boldsymbol{c} = [c_1, \dots, c_N]^T \in \mathbb{R}^N \tag{2.95}$$

$$\boldsymbol{A} = \begin{bmatrix} \varphi(||x^1 - x^1||) & \varphi(||x^1 - x^2||) & \dots & \varphi(||x^1 - x^N||) \\ \varphi(||x^2 - x^1||) & \varphi(||x^2 - x^2||) & \dots & \varphi(||x^2 - x^N||) \\ \vdots & \vdots & \ddots & \vdots \\ \varphi(||x^N - x^1||) & \varphi(||x^N - x^2||) & \dots & \varphi(||x^I - x^N||) \end{bmatrix} \tag{2.96}$$

for any set of pairwise distinct nodes $x^1, \dots, x^N \in \mathbb{R}^d$. Bochner's theorem [107, 110] can then be used to show that a particular function is indeed positive definite on all $\mathbb{R}^d$ $d \geq 1$ and will produce an invertible interpolation matrix $\boldsymbol{A}$. A selection of commonly used positive definite RBFs are shown in table 2.2 [111].

2.9 Radial point interpolation method

The main drawback of the above approach is that approximations schemes are not even first-order consistent [112]. This means that RBFs will not pass the patch test [107]. However we can add in polynomial consistency with a simple polynomial extension to the RBF interpolation [107]. This approach was originally proposed by Powell in 1992 [113] in the context of function approximation, and then introduced by Wang and Liu in the context of meshless methods as the radial point interpolation method (RPIM) [22].

The consistent approximation can be written [107]:

$$u_h(x) = \sum_{i=1}^{N} c_i \phi(\|x - x^i\|_2) + \sum_{j=1}^{M} d_j p_j(x) \tag{2.97}$$

where $\boldsymbol{p}(x)$ is a complete monomial of order m with M terms in x as used in the moving least-squares approximation method and d_j is a further set of coefficients to be found. By enforcing the interpolating conditions as in the standard RBF interpolation and including a further set of conditions to ensure a unique solution [107]:

$$\sum_{j=1}^{M} d_j p_k(x^j) = 0 \tag{2.98}$$

we can construct an augmented system of equations of the form [107]:

$$\begin{bmatrix} \boldsymbol{A} & \boldsymbol{P} \\ \boldsymbol{P}^T & \boldsymbol{0} \end{bmatrix} \begin{bmatrix} \boldsymbol{c} \\ \boldsymbol{d} \end{bmatrix} = \begin{bmatrix} \boldsymbol{y} \\ \boldsymbol{0} \end{bmatrix} \tag{2.99}$$

It can be shown that the above augmented equation is non-singular and has a unique solution [107]. If we let:

$$G = \begin{bmatrix} \boldsymbol{A} & \boldsymbol{P} \\ \boldsymbol{P}^T & \boldsymbol{0} \end{bmatrix} \tag{2.100}$$

Then we can write the consistent approximation in vector form as:

$$u_h(x) = \{\boldsymbol{\phi}^T(x)\ \boldsymbol{p}^T(x)\}\boldsymbol{G}^{-1}\boldsymbol{u} \tag{2.101}$$

And the basis function vector is therefore defined by:

$$\boldsymbol{\varphi}(x) = \{\boldsymbol{\phi}^T(x)\ \boldsymbol{p}^T(x)\}\boldsymbol{G}^{-1} \tag{2.102}$$

In this thesis we will refer to an approximation space constructed using the above radial point interpolation method eq. (2.102) of order p on a specified node set $\mathcal{N}_h$ with N nodes in the problem domain Ω with associated support radius vector ρ as:

$$RPIM_p(\Omega; \mathcal{N}_h, \rho) := \text{span}\,\{\varphi_i\}_{i=1}^N \tag{2.103}$$

Continuity

Even though we have added consistency to the RBF approximation we have introduced another problem; the RPIM basis functions are, in general, not continuous across the entire domain [4]. This happens because as new nodes enter and exit the connectivity set S_h the P matrix changes abruptly. This means that RPIM basis functions whilst being smooth almost everywhere, typically have very small discontinuities meaning that strictly speaking the RPIM basis functions are only members of the space $L^2(\Omega)$. Therefore, technically speaking, RPIM is not a suitable meshless basis function for discretising many weak forms arising from physical systems where we require at least $H^1(\Omega)$ continuity. In practice, and in our experience, it seems this is not a particularly significant issue, and the huge number of successful papers in the literature using RPIM basis functions would support this.

G. R. Liu has recently introduced the G space theory [114, 115]. It allows the basis functions to have lower continuity in Ω and thus allows RPIM functions to be used in so-called weakened-weak (W^2) variational forms. This works by relaxing or weakening the requirement that the basis function lie in the space H^1. The first derivatives are then calculated by constructing appropriate smoothing domains using background cells. This is a large topic that cannot be covered in full here, further details can be found in [4, 114, 115].

Computational Efficiency

Similarly to the MLS method, the equations used above should not be used directly to compute the basis functions. Liu and Gu [5] present an efficient method for computing the RPIM basis

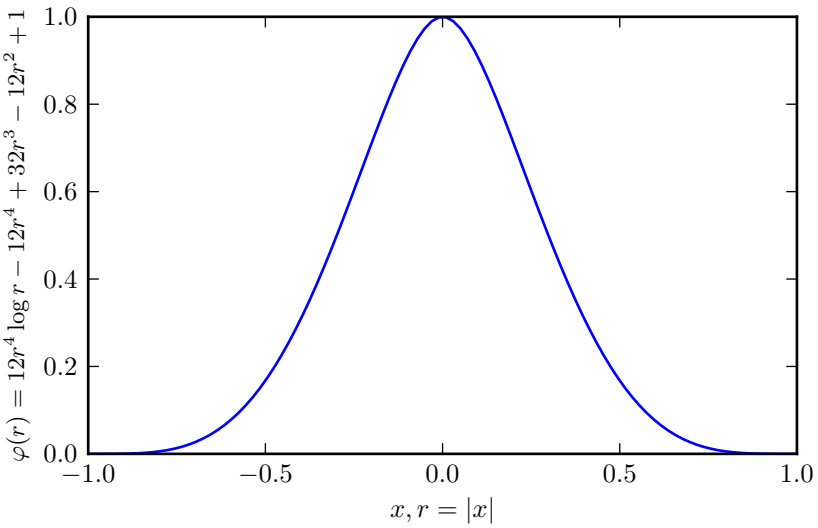

Figure 2.12: Wendland C^2 compactly supported radial basis function

functions utilising one LU-decomposition of $\boldsymbol{G}^T$ and then solving repeatedly for varying right hand sides of the linear system for increasing orders of derivatives.

2.10 Compactly supported radial basis functions

A new class of compactly supported radial basis functions (CSRBFs) were introduced by Wendland in 1995 [116]. These RBFs have compact support, in contrast to the RBFs introduced in the previous section that have global support. The primary advantage of compactly supported RBFs is that the interpolation matrix $\boldsymbol{A}$ becomes sparse, allowing for optimised sparse solvers to be used.

Buhmann's CSRBFs [117] contain the earlier CSRBFs of Wendland [116] and Wu [118] as a special case. An example of one of Buhmann's strictly positive definite CSRBF is [117]:

$$\phi(r) = 12r^4 \log r - 21r^4 + 32r^3 - 12r^2 + 1, \qquad 0 \leq r \leq 1 \tag{2.104}$$

$$\tag{2.105}$$

This function $\phi \in C^2(\Omega)$ and is positive definite and radial on $\mathbb{R}^d$ for $d \leq 3$.

Like the globally supported RBFs, CSRBFs also need polynomial extension to construct approximations that will pass the patch test. CSRBFs with first order polynomial consistency have been used successfully by Itoh et al. to reconstruct 3D surfaces from a set of scattered data

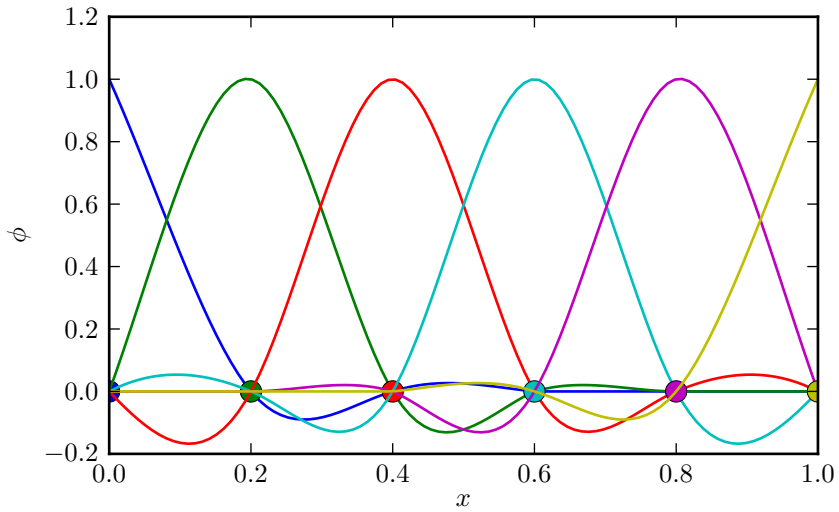

Figure 2.13: Basis functions constructed using Radial Point Interpolation Method (Wendland C^2 CSRBF) method on unit interval with 6 evenly spaced nodes and uniform support size. This basis has the Kronecker-delta property both on the boundary and on the inside of the domain.

points from an object scanner [119]. The augmented system of equations is of a very similar form to that for globally supported RBFs.

2.11 Enforcing Dirichlet boundary conditions

In the FEM the basis functions satisfy the Kronecker-delta property and therefore Dirichlet boundary conditions can be imposed simply by modification of the final system of linear equations. However, meshless basis functions do not typically satisfy the Kronecker-delta property and special techniques must be used to impose Dirichlet boundary conditions.

According to Fernandez-Mendez and Huerta [85] these special techniques can be classified into two main groups; the first are those based on modifying the weak form, such as the method of Lagrange multipliers, the penalty method and Nitsche's method. The second are those that modify the basis functions so that they do interpolate and satisfy the Kronecker-delta property on Γ_D, thus allowing direct imposition of the Dirichlet boundary conditions as in the FEM. In this section we discuss the the method of Lagrange multipliers, the penalty method, Nitsche's method and coupling to finite elements as these are the most commonly used and generally applicable techniques used in the literature.

2.11.1 Lagrange multipliers

The Lagrange multiplier approach was introduced in the context of finite element methods by Babuska [120]. By using Hamilton's principle we can write a general energy function of eq. (2.1) in the form [32]:

$$\Pi(v) = T - V - W \tag{2.106}$$

where T is the kinetic energy, V is the internal strain energy, and W is the work done by external forces on the system. The solution $u \in \mathcal{H}^1(\Omega)$ minimises the energy functional and verifies the essential boundary conditions on Γ_D [85]:

$$u = \arg \inf_{\substack{v \in \mathcal{H}^1(\Omega) \\ v = \bar{u}\ \forall x \in \Gamma_D}} \Pi(v) \tag{2.107}$$

Alternatively, if we cannot enforce the boundary conditions due to the lack of Kronecker-delta property we can re-write the above minimisation problem using the Lagrange multiplier $\lambda(x)$ as [85]:

$$(u, \lambda) = \arg \inf_{v \in \mathcal{H}^1(\Omega)} \sup_{\gamma \in \mathcal{H}^{-1/2}(\Gamma_D)} \Pi(v) + \int_{\Gamma_D} \gamma(v - \bar{u})\, \mathrm{d}\Gamma \tag{2.108}$$

This constrained minimisation problem leads to a system of equations in the standard saddle-point form [85]:

$$\begin{bmatrix} \boldsymbol{K} & \boldsymbol{G}^T \\ \boldsymbol{G} & \boldsymbol{0} \end{bmatrix} \begin{bmatrix} \boldsymbol{u} \\ \boldsymbol{\lambda} \end{bmatrix} = \begin{bmatrix} \boldsymbol{f} \\ \boldsymbol{q} \end{bmatrix} \tag{2.109}$$

where $\boldsymbol{K}$ is the standard stiffness matrix, $\boldsymbol{G}$ is a matrix of the integrated basis functions that approximate the Lagrange multipliers $\boldsymbol{\lambda}$ on Γ_D, $\boldsymbol{f}$ is the standard force vector, and $\boldsymbol{q}$ is a vector of the prescribed Dirichlet boundary conditions $\bar{u}$ integrated on Γ_D.

Whilst the Lagrange multiplier method is broadly applicable and straightforward to implement, the augmented system of equations has increased dimensions over $\boldsymbol{K}$, is no longer positive definite like $\boldsymbol{K}$, and can be singular if too many Lagrange multipliers are used to constrain the solution. These issues are discussed in depth by Fernandez-Mendez and Huerta [85].

2.11.2 Penalty method

The penalty method was introduced in context of meshless methods by Zhu and Atluri [121]. In the penalty method the minimisation problem can be solved by the use of the penalty parameter

α [85]:

$$u = \arg \inf_{v \in \mathcal{H}^1(\Omega)} \Pi(v) + \frac{1}{2}\alpha \int_{\Gamma_D} (v - \bar{u})^2 \, \mathrm{d}\Gamma \tag{2.110}$$

The constraint has been enforced by adding the square of the constraints $\bar{u}$ multiplied by a very large number α. The penalty method has the advantage that the size of the system of linear equations remains the same and is still positive definite [85]. However, with increasing α the system of equations becomes increasingly ill-conditioned [85]. Choosing α so that the boundary conditions are well imposed whilst still ensuring that the system of equations remains sufficiently well-conditioned can be difficult.

2.11.3 Nitsche's method

Nitsche's method [122] can be interpreted as a consistent improvement of the penalty method [85]. Only very low values of the new penalty parameter β need to be used, on the order of $\beta \backsim 100$ in Nitsche's method compared with to $\alpha \backsim 10^6$ in the penalty method, resulting in well-conditioned systems of equations [85]. The main problem with Nitsche's method is that the modified weak form must be specially derived for each problem, whereas for the Lagrange multiplier approach and penalty method generalisation to arbitrary weak forms is straightforward [85].

2.11.4 Coupling to finite elements

Coupling meshless approximants to finite elements is useful on two levels: firstly the FE basis functions satisfy the Kronecker-delta property and therefore boundary conditions can be directly imposed, and secondly it allows for regions of the problem solution to be approximated using computationally cheaper finite elements.

There have been multiple efforts to couple mesh-free approximations with finite elements. Belytschko et al. [123] used a ramp function to continuosly blend in a transition element between a coupled approximation consisting of the MLS approximation and finite elements. Huerta and Fernandez-Mendez [124] generalised Belytschko's approach to allow arbitrary consistency without any ramping function. Wagner and Liu [125] proposed a method that allows the mixing of different interpolation spaces with finite elements. As a side effect they found that it also solves the problem of imposing Dirichlet boundary conditions in meshless methods [125].

2.12 Implementation

All of the meshless numerical methods developed in this thesis have been implemented in the framework of a general meshless and finite element framework called pymfl. pymfl is primarily implemented in Python with various small pieces implemented in C/C++ for performance reasons. To calculate the meshless basis functions the pymfl package uses our external C++ library meshless wrapped via Boost.Python [126]. The meshless library supports maximum-entropy, MLS and RPIM basis functions. The pymfl package also uses various open-source software components. DOLFIN is used for the mesh data structure [127] and FIAT [128] for the finite element basis function tabulation. Nearest-neighbour searching is accelerated using the ckdtree library from Scipy [129]. Sparse linear algebra is handled using the PyTrilinos framework from Sandia National Labs. Because of the object-oriented design of pymfl it is relatively easy to implement new problems quickly into the framework. We show an example pymfl solver for the Timoshenko beam problem in the following chapter.

2.13 Conclusions

In this chapter we have explored various methods for constructing meshless basis functions and their corresponding mathematical properties. Particularly important is the problem of enforcing Dirichlet boundary conditions. Currently there are two options; the first option is to use a modified variational form with a basis function with the Kronecker-delta property, and the second is to use a basis function with the Kronecker-delta property. Whilst the maximum-entropy approach does have the `weak' Kronecker-delta property allowing direct enforcement of Dirichlet boundary conditions on convex node sets, this advantage comes at the expense of allowing easy extension to second-order or higher consistency. The radial point interpolation method (RPIM) has the standard Kronecker-delta property just like the FEM, but the basis functions are not necessarily continuous across the domain and strictly speaking requires the use of special weakened-weak variational forms for the best accuracy. Therefore in our view there is currently no meshless basis function construction which is suitable for all problem types and the best option must be chosen on a case-by-case evaluation.

3 A study of the shear-locking problem in the Timoshenko beam problem with meshless methods

In this chapter we outline the assumptions and the weak form of the Reissner-Mindlin plate problem before moving on to perform numerical experiments with the Reissner-Mindlin problem's one-dimensional analogue, the Timoshenko beam problem.

We define parameters ε and $\tilde{p}$ allowing an appropriate scaling of the applied load ensuring a sequence of problems with finite limit solution (Bernoulli) as the small parameter $\varepsilon \to 0$. We then transfer from the continuous problem to a discrete form suitable for solution via finite element or meshless methods. Using simple function space arguments we show that the origin of the locking problem in both the meshless and finite element methods; the inability of the basis functions to richly represent the limiting Kirchhoff mode.

We then present numerical results from both meshless and finite element methods showing the broadly similar behaviour with respect to the small parameter ε under h and p refinement. Additionally, we study the effect of the support width parameter β in meshless methods. We clearly identify the sensitivity of the meshless numerical methods shear-locking behaviour with respect to the discretisation parameters. This understanding is a key aspect in designing a meshless numerical method that is free of shear-locking. To our knowledge these fundamental experiments have not been performed using meshless basis functions before.

3.1 Introduction

Before solving a problem it is important to understand its origins. The aim of this chapter is to explore the origins of shear-locking problem in numerical methods and understand in what way the magnitude of the shear-locking problem depends on the discretisation parameters. In this chapter we perform a set of numerical experiments using both finite element and meshless

methods which reveal in a simple way the dependence of shear-locking upon the discretisation parameters in both meshless and finite element methods. To ascertain this we perform a numerical extended versions of an experiment originally suggested by Chapelle and Bathe [40]. To our knowledge this is the first time these experiments have been performed for the h and p-refinement finite element methods as well as h and p-refinement meshless methods and analysed in a comparative manner.

3.2 Plate theories

In this section we give an overview of the assumptions of both the Kirchhoff and the Reissner-Mindlin plate models and give an outline of the weak formulation of the Reissner-Mindlin problem.

3.2.1 The Kirchhoff-Love plate problem

The Kirchhoff-Love plate problem is illustrated in fig. 3.1. The assumptions made in the derivation of the Kirchhoff-Love plate problem are as follows:

Geometry The three-dimensional elasticity problem domain $\Omega \subset \mathbb{R}^3$ has one thin dimension in the x_3 direction. The plate mid-surface is then described by the domain $\Omega_0 \subset \mathbb{R}^2$ and the thickness by a function $t : \Omega_0 \to (0, \infty)$. The coordinates (x_1, x_2) lie on the mid-surface of the plate. Therefore the whole domain $\Omega \subset \mathbb{R}^3$ can be written as:

$$\Omega \equiv \left\{(x_1, x_2, x_3) \in \mathbb{R}^3 \ : \ (x_1, x_2) \in \Omega_0,\ x_3 \in [-t(x_1, x_2)/2,\ t(x_1, x_2)/2]\right\} \tag{3.1}$$

Mechanics Straight lines perpendicular to the mid-surface of the plate before loading occurs remain straight after loading. The transverse normals do not elongate. Therefore plane stress assumptions apply $\sigma_{33} = 0$.

Kinematics The transverse normals rotate such that they remain perpendicular to the middle surface after loading. We can then assume that the three-dimensional displacement vector $\boldsymbol{u} : \Omega \to \mathbb{R}^3$ can be written in the following form:

$$\boldsymbol{u}(x_1, x_2, x_3) = \left(z_1(x_1, x_2) - \frac{\partial z_3}{\partial x_1} x_3,\ z_2(x_1, x_2) - \frac{\partial z_3}{\partial x_2} x_3,\ z_3(x_1, x_2)\right) \tag{3.2}$$

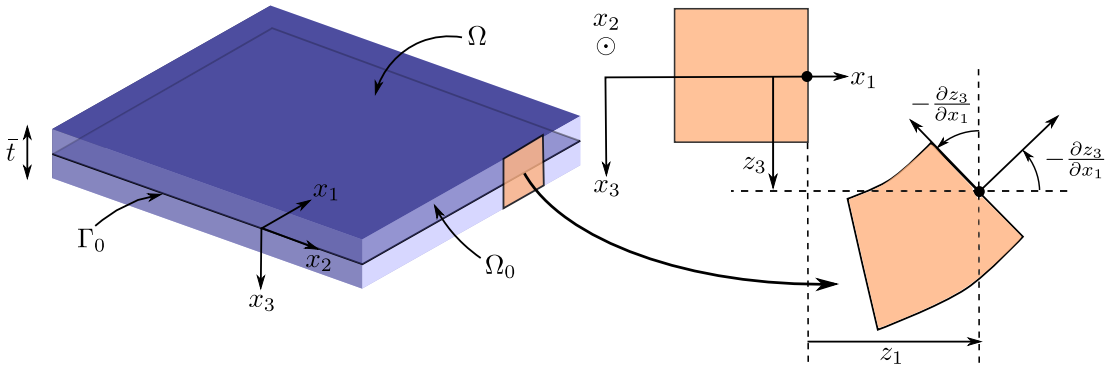

Figure 3.1: Illustration of the Kirchhoff plate problem.

3.2.2 The Reissner-Mindlin plate problem

The Reissner-Mindlin plate problem is illustrated in fig. 3.2. The assumptions made in the derivation of the Reissner-Mindlin problem are as follows:

Geometry The same geometrical assumptions are made as in the Kirchhoff-Love hypothesis.

Mechanics The same mechanical assumptions are made as in the Kirchhoff-Love hypothesis.

Kinematics The transverse normals are allowed to rotate relative to the middle surface after loading. We assume that the three-dimensional displacement vector $\boldsymbol{u} : \Omega \rightarrow \mathbb{R}^3$ can be written in the following form:

$$\boldsymbol{u}(x_1, x_2, x_3) = (z_1(x_1, x_2) - \theta_1(x_1, x_2)x_3,\ z_2(x_1, x_2) - \theta_2(x_1, x_2)x_3,\ z_3(x_1, x_2)) \tag{3.3}$$

In other words, the motion of a material line normal to the plate mid-surface can be decomposed into an in-plane displacement (z_1, z_2) along with a rotation $\boldsymbol{\theta} = (\theta_1, \theta_2)$ around the (x_2, x_1) axis respectively, along with a normal displacement z_3. These kinematic assumptions lead to transverse shear stresses $\varepsilon_{\alpha 3}(x) \neq 0 \quad \alpha = 1, 2$. Contrast this with the Kirchhoff plate model where it is assumed that $\boldsymbol{\theta} = \nabla z_3$, or material lines normal to the plate mid-surface remain normal to the surface after deformation, giving $\varepsilon_{\alpha 3}(x) = 0$. In this context the Reissner-Mindlin

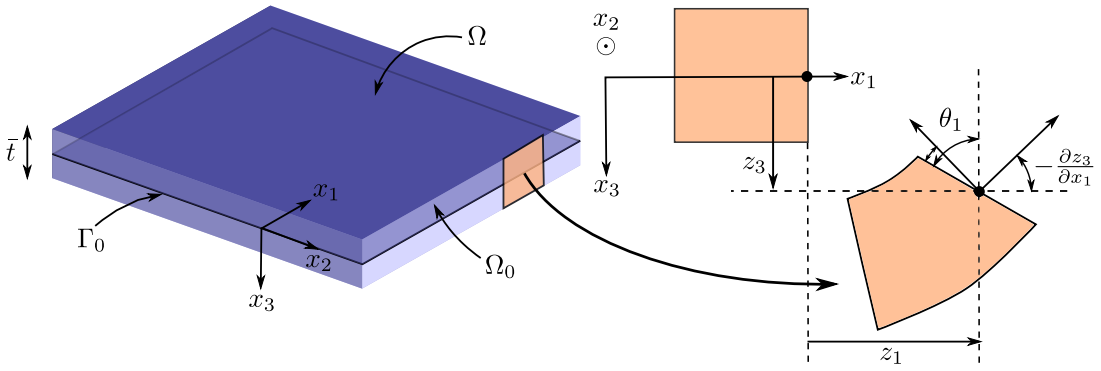

Figure 3.2: Illustration of the Reissner-Mindlin plate problem.

model can be seen as a first-order relaxation of the Kirchhoff model constraint $\boldsymbol{\theta} - \nabla z_3 = 0$. The relaxation of the Kirchhoff hypothesis in the Reissner-Mindlin model has three main advantages, two of which relate to the accuracy of the physical model of the plate, and one relating to the ease of constructing appropriate numerical methods. Firstly, the interior solution (far away from the edges) includes the effect of shear deformation, and is therefore more accurate than the Kirchhoff hypothesis for thicker plates [130]. Secondly, the Reissner-Mindlin model has a more physically representative approximation to the behaviour of the plate at the edge-zone portion [130], which typically includes boundary layer phenomenon [131]. Finally, the resulting weak form of the Reissner-Mindlin equations requires only that the solution $(z_3, \boldsymbol{\theta})$ be in the Sobolev space $[H^1(\Omega_0)]^3$, whereas the Kirchhoff weak form requires that the solution z_3 has greater regularity in the Sobolev space $H^2(\Omega_0)$ [40]. The practical outcome of this is that to solve the Reissner-Mindlin problem C^0 continuous finite element can be used, whereas for the Kirchhoff problem more exotic C^1 continuous finite elements such as the Argyris triangle [132] are required.

The actual derivation of the Reissner-Mindlin problem is somewhat lengthy and we opt to jump directly to the weak form of the Reissner-Mindlin plate problem here. A full derivation is given by Hardesty [133]. In this derivation it assumed that the thickness is independent of position ie. $t(x_1, x_2) = t$, that the plate material behaviour is homogeneous and isotropic and that loading is applied only in the transverse direction z_3.

Problem 3 (Displacement weak form of the Reissner-Mindlin plate problem)**.** *Find the trans-*

verse deflection and rotations $(z_3, \boldsymbol{\theta}) \in \mathcal{V}_3 \times \mathcal{R}$ *such that:*

$$\bar{t}^3 \int_{\Omega_0} \boldsymbol{L}[\boldsymbol{\varepsilon}(\boldsymbol{\theta})] : \boldsymbol{\varepsilon}(\boldsymbol{\eta})\, d\Omega + \lambda \bar{t} \int_{\Omega_0} (\nabla z_3 - \boldsymbol{\theta}) \cdot (\nabla y_3 - \boldsymbol{\eta})\, d\Omega = \int_{\Omega_0} p_3 y_3\, d\Omega \quad \forall (y_3, \boldsymbol{\eta}) \in \mathcal{V}_3 \times \mathcal{R} \tag{3.4a}$$

The operators $\boldsymbol{\varepsilon} : [H^1(\Omega_0)]^2 \to [L^2(\Omega_0)]^{2\times 2}$ *and* $\boldsymbol{L} : [L^2(\Omega_0)]^{2\times 2} \to [L^2(\Omega_0)]^{2\times 2}$ *are defined as:*

$$\boldsymbol{\varepsilon}(\boldsymbol{v}) = \frac{1}{2}\left((\nabla \boldsymbol{v}) + (\nabla \boldsymbol{v})^T\right) \qquad \boldsymbol{L}[\boldsymbol{\varepsilon}] \equiv D\left[(1-\nu)\boldsymbol{\varepsilon} + \nu \mathrm{tr}(\boldsymbol{\varepsilon})\boldsymbol{I}\right] \tag{3.4b}$$

where $\boldsymbol{I}$ *is the usual identity tensor,* $D = E/12(1-\nu^2)$ *is the bending modulus,* $\lambda = E\kappa/(2(1+\nu))$ *is the shear modulus,* $\kappa = 5/6$ *is a shear correction factor*[1]*,* ν *is Poisson's ratio,* E *is Young's modulus,* $\bar{t} = t/L$ *is the plate thickness scaled with respect to the characteristic in-plane dimension* L *and* p_3 *is the transverse loading function.*

We can write the above problem in a simplified short-hand form by defining:

$$a_b(\boldsymbol{\theta}; \boldsymbol{\eta}) := \int_{\Omega_0} \boldsymbol{L}[\boldsymbol{\varepsilon}(\boldsymbol{\theta})] : \boldsymbol{\varepsilon}(\boldsymbol{\eta})\, d\Omega \tag{3.5a}$$

$$a_s(\boldsymbol{\theta}, z_3; \boldsymbol{\eta}, y_3) := \int_{\Omega_0} (\nabla z_3 - \boldsymbol{\theta}) \cdot (\nabla y_3 - \boldsymbol{\eta})\, d\Omega \tag{3.5b}$$

$$g(y_3) := \int_{\Omega_0} p_3 y_3\, d\Omega \tag{3.5c}$$

as the bilinear and linear forms relating to the bending energy, shear energy and external loading of the plate, respectively, then we can re-write the Reissner-Mindlin problem in the following short-hand form:

$$\bar{t}^3 a_b(\boldsymbol{\theta}; \boldsymbol{\eta}) + \lambda \bar{t} a_s(\boldsymbol{\theta}, z_3; \boldsymbol{\eta}, y_3) = g(y_3) \tag{3.6}$$

3.3 The Timoshenko beam problem

The Timoshenko beam problem is a reduced-dimension version of the Reissner-Mindlin problem; it encapsulates the similar physics, that is, the deformation of a three-dimensional structure with planar dimensions far greater than the the thickness whilst taking into account the

[1] In the three dimensional elastic body the shear stresses vanish on the top and bottom surfaces of the plate, but the Reissner-Mindlin assumptions enforce a linear variation in shear stress. To correct this discrepancy the shear energy is multiplied through by κ.

effect of transverse shear stresses. Furthermore, naive numerical discretisations of the Timoshenko problem suffer from exactly the same shear-locking problem as those of the Reissner-Mindlin problem. In the more exacting mathematical aspects the Timoshenko beam problem is considerably simpler the the Reissner-Mindlin problem, and in terms of understanding how the discretisation parameters effect the strength of the shear-locking problem it is also much simpler. This makes it a good candidate problem for performing initial numerical experiments which will assist in the development of locking-free methods for the Reissner-Mindlin problem.

3.3.1 Continuous form

By setting Poisson's ratio $\nu = 0$, neglecting all terms involving variables in the x_2 direction and setting $\theta_1 = \theta$ in the Reissner-Mindlin plate problem eq. (3.4) we arrive at the following continuous form of the Timoshenko beam problem:

Problem 4 (Displacement form of the Timoshenko beam problem)**.** *Consider a straight beam of length L with constant rectangular cross-section depth b and constant thickness t. The problem domain is $\Omega = (0, L)$. The weak form of the problem can be written as follows:*

Find the transverse displacements and rotations $(z_3, \theta) \in \mathcal{V}^T$ such that:

$$EI \int_\Omega \theta' \eta' \, d\Omega + Gbt\kappa \int_\Omega (z_3' - \theta)(y_3' - \eta) \, d\Omega = \int_\Omega p_3 y_3 \, d\Omega \quad \forall (y_3, \eta) \in \mathcal{V}^T \tag{3.7}$$

where E is Young's modulus, G is the shear modulus, κ is a shear correction factor and I is the second moment of inertia of the cross section.

Boundary conditions are specified as being clamped at both ends giving the following specification for the function space $\mathcal{V}^T$:

$$\mathcal{V}^T = \left\{ (y_3, \eta) \in \mathcal{V}_3 \times \mathcal{R} = \left[H_0^1(\Omega) \right]^2 \right\} \tag{3.8}$$

where $H_0^1(\Omega) \subset H^1(\Omega)$ is the standard Sobelev space of square integrable functions with square integrable derivatives in Ω with vanishing values on the boundary Γ. We now define the following parameters:

$$\varepsilon = \frac{1}{L}\sqrt{\frac{EI}{Gbt\kappa}}, \quad \tilde{p} = \frac{p_3 L^2}{EI} \tag{3.9}$$

allowing us to scale the load by a factor of ε^3. In rough terms, this scaling with ε ensures a finite solution as the beam thickness t is reduced whilst keeping the other problem variables fixed.

After performing the appropriate scaling we have the following scaled version of the original problem:

Problem 5 (Scaled displacement Timoshenko beam problem)**.** *Find* $(z_3^\varepsilon, \theta^\varepsilon) \in \mathcal{V}^T$ *such that:*

$$L^2 \int_\Omega \theta^{\varepsilon'} \eta' \, d\Omega + \frac{1}{\varepsilon^2} \int_\Omega (z_3^{\varepsilon'} - \theta^\varepsilon)(y_3' - \eta) \, d\Omega = \int_\Omega \tilde{p} y_3 \, d\Omega \quad \forall (y_3, \eta) \in \mathcal{V}^T \tag{3.10}$$

We can now define a sequence of problems $\left\{(z_3^\varepsilon, \theta^\varepsilon)\right\}_\varepsilon$ that converges in the limit as $\varepsilon \to 0$ to the thin beam or Bernoulli solution (z_3^0, θ^0). We will refer to the solution (z_3^0, θ^0) as the Bernoulli solution or thin beam solution and this solution can be found by solving the following limit problem:

Problem 6 (Scaled Bernoulli beam problem in rotation variable)**.** *Find* $(z_3^0, \theta^0) \in \mathcal{V}_0^T$ *such that:*

$$L^2 \int_\Omega \theta^{0'} \eta' \, d\Omega = \int_\Omega \tilde{p} y_3 \, d\Omega \quad \forall (y_3, \eta) \in \mathcal{V}_0^T \tag{3.11}$$

where $\mathcal{V}_0^T$ *is the set of pure bending displacements:*

$$\mathcal{V}_0^T = \left\{ (y_3, \eta) \in \mathcal{V}^T \mid v_3' - \eta = 0 \right\} \tag{3.12}$$

Then by substituting $\theta^0 = z_3'$ and $\eta = y_3'$ into eq. (3.11) we can eliminate the rotation variables to obtain the classical Bernoulli beam problem in terms of the transverse displacement z_3^0 only:

Problem 7 (Scaled Bernoulli beam problem in transverse displacement variable)**.** *Find* $z_3^0 \in \mathcal{V}_3^0$ *such that:*

$$L^2 \int_\Omega z_3^{0\prime\prime} y_3'' \, d\Omega = \int_\Omega \tilde{p} y_3 \, d\Omega \quad \forall y_3 \in \mathcal{V}_3^0 \tag{3.13}$$

where $\mathcal{V}_3^0$ *is the space of square integrable functions with square integrable first and second derivatives with vanishing value and derivatives on* Γ*:*

$$\mathcal{V}_3^0 = H_0^2(\Omega_0) = \{ y_3 \in H^2(\Omega) \mid v(0) = v'(0) = v(L) = v'(L) = 0 \} \tag{3.14}$$

The classical Bernoulli beam problem is the reduced-dimension version of the Kirchhoff-Love plate problem. The strong form of the Bernoulli beam problem is a fourth-order PDE which results in a weak form with second-order partial derivatives requiring a solution $z_3 \in H_0^2(\Omega_0)$.

We can now see that in the limit as $\varepsilon \to 0$ the Timoshenko problem coincides exactly with the classical Bernoulli problem. This is what we would expect on an intuitive physical level; given that both mathematical models claim to accurately describe the deformation of a beam under mechanical loading we would naturally expect that both models would give the same answer for a thin beam. Of course, for moderately thick beams, the relaxed hypothesis of the Timoshenko theory gives a more physically accurate model of the three-dimensional body than the Bernoulli theory. We have seen mathematically that in the continuous form the two problems do indeed agree. However, on moving to a discretised form of the Timoshenko beam problem we typically find that as $\varepsilon \to 0$ the sequence of problems fails to converge to the corresponding Bernoulli solution, resulting in wildly inaccurate results. It is this problem which we call shear-locking. It is important to emphasise that the shear-locking problem is caused only by poorly designed numerical methods, not by any inherent issues with the mathematical models which describe the underlying physical phenomenon. We will demonstrate the shear-locking issue both mathematically and numerically in the following sections.

3.3.2 Discretised form and locking

To discretise the Timoshenko beam problem we introduce the finite-dimensional conforming subspace $\mathcal{V}_h^T \subset \mathcal{V}^T$ constructed with any standard partition of unity process such as the FEM or meshless methods. We then have the following discretised version of the scaled Timoshenko beam problem:

Problem 8 (Discretised scaled Timoshenko beam problem)**.** *Find* $(z_{3h}^{\varepsilon}, \theta_h^{\varepsilon}) \in \mathcal{V}_h^T$ *such that:*

$$L^2 \int_\Omega \theta' \eta' \, d\Omega + \frac{1}{\varepsilon^2} \int_\Omega (z_3' - \theta)(y_3' - \eta) \, d\Omega = \int_\Omega \tilde{p} y_3 \, d\Omega \quad \forall (y_3, \eta) \in \mathcal{V}_{3h} \times \mathcal{R}_h \tag{3.15}$$

Remember previously that we defined the thin-beam or Bernoulli solution (z_3^0, θ^0) as the solution to the limit problem. In exactly the same manner we can define the discrete Bernoulli solution $(z_{3h}^0, \theta_{3h}^0)$ as the solution to the following discrete limit problem:

Problem 9 (Discrete scaled Bernoulli beam problem in rotations)**.** *Find* $(z_{3h}^0, \theta_h^0) \in \mathcal{V}_{0h}$ *such that:*

$$L^2 \int_\Omega \theta^{0'} \eta' \, d\Omega = \int_\Omega \tilde{p} y_3 \, d\Omega \quad \forall \, (y_3, \eta) \in \mathcal{V}_{0h} \tag{3.16}$$

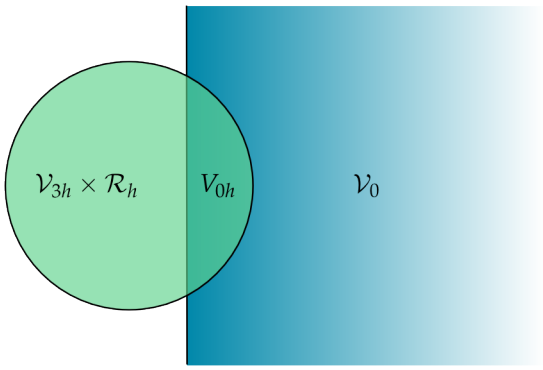

Figure 3.3: Illustrative Venn diagram of the space of discrete pure bending displacements.

where $\mathcal{V}_{0h}$ is the set of discrete pure bending displacements:

$$\mathcal{V}_{0h} = \left\{ (v_3, \eta) \in \mathcal{V}_{3h} \times \mathcal{R}_h \mid v_3' - \eta = 0 \right\} \tag{3.17}$$

The key to understanding locking is to examine the function space $\mathcal{V}_{0h}$ closely. We can re-write the function space $\mathcal{V}_{0h}$ as:

$$\mathcal{V}_{0h} = \left(\mathcal{V}_{3h} \times \mathcal{R}_h \right) \cap \mathcal{V}_0 \tag{3.18}$$

That is, the space of discrete pure bending displacements is the intersection of the discrete spaces ($\mathcal{V}_{3h}$, $\mathcal{R}_h$) and the space of pure bending displacements. It is the `richness' of this intersection space which governs the quality of the solution; if the space is not `rich' enough, then shear-locking will occur.

In some extreme cases the space $\mathcal{V}_{0h}$ reduces to the zero function. We can show this extreme case using a very simple example. We take $\mathcal{V}_{3h}$ and $\mathcal{R}_h$ to be constructed using piecewise linear finite elements on a mesh with uniform element size. We enforce fully clamped Dirichlet boundary conditions at both ends of the beam, that is:

$$\mathcal{V}_{3h} = \mathcal{R}_h \subset H_0^1(\Omega) \tag{3.19}$$

First note that the rotations θ_h must be zero on the boundary. Furthermore as a natural consequence of using piecewise linear elements the derivatives of the transverse displacements are piecewise constant. Because we are looking for a pure bending solution, that is, one that satisfies the Kirchhoff constraint $z_{3h}' - \theta_h = 0$, then the only possible solution is $\theta_h = 0$ and $z_{3h} = 0$.

The finite element discretisation has produced a numerical model that is overly-stiff, hence the term `locking'. Essentially this discretisation scheme is useless.

3.3.3 Shear-locking in the finite element method

We can demonstrate shear-locking numerically and examine the effect of h and p refinement on shear-locking using the DOLFIN finite element framework [127]. We choose a simple problem, namely a cantilever beam with a point load as illustrated in fig. 3.4. Using the same scaling as for the weak form of the problem, the strong form has the following classical analytical solution for the tip deflection:

$$z_3^T(x_3 = L) = \frac{\tilde{p}L}{3}(1 + 3\varepsilon^2) \tag{3.20}$$

which in the limit as $\varepsilon \to 0$ corresponds to the well-known Bernoulli solution:

$$z_3^0(x_3 = L) = \frac{\tilde{p}L}{3} = \frac{PL^3}{3EI} \tag{3.21}$$

We set $\tilde{p} = 3$ and $L = 1$ so that our limit Bernoulli solution is exactly 1 and the Timoshenko solution is:

$$z_3^T(L) = 1 + 3\varepsilon^2 \tag{3.22}$$

We then implement a numerical scheme using N equal-sized linear polynomial finite elements CG_1 to discretise the domain Ω. An example solver implemented using DOLFIN is shown in algorithm 1.

Locking

In figs. 3.5(a) to 3.5(c) we show deflection z_3 plotted along the length of the beam $[0, L]$ for three values of $\varepsilon = \{1.0, 0.01, 0.001\}$ respectively, whilst keeping the discretisation fixed with $N = 10$ finite elements along the length of the beam. For $\varepsilon = 1.0$ the numerical solution clearly matches the exact solution. For $\varepsilon = 0.01$ there is a significant discrepancy between the numerical and exact solutions. Finally for $\varepsilon = 0.001$ shear-locking has produced the zero function, matching the theoretical prediction above. The shear-locking phenomenon has effectively rendered this discretisation scheme completely useless for thin beams.

Algorithm 1 Code for implementing cantilever beam problem in the Python interface to DOLFIN

```
import numpy as np
from dolfin import *

# Mesh and functions
nx = 10
mesh = UnitInterval(nx)
degree = 1
V_3 = FunctionSpace(mesh, "CG", degree)
R = FunctionSpace(mesh, "CG", degree)
U = MixedFunctionSpace([R, V_3])
R, V_3 = U.split()

theta, z_3 = TrialFunctions(U)
eta, y_3 = TestFunctions(U)

# Loading
end_point = Point(1.0)
f = PointSource(V_3, end_point, 1.0)

# Constants
epsilon = 1.0
L = 1.0
C_s = Constant(epsilon**-2.0)
C_b = Constant(L**2.0)

# Bilinear and linear forms
A = inner(grad(theta), grad(eta))*dx + epsilon**-2*inner(grad(z_3) - theta,
    grad(y_3) - eta)*dx
L = Constant(0.0)*y_3*dx

# Cantilever BC
def left_boundary(x, on_boundary):
    tol = 1E-14
    return on_boundary and np.abs(x[0]) < tol

zero = Constant(0.0)
bc1 = DirichletBC(V_3, zero, left_boundary)
bc2 = DirichletBC(R, zero, left_boundary)
bcs = [bc1, bc2]

# Assemble, apply boundary conditions, apply point load and solve
u_h = Function(U)
A_matrix = assemble(A)
b_vector = assemble(L)
for bc in bcs:
    bc.apply(A_matrix, b_vector)
f.apply(b_vector)

solver = LUSolver(A_matrix)
solver.solve(u_h.vector(), b_vector)
```

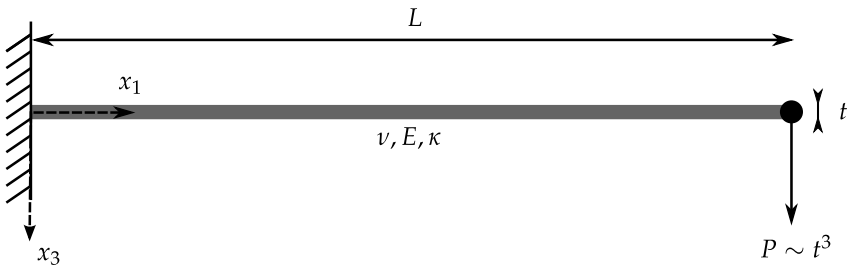

Figure 3.4: Cantilever beam loaded with transverse point load at tip.

h-refinement

Let's take a closer look at the effect of the parameter ε on the convergence of the transverse deflection at the tip of the beam $x_1 = L$. We take as a measurement of error the value of $z_{3h}(L)/z_3^T(L)$, therefore a value close to 0 denotes a very large error, and a value close to 1 denotes a very small error. This is a suitable error measure for the one-dimensional problem because point-wise convergence implies convergence in the H^1 norm.

We run the simulation for varying values of ε and varying numbers of elements N. This experiment was also performed by Chapelle and Bathe [40]. The results are shown in table 3.1. Increasing the number of elements N corresponds to the classical h-refinement procedure. First of all we note that for any N the convergence of the numerical scheme *always* deteriorates for decreasing values of ε. Secondly, to achieve convergence for small values of ε we require extremely large values of N. Finally, there is a clear diagonal pattern in the table; for example, to achieve a fixed convergence value of 0.92308 for decreasing ε the number of elements must be varied as $1/\varepsilon$.

From a practical perspective it is clear that the standard CG_1 finite element scheme is incapable of obtaining convergence without using an unfeasibly high number of elements which naturally consumes significantly more computational resources. For example, to achieve an error of 0.99917, for a moderately thin structure with $\varepsilon = 0.01$ we must use 1000 CG_1 finite elements, resulting in a linear system of size 3003×3003. However if our numerical scheme behaved in a more uniform manner with respect to ε we might expect in the best case to achieve the same level of convergence with only 10 CG_1 finite elements, which results in a linear system of size 33×33. A rough estimate based on a solver with $O(N \log N)$ complexity results in the linear system solve alone taking roughly 200 times longer for the larger problem, not to mention the increased memory requirements and assembly time. In summary, the CG_1 finite

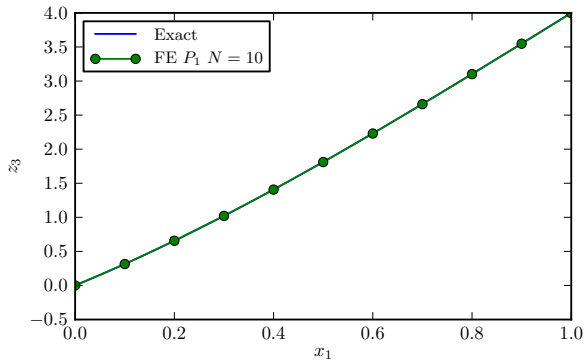

(a) Beam deflection z_3 for $\varepsilon = 1.0$ along the length of the beam. Numerical solution and exact solution are nearly indistinguishable.

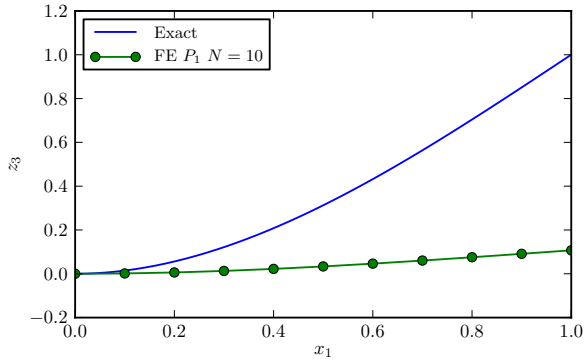

(b) Beam deflection z_3 for $\varepsilon = 0.01$ along the length of the beam. Numerical locking is beginning to occur.

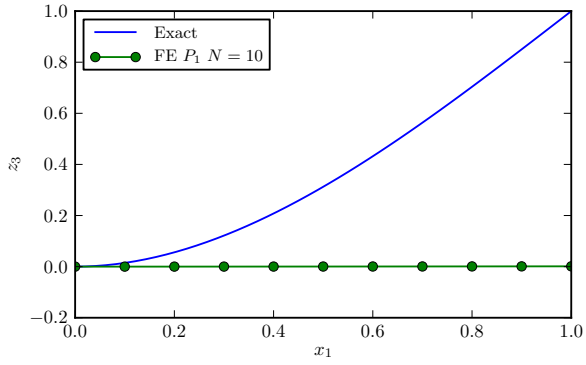

(c) Beam deflection z_3 for $\varepsilon = 0.001$ along the length of the beam. The numerical scheme produces the zero function.

Figure 3.5: Beam deflection z_3 for increasingly thin beams using CG_1 finite element method.

Table 3.1: The effect of h-refinement on the error $z_{3h}(L)/z_3(L)$ at the tip of the cantilever beam. CG_1 FEM.

N	dim(U)	$\varepsilon = 1$	$\varepsilon = 0.1$	$\varepsilon = 0.01$	$\varepsilon = 0.001$	$\varepsilon = 0.0001$
1	4	0.92308	0.10714	0.00120	0.00001	0.00000
10	22	0.99917	0.92308	0.10714	0.00120	0.00001
100	202	0.99999	0.99917	0.92308	0.10714	0.00120
1000	2002	1.00000	0.99999	0.99917	0.92308	0.10714
10000	20002	1.00000	1.00000	0.99999	0.99942	0.92292

element scheme requires unfeasibly large computational resources to achieve only mediocre results for the Timoshenko beam problem.

The above numerical results can be summarised with the following standard error bound [134]:

$$\|z_3 - z_{3h}\|_{L^2(\Omega)} \leq C(\varepsilon^{-n}, \Omega)\, h^2\, |z_3|_{H^2(\Omega)} \tag{3.23}$$

where C is a positive constant that *is* a function of the parameter ε raised to some negative power $n \in \mathbb{N}$ and $h = 1/N$ is the element length. The above standard estimate states that the error in the solution $\|z_3 - z_{3h}\|_{L^2(\Omega)}$ is bounded by three main quantities; firstly the second derivatives of the solution $|z_3|_{H^2}$, secondly the element size squared h^2, and finally the constant C which is dependent on both the small parameter raised to some negative power ε^{-n} and the domain Ω. If ε is very small, the constant C will consequently be extremely large. As $|z_3|_{H^2}$ is fixed for any given problem the only way to counteract the effect of a large C on the error bound is to drastically decrease the element size h. This analytical result reflects exactly the numerical results shown in table 3.1.

p-refinement

The analytical result in section 3.3.3 can be extended to cover Lagrangian elements CG_p of arbitrary polynomial order p. The resulting error bound is [134]:

$$\|z_3 - z_{3h}\|_{L^2(\Omega)} \leq C(\varepsilon^{-n}, \Omega)\, h^{p+1}\, |z_3|_{H^{p+1}(\Omega)} \tag{3.24}$$

This immediately suggests that another way of combating the growing constant C is to increase the polynomial order p of the approximation. To investigate this approach we run the simu-

lation for varying values of ε and varying values of p, whilst keeping the discretisation fixed with $N = 10$. The results are shown in table 3.2. We can see that convergence does improve for increasing polynomial order p, although it still deteriorates as $\varepsilon \to 0$. Furthermore there appear to be some numerical issues when $p = 5$, probably related to ill-conditioning of the finite element basis for higher p.

Table 3.2: The effect of p-refinement on the error $z_{3h}(L)/z_3(L)$ at the tip of the cantilever beam. CG_p FEM.

p	$\dim(U)$	$\varepsilon = 1$	$\varepsilon = 0.1$	$\varepsilon = 0.01$	$\varepsilon = 0.001$	$\varepsilon = 0.0001$	$\varepsilon = 1e-05$	$\varepsilon = 1e-06$
1	22	0.99917	0.92308	0.10714	0.00120	0.00001	0.00000	0.00000
2	42	1.00000	0.99996	0.99844	0.99752	0.99752	0.99935	1.23745
3	62	1.00000	1.00000	1.00000	1.00000	1.00000	0.99970	0.97675
4	82	1.00000	1.00000	1.00000	1.00000	0.99996	0.99638	0.75800
5	102	1.00000	1.00000	1.00000	1.00000	0.99984	0.98451	0.39758

3.3.4 Shear-locking in meshless methods

Similar results can be obtained using the pymfl meshless package. The purpose of this section is to demonstrate that moving to meshless methods does not solve the shear-locking problem, and to compare and contrast the behaviour of the meshless method to the finite element method. An example solver using the pymfl library is shown in algorithm 2.

Locking

Similarly to before, in figs. 3.6(a) to 3.6(c) we show the deflection z_3 plotted along the length of the beam $[0, L]$ for three values of $\varepsilon = \{1.0, 0.01, 0.001\}$ respectively, whilst keeping the discretisation fixed (maximum-entropy basis functions, $N = 10$, fixed and constant support size $\rho = 0.24$). We can see that for $\varepsilon = 1.0$ the numerical solution and the exact solution are nearly indistinguishable, and as ε decreases severe numerical locking begins to occur. This is the same behaviour that the CG_1 finite element scheme shows, and demonstrates that there is nothing inherent in moving to a meshless formulation that alleviates locking.

In fig. 3.7 we compare the behaviour of the CG_1 and meshless formulation by plotting the tip deflection $z_3(x_1 = L)$ against the parameter ε. Additionally, we show both the Bernoulli and

Algorithm 2 Code for implementing cantilever beam problem using the pymfl library

```
import numpy as np

import dolfin as df
import pymfl as mfl

from pymfl.forms.timoshenko import Bending, Shear

nx = 10
beta = 2.0

mesh = df.UnitInterval(nx)
nodes = mfl.UnitInterval(nx + 1)

support_radius = (1.0/float(nx))*beta*1.2
nodes.set_constant_support_radius(support_radius)
nodes.init()

V_3 = mfl.MaxEnt(mesh, nodes, description='transverse displacement')
R = mfl.MaxEnt(mesh, nodes, description='rotations')

U = mfl.MixedFunctionSpace(mesh, [R, V_3], description='timoshenko beam space')
U.finalise()

R, V_3 = U.split()

quadrature_order = 6
points_hat, weights_hat = mfl.quadrature_schemes.create_quadrature("interval",
    quadrature_order)

R.clone_basis_functions_cache(V_3)

bending = Bending(R=R, points_hat=points_hat, weights_hat=weights_hat)
shear = Shear(U=U, epsilon=epsilon, points_hat=points_hat, weights_hat=weights_hat)

a = [bending, shear]
L = []

u_h = mfl.Function(U)
problem = mfl.LinearVariationalProblem(a, L, u_h)
problem.assemble()

end_point = np.array([1.0])
f = mfl.PointSource(V_3, end_point, 3.0)
f.apply(problem.b_vector())

d = lambda x: 0.0
bc_left_theta = mfl.DirichletBC(R, d, left_boundary)
bc_left_w = mfl.DirichletBC(V_3, d, left_boundary)
bcs = [bc_left_theta, bc_left_w]

for bc in bcs:
    bc.apply(problem.A_matrix(), problem.b_vector())

problem.solve()
```

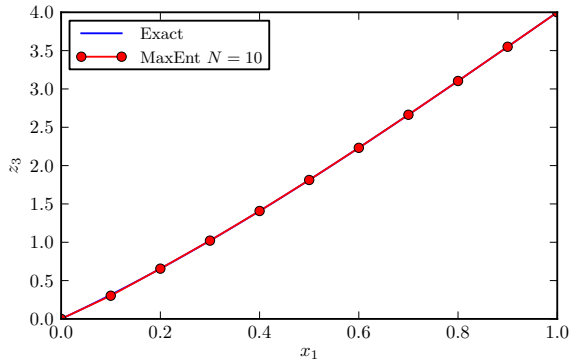

(a) Beam deflection z_3 for $\varepsilon = 1.0$ along the length of the beam. Numerical solution and exact solution are nearly indistinguishable.

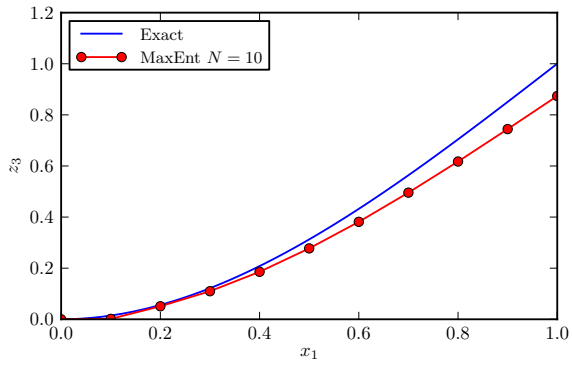

(b) Beam deflection z_3 for $\varepsilon = 0.01$ along the length of the beam. Numerical locking is beginning to occur.

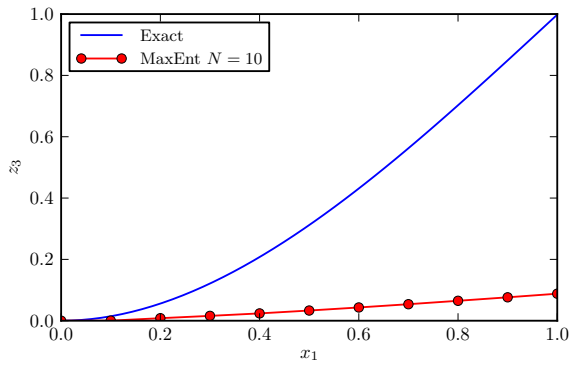

(c) Beam deflection z_3 for $\varepsilon = 0.001$ along the length of the beam. Servere numerical locking has occurred.

Figure 3.6: Beam deflection z_3 for increasingly thin beams using MaxEnt meshless method.

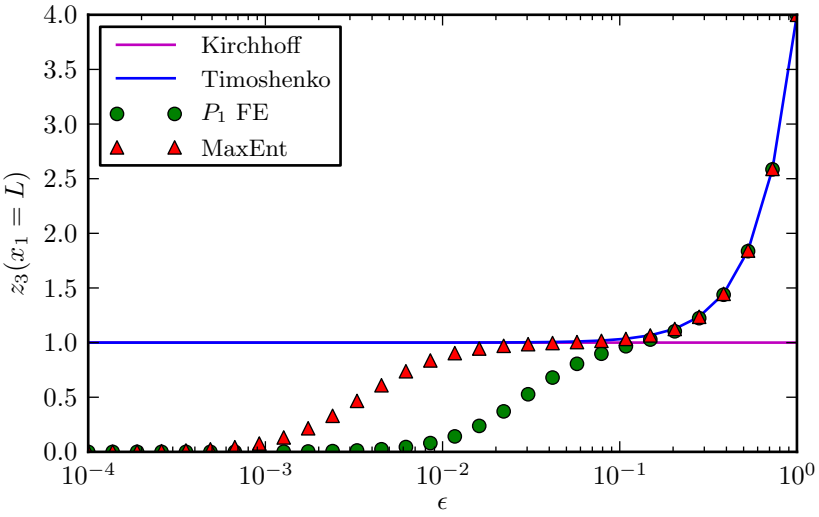

Figure 3.7: Graph showing the tip deflection computed with CG_1 FE and MaxEnt meshless methods with $N = 10$ for varying values of ε. The analytical Timoshenko solution coincides exactly with the analytical Bernoulli solution in the thin plate limit at around $\varepsilon < 5 \times 10^{-2}$.

Timoshenko analytical solutions. Neither numerical method matches the Timoshenko analytical solution for the full range of ε. Additionally we can see that whilst the meshless formulation behaves better than the CG_1 formulation, both have begin to lock in the range $10^{-2} \leq \varepsilon \leq 10^{-1}$.

h-refinement

We begin by performing the equivalent of an h-refinement experiment using maximum-entropy basis functions. The domain is discretised using $N+1$ equally spaced nodes. We keep the support size ρ_a constant with respect to the average nodal spacing; that is, if h is the distance to the nearest node, then $2h$ is the distance to the second nearest node. We then multiply by a small constant factor $\alpha_\rho = 1.2$ to ensure that a total of 4 nodes are in the support of every node situated far away from the boundary:

$$\rho_a = \alpha_\rho \times 2h \tag{3.25}$$

We run the simulation for varying values of N and varying values of ε and the results are shown in table 3.3. For $N = 1$ the errors are identical to those for the CG_1 FE scheme, due to the

maximum-entropy shape functions coinciding with the linear finite element in the limit. For any N the convergence of the numerical method always deteriorates for decreasing values of ε, and extremely large values of N are required to obtain convergence with small values of ε. Finally, there is a clear diagonal pattern in the table once $N > 1$ or once the meshless character of the shape functions is activated. Thus to achieve a fixed convergence value of around 0.998 the nodal spacing must be varied on the order of $1/\varepsilon$. In summary the meshless method shows broadly similar behaviour with respects to the parameter ε to that of the finite element method under an equivalent of the h-refinement procedure.

Table 3.3: The effect of h-refinement on the error $z_{3h}(L)/z_3(L)$ at the tip of the cantilever beam.

N	$\dim(U)$	$\varepsilon = 1$	$\varepsilon = 0.1$	$\varepsilon = 0.01$	$\varepsilon = 0.001$	$\varepsilon = 0.0001$
1	4	0.92308	0.10714	0.00120	0.00001	0.00000
10	22	0.99997	0.99825	0.87357	0.08809	0.00101
100	202	1.00000	0.99998	0.99818	0.84727	0.05535
1000	2002	1.00000	1.00000	0.99998	0.99816	0.84419
10000	20002	1.00000	1.00000	1.00000	0.99984	0.98166

Support radius

In addition to being able to perform h and p refinement it is also possible to increase the support width of the shape functions ρ. This parameter is not available in the CG_1 FE scheme where we are naturally limited to the local approximation. We introduce a parameter $\beta \in \mathbb{N}^+$ which controls the support size as follows:

$$\rho_a = \alpha_\rho \times \beta h \tag{3.26}$$

In table 3.4 we show the effect of varying the support size for various discretisations on the error at the tip of a moderately thin cantilever beam $\varepsilon = 0.01$. For $N = 1$ adjusting the support-size has no effect; this is already the most-local approximation and the shape functions are identical for any β. For $N > 1$ when the meshless nature of the shape functions is realised we see that increasing β improves convergence for all of the discretisations considered. However this also increases the bandwidth of the assembled stiffness matrix, which in turn increases assembly time, storage requirements and linear system solution time. The effect of support size on the sparsity of the linear system is shown in table 3.5. Clearly a proper solution the shear-locking problem would retain the relatively local character of the meshless shape functions whilst pro-

viding optimal convergence for all values of ε. In conclusion it is our view that increasing the support size of the shape functions is *not* a satisfactory or particularly robust remedy of the shear-locking problem.

Table 3.4: The effect of support size on the error $z_{3h}(L)/z_3(L)$ at the tip of the cantilever beam with $\varepsilon = 0.01$. MaxEnt meshless.

N	$\beta = 1$	$\beta = 2$	$\beta = 3$	$\beta = 4$	$\beta = 5$
1	0.00120	0.00120	0.00120	0.00120	0.00120
10	0.12602	0.87357	0.99049	0.99824	0.99912
100	0.93676	0.99818	0.99991	0.99999	0.99999
1000	0.99933	0.99998	1.00000	1.00000	1.00000

Table 3.5: The effect of support size on the sparsity of the linear system $\mathrm{nnz}(A)/(\dim U)^2$ for the cantilever beam problem. MaxEnt meshless.

N	$\beta = 1$	$\beta = 2$	$\beta = 3$	$\beta = 4$	$\beta = 5$
1	1.000	1.000	1.000	1.000	1.000
10	0.537	0.752	0.901	0.983	1.000
100	0.068	0.106	0.143	0.179	0.215
1000	0.007	0.011	0.015	0.019	0.023

p-refinement

We perform an equivalent of a p-refinement experiment using RPIM basis functions. MaxEnt basis functions do not allow p-refinement without loss of the Kronecker-delta property. The domain is discretised using $N + 1$ equally spaced nodes and $\beta = 4$. The results are shown in table 3.6. We can see that p-refinement does improve convergence, but still deteriorates as $\varepsilon \to 0$. The meshless method therefore shows similar trends to the FE method.

3.4 Conclusions

By considering the one-dimensional counterpart of the Reissner-Mindlin plate problem, the Timoshenko beam problem, we have demonstrated the shear-locking phenomenon numeri-

Table 3.6: The effect of p-refinement on the error $z_{3h}(L)/z_3(L)$ at the tip of the cantilever beam.

p	$\varepsilon = 1$	$\varepsilon = 0.1$	$\varepsilon = 0.01$	$\varepsilon = 0.001$	$\varepsilon = 0.0001$	$\varepsilon = 1e-05$	$\varepsilon = 1e-06$
1	0.99992	0.99157	0.81082	0.46261	0.03430	0.00037	0.00000
2	1.00000	0.99949	0.98844	0.95931	0.77657	0.75030	0.75107
3	1.00000	1.00000	1.00000	1.00000	1.00000	1.00001	1.00161
4	1.00000	1.00000	1.00000	1.00000	1.00000	1.00000	0.99688

cally and explained its origins through simple function space arguments. The shear-locking problem is the inability of the basis functions to richly represent the Kirchhoff or thin beam limit. Analogously, in the shear-deformable Reissner-Mindlin plate problem the shear-locking problem is the inability of the basis functions to richly represent the Kirchhoff or thin plate limit. We have performed simple numerical experiments to compare the behaviour of the standard Lagrangian finite element method and meshless methods with respect to the small parameter ε under both h and p refinement. In addition for the meshless method we have examined the role of the parameter β which controls the basis function support size.

Under h-refinement, the meshless basis functions show broadly similar behaviour to the CG_1 finite element method with roughly a $1/\varepsilon$ scaling of the nodal spacing required to ensure convergence. Similarly, under p-refinement the meshless and finite-element basis functions are better able to richly represent the limiting Kirchhoff mode and convergence can be improved. Both results can be explained using a traditional error bound argument from the finite element method literature. The parameter β, which controls the shape function width only in the meshless method can also be used to improve convergence with respect to the small parameter ε, but at significant computational cost.

In summary, none of the above methods ensure optimal rates of convergence for any ε as they all essentially work by attempting to beat the rapidly growing constant $C(\varepsilon^{-n}, \Omega)$ which bounds the error. Furthermore all require additional computational resources without necessarily providing improved convergence. As a result, all offer sub-optimal convergence that is dependent on the small parameter ε. All of the above methods will lock if ε is small enough. This situation is far from ideal, and motivates the construction of a meshless numerical method that *removes* the dependence of the constant C on the small parameter ε, providing uniform, consistent and reliable convergence behaviour for any ε. Such a method will be free from the negative effects of shear-locking. It is this goal that is the topic of the remaining chapters of this thesis.

4 Meshless methods for the shear-deformable beam problem based on a mixed weak form

In this chapter we demonstrate the ability of a mixed variational formulation to produce meshless numerical methods for the Timoshenko beam problem that are free from shear-locking. We begin by moving from the primal or displacement form of the Timoshenko beam problem to a mixed formulation where the shear stresses are treated as an independent variational quantity in the weak form.

We present a solution to the discretisation problem using a hybrid meshless-element method where the shear stresses are approximated directly on an underlying mesh. As no transform is used between reference and global elements of the mesh the robustness of the meshless approximation field is retained and the implementation is greatly simplified.

In the particular case of maximum entropy shape functions we prove that the scheme D1 converges to the well-known $CG_1 - DG_0$ Timoshenko beam finite element in the Delaunay limit. One of the proposed schemes, D2, suffers from spurious or zero-energy modes due to it not satisfying the kernel coercivity condition.

We demonstrate the good performance of the proposed method using three test problems with known analytical solutions in polynomial form. Using the problem of a beam in pure bending we present new insight into the `Kirchhoff mode reproducing conditions' (KMRC) of Wang and Chen. Whilst it is necessary to use a second-order monomial basis to ensure bending exactness to machine precision, it is not necessary to ensure convergence in general problems.

We show that using a first-order maximum entropy basis with our method we can obtain convergence rates of $\rho = -h \sim -2.5$ in the L^2 norm for the transverse displacement variable, and using a second-order RPIM basis we can obtain convergence rates of $\rho \sim -3.3$, in comparison with the work of Wang and Chen who achieve a convergence rate of $\rho \sim -2.8$ using a second-order monomial basis.

For two standard test problems our method shows convergence in all relevant norms for all problem variables. Because of the lack of results available in the literature for other norms

we are unable to make a comparison with other meshless methods.

4.1 Introduction

In the previous chapter we demonstrated that standard meshless methods suffer from shear-locking when solving the Timoshenko beam problem in a very similar manner as the standard finite element method. Whilst it was possible to alleviate locking to some extent via either h or p refinement, and additionally in meshless methods by increasing the support size ρ, none of these approaches alleviates locking entirely or does so with optimal use of computational resources. Therefore the aim is to remove the dependency on the small thickness parameter ε on the convergence of the numerical method in a robust and computationally inexpensive manner.

Following the experience from the FEM community, the most robust and effective method for removing this dependency on the small parameter ε is designing a meshless discretisation scheme based on a mixed weak form, where shear stresses are treated as an independent variational quantity. We will derive the mixed weak form of the Timoshenko beam problem directly from the displacement form already shown. We will then discuss the importance of considering the issue of stability; in numerical methods based on displacement weak forms stability is usually inherited directly from the stability of the continuous weak form, however for numerical methods based on mixed weak forms stability is no longer guaranteed. Two conditions, commonly known as the Ladyzhenskaya-Babuška-Brezzi condition, LBB condition, or inf-sup condition [52], in addition to the kernel coercivity or coercivity condition [52], must be met if the numerical method based on the mixed weak form is to be stable.

We then introduce three novel discretisation designs for the mixed weak form. The displacement variables are approximated by a meshless method on a set of nodes and the shear stresses on an underlying finite element mesh. Because no derivatives of the basis functions are required no map is needed between reference and global elements in the mesh and there is therefore no need to use a second meshless basis. We find that one of the discretisation designs, namely scheme D2, suffers from spurious or zero-energy modes due to it not satisfying the kernel coercivity condition. Fortunately schemes D1 and D3 prove to be stable. We also show that scheme D1 coincides with the well known $CG_1 - DG_0$ finite element method in the local limit, for which an analytical proof of stability is readily available.

4.2 Formulation

In this section we derive the mixed form of the scaled Timoshenko problem directly from the displacement form. We then identify the mixed problem as one in the general form of a saddle point problem with a penalty parameter. We discuss the $CG_1 - DG_0$ finite element method and introduce three discretisation schemes and develop the discrete matrix equations. The designs are implemented into the pymfl library. We then perform some basic tests to examine the performance of the three proposed schemes.

4.2.1 Derivation of mixed weak form

We begin with the scaled Timoshenko beam problem originally derived in chapter 3:

Problem 10 (Scaled Timoshenko beam problem)**.** *Find* $(z_3^\varepsilon, \theta^\varepsilon) \in \mathcal{V}^T$ *such that:*

$$L^2 \int_\Omega \theta^{\varepsilon'} \eta' \, d\Omega + \frac{1}{\varepsilon^2} \int_\Omega (z_3^{\varepsilon'} - \theta^\varepsilon)(y_3' - \eta) \, d\Omega = \int_\Omega \tilde{p} y_3 \, d\Omega \quad \forall (y_3, \eta) \in \mathcal{V}^T \tag{4.1}$$

We then introduce the shear stress trial function $\gamma^\varepsilon \in S$ as a new variable, where S is an appropriate function space:

$$\gamma^\varepsilon = \varepsilon^{-2}(z_3^{\varepsilon'} - \theta^\varepsilon) \in S \tag{4.2}$$

Upon substituting eq. (4.2) into eq. (4.1) we obtain the following equation:

$$L^2 \int_\Omega \theta^{\varepsilon'} \eta' \, d\Omega + \int_\Omega \gamma^\varepsilon (y_3' - \eta) \, d\Omega = \int_\Omega \tilde{p} y_3 \, d\Omega \tag{4.3}$$

As we now have an extra unknown γ^ε we clearly require an additional equation to solve. With this goal in mind we define the associated test function $\psi \in S$ and derive the weak form of eq. (4.2) in the standard Galerkin manner by multiplying through with ψ and integrating across the domain Ω:

$$\int_\Omega \gamma^\varepsilon \psi \, d\Omega = \int_\Omega \varepsilon^{-2}(z_3^{\varepsilon'} - \theta^\varepsilon)\psi \, d\Omega \tag{4.4}$$

Rearranging gives the following mixed weak form of the Timoshenko beam problem where the shear stress γ^ε is now treated as an independent variational quantity:

Problem 11 (Mixed scaled Timoshenko beam problem)**.** *Find* $(z_3^\varepsilon, \theta^\varepsilon, \gamma^\varepsilon) \in \mathcal{V}^T \times S$ *such that:*

$$L^2 \int_\Omega \theta^{\varepsilon'} \eta' \, d\Omega + \int_\Omega \gamma^\varepsilon (y_3' - \eta) \, d\Omega = \int_\Omega \tilde{p} y_3 \, d\Omega \qquad \forall (y_3, \eta) \in \mathcal{V}^T \tag{4.5a}$$

$$\int_\Omega (z_3^{\varepsilon'} - \theta^\varepsilon)\psi \, d\Omega - \varepsilon^2 \int_\Omega \gamma^\varepsilon \psi \, d\Omega = 0 \qquad \forall \psi \in S \tag{4.5b}$$

Examining Problem 11 we notice that no derivatives of either the trial or test shear stresses appear in the weak form, allowing us to identify the space S as:

$$S = L^2(\Omega) \tag{4.6}$$

Therefore the shear stresses have significantly less regularity than the primary problem variables $(z_3^\varepsilon, \theta^\varepsilon)$ which lie in the space $H_0^1(\Omega)^2$, which in practical terms means that a basis function with low continuity (C^{-1}) can be used for discretisation. Now in a general sense, that is without making any specific design choices at this stage, we introduce the discrete function spaces $V_h^T \subset V^T$ and $S_h \subset S$ allowing us to write the mixed problem in the following equivalent discrete form:

Problem 12 (Discrete mixed scaled Timoshenko beam problem)**.** *Find* $(z_{3h}^\varepsilon, \theta_h^\varepsilon, \gamma_h^\varepsilon) \in \mathcal{V}_h^T \times S_h$ *such that:*

$$L^2 \int_\Omega \theta_h^{\varepsilon'} \eta' \, d\Omega + \int_\Omega \gamma_h^\varepsilon (y_3' - \eta) \, d\Omega = \int_\Omega \tilde{p} y_3 \, d\Omega \qquad \forall (y_3, \eta) \in \mathcal{V}_h^T \tag{4.7a}$$

$$\int_\Omega (z_{3h}^{\varepsilon'} - \theta_h^\varepsilon)\psi \, d\Omega - \varepsilon^2 \int_\Omega \gamma_h^\varepsilon \psi \, d\Omega = 0 \qquad \forall \psi \in S_h \tag{4.7b}$$

All of the discretisations in this chapter are based upon the discrete mixed scaled Timoshenko beam problem in eq. (4.7).

4.2.2 Stability

The problem derived in the previous section can be identified as a saddle-point problem with a penalty term controlled by the small parameter ε and fits into the framework introduced by Braess [135], which is an extension of the classic work of Brezzi [52]. This mixed formulation has the clear advantage over the original displacement formulation in that the thickness-type parameter ε now enters as a small parameter with positive exponent. When $\varepsilon = 0$ the shear

stress variables γ and ψ take the role of Lagrange multipliers which act to enforce the Kirchhoff constraint $z_3^{\varepsilon'} - \theta = 0$ [135].

It is well known that whilst any reasonable discretisation $V_h^T \subset V^T$ of the displacement formulation are automatically stable, the required conditions for good performance of discretisations of saddle point problem are significantly more difficult to achieve. We give an overview of the results of Braess [135] and Brezzi [52] here, results which are crucial in giving us an insight into how to design a stable discretisations of the mixed Timoshenko beam problem.

Definition 1 (General form of a penalised saddle point problem (Braess [135]))**.** *Let $\mathcal{X}$ and $\mathcal{M}$ be Hilbert spaces with norms $\|\cdot\|_{\mathcal{X}}$ and $\|\cdot\|_{\mathcal{M}}$ and let $\mathcal{M}_c$ be a dense linear subset of $\mathcal{M}$. The penalised saddle point problem can be described by three bilinear forms*

$$a \ : \ \mathcal{X} \times \mathcal{X} \to \mathbb{R}, \qquad a(u;v) = a(v;u) \tag{4.8a}$$

$$b \ : \ \mathcal{X} \times \mathcal{M} \to \mathbb{R}, \tag{4.8b}$$

$$c \ : \ \mathcal{M}_c \times \mathcal{M}_c \to \mathbb{R}, \qquad c(p;q) = c(q;p) \tag{4.8c}$$

Then given $f \in \mathcal{X}'$ and $g \in \mathcal{M}_c'$ the generalised form of a penalised saddle point problem can be stated as: Find $(u,p) \in \mathcal{X} \times \mathcal{M}_c$ such that:

$$a(u;v) + b(p;v) =< f, v > \qquad \forall v \in \mathcal{X} \tag{4.9a}$$

$$b(u;q) - t^2 c(p;q) =< g, q > \qquad \forall q \in \mathcal{M}_c \tag{4.9b}$$

where $\mathcal{X}'$ and $\mathcal{M}_c'$ are the associated duals of the spaces $\mathcal{X}$ and $\mathcal{M}_c$ respectively and the notation $<,>$ denotes a dual pairing between both arguments. The notation $(;)$ has been used to denote the split between trial and test functions in the bilinear forms. Furthermore we assume that the bilinear forms a and b are bounded. The form c gives rise to a semi-norm:

$$|q|_c := c(q,q)^{1/2} \quad , q \in \mathcal{M}_c \tag{4.10}$$

The saddle point problem is then simply the specific case of the above problem when $\varepsilon = 0$:

Definition 2 (General form of a saddle point problem)**.** *(Brezzi [52])] Given $f \in \mathcal{X}'$ and $g \in \mathcal{M}_c'$*

the generalised form of a saddle point problem can be stated as: Find $(u, p) \in \mathcal{X} \times \mathcal{M}_c$ *such that:*

$$a(u; v) + b(p; v) = \langle f, v \rangle \qquad \forall v \in \mathcal{X} \tag{4.11a}$$

$$b(u; q) = \langle g, q \rangle \qquad \forall q \in \mathcal{M}_c \tag{4.11b}$$

We can then recognise the mixed Timoshenko problem eq. 11 as a penalised saddle point problem in the form of eqs. (4.8) and (4.11) with the following choices:

$$\mathcal{X} := \mathcal{V}^T := H_0^1(\Omega)^2, \qquad a(z_3, \theta; v_3, \eta) := L^2(\theta; \eta)_{L^2(\Omega)} \tag{4.12a}$$

$$\mathcal{M} := S := L^2(\Omega), \qquad b(y_3, \eta; \psi) := (\nabla y_3 - \eta; \psi)_{L^2(\Omega)} \tag{4.12b}$$

$$\mathcal{M}_c := L^2(\Omega), \qquad c(\gamma, \psi) := (\gamma; \psi)_{L^2(\Omega)} \tag{4.12c}$$

where the notation $(;)_{L^2(\Omega)}$ has been used as shorthand to denote the L^2 inner product on the domain Ω between the trial and test arguments:

$$(v; q)_{L^2(\Omega)} = \int_\Omega v \cdot q \, d\Omega \tag{4.13}$$

We can write the above penalised saddle point problem in the following combined form [52]:

$$A(u, p; v, q) = a(u; v) + b(p; v) + b(u; q) - t^2 c(p; q) \tag{4.14}$$

which gives rise to the following natural norm:

$$\left|\left|\left|(v, q)\right|\right|\right| = \|v\|_X + \|q\|_M - t\,|q|_c \tag{4.15}$$

Then it is possible to show that the penalised saddle point problem will be stable if and only if there exists a constant γ for all $(u, p) \in \mathcal{X} \times \mathcal{M}_c$ and $0 \leq t \leq 1$:

$$\sup_{v,q} \frac{\left|A(u, p; v, q)\right|}{\left|\left|\left|(v, q)\right|\right|\right|} \geq \gamma \left|\left|\left|(u, p)\right|\right|\right| \tag{4.16}$$

Then we can recall the following theorem due to Brezzi's splitting theorem [52]. As the name suggests, Brezzi's splitting theorem splits the very general stability condition stated in eq. (4.16) into two constituent parts suitable for the analysis of problems in the saddle point form of eq. (4.11).

Theorem 1. *The classical saddle point problem ($\bar{t} = 0$) is stable, if and only if, the following conditions hold:*

1. *($\mathcal{Z}$-Ellipticity of a) There exists a constant $\alpha \geq 0$ such that:*

$$a(v, v) \geq \alpha \|v\|_{\mathcal{X}}^2 \quad \forall v \in \mathcal{Z} \tag{4.17}$$

where $\mathcal{Z}$ is the kernel of the bilinear form b:

$$\mathcal{Z} := \left\{ v \in \mathcal{X} \mid b(v, q) = 0 \quad \forall q \in \mathcal{M} \right\} \tag{4.18}$$

2. *(inf-sup condition on b) The bilinear form b satisfies an inf-sup condition:*

$$\inf_{q \in \mathcal{M}} \sup_{v \in \mathcal{X}} \frac{b(v, q)}{\|v\|_{\mathcal{X}} \|q\|_{\mathcal{M}}} = \beta > 0 \tag{4.19}$$

Then if the classical saddle point problem is stable then the penalised form is stable if either the following two cases applies [135]:

Theorem 2. *(Boundedness of c) If the classical saddle point problem ($\bar{t} = 0$) is stable, and if there exists a positive constant C such that:*

$$c(p, q) \leq C \|p\|_{\mathcal{M}} \|q\|_{\mathcal{M}} \quad \forall p,\ q \in \mathcal{M} \tag{4.20}$$

then the penalised saddle point problem is stable.

or alternatively:

Theorem 3. *($\mathcal{X}$-Ellipticity of a) If the classical saddle point problem ($\bar{t} = 0$) is stable, and if there exists a positive constant α such that:*

$$a(v, v) \geq \alpha \|v\|_{\mathcal{X}}^2 \quad \forall v \in \mathcal{X} \tag{4.21}$$

then the penalised saddle point problem is stable.

With these three theorems in mind we make the following remarks about the mixed formulation of the Timoshenko beam problem; Firstly, the bilinear form $a := a_b$ in the mixed formulation eq. 11 is *not* coercive on the entire space $\mathcal{X} := \mathcal{V}^T := H_0^1(\Omega_0)^2$, but only on the

subset of functions which satisfy the Kirchhoff constraint $z_3' - \theta = 0$. This is due to the loss of the quadric terms in transverse displacement which were present in the bilinear form $a := a_b + a_s$ for the displacement formulation in eq. (4.1). Indeed, this loss of coercivity in a is typical of most mixed formulations, except notably for the Stokes problem.

Secondly, for a discretisation of Problem 11 to be successful, that is, the construction of the subspaces $\mathcal{X}_h \subset \mathcal{X}$ and $\mathcal{M}_h \subset \mathcal{M}$ to be suitable, we must satisfy the discrete equivalents of theorems 1 to 3. The satisfaction of these conditions is not a trivial matter. We will refer to condition 1 of theorem 1 as the kernel coercivity condition, and condition 2 of theorem 1 as the inf-sup condition.

Very broadly speaking, we must choose a larger (or `richer') space $\mathcal{X}_h$ (whilst keeping the same $\mathcal{M}_h$) to ensure the inf-sup condition is satisfied [53]. However, if $\mathcal{X}_h$ is too rich then the kernel coercivity condition becomes harder to satisfy [53]. It is these two competing requirements that make the design of mixed discretisations for the Timoshenko beam problem so difficult.

4.2.3 FE discretisation

The most successful and widely used discretisation of the mixed Timoshenko problem is the $CG_1 - DG_0$ finite element method. In this finite element design the transverse displacement z_3^ε and rotation θ^ε are approximated using CG_1 continuous Lagrangian finite elements and the transverse shear stress γ^ε is approximated using DG_0 discontinuous Lagrangian finite elements [40].

This commonly used element design is part of a broader (and less widely known and used) family of elements $CG_p - DG_{(p-1)}$ parameterised by the index $p \in \mathbb{N}$ for $p \geq 1$ where CG_p continuous elements are used to discretise the transverse displacement z_3^ε and rotation θ^ε whilst $DG_{(p-1)}$ discontinuous Lagrangian elements are used to discretise the shear stress γ^ε [40]. We show the two lowest-order members of this family in fig. 4.1.

The space of discontinuous Lagrange elements DG_p form a subspace of L^2 meaning that the approximated quantity can be discontinuous between elements. The basis functions are identical to those used in the standard Lagrangian finite element space $CG_p \subset H^1$, but adjacent elements do not share degrees of freedom. For example, in one-dimension a DG_1 space constructed on a two element mesh will have four degrees of freedom, whilst a CG_1 space constructed from the same mesh will only have three degrees of freedom due to the two elements sharing an internal degree of freedom.

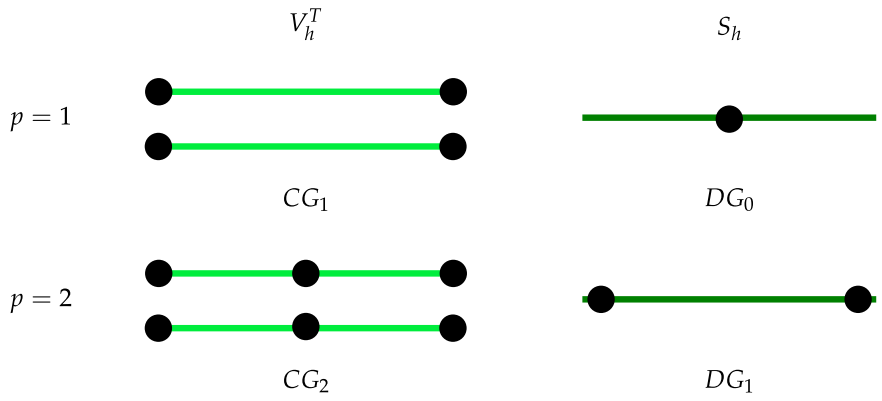

Figure 4.1: First two members of the family $CG_p - DG_{(p-1)}$ for the mixed Timoshenko beam problem. Black circles represent degrees of freedom. For the DG_p discontinuous Lagrangian elements degrees of freedom are internal to each element.

A formal proof that the $CG_p - DG_{(p-1)}$ family of elements satisfies the discrete counterparts of the kernel coercivity condition and inf-sup condition is given by Chapelle and Bathe in [40]. Given the success of this discretisation family it seems to make sense to use it as the starting point for the design of novel meshless discretisations of the mixed Timoshenko beam problem as well.

With regards to the broad conditions regarding stability outlined above, we can see that the space for the transverse displacement and rotation:

$$(z_{3h}^{\varepsilon}, \theta_h^{\varepsilon}) \in \mathcal{V}_h^T \equiv [CG_p]^2 \subset H_0^1(\Omega)^2 \tag{4.22}$$

is indeed richer than the space chosen for the transverse shear stress:

$$\gamma^{\varepsilon} \in S_h \equiv DG_{(p-1)} \subset L^2(\Omega) \tag{4.23}$$

It is also worth noting that the construction $CG_p - DG_{(p-1)}$ has taken advantage of the fact that the shear space S_h can be a subset of the low-regularity space L^2 (allowing lower C^{-1} continuity between elements) rather than the higher regularity required for $\mathcal{V}_h^T$ (requiring C^0 continuity between elements).

We can also examine the constraint ratio of the family $CG_p - DG_{(p-1)}$. For a mesh $\mathcal{T}_h$ consisting

of n cells of length h we can easily obtain that the dimension of the space $[CG_p]^2$ is:

$$\dim([CG_p]^2) = 2(pn - 1) \tag{4.24}$$

and the dimension of the space DG_p is:

$$\dim([DG_p]) = n(p + 1) \tag{4.25}$$

and therefore we can state the constraint ratio of unknowns for the transverse displacement and rotation degrees of freedom to the shear stress degrees of freedom can be written:

$$\frac{\dim(\mathcal{V}_h^T)}{\dim(S_h)} := \frac{\dim([CG_p]^2)}{\dim([DG_{(p-1)})} = \frac{2(pn - 1)}{pn} \tag{4.26}$$

which in the limit as the mesh becomes infinitely refined becomes:

$$\lim_{n\to\infty} \frac{2(pn - 1)}{pn} = 2 \tag{4.27}$$

so the constraint ratio tends to the value 2 for the family of $CG_p - DG_{(p-1)}$ finite elements, which means that the necessary (but not sufficient) condition for stability that $\dim(\mathcal{V}_h^T) > \dim(S_h)$ is at least satisfied. With this in mind it seems sensible to design a mixed meshless method along similar lines.

4.2.4 Meshless discretisation

In this section we will outline the design and computational implementation of the novel meshless discretisations. In this section we will introduce three discretisation designs; the first, which will refer to as discretisation 1, or D1 we will explain in full whilst the other two, discretisation 2 and discretisation 3, or D2 or D3 respectively, are simple modifications of D1. The three discretisations D1, D2 and D3 are shown in figs. 4.2(a) to 4.2(c).

Discretisation Design

Beginning with D1, we define a node set $\mathcal{N}_h$ and support size set ρ_h upon which our meshless discretisations for the rotations and transverse displacements $\mathcal{V}_h^T$ will be constructed. We discretise the problem domain Ω using N equally spaced nodes resulting in characteristic nodal

spacing of length h:

$$\mathcal{N}_h = \{x^1, x^2, \dots, x^N \in \Omega \mid \|x_{i+1} - x_i\| = h \quad \forall\, i \in \{1, 2, \dots, N-1\}\} \tag{4.28}$$

and with each node x^i in $\mathcal{N}_h$ we associate a support radius ρ_i resulting in the following definition of the support radius vector ρ:

$$\rho = \{\rho_1, \rho_2, \dots, \rho_N\} \tag{4.29}$$

On a regular distribution of nodes where $\left\|x^{i+1} - x^i\right\| = h \quad \forall\, i \in \{1, 2, \dots, N-1\}$ we can define a uniform support size for all nodes with the formula:

$$\rho_i = \alpha_\rho \beta h \quad \forall i \tag{4.30}$$

and we set $\alpha_\rho = 1.05$ and we take $\beta = 2$. We now have everything we need to define a unique meshless discretisation based on the MLS, MaxEnt or RPIM methods. For the MaxEnt method we set:

$$\mathcal{V}_h^T := [ME(\Omega; \mathcal{N}_h, \rho_h)]^2 \tag{4.31}$$

for the MLS first-order method we set:

$$\mathcal{V}_h^T := [MLS_1(\Omega; \mathcal{N}_h, \rho_h)]^2 \tag{4.32}$$

and finally for the RPIM first-order and second-order using $p = 1, 2$ we set:

$$\mathcal{V}_h^T := [RPIM_p(\Omega; \mathcal{N}_h, \rho_h)]^2 \tag{4.33}$$

Turning to the specification of the discretisation for the shear space S_h we introduce a mesh $\mathcal{T}_h$ by partitioning the problem domain Ω into a finite set of cells T with disjoint interiors such that:

$$\cup_{T \in \mathcal{T}_h} = \Omega \tag{4.34}$$

The straightforward choice is to choose the end-points of the cells to be coincident with the nodes specified in $\mathcal{N}_h$ which also makes sense when considering the computational implementation of the method, resulting in a mesh $\mathcal{T}_h$ consisting of n cells with characteristic length

h. We then choose the space S_h to be constructed from discontinuous Lagrangian elements:

$$S_h := DG_0(\Omega; \mathcal{T}_h) \tag{4.35}$$

D2 and D3 are then slight modifications of D1. With D2 (fig. 4.2(b)) additional meshless nodes are inserted equidistant between each pair of existing meshless nodes, resulting in a characteristic nodal spacing of $h/2$. Note that the mesh $\mathcal{T}_h$ for D2 is left unchanged from the original in D1. Finally, with D3 (fig. 4.2(c)) we keep the underlying node set $\mathcal{N}_h$ and mesh $\mathcal{T}_h$ the same as in D1, but instead choose the space S_h to be constructed from continuous Lagrangian elements of lowest order:

$$S_h := CG_1(\Omega; \mathcal{T}_h) \tag{4.36}$$

An interesting mathematical aspect of scheme D1 is that in the local limit ($\rho \to 2h$) the scheme $[ME(\Omega; \mathcal{N}_h, \rho_h)]^2 \times DG_0(\Omega; \mathcal{T}_h)$ is identical to the $[CG_1(\Omega; \mathcal{T}_h)]^2 \times DG_0(\Omega; \mathcal{T}_h))$ scheme from the finite element literature. This is because the MaxEnt shape functions always tend towards the linear interpolant $CG_1(\Omega; \mathcal{T}_h)$ in the local limit [21]. Therefore we can say that, at least in this local limit, the D1 scheme satisfies the discrete kernel coercivity and inf-sup conditions by virtue of the proof for the corresponding CG_1-DG_0 finite element scheme [40].

Discrete equations

Now we will develop the discrete stiffness matrix $\boldsymbol{K}$ and force vector $\boldsymbol{f}$ equations required to implement the proposed D1, D2 and D3 methods. We begin by writing the approximated transverse displacement $z_{3h}(x_1), y_3(x_1)$ and rotation $\theta_h(x_1), \eta(x_1)$ trial and test functions using the meshless basis $\varphi_i(x_1) \in \mathcal{V}_h^T$:

$$z_{3h}(x_1) = \sum_{i=1}^{N} \varphi_i(x_1) z_{3i} \quad y_3(x_1) = \sum_{i=1}^{N} \varphi_i(x_1) \tag{4.37}$$

$$\theta_h(x_1) = \sum_{i=1}^{N} \varphi_i(x_1) \theta_i \quad y_3(x_1) = \sum_{i=1}^{N} \varphi_i(x_1) \tag{4.38}$$

where N is the number of meshless nodes in $\mathcal{N}_h$. z_{3i} and θ_{hi} are the associated nodal unknowns for the transverse displacements and rotations, respectively.

Similarly we write the approximated shear stress $\gamma_h(x_1)$ trial and test functions using the finite

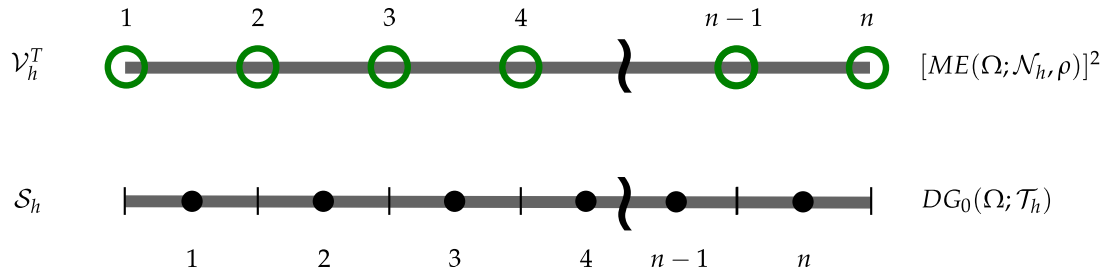

(a) Discretisation 1 (D1): MaxEnt discretisation with characteristic nodal spacing of h to discretise the displacements $\mathcal{V}_h^T$ and discontinuous Lagrangian elements of zero-order with element vertices coinciding with the nodal positions of the MaxEnt discretisation to discretise the shear stress S_h

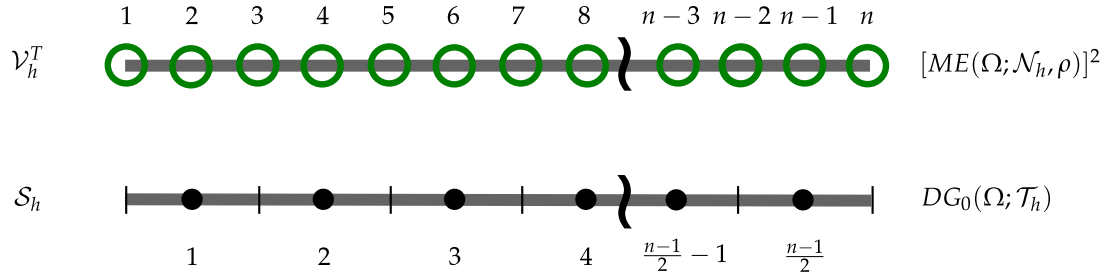

(b) Discretisation 2 (D2): The same as D1, but with an additional meshless node inserted equidistant between each pair of existing meshless nodes, resulting in characteristic nodal spacing of $h/2$

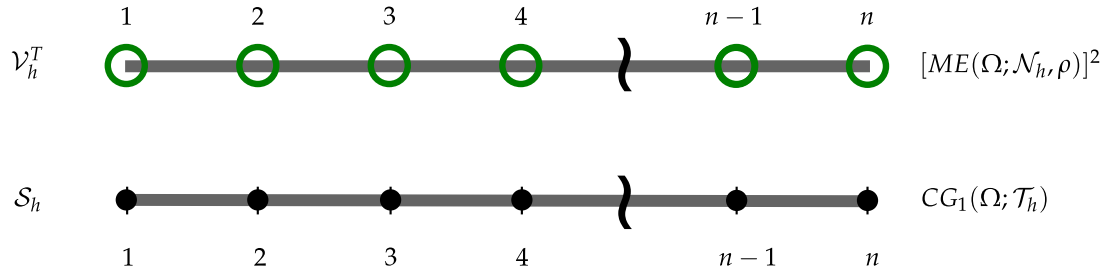

(c) Discretisation 3 (D3): The same as D1, except continuous Lagrangian elements of first-order are used to discretise the shear stress S_h

Figure 4.2: The three discretisation D1, D2 and D3 considered in this chapter. Green hollow circles represent degrees of freedom for the meshless discretisation used for the displacements (ie. two per circle), solid black circles represent degrees of freedom for the finite element discretisation used for the shear stress, and (integration and finite element) cell vertices are shown by black vertical lines.

element basis functions $N_i(x_1) \in S_h$:

$$\gamma_h(x_1) = \sum_{j=1}^{M} N_i(x_1)\gamma_i \quad \psi(x_1) = \sum_{j=1}^{M} N_i(x_1)\gamma_i \tag{4.39}$$

where M is the number of cells in $\mathcal{T}_h$ if $S_h := DG_0(\Omega; \mathcal{T}_h)$ and M is the number of vertices in $\mathcal{T}_h$ if $S_h := CG_1(\Omega; \mathcal{T}_h)$.

For simplicity the explicit dependence on x_1 is dropped, and the above expressions are re-written in vectorial form as follows:

$$z_{3h} = \boldsymbol{\varphi} \boldsymbol{z}_3, \quad y_3 = \boldsymbol{\varphi} \tag{4.40a}$$

$$\theta_{3h} = \boldsymbol{\varphi} \boldsymbol{\theta}, \quad \eta = \boldsymbol{\varphi} \tag{4.40b}$$

$$\gamma_h = \boldsymbol{N} \boldsymbol{\gamma}, \quad \psi = \boldsymbol{N} \tag{4.40c}$$

where $\boldsymbol{\varphi}$ is a vector of size $1 \times N$, $\boldsymbol{N}$ is a vector of size $1 \times M$ containing the finite element basis functions, $\boldsymbol{z}_3$ and $\boldsymbol{\theta}$ are vectors of size $N \times 1$ containing the displacement nodal unknowns, and $\boldsymbol{\gamma}$ is a vector of size $M \times 1$ containing shear stress nodal unknowns. Substituting eq. (4.40) into eq. (4.7) results in the following discrete equations written in terms of the basis functions and nodal unknowns:

$$L^2 \int_\Omega \boldsymbol{\varphi}'^T \boldsymbol{\varphi}' \, d\Omega \, \boldsymbol{\theta} + \int_\Omega \boldsymbol{B}_s^T \boldsymbol{N} \, d\Omega \, \boldsymbol{\gamma} = \int_\Omega \boldsymbol{\varphi}^T \tilde{p} \, d\Omega \tag{4.41a}$$

$$\int_\Omega \boldsymbol{N}^T \boldsymbol{B}_s \, d\Omega \begin{Bmatrix} \boldsymbol{\theta} \\ \boldsymbol{z}_3 \end{Bmatrix} - \varepsilon^2 \int_\Omega \boldsymbol{N}^T \boldsymbol{N} \, d\Omega \, \boldsymbol{\gamma} = 0 \tag{4.41b}$$

where $\boldsymbol{B}_s$ is the discretised shear matrix of size $2 \times 2N$:

$$\boldsymbol{B}_s = \begin{bmatrix} -\boldsymbol{\varphi} & 0 \\ 0 & \boldsymbol{\varphi}' \end{bmatrix} \tag{4.42}$$

The above equations is a linear system in the following block form:

$$\left[\begin{array}{c|c} \begin{array}{c|c} \boldsymbol{K}_b & \boldsymbol{0} \\ \hline \boldsymbol{0} & \boldsymbol{0} \end{array} & \boldsymbol{C} \\ \hline \boldsymbol{C}^T & \boldsymbol{V} \end{array}\right] \left\{\begin{array}{c} \boldsymbol{\theta} \\ \hline \boldsymbol{z}_3 \\ \hline \boldsymbol{\gamma} \end{array}\right\} = \left\{\begin{array}{c} \boldsymbol{0} \\ \hline \boldsymbol{f} \\ \hline \boldsymbol{0} \end{array}\right\} \tag{4.43a}$$

where the block entries are defined as follows from section 4.2.4:

$$\boldsymbol{K}_b = L^2 \int_\Omega \boldsymbol{\varphi}'^T \boldsymbol{\varphi}' \, d\Omega \tag{4.43b}$$

$$\boldsymbol{C} = \int_\Omega \boldsymbol{B}_s^T \boldsymbol{N} \, d\Omega \tag{4.43c}$$

$$\boldsymbol{V} = -\varepsilon^2 \int_\Omega \boldsymbol{N}^T \boldsymbol{N} \, d\Omega \tag{4.43d}$$

where the matrices $\boldsymbol{K}_b \in \mathbb{R}^{N\times N}$, $\boldsymbol{C} \in \mathbb{R}^{2N\times M}$ and $\boldsymbol{V} \in \mathbb{R}^{M\times M}$ and the vector $\boldsymbol{f} \in \mathbb{R}^{N\times 1}$. The linear system for the entire problem has $2N + M$ unknowns, or M more than a standard displacement discretisation. Designs D1, D2 and D3 are implemented into the pymfl framework.

Basic testing of schemes D1, D2 and D3

Before continuing to in-depth testing we examine the basic performance of the proposed discretisation schemes D1, D2 and D3.

We begin with D2, that is the discretisation with the additional degrees of freedom, and solve the cantilever beam problem with point load described previously in chapter 3. D2 has more displacement degrees of freedom than D1, or a relatively `richer' space $\mathcal{V}_h^T$ than D1 (which is stable in the local limit) and therefore we might expect that D2 will fail to meet the kernel coercivity condition. This indeed appears to be the case. In fig. 4.3 we show the transverse displacements z_{3h} plotted along with the analytical solution. The solution is highly oscillatory and this oscillation is the result of a spurious or zero-energy mode. This spurious oscillation occurs regardless of the value of the small parameter ε (results not shown). We note that this spurious oscillation in the transverse displacement z_{3h} does not propagate to the rotation θ_h, as shown in fig. 4.4. Despite this, scheme D2 is essentially useless due to its highly unstable nature.
We already know that when using MaxEnt meshless shape functions the scheme D1 converges to the stable $[CG_1(\Omega; \mathcal{T}_h)]^2 \times DG_0(\Omega; \mathcal{T}_h)$ FE scheme. In fig. 4.5 we show the cantilever beam problem with point load solved using the D1 scheme in the local limit, resulting in the stable

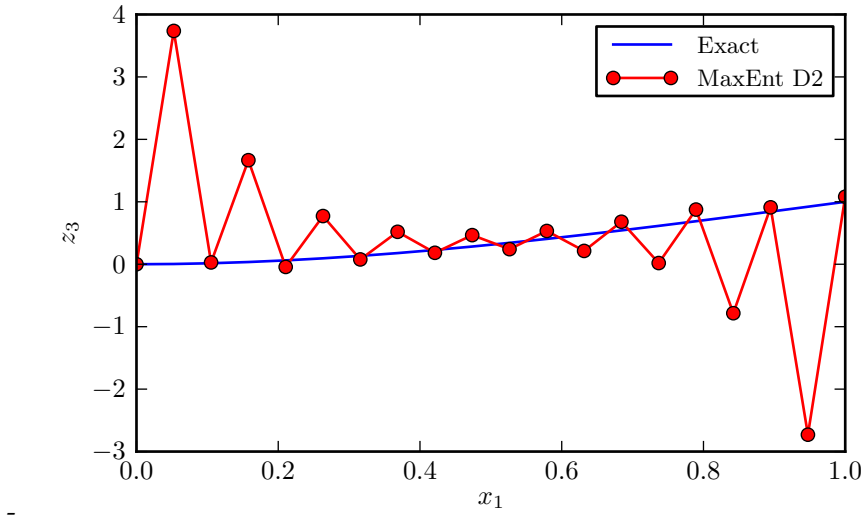

Figure 4.3: Transverse displacement for the cantilever beam problem solved using scheme D2, resulting in $\dim(\mathcal{V}_h^T) = 42$ and $\dim(S_h) = 10$. Spurious or zero-energy modes occur, this scheme is unstable as it fails the kernel coercivity condition. Numerical results are plotted at 20 uniformly distributed points in $[0, 1]$.

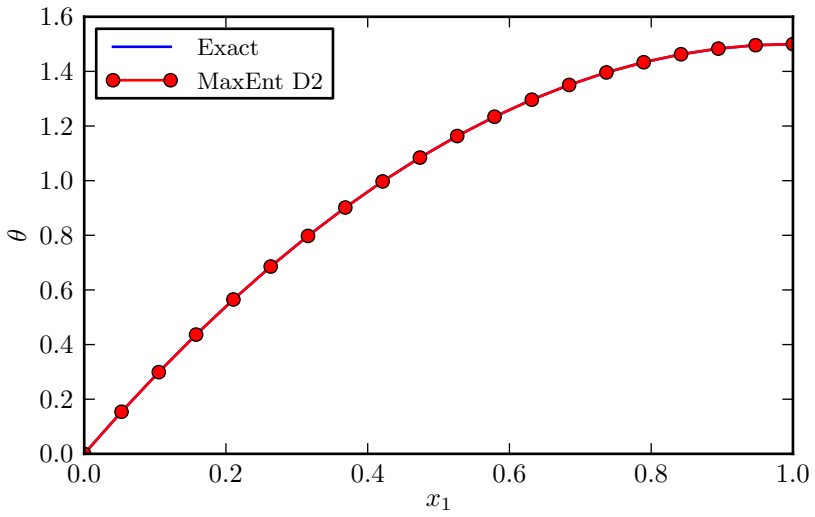

Figure 4.4: Rotation for the cantilever beam problem solved using scheme D2, resulting in $\dim(\mathcal{V}_h^T) = 42$ and $\dim(S_h) = 10$. Even though the transverse displacements have spurious or zero-energy modes, the rotations are unaffected. Numerical results are plotted at 20 uniformly distributed points in $[0, 1]$.

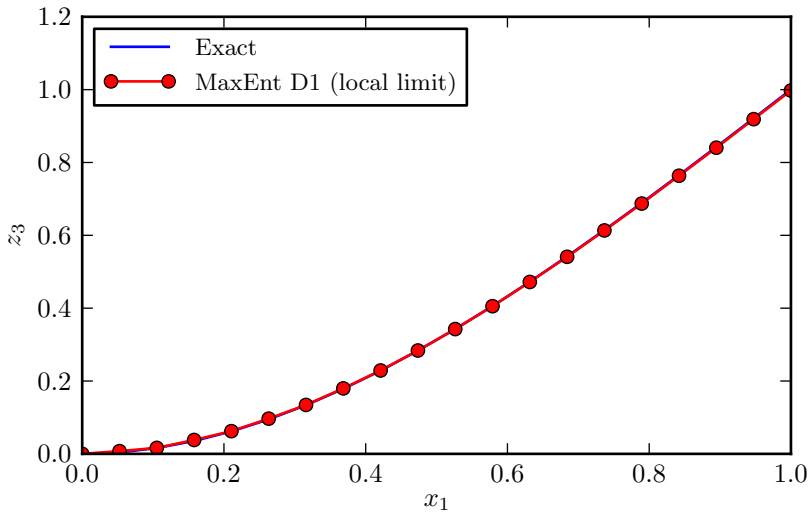

Figure 4.5: Transverse displacements for the cantilever beam problem solved using scheme D1 in the local limit, resulting in $\dim(\mathcal{V}_h^T) = 22$ and $\dim(S_h) = 10$. Numerical results are plotted at 20 uniformly distributed points in $[0, 1]$.

FE scheme. Clearly the solution is not affected by the spurious modes which made the D2 scheme useless, which is the result we expect given the analytical proof available. Increasing the support size ($\beta = 2, 3, 4$) makes no difference to the stability of this scheme and no spurious modes develop. The transverse displacement for $\beta = 3$ is shown in fig. 4.6.

Finally we examine scheme D3, which is the same as D1 except that the shear space is selected to be $CG_1(\Omega; \mathcal{T}_h)$ instead of $DG_0(\Omega; \mathcal{T}_h)$. In terms of constraint ratio $\dim(\mathcal{V}_h^T)/\dim(S_h)$ this results in a constraint ratio of 2 (the same as D1) as the discretisation becomes infinitely refined. Because of this we might expect D3 to be a successful design and this turns out to be the case (results not shown).

In fig. 4.7 we compare the convergence of schemes D1 and D3 in the H^1 norm. The convergence rate ρ is the slope of the line created by plotting the error $e(u)_V$ of the problem variable u in the norm $\mathcal{V}$ against the number of degrees of freedom $\dim(\mathcal{U}_h)$ on a log-log plot. The convergence performance in the transverse displacement variable z_3 of schemes D1 and D3 is almost identical. In the rotation variable θ the performance of scheme D1 is slightly better with a convergence rate ρ of -1.51 against -1.24 for scheme D3. On these results alone there is not much to separate schemes D1 and D3. However, as we will see in chapter 6 because of the L^2 continuity of the shear stress variable in scheme D1 it is easier to eliminate the shear stress a priori to the solution of the linear system of equations in terms of the displacement unknowns

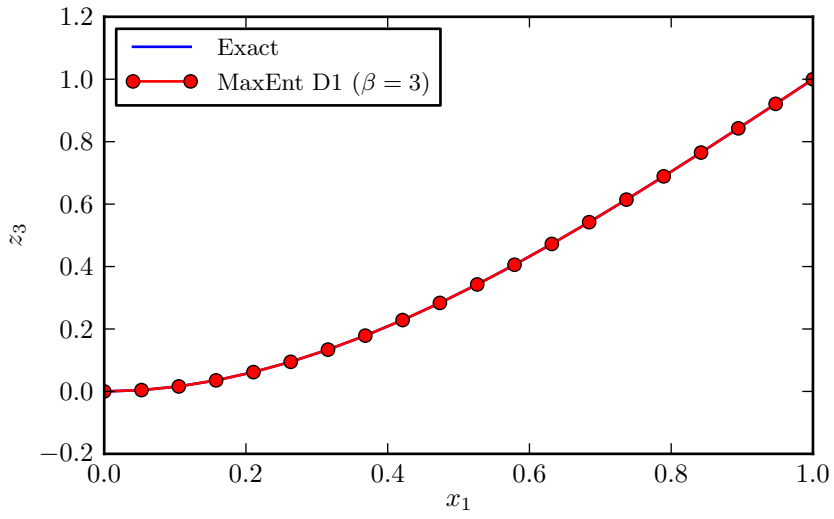

Figure 4.6: Transverse displacements for the cantilever beam problem solved using scheme D1 with $\beta = 3$, resulting in $\dim(\mathcal{V}_h^T) = 22$ and $\dim(S_h) = 10$. Numerical results are plotted at 20 uniformly distributed points in $[0, 1]$.

only. For this reason all further results in this chapter are computed with scheme D1.

4.3 Results

In this section we examine three simple test cases and show that scheme D1 is free from the effects of shear-locking. All of the results in this section are performed with scheme D1 and $\beta = 2$. Additionally, we implement scheme D1 with MaxEnt, MLS and RPIM first-order and second-order basis functions to examine the generality of the approach.

4.3.1 Cantilever beam subject to point load

We consider a cantilever beam of length $L = 1$ and varying thickness parameter ε subject to a point load $\tilde{p} = 3$ at the tip as shown in fig. 4.8. This problem is the same as that used to demonstrate numerical locking in chapter 3. Using the same normalisation procedure as before

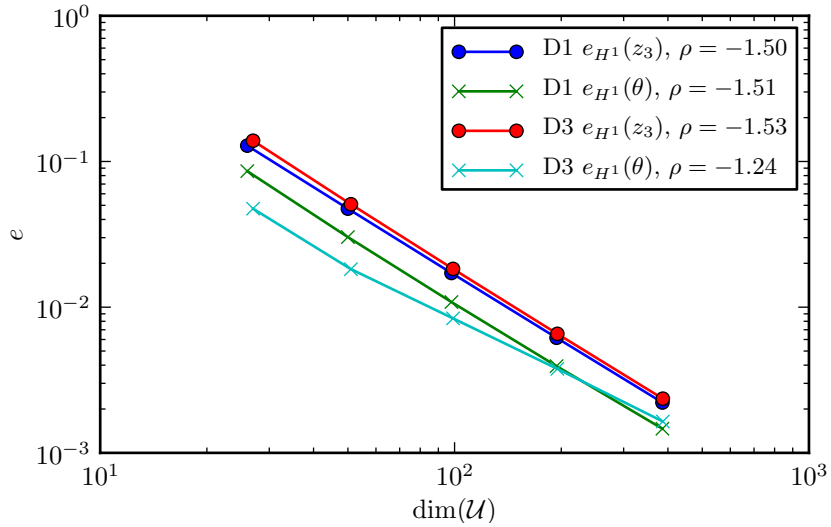

Figure 4.7: Comparison of convergence in H^1 norm between schemes D1 and D3.

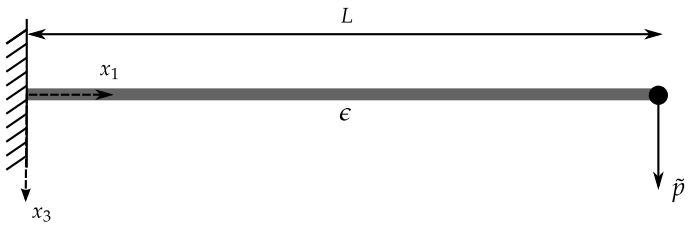

Figure 4.8: Scaled cantilever beam loaded with transverse point load at tip.

the Timoshenko theory solution to this problem is:

$$z_3(x_1) = \frac{\tilde{p}L}{6}\left(2 - \frac{3(L-x_1)}{L} + \frac{(L-x_1)^3}{L^3} + 6\varepsilon^2\left[1 - \frac{(L-x_1)}{L}\right]\right) \tag{4.44}$$

$$\theta(x_1) = \frac{\tilde{p}}{2}\left(1 - \frac{(L-x_1)^2}{L^2}\right) \tag{4.45}$$

In fig. 4.9 we show the computed tip deflection for both the MaxEnt displacement and the proposed MaxEnt mixed method alongside the analytical tip deflections predicted by Kirchhoff and Timoshenko theory for a wide range of ε. As before, the MaxEnt displacement method locks at around $\varepsilon < 10^{-2}$ whilst the proposed MaxEnt mixed method matches the Timoshenko solution for a full range of ε. We can see that moving to a mixed formulation has alleviated

the numerical shear locking problem. Results for MLS and RPIM basis functions (not shown) demonstrate that the proposed mixed method eliminates shear-locking in a generic way for a variety of meshless basis constructions.

We now examine the convergence behaviour of the mixed method using MaxEnt, first-order MLS, first-order RPIM and second-order RPIM basis functions for both thick $\varepsilon = 1.0$ (figs. 4.10, 4.14 and 4.16 and section 4.3.1) and thin $\varepsilon = 0.001$ (figs. 4.11, 4.13, 4.15 and 4.17) beams. The algebraic convergence rates ρ for each method are summarised in tables 4.1 and 4.2. We remark that the expected algebraic convergence rates ρ for first-order shape functions (MaxEnt, MLS, RPIM first-order) are 2 in the L^2 norm and 1 in the H^1 norm for both problem variables z_3 and θ. MaxEnt achieves an additional -0.5 increase in the rate of convergence over MLS and first-order RPIM, both of which achieve the expected values. Second-order RPIM gains an additional -1.0 increase in the rate of convergence over first-order RPIM which is the expected behaviour when moving from a first to second order approximation scheme. Because of the quadratic polynomial nature of the Timoshenko analytical solution for the rotation variable the second-order RPIM scheme which is capable of reproducing second-order polynomials exactly provides rapid convergence to machine precision for the rotation variable in both the L^2 and H^1 norms. This behaviour should not be expected for more complicated problems.

Table 4.1: Algebraic convergence rate ρ for mixed methods using different meshless basis functions for the thick $\varepsilon = 1.0$ cantilever beam problem subject to a point load.

e	MaxEnt	MLS	RPIM first-order	RPIM second-order
$e_{L^2}(z_3)$	-2.55	-2.16	-2.25	-3.34
$e_{H^1}(z_3)$	-1.53	-1.08	-1.03	-2.15
$e_{L^2}(\theta)$	-2.56	-2.03	-2.09	-3.30
$e_{H^1}(\theta)$	-1.54	-0.97	-1.01	-3.39

In figs. 4.18 and 4.19 we show the convergence of z_{3h} and θ_h in the H^1 norm for the MaxEnt mixed method for three values of ε. In fig. 4.18 we can see that there is a slight deterioration of approximately one half an order of magnitude in absolute convergence of z_{3h} in the H^1 norm when moving from a thick through to a thin beam, however the rate of convergence stays the same. In fig. 4.19 we can see that the absolute convergence of θ_h is entirely insensitive to the thickness parameter ε. Results for MLS and RPIM basis functions (not shown) demonstrate similar trends. In summary for this problem the proposed methods are free of shear-locking in the limit as $\varepsilon \to 0$.

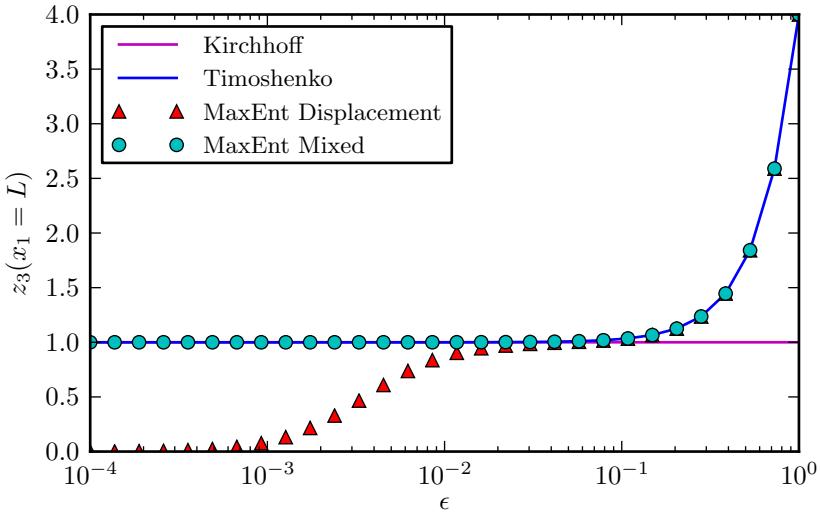

Figure 4.9: Graph showing the tip deflection for the cantilever beam problem with point load computed for MaxEnt displacement method and MaxEnt mixed method with $N = 10$ for varying values of ε. The analytical Timoshenko solution coincides exactly with the analytical Kirchhoff solution in the thin plate limit. The MaxEnt displacement method locks at around $\varepsilon < 10^{-2}$ whilst the proposed MaxEnt mixed method is free from the effects of shear locking and matches the Timoshenko solution for all ε.

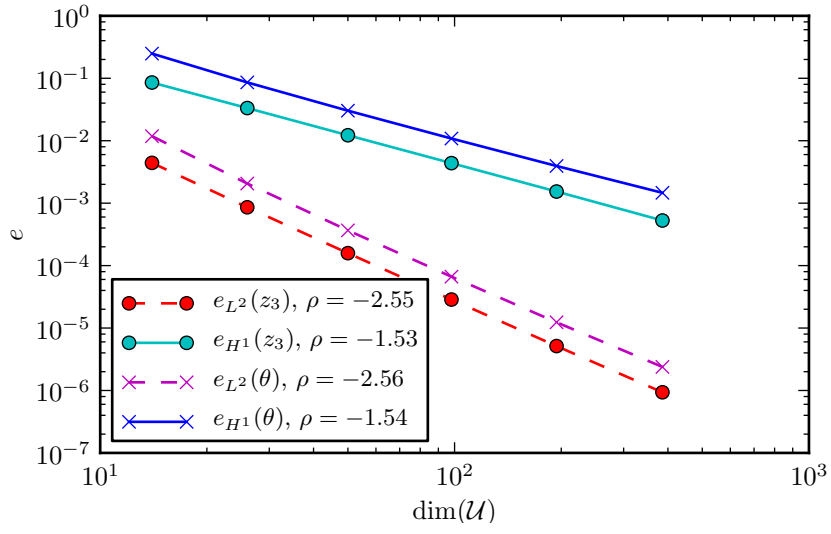

Figure 4.10: Convergence of MaxEnt mixed method for a thick cantilever beam problem $\varepsilon = 1.0$.

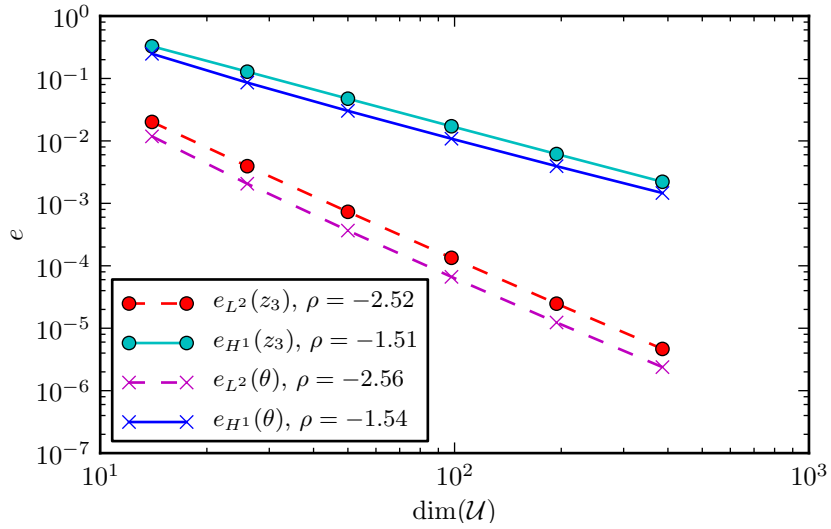

Figure 4.11: Convergence of MaxEnt mixed method for the thin cantilever beam problem $\varepsilon = 0.001$.

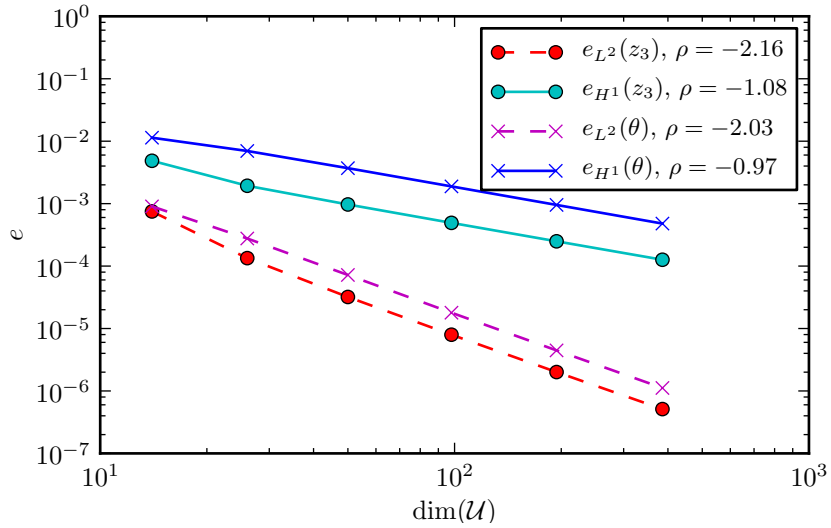

Figure 4.12: Convergence of MLS (first-order) mixed method for the thick cantilever beam problem $\varepsilon = 1.0$.

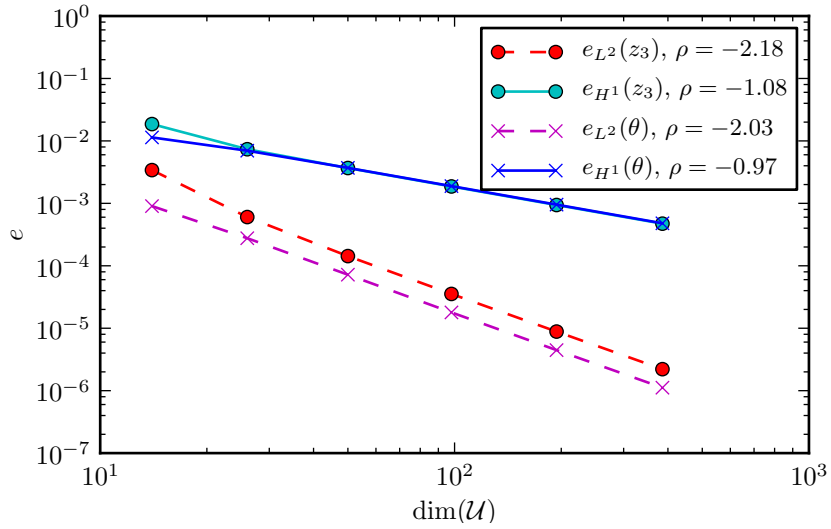

Figure 4.13: Convergence of MLS (first-order) mixed method for the thin cantilever beam problem $\varepsilon = 0.001$.

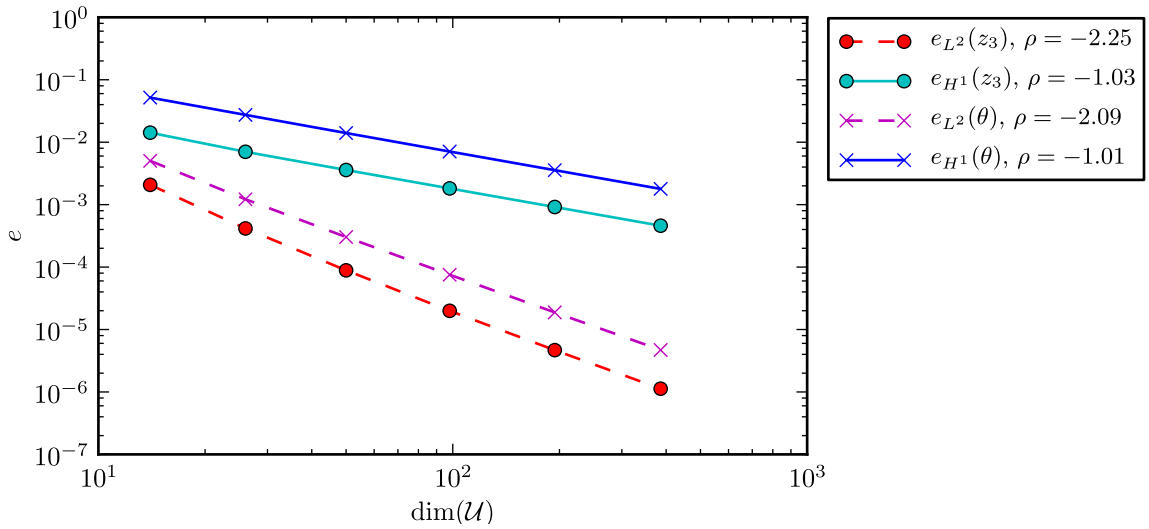

Figure 4.14: Convergence of RPIM (first-order) mixed method for the thick cantilever beam problem $\varepsilon = 1.0$.

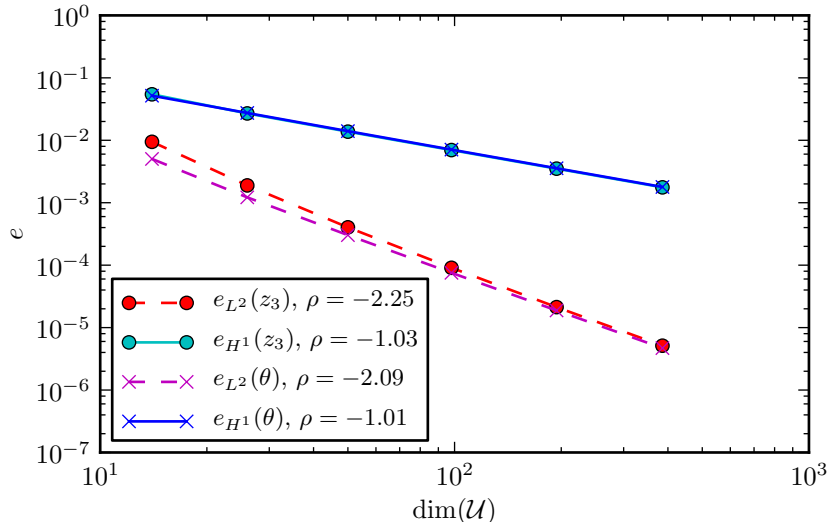

Figure 4.15: Convergence of RPIM (first-order) mixed method for the thin cantilever beam problem $\varepsilon = 0.001$.

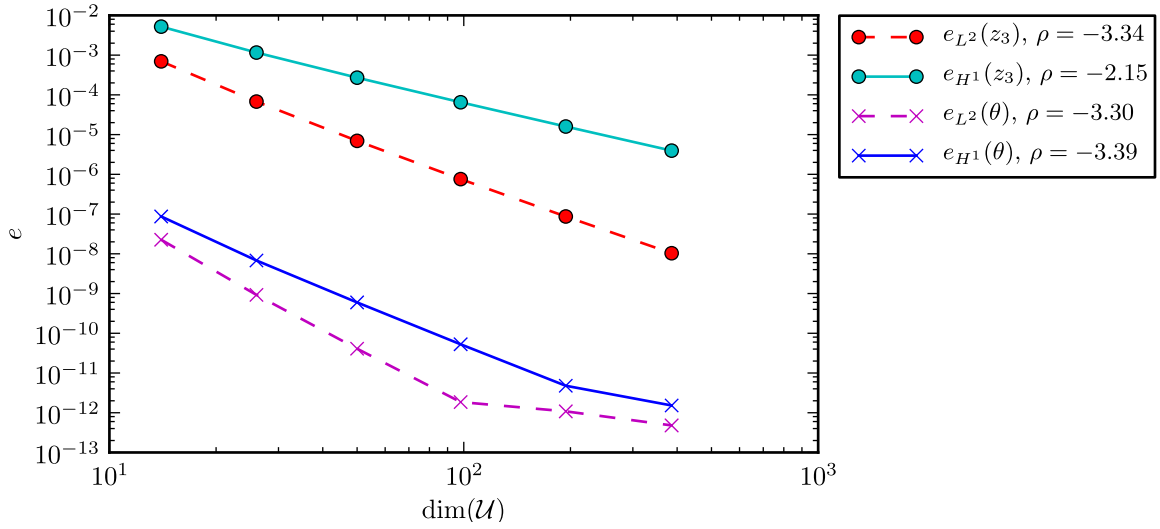

Figure 4.16: Convergence of RPIM (second-order) mixed method for the thick cantilever beam problem $\varepsilon = 1.0$. Note: Flattening of results at around $e = 10^{-12}$ due to reaching limits of arithmetic precision (Intel Core i7 using double-precision arithmetic).

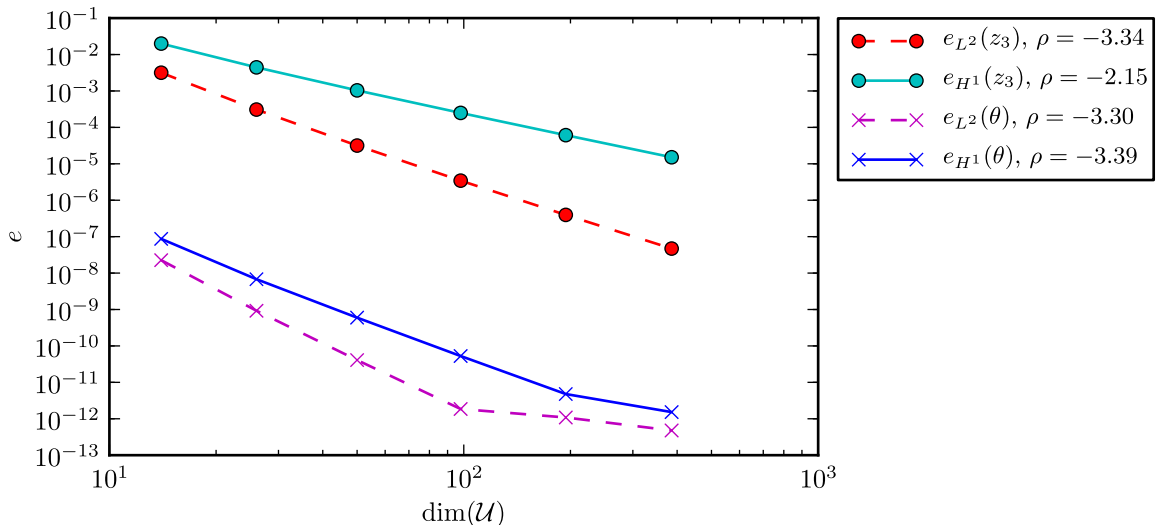

Figure 4.17: Convergence of RPIM (second order) mixed method for the thin cantilever beam problem $\varepsilon = 0.001$. Note: Flattening of results at around $e = 10^{-12}$ due to reaching limits of arithmetic precision (Intel Core i7 using double-precision arithmetic).

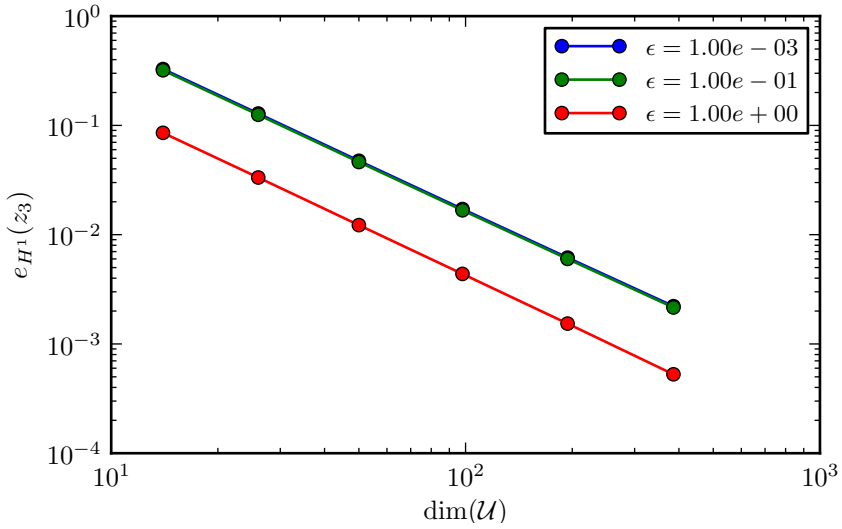

Figure 4.18: Graph showing convergence of z_3 in the H^1 norm of the MaxEnt mixed method for the cantilever beam problem for varying values of ε. Absolute convergence deteriorates marginally for thinner beams. Rate of convergence stays fixed. Note: Convergence lines for $\varepsilon = 10^{-3}$ and $\varepsilon = 10^{-1}$ coincide.

Table 4.2: Algebraic convergence rate ρ for mixed methods using different meshless basis functions for the thin $\varepsilon = 0.001$ cantilever beam problem subject to a point load.

e	MaxEnt	MLS	RPIM first-order	RPIM second-order
$e_{L^2}(z_3)$	-2.52	-2.18	-2.25	-3.34
$e_{H^1}(z_3)$	-1.51	-1.08	-1.03	-2.15
$e_{L^2}(\theta)$	-2.56	-2.03	-2.09	-3.30
$e_{H^1}(\theta)$	-1.54	-0.97	-1.01	-3.39

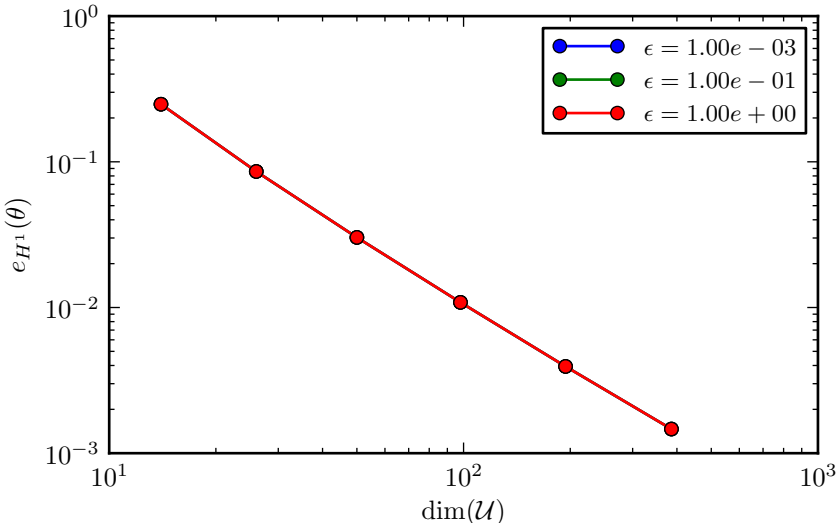

Figure 4.19: Graph showing convergence of θ in the H^1 norm of the MaxEnt mixed method for the cantilever beam problem for varying values of ε. Convergence is insensitive to varying ε. Note: All convergence lines coincide.

4.3.2 Cantilever beam in pure bending

A beam is in a state of pure bending when the shear term bilinear form a_s is inactive. This set of solutions was defined as $\mathcal{V}_0^T$ previously, and as a reminder it is defined by:

$$\mathcal{V}_0^T = \left\{ (v_3, \eta) \in \mathcal{V}^T \mid v_3' - \eta = 0 \right\} \tag{4.46}$$

Then, for our numerical solution of the Timoshenko problem $(z_{3h}, \theta_h) \in \mathcal{V}_h^T$ to be free of shear-locking, the space of discrete pure bending displacements $\mathcal{V}_{0h} = \mathcal{V}_h^T \cup \mathcal{V}_0^T$ must be sufficiently `rich' to ensure convergence:

$$\mathcal{V}_{0h} = \mathcal{V}_h^T \cap \mathcal{V}_0^T \tag{4.47}$$

This idea expressed in function space theory by Chapelle and Bathe [40] is very similar to the concept introduced by Wang and Chen [68] called the Kirchhoff mode reproducing conditions (KMRC). They identified the cause of the shear-locking problem in both the Reissner-Mindlin plate problem and the Timoshenko beam problem to be related to two main issues [68]; the first is the inability of the approximation functions to reproduce the Kirchhoff mode, and the second is the inability of the numerical method to achieve pure bending exactness in the Galerkin approximation. They conclude that to meet KMRC the numerical method must meet two criteria; the basis employed to approximate the transverse displacement and rotation variables must be able to reproduce quadratic functions, and the integration must be accurate so that bending exactness is achieved. This integration criteria is not typically considered in the FE literature as integration rules can be designed to integrate the discretised variational form exactly, but in meshless methods it becomes an additional concern.

However, we have just demonstrated in the previous section that it is indeed possible to construct a method using three different types of first-order meshless basis and still achieve convergence in all of the relevant norms for all values of ε (ie. in a bending dominated situation). Furthermore the classic $CG_1 - DG_0$ Timoshenko beam element also only employs a basis capable of reproducing linear functions only and is used widely in its reduced integration form. So a natural question to ask is why is this possible and does it invalidate the KMRC hypothesis proposed in the paper by Wang and Chen [68]?

To examine this potential contradiction we use the same problem proposed by Wang and Chen in [68] to demonstrate the KMRC. We consider a cantilever beam of length L with thickness parameter ε loaded with a scaled moment $\tilde{m}$ at the tip as shown in fig. 4.20:

$$\tilde{m} = \frac{L}{EI} \tag{4.48}$$

The analytical solution for this problem given by both the Bernoulli and Timoshenko theory is:

$$z_3(x_1) = \frac{\tilde{m}x^2}{2L} \tag{4.49}$$

$$\theta(x_1) = \frac{\tilde{m}x}{L} \tag{4.50}$$

The reasoning behind the stipulation of a basis capable of reproducing a second-order polynomial should be clear upon examining the analytical solution for this problem. If the basis is capable of reproducing a second-order polynomial then the displacement solution will be reproduced exactly (to within machine precision) as long as the numerical integration of the weak

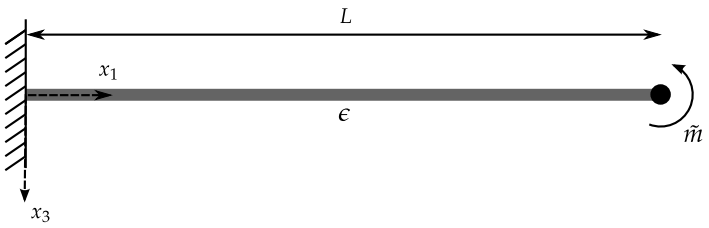

Figure 4.20: Scaled cantilever beam loaded with moment at tip.

form is sufficiently accurate (bending exactness). If the basis is only capable of reproducing a first-order polynomial, as is the case with MaxEnt and first-order MLS basis functions, then the function will not be reproduced exactly. However, not being able to reproduce a function exactly is not necessarily a barrier to achieving a method which converges.

We will now demonstrate that the proposed method is capable of achieving bending exactness when used with a second-order RPIM basis, but that convergence can still be achieved using first-order RPIM basis functions and a reduced rate of convergence can still be achieved when using MaxEnt and first-order MLS basis functions. In fig. 4.21 we show the convergence of the proposed method using second-order RPIM basis functions. The proposed method clearly achieves bending exactness as the errors are on the order of machine-precision for all the discretisations considered. In figs. 4.22 and 4.23 it is clear that the method does not achieve bending exactness using first-order MaxEnt and MLS basis functions, but convergence is still achieved in all norms, albeit at a reduced rate for the rotation variable θ_h. Interestingly, for the first-order RPIM method we do not achieve bending exactness, but the convergence rates for the rotation variable θ_h is above the optimal rates and higher than that achieved by the first-order RPIM for other problems. The reason for this result is currently unclear and is under further investigation.

Table 4.3: Algebraic convergence rate ρ for mixed methods using different meshless basis functions for the cantilever beam in pure bending.

e	MaxEnt	MLS	RPIM first-order	RPIM second-order
$e_{L^2}(z_3)$	-2.46	-2.05	-2.14	exact
$e_{H^1}(z_3)$	-1.52	-1.00	-1.01	exact
$e_{L^2}(\theta)$	-1.52	-1.51	-2.67	exact
$e_{H^1}(\theta)$	-0.46	-0.46	-2.56	exact

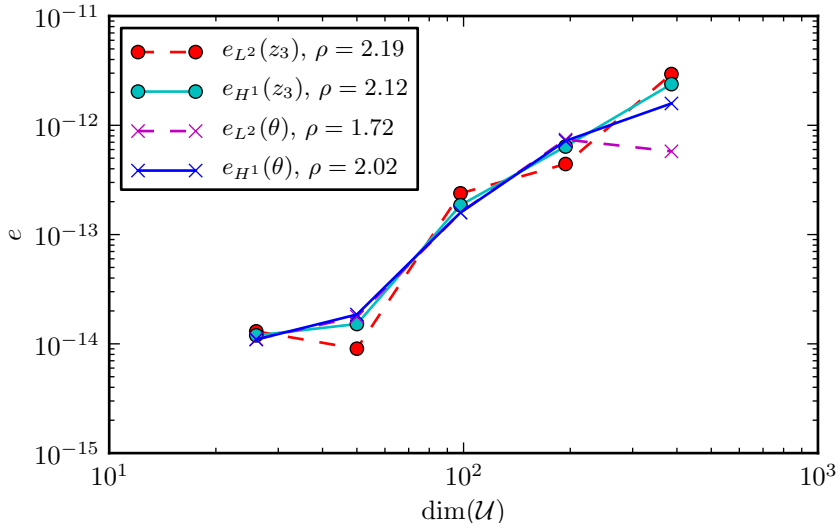

Figure 4.21: Convergence of RPIM (second-order) mixed method for a cantilever beam in pure bending. Note: RPIM achieves machine-precision for this problem for all discretisations.

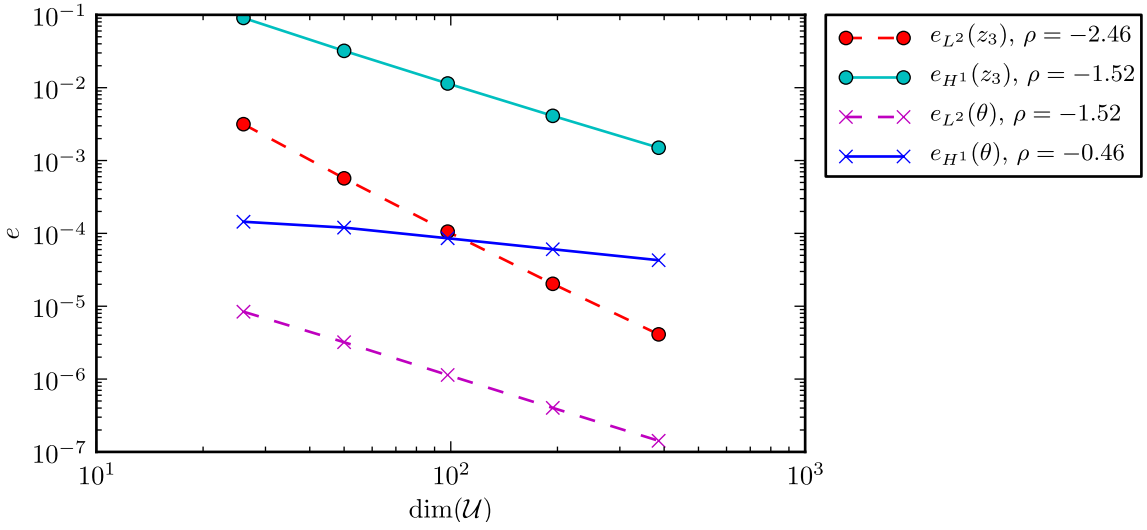

Figure 4.22: Convergence of MaxEnt mixed method for a cantilever beam in pure bending.

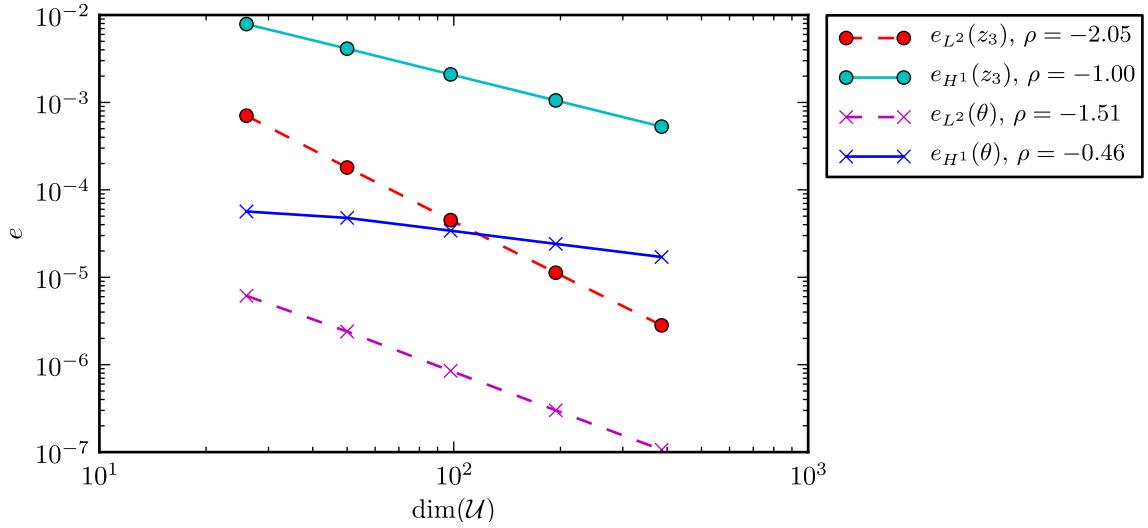

Figure 4.23: Convergence of MLS (first-order) mixed method for a cantilever beam in pure bending.

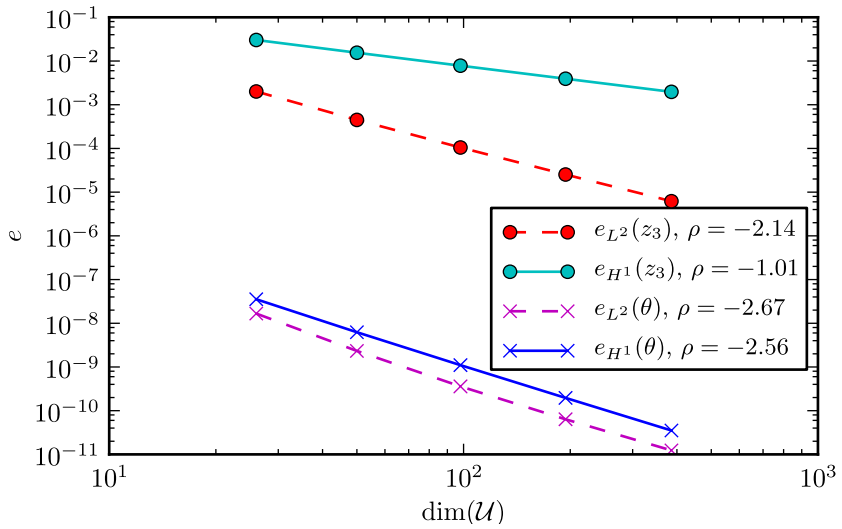

Figure 4.24: Convergence of RPIM (first-order) mixed method for a cantilever beam in pure bending.

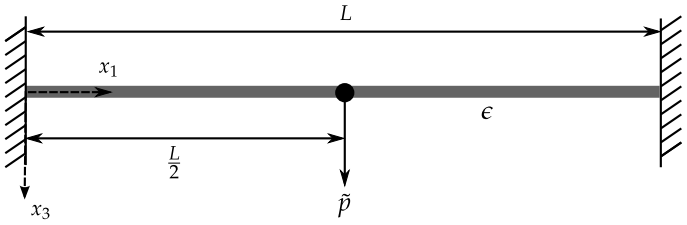

Figure 4.25: Scaled clamped-clamped beam loaded with point load at centre. Full beam is shown, only half beam is modelled in numerical simulations.

In summary, we have demonstrated that to meet bending exactness a basis capable of reproducing a second-order polynomial is required, along with accurate integration of the weak form of the problem. This finding confirms the KMRC hypothesis of Wang and Chen [68]. However, in practice we have not found it necessary to meet KMRC to ensure the convergence of a numerical method in bending dominated situations. Our findings are supported by the many shell and plate finite elements available in the literature and used in practice which use first-order polynomial basis functions.

4.3.3 Clamped-clamped beam subject to point load

We consider a clamped-clamped beam of length $L = 2$ and thickness parameter $\varepsilon = 10^{-4}$ with a point load $\tilde{p} = 3$ at the centre as shown in fig. 4.25. Due to the inherent symmetry only half of the beam is modelled. This problem is the same as the one used by Wang and Chen in [68] to demonstrate the performance of their SCNI method. Using the same normalisation of the loading as before the Kirchhoff theory solution to this problem is [68]:

$$z_3(x_1) = \tilde{p}L^2\left[\frac{x_1^2}{16L^2} - \frac{x_1^3}{12L^3}\right] \tag{4.51}$$

$$\theta(x_1) = \tilde{p}L\left[\frac{x_1}{8L} - \frac{x_1^2}{4L^2}\right] \tag{4.52}$$

In this example we compare the convergence of the Timoshenko problem with a very low thickness parameter ($\varepsilon = 0.0001$) to the Kirchhoff solution. The convergence for MaxEnt, MLS, first-order RPIM and second-order RPIM are shown in figs. 4.26 to 4.29 and the convergence rates for each method is summarised in table 4.4. MaxEnt again achieves an additional -0.5 increase in the rate of convergence over the expected values for a first-order shape function. MLS

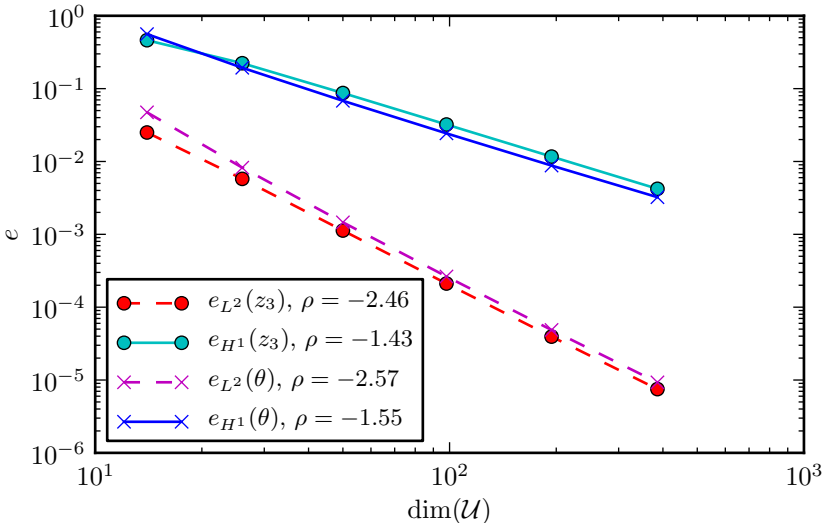

Figure 4.26: Convergence of MaxEnt mixed method for a clamped-clamped beam with centre loading with $\varepsilon = 0.0001$.

has sub-optimal convergence in both the transverse displacement and rotation variables. First-order RPIM either matches or achieves an additional rate of convergence over the expected values. RPIM second-order matches the expected rate of convergence for a second-order shape function in the transverse displacement variable, and rapidly achieves machine precision for the rotation variable due to the second-order polynomial nature of the analytical solution.

Table 4.4: Algebraic convergence rate ρ for mixed methods using different meshless basis functions for the clamped-clamped beam.

e	MaxEnt	MLS	RPIM first-order	RPIM second-order
$e_{L^2}(z_3)$	-2.46	-1.47	-2.40	-3.34
$e_{H^1}(z_3)$	-1.43	-1.28	-1.05	-2.15
$e_{L^2}(\theta)$	-2.57	-1.57	-2.09	-3.72
$e_{H^1}(\theta)$	-1.55	-0.58	-1.01	-3.47

4.4 Conclusions

In this chapter we have demonstrated that using the mixed weak form of the Timoshenko beam problem is an effective and robust method of designing meshless methods that are convergent

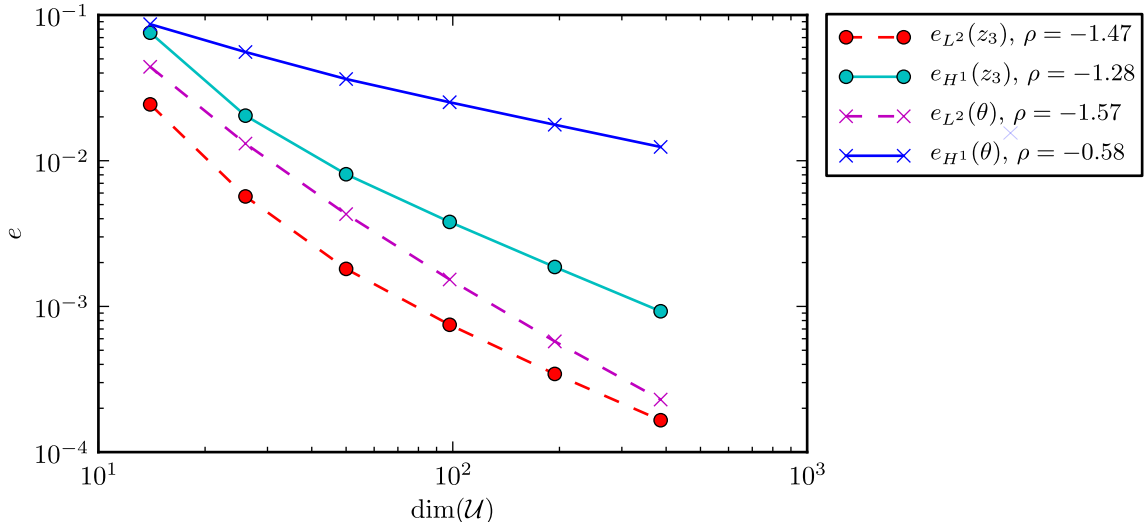

Figure 4.27: Convergence of first-order MLS mixed method for a clamped-clamped beam with centre loading with $\varepsilon = 0.0001$.

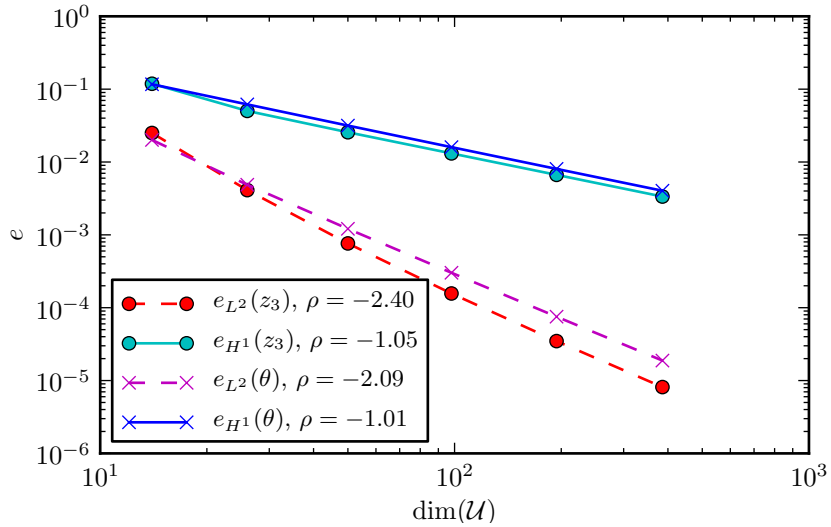

Figure 4.28: Convergence of first-order RPIM mixed method for a clamped-clamped beam with centre loading with $\varepsilon = 0.0001$.

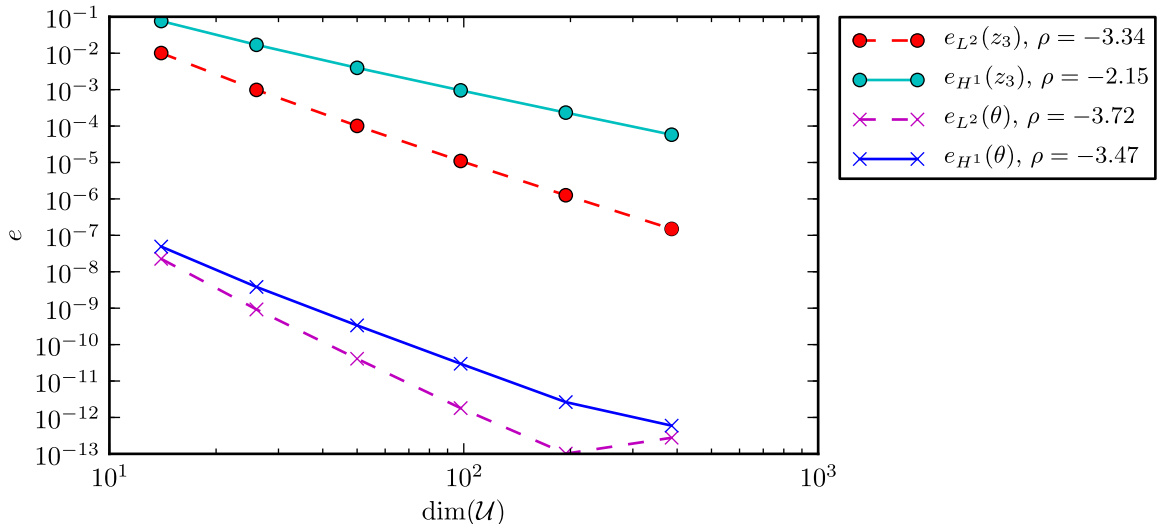

Figure 4.29: Convergence of second-order RPIM mixed method for a clamped-clamped beam with centre loading with $\varepsilon = 0.0001$.

and free from the negative effects of shear-locking.

The proposed design, scheme D1, is a hybrid meshless-finite element formulation where meshless basis functions are used to discretise the displacement variables, and discontinuous Lagrangian finite elements are used to discretise the shear stresses. We have also demonstrated that it is important to consider both the kernel coercivity condition and inf-sup condition when designing such a method. One of the proposed designs, scheme D2, which added additional displacement degrees of freedom, fails the kernel coercivity condition, resulting in spurious or zero-energy modes which lead to a highly oscillatory and unstable solution for the transverse displacements.

We have shown that the Kirchhoff mode reproducing conditions (KMRC) [68] of Wang and Chen are necessary if the transverse displacement is a second-order polynomial and must be reproduced exactly to within machine precision. If the basis functions are only first-order as is the case with MaxEnt and first-order MLS basis functions, then the function will not be reproduced exactly. However, we have clearly demonstrated that this lack of exactness is not necessarily a barrier to achieving a method which converges.

In summary we have shown that employing a mixed weak form is a viable way of eliminating shear-locking in meshless methods, just like in the finite element method. Therefore it seems that this methodology can equally be applied to solving the shear-locking problem in the related Reissner-Mindlin plate problem. We will explore this possibility in the following two chapters.

5 Meshless methods for the shear-deformable plate problem based on a mixed weak form

In this chapter we examine the ability of a mixed weak form to produce a numerical method for the Reissner-Mindlin problem which is free of shear-locking. Similarly to the previous chapter, we begin by moving from the primal or displacement form of the Reissner-Mindlin problem to a mixed problem where the shear stresses are treated as an independent variational quantity in the weak form.

Using standard arguments we identify the correct function space setting for the shear stresses as the Sobolev space of functions with square integrable rotation. To construct a conforming subspace of the shear stresses we use the lowest-order rotated Raviart–Thomas-Nédélec elements. This has parallels with the classic mixed interpolation of tensorial components (MITC) family of plate finite elements which are considered some of the most robust designs available. Meshless maximum-entropy basis functions are used to discretise the displacements. Because of the inherent properties of the maximum-entropy basis functions our method allows for the direct imposition of Dirichlet (essential) boundary conditions, in contrast to methods based on moving least squares (MLS) basis functions.

We present standard benchmark problems that demonstrate the accurate and shear-locking free nature of the proposed method.

Note: This chapter contains material from and is closely based upon the following international journal paper: Hale, J. & Baiz, P. A locking-free meshfree method for the simulation of shear-deformable plates based on a mixed variational formulation. *Computer Methods in Applied Mechanics and Engineering* **241–244,** 311–322 (2012)

5.1 Introduction

In this chapter an approach based on the mixed weak form of the Reissner-Mindlin plate problem is used within the context of a meshless method to solve the problem of shear-locking. To our knowledge this is the first time this approach has been used in the context of a meshless

method. We use first order consistent maximum-entropy basis functions [21, 99] combined with lowest-order rotated Raviart-Thomas-Nédélec [136, 137] finite elements to construct a hybrid meshless/finite element method that is free of shear-locking. Due to the inherent properties of the maximum-entropy basis functions our method possesses a so-called `weak' Kronecker delta property and positive mass matrix amongst other advantages. We show that the approach alleviates shear-locking for a variety of test problems.

5.2 Formulation

5.2.1 Derivation of mixed weak form

In this section we derive the mixed weak form of the Reissner-Mindlin plate problem. The steps required for this are broadly the same as for the derivation of the scaled mixed Timoshenko problem in chapter 4, however the shear stress and rotation fields are now vectorial quantities. As a consequence, the identification of the correct Sobolev space for the shear stresses is a more delicate issue.

We begin with a reminder of the displacement or primal weak form of the Reissner-Mindlin problem:

Problem 13 (Displacement weak form of the Reissner-Mindlin plate problem)**.** *Find the transverse deflection and rotations* $(z_3, \boldsymbol{\theta}) \in \mathcal{V}_3 \times \mathcal{R}$ *such that:*

$$\bar{t}^3 \int_{\Omega_0} \boldsymbol{L}[\boldsymbol{\varepsilon}(\boldsymbol{\theta})] : \boldsymbol{\varepsilon}(\boldsymbol{\eta})\, d\Omega + \lambda \bar{t} \int_{\Omega_0} (\nabla z_3 - \boldsymbol{\theta}) \cdot (\nabla y_3 - \boldsymbol{\eta})\, d\Omega = \int_{\Omega_0} p_3 y_3\, d\Omega \quad \forall (y_3, \boldsymbol{\eta}) \in \mathcal{V}_3 \times \mathcal{R} \tag{5.1a}$$

The operators $\boldsymbol{\varepsilon} : [H^1(\Omega_0)]^2 \to [L^2(\Omega_0)]^{2\times 2}$ *and* $\boldsymbol{L} : [L^2(\Omega_0)]^{2\times 2} \to [L^2(\Omega_0)]^{2\times 2}$ *are defined as:*

$$\boldsymbol{\varepsilon}(\boldsymbol{v}) = \frac{1}{2}\left((\nabla \boldsymbol{v}) + (\nabla \boldsymbol{v})^T\right) \qquad \boldsymbol{L}[\boldsymbol{\varepsilon}] \equiv D\left[(1-\nu)\boldsymbol{\varepsilon} + \nu \mathrm{tr}(\boldsymbol{\varepsilon})\boldsymbol{I}\right] \tag{5.1b}$$

where $\boldsymbol{I}$ *is the usual identity tensor,* $D = E/12(1-\nu^2)$ *is the bending modulus,* $\lambda = E\kappa/(2(1+\nu))$ *is the shear modulus,* $\kappa = 5/6$ *is a shear correction factor,* ν *is Poisson's ratio,* E *is Young's modulus,* $\bar{t} = t/L$ *is the plate thickness scaled with respect to the characteristic in-plane dimension* L *and* p_3 *is the transverse loading function.*

We can write the above problem in a simplified short-hand form by defining:

$$a_b(\boldsymbol{\theta};\boldsymbol{\eta}) := \int_{\Omega_0} L\varepsilon(\boldsymbol{\theta}) : \varepsilon(\boldsymbol{\eta})\, d\Omega \tag{5.2a}$$

$$a_s(\boldsymbol{\theta}, z_3; \boldsymbol{\eta}, y_3) := \int_{\Omega_0} (\nabla z_3 - \boldsymbol{\theta}) \cdot (\nabla y_3 - \boldsymbol{\eta})\, d\Omega \tag{5.2b}$$

$$g(y_3) := \int_{\Omega_0} p_3 y_3\, d\Omega \tag{5.2c}$$

as the bilinear and linear forms relating to the bending energy, shear energy and loading of the plate, respectively, then we can re-write the Reissner-Mindlin problem in the following equivalent form:

$$\bar{t}^3 a_b(\boldsymbol{\theta};\boldsymbol{\eta}) + \lambda \bar{t} a_s(\boldsymbol{\theta}, z_3; \boldsymbol{\eta}, y_3) = g(y_3) \tag{5.3}$$

In a similar manner to the Timoshenko beam problem we scale the loading to ensure that we have a bounded solution as the scaled plate thickness $\bar{t} = t/L$ approaches zero:

$$p_3 = g\bar{t}^3 \tag{5.4}$$

The scaled weak form of the Reissner-Mindlin plate problem can then be written as:

Problem 14 (Scaled Reissner-Mindlin plate problem)**.** *Find the transverse deflection and rotations* $(z_3, \boldsymbol{\theta}) \in \mathcal{V}_3 \times \mathcal{R}$ *such that :*

$$\int_{\Omega_0} L\varepsilon(\boldsymbol{\theta}) : \varepsilon(\boldsymbol{\eta})\, d\Omega + \lambda\bar{t}^{-2} \int_{\Omega_0} (\nabla z_3 - \boldsymbol{\theta}) \cdot (\nabla y_3 - \boldsymbol{\eta})\, d\Omega = \int_{\Omega_0} g y_3\, d\Omega \quad \forall (y_3, \boldsymbol{\eta}) \in \mathcal{V}_3 \times \mathcal{R} \tag{5.5}$$

Again, in rough terms this scaling ensures a finite solution as the scaled plate thickness $\bar{t}$ approaches zero whilst keeping the other problem variables fixed.

We then define the scaled shear stress trial function $\boldsymbol{\gamma}$ as a new variable, where S is an appropriate function space:

$$\boldsymbol{\gamma} = \lambda\bar{t}^{-2}(\nabla z_3 - \boldsymbol{\theta}) \in S \tag{5.6}$$

Note that the shear stress is now a vectorial quantity, ie.:

$$\boldsymbol{\gamma} = \begin{Bmatrix} \gamma_{13} \\ \gamma_{23} \end{Bmatrix} = \lambda\bar{t}^{-2} \begin{Bmatrix} \frac{\partial z_3}{\partial x_1} - \theta_1 \\ \frac{\partial z_3}{\partial x_2} - \theta_2 \end{Bmatrix} \tag{5.7}$$

which is a natural consequence of the move from the one-dimensional Timoshenko beam problem to the two-dimensional Reissner-Mindlin plate problem. Multiplying eq. (5.6) with test functions $\boldsymbol{\psi} \in S$ and integrating across the domain Ω_0 gives:

$$\int_{\Omega_0} \boldsymbol{\gamma} \cdot \boldsymbol{\psi} \, d\Omega = \lambda \bar{t}^{-2} \int_{\Omega_0} (\nabla z_3 - \boldsymbol{\theta}) \cdot \boldsymbol{\psi} \, d\Omega \tag{5.8}$$

By substituting eq. (5.6) into our original displacement weak form eq. (5.5) and re-arranging we arrive at the following mixed variational formulation [138]:

Problem 15 (Mixed scaled Reissner-Mindlin plate problem)**.** *Find* $(z_3, \boldsymbol{\theta}, \boldsymbol{\gamma}) \in \mathcal{V}_3 \times \mathcal{R} \times S$ *such that:*

$$\int_{\Omega_0} L\varepsilon(\boldsymbol{\theta}) : \varepsilon(\boldsymbol{\eta}) \, d\Omega + \int_{\Omega_0} \boldsymbol{\gamma} \cdot (\nabla y_3 - \boldsymbol{\eta}) \, d\Omega = \int_{\Omega_0} g y_3 \, d\Omega \tag{5.9a}$$

$$\int_{\Omega_0} (\nabla z_3 - \boldsymbol{\theta}) \cdot \boldsymbol{\psi} \, d\Omega - \frac{\bar{t}^2}{\lambda} \int_{\Omega_0} \boldsymbol{\gamma} \cdot \boldsymbol{\psi} \, d\Omega = 0 \quad \forall (y_3, \boldsymbol{\eta}, \boldsymbol{\psi}) \in \mathcal{V}_3 \times \mathcal{R} \times S \tag{5.9b}$$

5.2.2 Function space identification

On first inspection of eq. (5.9) we can see that no derivatives of the shear stress trial $\boldsymbol{\gamma}$ or test functions $\boldsymbol{\psi}$ appear as part of the weak form. This would suggest that a possible identification of the function space S might be:

$$S := [L^2(\Omega_0)]^2 \tag{5.10}$$

However, it is possible to come up with a more specific result. We begin by defining the rot or rotation operator which acts on a two-component vector field $\boldsymbol{q} = \{q_1, q_2\}^T$ as:

$$\operatorname{rot}(\boldsymbol{q}) = \frac{\partial q_2}{\partial x_1} - \frac{\partial q_1}{\partial x_2} \tag{5.11}$$

The rot operator is identical to the curl operator in $\mathbb{R}^2$, the latter notation used more frequently in electromagnetic applications, see eg. [139]. However, the curl operator extends its definition to $\mathbb{R}^3$ so we will use rot here to denote the restriction for our application.

Now, given that our transverse displacements $z_3 \in H_0^1(\Omega_0)$ (ie. a sufficiently smooth scalar field) it must hold that:

$$\operatorname{rot}(\operatorname{grad} z_3) = \operatorname{rot} \begin{Bmatrix} \frac{\partial z_3}{\partial x_1} \\ \frac{\partial z_3}{\partial x_2} \end{Bmatrix} = \frac{\partial^2 z_3}{\partial x_1 \partial x_2} - \frac{\partial^2 z_3}{\partial x_2 \partial x_1} = 0 \in L^2(\Omega_0) \tag{5.12}$$

Futhermore, for $\theta \in [H_0^1(\Omega_0)]^2$ it holds that rot $\boldsymbol{\theta} \in L^2(\Omega_0)$, and we then have:

$$\gamma = \lambda \bar{t}^{-2} \nabla z_3 - \boldsymbol{\theta} \in H(\text{rot}; \Omega_0) \tag{5.13}$$

where the space $H(\text{rot}; \Omega_0)$ is the Sobolev space of square integrable functions with square integrable rotation and is defined as [138]:

$$H(\text{rot}; \Omega_0) := \left\{ \boldsymbol{q} \in [L^2(\Omega_0)]^2 \mid \text{rot}\, \boldsymbol{q} \in L^2(\Omega_0) \right\} \tag{5.14}$$

Thus the shear space S for fixed $\bar{t}$ can be identified with the space $H(\text{rot}; \Omega_0)$:

$$S := H(\text{rot}; \Omega_0) \tag{5.15}$$

By inspection it is possible to see that this space is somewhere `in-between' the spaces $[L^2(\Omega)]^2$ and $[H_0^1(\Omega)]^2$ in terms of smoothness, and the following chain of inclusions holds:

$$[H^1(\Omega_0)]^2 \subset H(\text{rot}; \Omega_0) \subset [L^2(\Omega_0)]^2 \tag{5.16}$$

This result has important ramifications in that we are no longer limited to discretising the shear-stress field with compounded vector discontinuous Lagrangian elements. By compounded vector discontinuous Lagrangian elements, it is meant that each individual component of a vector field $\boldsymbol{q}_h = \{q_{1h}, q_{2h}\}^T$ is discretised by its own individual discontinuous Lagrangian space, that is:

$$q_{1h} \in DG_p(\Omega_0; \mathcal{T}_h) \subset L^2(\Omega), \qquad q_{2h} \in DG_p(\Omega_0; \mathcal{T}_h) \subset L^2(\Omega) \tag{5.17}$$

where $\mathcal{T}_h$ is a triangulation of the plate mid-surface Ω_0 and $p \in \mathbb{N}$ is the polynomial order. The two discretised components are then compounded to discretise the vector field $\boldsymbol{q}_h$ as:

$$\boldsymbol{q}_h \in DG_p(\Omega_0; \mathcal{T}_h) \times DG_p(\Omega_0; \mathcal{T}_h) = [DG_p(\Omega_0; \mathcal{T}_h)]^2 \subset [L^2(\Omega_0)]^2 \tag{5.18}$$

However, because we have the result $\boldsymbol{q} \in H(\text{rot}; \Omega_0)$ we can use the family of rotated Raviart–Thomas-Nédélec elements NED_p to build conforming subspace of $H(\text{rot}; \Omega_0)$. These elements naturally discretise a vector field with the higher level of smoothness without the need to compound two individual spaces, that is we have:

$$\boldsymbol{q}_h \in NED_p(\Omega_0; \mathcal{T}_h) \subset H(\text{rot}; \Omega_0) \tag{5.19}$$

We will cover the construction of the spaces NED_p in section 5.2.5.

5.2.3 Stability

With regards to stability, we can recognise the mixed Reissner-Mindlin problem eq. (5.9) as a penalised saddle point problem in the form of eqs. (4.8) and (4.11), just like the mixed Timoshenko problem, but with the following choices for fixed $\bar{t}$ and for fully clamped boundary conditions [135]:

$$\mathcal{X} := \mathcal{V}_3 \times \mathcal{R} := H_0^1(\Omega_0) \times H_0^1(\Omega_0)^2, \qquad a(z_3, \boldsymbol{\theta}; v_3, \boldsymbol{\eta}) := a_b(\boldsymbol{\theta}; \boldsymbol{\eta}) \tag{5.20a}$$

$$\mathcal{M} := S := H(\mathrm{rot}; \Omega_0), \qquad b(y_3, \boldsymbol{\eta}; \boldsymbol{\psi}) := (\nabla y_3 - \boldsymbol{\eta}; \boldsymbol{\psi})_{L^2(\Omega_0)} \tag{5.20b}$$

$$\mathcal{M}_c := [L^2(\Omega_0)]^2, \qquad c(\boldsymbol{\gamma}, \boldsymbol{\psi}) := (\boldsymbol{\gamma}; \boldsymbol{\psi})_{L^2(\Omega_0)} \tag{5.20c}$$

The saddle point problem is then simply the specific case of the above problem when $\bar{t} = 0$, where the shear stress $\boldsymbol{\gamma}$ takes the role of a Lagrange multiplier which acts to enforce the Kirchhoff constraint $\nabla z_3 - \theta = 0$. When $\bar{t} = 0$ it is no longer the case that $S = H(\mathrm{rot}; \Omega_0)$ and instead the following result holds:

$$S := H^{-1}(\mathrm{div}; \Omega_0) \tag{5.21}$$

because of the duality pairing between the two spaces [135]:

$$(H(\mathrm{rot}; \Omega_0))' = H^{-1}(\mathrm{div}; \Omega_0) \tag{5.22}$$

In comparison, for the Timoshenko beam problem we have the significantly simpler result for both fixed ε and $\varepsilon = 0$ that:

$$S := L^2(\Omega_0) \tag{5.23}$$

This is because the L^2 space is dual to itself, that is:

$$(L^2(\Omega_0))' = L^2(\Omega_0) \tag{5.24}$$

We refer the reader to the book by Chapelle and Bathe for a more in-depth discussion of these results [40].

Similarly to the Timoshenko beam problem we can make the following observations about the mixed formulation of the Reissner-Mindlin problem with theorems 1 to 3 in mind. Firstly, the bilinear form $a := a_b$ in the mixed formulation eq. 11 is *not* coercive on the entire space

$\mathcal{X} := \mathcal{V}_3 \times \mathcal{R} := H_0^1(\Omega_0)^3$, but only the subset of functions which satisfy the Kirchhoff constraint $\nabla z_3 - \boldsymbol{\theta} = 0$. This is due to the loss of the quadric terms in transverse displacement which were present in the bilinear form $a := a_b + a_s$ for the displacement formulation in eq. (5.5). Indeed, this loss of coercivity in a is typical of most mixed formulations, except notably for the Stokes problem.

Secondly, for a discretisation of eq. (5.9) to be successful, that is, the construction of the subspaces $\mathcal{X}_h \subset \mathcal{X}$ and $\mathcal{M}_h \subset \mathcal{M}$ to be suitable, we must satisfy the discrete equivalents of theorems 1 to 3. The satisfaction of these conditions is not a trivial matter. Just as before, we will refer to condition 1 of theorem 1 as the kernel coercivity condition, and condition 2 of theorem 1 as the inf-sup condition.

In a similar way to the Timoshenko beam problem a larger or `richer' discretised space $\mathcal{X}_h$ (whilst keeping the same $\mathcal{M}_h$) must be chosen to ensure the inf-sup condition is satisfied, whilst if $\mathcal{X}_h$ is too rich then the kernel ellipticity condition becomes harder to satisfy. These two competing requirements make the design of good discretisations of mixed weak forms particularly tricky.

5.2.4 FE discretisation

One of the most commonly used and widely studied approaches to the shear-locking problem in the finite element literature is the mixed interpolation of tensorial components (MITC) technique. The particularly appealing aspect of the MITC technique is that instead of treating the shear stress directly it is treated implicitly via a reduction operator which acts upon the standard displacement variables. Therefore the weak form in the MITC formulation is expressed in terms of the displacements only. Nonetheless, the underlying reason that the MITC family of elements work is that they are based upon the application of a mixed weak form.

In the MITC approach a reduction operator R_h is defined which maps values in the discrete space to an underlying shear space S_h:

$$R_h : H(\mathrm{rot}; \Omega_0) \to S_h \tag{5.25}$$

So instead of using the standard discrete displacement formulation:

$$a_b(\boldsymbol{\theta}_h; \boldsymbol{\eta}_h) + \lambda \bar{t}^{-2} (\nabla z_{3h} - \boldsymbol{\theta}_h; \nabla y_3 - \boldsymbol{\eta}_h)_{L^2(\Omega_0)} = g(y_3) \quad \forall (y_3, \boldsymbol{\eta}) \in \mathcal{V}_{3h} \times \mathcal{R}_h \tag{5.26}$$

the following is used instead:

$$a_b(\boldsymbol{\theta}_h; \boldsymbol{\eta}_h) + \lambda \bar{t}^{-2}(R_h(\nabla z_{3h} - \boldsymbol{\theta}_h); R_h(\nabla y_3 - \boldsymbol{\eta}_h))_{L^2(\Omega_0)} = g(y_3) \quad \forall (y_3, \boldsymbol{\eta}) \in \mathcal{V}_{3h} \times \mathcal{R}_h \tag{5.27}$$

The reduction operator $\mathcal{R}_h$ essentially unlocks the element by allowing the Kirchhoff constraint to hold for a richer set of displacement functions than the zero set. The underlying shear space S_h is typically chosen to be a conforming subspace of $H(\text{rot}; \Omega_0)$ which can be constructed using rotated Raviart-Thomas-Nédélec elements. These elements are sometimes referred to as `edge' elements as the degrees of freedom lie on the edges of the element. Higher-order versions also have internal moment degrees of freedom. Given the success of the MITC family of elements it seems logical to use similar ideas for the discretisation of the shear stress field.

5.2.5 Meshless discretisation

We begin by discretising the shear stress $\boldsymbol{\gamma}$. To build a conforming subspace of $H(\text{rot}; \Omega_0)$ we use rotated Raviart-Thomas-Nédélec [136, 137] elements of lowest order on a triangular background mesh. These elements are often referred to as edge elements as their degrees of freedom are defined as integrals along the element edges. We refer to this family of elements as NED_q for $q = 1, 2, \ldots$, where q refers to the order of polynomial included in the basis[1]. These elements can be viewed as rotated versions of those introduced by Raviart and Thomas [136] to build conforming subspaces of $H(\text{div}; \Omega)$ as the rot and div operator can be related by a rotation of a two component vector field $\boldsymbol{q}$ by $\pi/2$. We denote the discrete solution for the shear stress as $\gamma_h(\boldsymbol{x}) \in S_h$ where $S_h := \text{NED}_1(\Omega_0; \mathcal{T}_h) \subset H(\text{rot}; \Omega_0)$. $\mathcal{T}_h$ is a triangulation on Ω_0 with edges $\mathcal{E}_h$. For a reference triangle $\hat{K}$ with edges $e_i \in \mathcal{E}_h(\hat{K})$ and degrees of freedom Σ_i defined on the

[2] In Raviart and Thomas's original paper [136] on constructing conforming subspaces of $H(\text{div}; \Omega)$ they numbered their elements starting with $q = 0$, so the lowest-order element is called RT_0. In this paper we use the convention of Nédélec [137] and start with $q = 1$ as the final polynomial space for the element includes terms of order $P_q(\hat{K})$

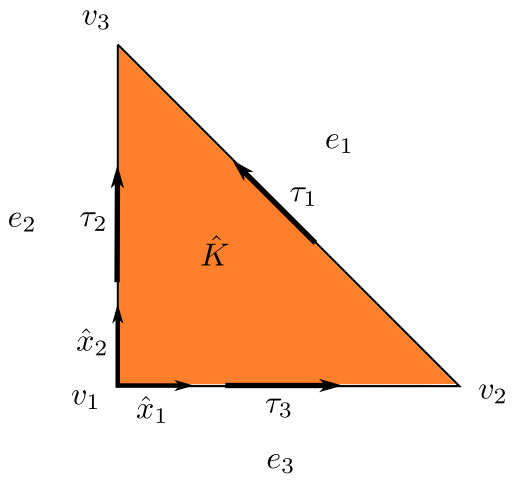

Figure 5.1: Geometry of reference element $\hat{K}$ with vertices v_1, v_2, v_3, and edges e_1, e_2, e_3 associated with tangential vectors τ_1, τ_2, τ_3.

edges e_i as shown in fig. 5.1 the interpolation across $\hat{K}$ can be written as:

$$\begin{aligned} \boldsymbol{\gamma}_h(\hat{x}_1, \hat{x}_2) &= \sum_{i=1}^{3} \boldsymbol{N}_i \gamma_i \\ &= \left[\begin{pmatrix} -\hat{x}_2 \\ \hat{x}_1 \end{pmatrix} \begin{pmatrix} \hat{x}_2 \\ 1-\hat{x}_1 \end{pmatrix} \begin{pmatrix} 1-\hat{x}_2 \\ \hat{x}_1 \end{pmatrix} \right] \begin{Bmatrix} \gamma_1 \\ \gamma_2 \\ \gamma_3 \end{Bmatrix} \\ &= \boldsymbol{N}_\gamma \boldsymbol{\gamma} \quad \forall (\hat{x}_1, \hat{x}_2) \in \hat{K} \end{aligned} \tag{5.28}$$

where $(\hat{x}_1, \hat{x}_2)$ is the coordinate system in the reference triangle $\hat{K}$. We plot these vector basis functions in fig. 5.3. An overview of the construction of these shape functions on the reference element and the transformation to a general element K in the mesh is given in the following section.

Rotated Raviart-Thomas-Nédélec element

This section gives a brief overview of the construction of the lowest-order rotated Raviart-Thomas-Nédélec elements denoted NED_1. Whilst these elements are well known in the mathematics literature they seem to be less well known in the engineering community so we give a full overview here.

We begin with the classical Ciarlet triple definition of a finite element $(T, \mathcal{V}, \mathcal{L})$ where T is an element geometry (interval, triangle, tetrahedron, quadrilateral etc.), $\mathcal{V}$ is a function space (typically a polynomial) defined on T, and $\mathcal{L} = \{l_1, l_2, \dots, l_n\}$ is a set of degree of freedom which are a set of linear functions on $\mathcal{V}$[140]. The degrees of freedom l_i must be linearly independent.

First of all we will define some polynomial spaces that will be used to define the space $\mathcal{V}$ for our element NED_1. We denote $P_k(\Sigma)$ as the set of polynomials of degree k on Σ, where Σ is entity of the reference element T such as the edges, faces, or the element itself. So as an example, the set $P_2(\hat{K})$ of polynomials on the reference triangle $\hat{K}$ is:

$$P_2(\hat{K}) = \left\{1,\ \hat{x}_1,\ \hat{x}_2,\ \hat{x}_1^2,\ \hat{x}_1\hat{x}_2,\ \hat{x}_2^2\right\} \tag{5.29}$$

Similarly, we denote $\tilde{P}_k(\Sigma)$ as the set of homogeneous polynomials of degree k on Σ. So for example, the set $\tilde{P}_2(\hat{K})$ of homogeneous polynomials of second-order on the reference triangle is:

$$\tilde{P}_2(\hat{K}) = \left\{\hat{x}_1^2,\ \hat{x}_1\hat{x}_2,\ \hat{x}_2^2\right\} \tag{5.30}$$

We now define a new polynomial space $S_k(\hat{K})$ as:

$$S_k(\hat{K}) := \left\{\boldsymbol{p} \in [\tilde{P}(\hat{K})]^2 \mid \boldsymbol{p} \cdot \hat{\boldsymbol{x}} = 0\right\} \tag{5.31}$$

We now have all the necessary components ready to define the finite element $\mathrm{NED}_1(\hat{K})$ which will construct a conforming subspace of $H(\mathrm{rot}, \Omega_0)$:

Geometry The geometry is the standard reference triangle $\hat{K} \subset \mathbb{R}^2$ as shown in fig. 5.1.

Function Space Nédélec characterised the function space $\mathcal{V}_{\mathrm{NED}_k}$ in $\mathbb{R}^d$ for $d = 2, 3$ as the polynomial space:

$$\mathcal{V}_{\mathrm{NED}_k} := \left(P_{k-1}(\hat{K})\right)^d \oplus S^k \tag{5.32}$$

where the symbol $\oplus$ means the direct sum of the two vector spaces.

In $\mathbb{R}^2$ this space can be written in an equivalent form:

$$\mathcal{V}_{\mathrm{NED}_k} = \left(P_{k-1}(\hat{K})\right)^2 \oplus \tilde{P}_{k-1}\begin{pmatrix}-\hat{x}_2\\ \hat{x}_1\end{pmatrix} \tag{5.33}$$

As we will only be deriving the lowest-order element $k = 1$ we can write the space $\mathcal{V}_{\mathrm{NED}_1}$

as:

$$\mathcal{V}_{\mathrm{NED}_1} = \left(P_0(\hat{K})\right)^2 \oplus \tilde{P}_0 \begin{pmatrix} -\hat{x}_2 \\ \hat{x}_1 \end{pmatrix} \tag{5.34}$$

$$= \left\langle \begin{pmatrix} 1 \\ 0 \end{pmatrix}, \begin{pmatrix} 0 \\ 1 \end{pmatrix}, \begin{pmatrix} -\hat{x}_2 \\ \hat{x}_1 \end{pmatrix} \right\rangle \tag{5.35}$$

We can therefore write the shape functions $\boldsymbol{N}_i \in \mathcal{V}_{\mathrm{NED}_1}(\mathbb{R})$ as:

$$\boldsymbol{N}_i = \boldsymbol{a}_i + b_i \begin{pmatrix} -\hat{x}_2 \\ \hat{x}_1 \end{pmatrix} \tag{5.36}$$

Degrees of Freedom The set of degrees of freedom $\mathcal{L}$ defined on $\mathcal{V}_{\mathrm{NED}_1}$ in the 2 dimensional case consist of two types of linear functionals:

1. edge degrees of freedom on $\hat{e}$

$$l(\boldsymbol{v}) = \int_{\hat{e}} (\boldsymbol{v} \cdot \hat{\boldsymbol{\tau}}) p \, d\hat{s} \quad \forall p \in P_{k-1}(\hat{e}) \quad \forall \hat{e} \in \hat{K} \tag{5.37}$$

   giving a total of $3k$ edge degrees of freedom.

2. inner degrees of freedom on $\hat{K}$

$$l(\boldsymbol{v}) = \int_{\hat{K}} \boldsymbol{v} \cdot \boldsymbol{p} \, d\hat{\boldsymbol{x}} \quad \forall p \in (P_{k-2}(\hat{K}))^2 \quad k \geq 2 \text{ only} \tag{5.38}$$

   giving a total of $k(k-1)$ inner degrees of freedom

Fortunately in our case $k = 1$ we only have 3 edge degrees of freedom specified by eq. (5.37) and the calculations are relatively simple.

We label the edges as in fig. 5.1 and orient the unit tangent vectors as shown giving:

$$\hat{\boldsymbol{\tau}}_1 = \frac{1}{\sqrt{2}} \begin{pmatrix} -1 \\ 1 \end{pmatrix}, \quad \hat{\boldsymbol{\tau}}_2 = \begin{pmatrix} 0 \\ 1 \end{pmatrix}, \quad \hat{\boldsymbol{\tau}}_3 = \begin{pmatrix} 1 \\ 0 \end{pmatrix} \tag{5.39}$$

We can then write the set of edge degrees of freedom l_i using eq. (5.37) as:

$$l_i(\boldsymbol{v}) = \int_{\hat{e}_i} (\boldsymbol{v} \cdot \hat{\boldsymbol{\tau}}_i) \times 1 \, d\hat{s} \quad i = 1, 2, 3 \tag{5.40}$$

The final step is to construct a finite-element basis $\boldsymbol{N}_1, \boldsymbol{N}_2, \boldsymbol{N}_3$. To do this we require:

$$l_i(\boldsymbol{N}_j) = \delta_{ij} \tag{5.41}$$

We will perform this calculation for the degree of freedom l_1 defined across the edge e_1 as this is the trickiest calculation.

$$l_1(\boldsymbol{N}_j) = \int_{\hat{e}_1} \left(\boldsymbol{a}_j + b_j \begin{pmatrix} -\hat{x}_2 \\ \hat{x}_1 \end{pmatrix} \right) \cdot \frac{1}{\sqrt{2}} \begin{pmatrix} -1 \\ 1 \end{pmatrix} d\hat{s} \tag{5.42}$$

We then parametrise the edge $\hat{e}_1$ as:

$$\boldsymbol{r}(t) = \langle 1 - t, t \rangle, \quad \hat{x}_1 = 1 - t, \quad \hat{x}_2 = t \tag{5.43}$$

$$d\hat{s}^2 = (-dt)^2 + (dt)^2 = 2dt^2 \tag{5.44}$$

giving the transformed line integral as:

$$l_1(\boldsymbol{N}_j) = \frac{1}{\sqrt{2}} \int_{t=0}^{t=1} \left(-a_{1j} + a_{2j} + b_j t + b(1-t) \right) \sqrt{2}\, dt \tag{5.45}$$

$$= -a_{1j} + a_{2j} + b_j \tag{5.46}$$

After repeating the above integration procedure for l_2 and l_3 we get the following set of equations for $i = 1, 2, 3$:

$$\left[\begin{array}{ccc} -1 & 1 & 1 \\ 0 & 1 & 0 \\ 1 & 0 & 0 \end{array}\right] \begin{pmatrix} a_{1i} \\ a_{2i} \\ b_i \end{pmatrix} = \left[\begin{array}{c|c|c} 1 & 0 & 0 \\ 0 & 1 & 0 \\ 0 & 0 & 1 \end{array}\right] \tag{5.47}$$

Solving gives:

$$a_{11} = a_{21} = a_{12} = a_{23} = 0 \tag{5.48a}$$

$$b_1 = a_{22} = a_{13} = b_3 = 1 \tag{5.48b}$$

$$b_2 = -1 \tag{5.48c}$$

The coefficients are then substituted into eq. (5.36) giving the final set basis functions as shown in eq. (5.28).

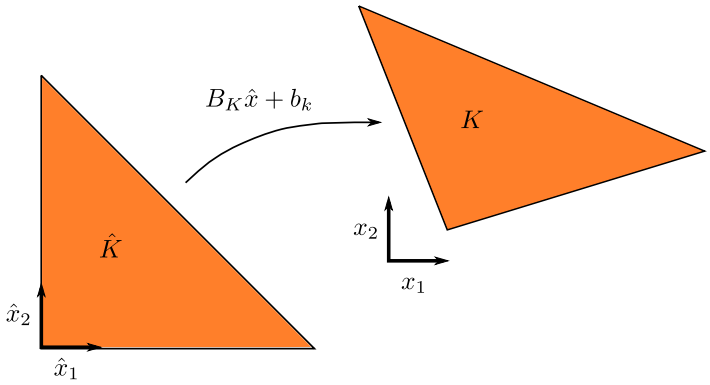

Figure 5.2: Transform between reference element $\hat{K}$ and physical element K

Conforming affine transform

We define an affine map F_K between a general cell K in the global coordinate system x and the reference cell $\hat{K}$ as:

$$\hat{K} \ni \boldsymbol{x} = \boldsymbol{F}_K(\hat{\boldsymbol{x}}) = \boldsymbol{B}_K\hat{\boldsymbol{x}} + \boldsymbol{b}_K \tag{5.49}$$

To ensure that we construct an $H(\text{rot}; \Omega)$ conforming field across the triangulation $\mathcal{T}_h$ we must use the covariant vector-field transform. To obtain the element shape functions $\boldsymbol{N}_i(\boldsymbol{x})$ from the reference shape functions $\hat{\boldsymbol{N}}_i(\hat{\boldsymbol{x}})$ we use the following covariant transform:

$$\boldsymbol{N}_i(\boldsymbol{x}) = (\boldsymbol{D}\hat{\boldsymbol{F}}_K{}^{-T}\hat{\boldsymbol{N}}_i) \circ \boldsymbol{F}_K^{-1}(\boldsymbol{x}) \tag{5.50}$$

where $\boldsymbol{D}\hat{\boldsymbol{F}}_K \in \mathbb{R}^{2\times 2}$ is the Jacobian of the element map:

$$\boldsymbol{D}\hat{\boldsymbol{F}}_K = \frac{\partial}{\partial \hat{\boldsymbol{x}}}\boldsymbol{F}_K(\hat{\boldsymbol{x}}) \tag{5.51}$$

This transform is the same as that used to transform the *gradients* of the shape functions in the standard $H^1(\Omega)$ conforming finite element methods. In the case of the affine map defined above the Jacobian is simply a constant for each K:

$$\boldsymbol{D}\hat{\boldsymbol{F}}_K = \boldsymbol{B}_K \tag{5.52}$$

In other words, the components of the vector field transform in a manner similarly to the derivatives of the standard Lagrangian finite element basis functions.

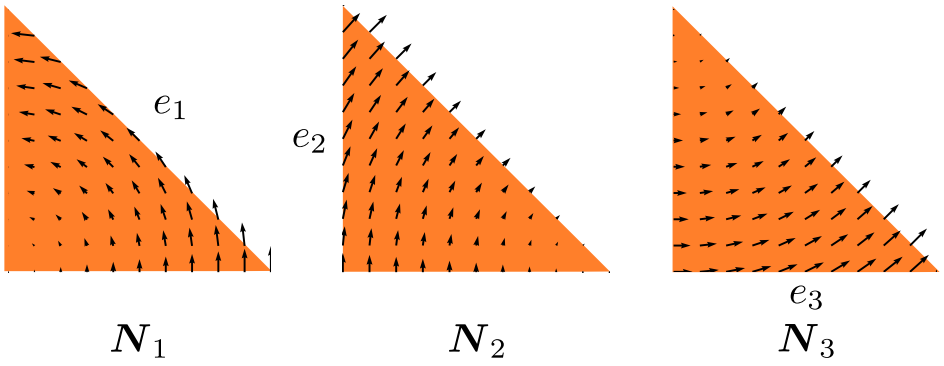

Figure 5.3: Basis functions $\boldsymbol{N}_i$ associated with edge e_i on the reference triangle $\hat{K}$.

Similarly, we denote the discrete solution for the transverse displacement and rotations as $z_{3h} \in \mathcal{V}_{3h}$ and $\boldsymbol{\theta}_h \in \mathcal{R}_h$ where $\mathcal{V}_{3h} = \mathcal{R}_h := ME(\Omega_0; \mathcal{N}_h, \rho) \subset H_0^1(\Omega_0)$. $\mathcal{N}_h$ is a set of nodes in Ω_0 associated with a set of support sizes ρ. Here we assume that Ω_0 is a convex domain so that all basis functions φ_i associated with nodes inside the domain vanish on the boundary. We can then write the trial functions for the displacement and rotations as:

$$z_{3h}(x) = \sum_{i=1}^{N} \varphi_i z_{3i} = \begin{bmatrix} \varphi_1 & \varphi_2 & \dots & \varphi_N \end{bmatrix} \begin{Bmatrix} z_{31} \\ z_{32} \\ \vdots \\ z_{3N} \end{Bmatrix} \tag{5.53a}$$

$$= \boldsymbol{\varphi}_{z_3} \boldsymbol{z}_3 \quad \forall x \in \Omega_0$$

$$
\begin{aligned}
\boldsymbol{\theta}_h(\boldsymbol{x}) &= \sum_{i=1}^{N} \boldsymbol{\varphi}_i \boldsymbol{\theta}_i \\
&= \begin{bmatrix} \varphi_1 & \varphi_2 & \dots & \varphi_N & 0 & 0 & \dots & 0 \\ 0 & 0 & \dots & 0 & \varphi_1 & \varphi_2 & \dots & \varphi_N \end{bmatrix} \begin{Bmatrix} \theta_{11} \\ \theta_{12} \\ \vdots \\ \theta_{1N} \\ \theta_{21} \\ \theta_{22} \\ \vdots \\ \theta_{2N} \end{Bmatrix} \\
&= \begin{bmatrix} \boldsymbol{\varphi}_{\theta_1} & \mathbf{0} \\ \mathbf{0} & \boldsymbol{\varphi}_{\theta_2} \end{bmatrix} \begin{Bmatrix} \boldsymbol{\theta}_1 \\ \boldsymbol{\theta}_2 \end{Bmatrix} \\
&= \boldsymbol{\Phi}_\theta \boldsymbol{\theta} \quad \forall \boldsymbol{x} \in \Omega_0
\end{aligned}
\tag{5.53b}
$$

We define the trial functions using the same basis as the test functions:

$$
y_{3h} = \boldsymbol{\varphi}_{z3}, \qquad \boldsymbol{\eta}_h = \boldsymbol{\Phi}_\theta, \qquad \boldsymbol{\psi}_h = \boldsymbol{N}_\gamma \tag{5.54}
$$

We can then write the discrete linear set of equations as:

$$
\int_{\Omega_0} \boldsymbol{B}_b^T \boldsymbol{D}_b \boldsymbol{B}_b \, d\Omega \, \boldsymbol{\theta} + \int_{\Omega_0} \boldsymbol{B}_s^T \boldsymbol{N}_\gamma \, d\Omega \, \boldsymbol{\gamma} = \int_{\Omega_0} \boldsymbol{\varphi}_{z3} g \, d\Omega \tag{5.55a}
$$

$$
\int_{\Omega_0} \boldsymbol{N}_\gamma^T \boldsymbol{B}_s \, d\Omega \begin{Bmatrix} \boldsymbol{\theta} \\ \boldsymbol{z}_3 \end{Bmatrix} - \bar{t}^2 \boldsymbol{D}_s^{-1} \int_{\Omega_0} \boldsymbol{N}_\gamma^T \boldsymbol{N}_\gamma \, d\Omega \, \boldsymbol{\gamma} = 0 \tag{5.55b}
$$

where the $\boldsymbol{B}_b \in \mathbb{R}^{3\times 3N}$ and $\boldsymbol{B}_s \in \mathbb{R}^{2\times 3N}$ are matrices containing component-wise derivatives of the shape function vectors:

$$
\boldsymbol{B}_b = \begin{bmatrix} \frac{\partial \varphi_{\theta 1}}{\partial x_1} & \mathbf{0} \\ \mathbf{0} & \frac{\partial \varphi_{\theta 2}}{\partial x_2} \\ \frac{\partial \varphi_{\theta 1}}{\partial x_2} & \frac{\partial \varphi_{\theta 2}}{\partial x_1} \end{bmatrix} \tag{5.56}
$$

$$
\boldsymbol{B}_s = \begin{bmatrix} -\boldsymbol{\varphi}_{\theta 1} & \mathbf{0} & \frac{\partial \varphi_{z3}}{\partial x_1} \\ \mathbf{0} & -\boldsymbol{\varphi}_{\theta 2} & \frac{\partial \varphi_{z3}}{\partial x_2} \end{bmatrix} \tag{5.57}
$$

and $\boldsymbol{D}_s \in \mathbb{R}^{2\times 2}$ and $\boldsymbol{D}_b \in \mathbb{R}^{3\times 3}$ are matrices containing the material properties of the plate:

$$\boldsymbol{D}_s = \begin{bmatrix} \lambda & 0 \\ 0 & \lambda \end{bmatrix} \tag{5.58}$$

$$\boldsymbol{D}_b = D \begin{bmatrix} 1 & \nu & 0 \\ \nu & 1 & 0 \\ 0 & 0 & \frac{1-\nu}{2} \end{bmatrix} \tag{5.59}$$

The above set of equations is a linear system of the following form:

$$\left[\begin{array}{c|c} \begin{array}{c|c} \boldsymbol{K}_b & \boldsymbol{0} \\ \hline \boldsymbol{0} & \boldsymbol{0} \end{array} & \boldsymbol{C} \\ \hline \boldsymbol{C}^T & -\boldsymbol{V} \end{array}\right] \left\{\begin{array}{c} \boldsymbol{\theta} \\ \hline \boldsymbol{z}_3 \\ \hline \boldsymbol{\gamma} \end{array}\right\} = \left\{\begin{array}{c} \boldsymbol{0} \\ \hline \boldsymbol{f} \\ \hline \boldsymbol{0} \end{array}\right\} \tag{5.60a}$$

where

$$\boldsymbol{K}_b = \int_{\Omega_0} \boldsymbol{B}_b \boldsymbol{D}_b \boldsymbol{B}_b \, d\Omega \tag{5.60b}$$

$$\boldsymbol{C} = \int_{\Omega_0} \boldsymbol{B}_s^T \boldsymbol{N}_\gamma \, d\Omega \tag{5.60c}$$

$$\boldsymbol{V} = \int_{\Omega_0} \boldsymbol{N}_\gamma^T \boldsymbol{N}_\gamma \, d\Omega \tag{5.60d}$$

$$\boldsymbol{f} = \int_{\Omega_0} \boldsymbol{\varphi}_{z3} g \, d\Omega \tag{5.60e}$$

where $\boldsymbol{K}_b \in \mathbb{R}^{2N\times 2N}$, $\boldsymbol{C} \in \mathbb{R}^{3N\times|\mathcal{E}_h|}$, $\boldsymbol{V} \in \mathbb{R}^{|\mathcal{E}_h|\times|\mathcal{E}_h|}$ and $\boldsymbol{f} \in \mathbb{R}^{N\times 1}$ where $|\mathcal{E}_h|$ is the number of edges in the triangulation $\mathcal{T}_h$ and N is the number of nodes in the node set $\mathcal{N}_h$. The total solution vector sizes is of size $3N + |\mathcal{E}_h|$.

5.3 Results

5.3.1 Methods used for comparison

FE 1 displacement We use standard linear C^0 continuous Lagrangian elements, denoted CG_1, for all fields $(\boldsymbol{\theta}, z_3)$ in a displacements-only weak form eq. (5.5). This formulation is prone to shear-locking.

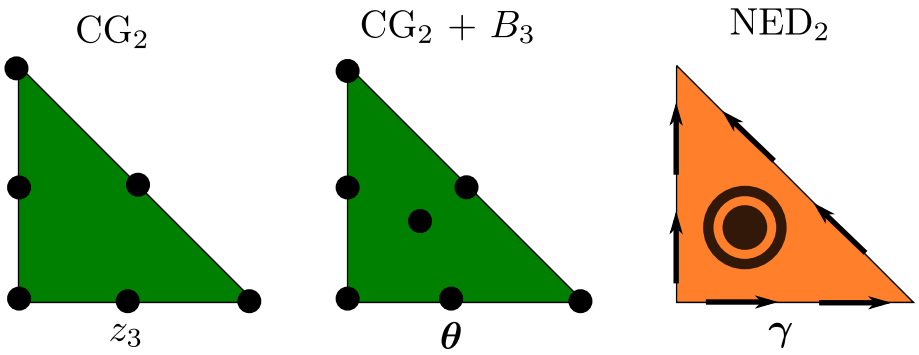

Figure 5.4: FE 2 mixed element; transverse deflections are approximated using continuous second-order Lagrangian element CG_2 whilst the rotations are approximated using CG2 enriched with third-order bubble functions B_3. The shear stresses are approximated using NED_2 elements which have two internal `moment' degrees of freedom in addition to two degrees of freedom on each edge.

FE 2 displacement We use standard quadratic C^0 continuous Lagrangian elements, denoted CG_2, for all fields $(\boldsymbol{\theta}, z_3)$ in the displacements-only weak form eq. (5.5). This formulation is prone to shear-locking.

FE 2 mixed We use the element structure shown in fig. 5.4 in a mixed weak form eq. (5.9).

Maximum-Entropy (MaxEnt) mixed This novel method we propose in this chapter using maximum-entropy basis functions for the displacements and rotated Raviart-Thomas-Nédélec elements of lowest-order for the shear stresses.

5.3.2 Parameters

We define the following parameters as quantities of interest in the construction of both $\mathcal{N}_h$ and $\mathcal{T}_h$.

On node set $\mathcal{N}_h$ we define h_a as the distance between node i and its nearest neighbouring node. On a regular grid the distance h will be the same for all nodes. We then define the support ρ_i of node i with the following formula:

$$\rho_a = \alpha_\rho \beta h_a \quad \forall a \tag{5.61}$$

On uniform grids of nodes we will take values $\beta = \sqrt{2}, 2, \sqrt{4+1}, 3$ and $\alpha_\rho = 1.05$ in an attempt to find a roughly optimal value.

We define the constraint ratio r as the ratio of the number of degrees of freedom in the displacement variable function spaces $(\mathcal{V}_h, \mathcal{R}_h)$ to the number of degrees of freedom in the shear stress function space S_h:

$$r = \frac{\dim \mathcal{V}_h + \dim \mathcal{R}_h}{\dim S_h} \tag{5.62}$$

This quantity is of interest because it gives a rough measure of the relative sizes of the spaces which is inherently related to the stability and performance of the final linear system of equations. We will show through numerical experiments that if the ratio r is too low the method becomes over-constrained and solution quality decreases, and if the ratio r is too high the method becomes under-constrained and unstable.

5.3.3 Simply supported square plate with uniform pressure

We use the common setup of a simply supported square plate with uniform pressure as a test problem as it has a closed-form analytical solution [32]. The problem domain Ω_0 is defined by:

$$\Omega_0 = \left\{(x_1, x_2) \in \mathbb{R}^2 : 0 < x_1 < 1,\ 0 < x_2 < 1\right\} \tag{5.63}$$

and the boundary conditions are hard simply supported:

$$\boldsymbol{\theta} \cdot \boldsymbol{\tau} = \boldsymbol{n} \cdot L\varepsilon(\boldsymbol{\theta})\boldsymbol{n} = z_3 = 0 \quad \forall \boldsymbol{x} \in \Gamma_0 \tag{5.64}$$

where $\boldsymbol{n}$ is the unit normal vector to the boundary and $\boldsymbol{\tau}$ is the unit tangent vector to the boundary. The SSSS domain and boundary conditions are shown in fig. 5.5a.

We take the following numerical values: $E = 10920$, $\nu = 0.3$, $\kappa = 5/6$, $g = 1$ and define the following normalised transverse displacement $\hat{z}_3$ [32]:

$$\hat{z}_3 = \frac{E}{12(1-\nu^2)} z_3 \times 10^2 = z_3 \times 10^5 \tag{5.65}$$

Note that there is no factor of $\bar{t}^3$ as in Reddy [32] as we have already scaled the loading f by a factor of $g\bar{t}^3$ in the governing weak form to ensure the solution is bounded as $\bar{t} \to 0$.

We define the L^2 relative error in $e_{L^2}(u_h, u)$ between the numerical solution u_h and exact

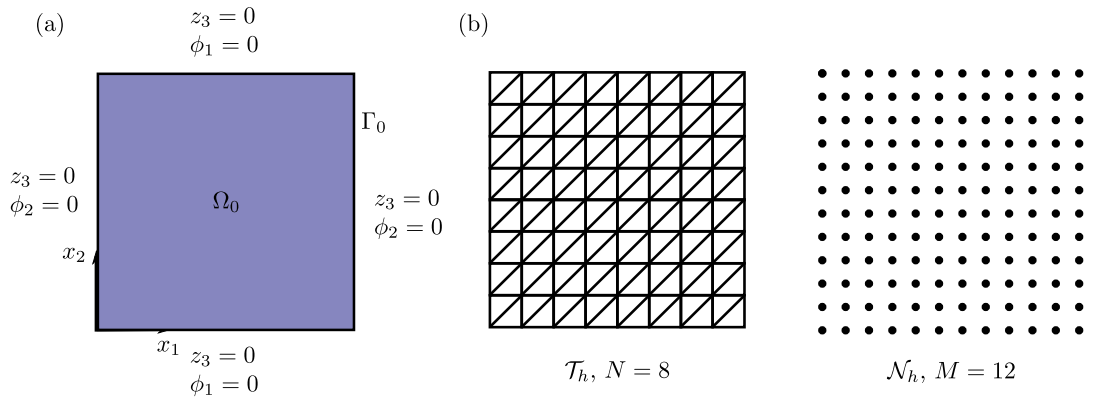

Figure 5.5: (a) Domain Ω_0 for the SSSS square plate showing boundary conditions on each edge. (b) Example discretisation of square domain.

solution u as:

$$e_{L^2}(u_h, u) = \frac{\|u - u_h\|_{L^2(\Omega)}}{\|u\|_{L^2(\Omega)}} = \frac{\left(\int_{\Omega_0} (u - u_h)^2 \ d\Omega\right)^{1/2}}{\left(\int_{\Omega_0} u^2 \ d\Omega\right)^{1/2}} \tag{5.66}$$

In the case of the simply supported plate where we have an analytical solution available we will use the above as an indicator of solution quality.

Parameters

In fig. 5.6 we show the effect of the parameter β on the error in the L^2 norm for thick $\bar{t} = 0.2$ and thin $\bar{t} = 0.001$ plates. We can see that a value of $\beta = \sqrt{2}$ is insufficient and that values of $\beta \geq 2$ appear to be optimal. For $\beta \geq \sqrt{4+1}$ there seems to a slight increase in error for the thick plate, whilst error is minimised at $\beta = \sqrt{4+1}$ for the thin plate. However these variations are small enough that we take a value of $\beta = 2$ to minimise the bandwidth of the linear system as well as shape function computation time.

We discretise the domain as shown in fig. 5.5b, using a uniform triangulation $\mathcal{T}_h$ with N cells along an edge, and a uniform node set $\mathcal{N}_h$ with M nodes along an edge.

In fig. 5.7 we demonstrate the effect of the constraint ratio r on the error in the L^2 norm for varying $\bar{t}$. We use a fixed maximum-entropy node set $\mathcal{N}_h$ with $M = 12$ and vary the underlying uniform triangulation $\mathcal{T}_h$ by adjusting N to achieve combinations of $\left(\mathcal{N}_h, \mathcal{T}_h\right)$ with varying constraint ratios r.

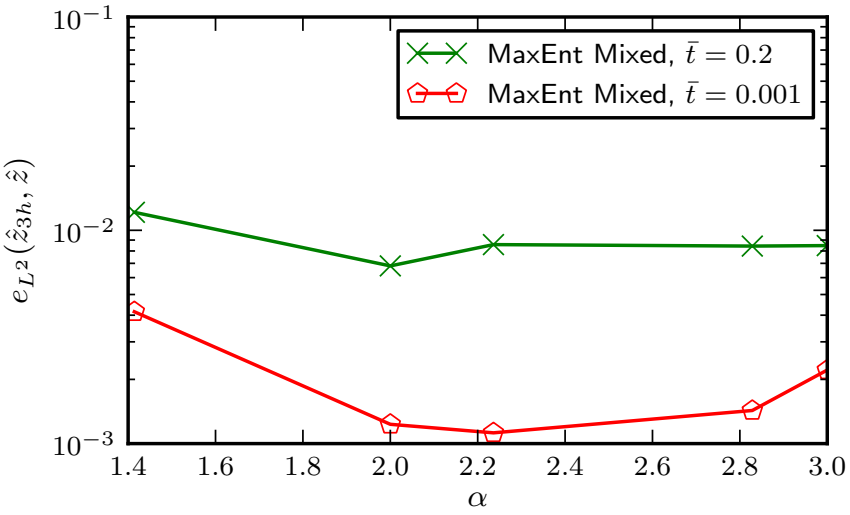

Figure 5.6: Graph showing the effect of the parameter β on convergence. $N = 8, M = 12$. These results correspond with those in series 3 (green dashed line) of fig. 5.7

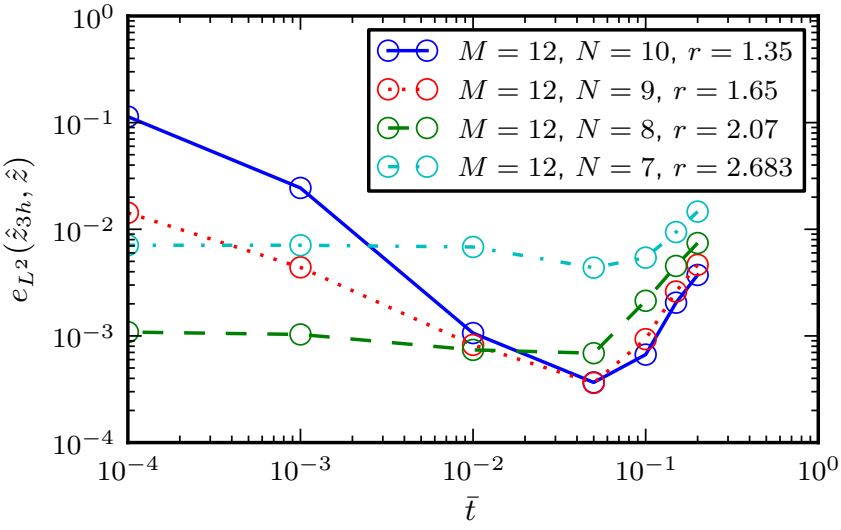

Figure 5.7: Graph showing the effect of the constraint ratio r on the solution for varying $\bar{t}$. $\beta = 2$. The slightly better performance of the method for thin-plates agrees with the results shown in fig. 5.6

We note that for thick plates $t \geq 10^{-1}$ the combinations of $\left(\mathcal{N}_h, \mathcal{T}_h\right)$ with the lowest r value achieve the lowest error, whilst those with the highest r values have the highest error. However, it is clear that the differences in error for thick plates for varying r are small compared to those when the plate is thin $\bar{t} \leq 10^{-2}$ thus we make decisions on the optimal values of r based on results for thin plates alone. We can see that for $N = 9$, 10 corresponding to $r = 1.35$, 1.65 the error increases rapidly as $\bar{t}$ decreases. However, for $N = 8$, corresponding to $r = 2.07$, the error stays bounded at around 10^{-3}. For $N = 7$, corresponding to $r = 2.683$ we have uniformly worse convergence across the entire range of $\bar{t}$. Furthermore to the results shown in fig. 5.7, we found that the method became unstable for $N \leq 6$ corresponding to values of $r \geq 3.6$ and for $N \geq 10$ we found increasingly poor convergence performance. For the discretisations used in our convergence studies we have found that constraint ratios between 2.0 and 2.5 to be satisfactory.

Because of the non-polynomial nature of the maximum-entropy shape functions accurate integration of the weak form typically requires quadrature rules of higher order than those used in the FEM. In this study we use the collapsed quadrature rules of Karniadakis and Sherwin [141]. To ensure that we are integrating the weak form with sufficient accuracy we examined the effect of quadrature order on the error in the L^2 norm. We begin by computing the solution using a quadrature rule of order 7 (49 points per cell) per cell giving our `reference' error as $e_{L^2}^{\text{ref}} = 6.9243 \times 10^{-3}$. In fig. 5.8 we show the difference between the reference solution and the solutions computed with increasing quadrature order. The difference is highest for quadrature of order 2 (4 points per cell), but for quadrature order 3 (9 points per cell) the difference is reduced to around 2.0×10^{-4}, which is less than the solution error of 7.1×10^{-3}. With this in mind we use an excessive quadrature rule of order 5 (25 points per cell) in all subsequent results to guarantee accurate integration whilst still maintaining acceptable computational times.

Locking

In fig. 5.9 we demonstrate the shear-locking-free property of the proposed method through the convergence of the centre point transverse deflection $\hat{z}_{3h}(0.5, 0.5)$ to the Kirchhoff thin plate solution. We show both the Kirchhoff and Reissner-Mindlin analytical solutions; for thin plates $10^{-4} \leq \bar{t} \leq 10^{-2}$ the two almost coincide, whilst for thicker plates $t \geq 10^{-2}$ they diverge as the Reissner-Mindlin theory's relaxation upon the rotation of the transverse normals $\nabla z_3 \neq \theta$ becomes increasingly important. The FE 2 Displacement result clearly shows the pitfalls of using an unmodified displacement-based formulation with severe shear-locking for values of

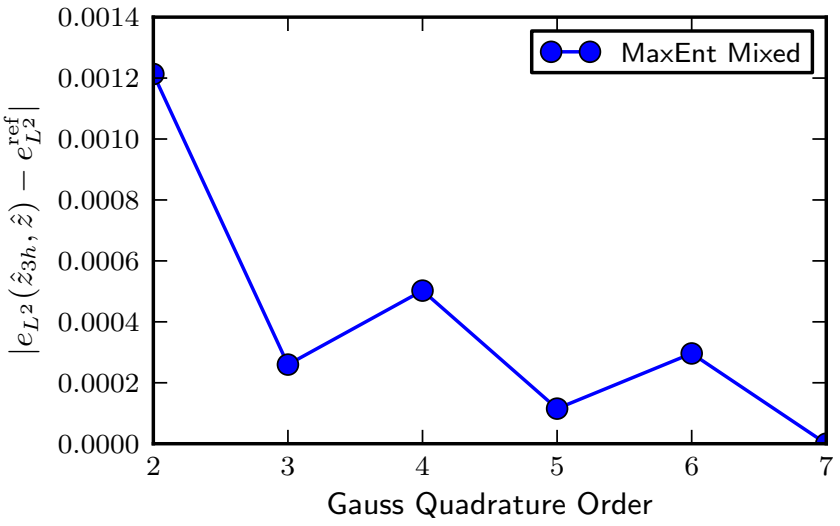

Figure 5.8: Graph showing the effect of the order of the Gauss quadrature rule used for integration on convergence. $N = 8$, $M = 12$, $\beta = 2.0$. Note that the y-axis scale is linear, not logarithmic as in the other convergence plots.

$\bar{t} \leq 10^{-2}$. We note that shear-locking would also occur using the maximum-entropy basis functions, or indeed any other type of standard basis functions using an unmodified displacement-based weak form. Clearly the proposed maximum-entropy mixed method matches, as desired, the analytical solution throughout the full range of thick and thin plates.

In fig. 5.10 we show the convergence of $\hat{z}_{3h}$ to the analytical solution $\hat{z}_3$ in the L^2-norm for varying $\bar{t}$. The error for the proposed maximum-entropy mixed method stays bounded below 10^{-2} as $\bar{t} \to 0$ whilst for the FE 1 displacement method error increases rapidly for $t < 10^{-1}$ as the formulation locks. The FE 2 mixed formulation also provides results that are free from shear-locking.

In fig. 5.11 we show the convergence of z_{3h} to the analytical solution $\hat{z}_3$ in the L^2-norm against number of degrees of freedom for various shear-locking and shear-locking-free methods for a thick plate $\bar{t} = 0.2$. We note that all of the methods converge in the L^2-norm. The FE 2 mixed, maximum-entropy mixed and maximum-entropy displacement formulations provide significantly lower errors than the FE 1 mixed and FE 1 displacement methods. The FE 2 mixed formulation has the highest rates of convergence at around $\rho = O(\text{dof}^{-3/2}) \sim O(h^3)$, consistent with quadratic interpolation. The FE 1 displacement, maximum-entropy mixed and maximum-entropy displacement formulations have convergence rates of $\rho = O(\text{dof}^{-1})$

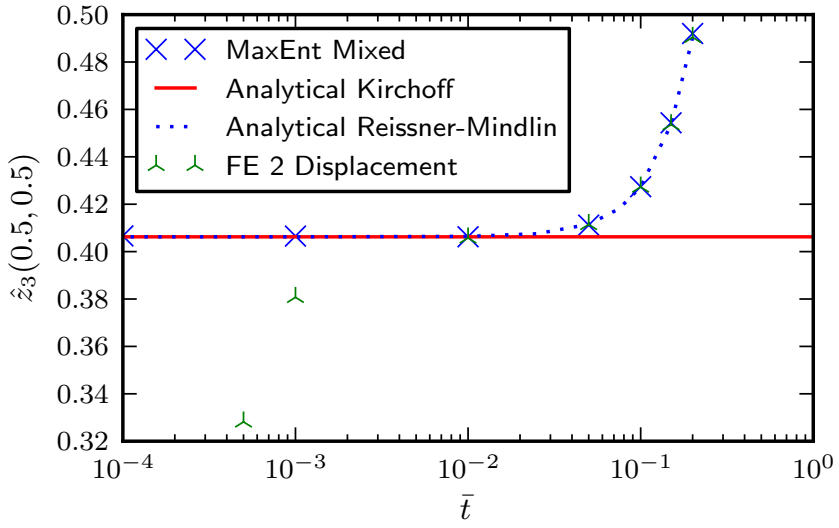

Figure 5.9: Graph showing normalised central deflection $z_3(0.5, 0.5)$ of SSSS square plate for varying $\bar{t}$.

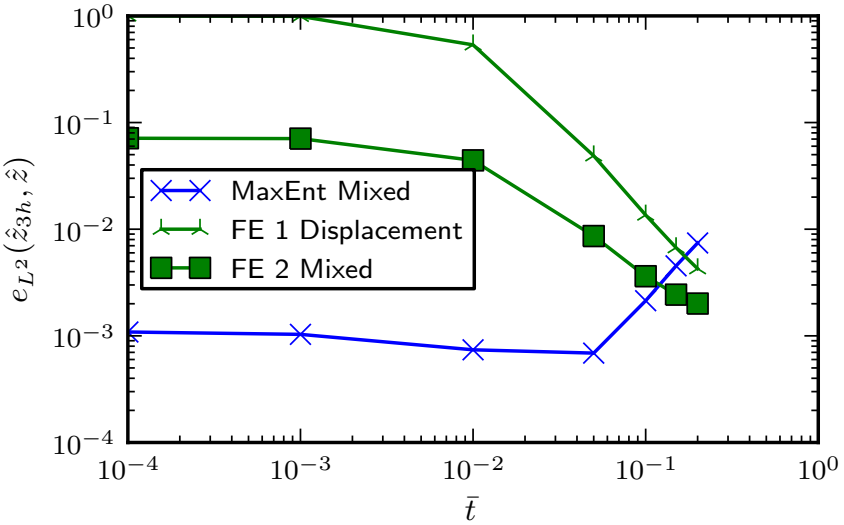

Figure 5.10: Graph showing error in $\hat{z}_{3h}$ for varying $\bar{t}$. Maximum-entropy mixed: $N = 8$, $M = 12$, $\beta = 2.0$. FE 1 displacement: $N = 30$. FE 2 mixed $N = 8$.

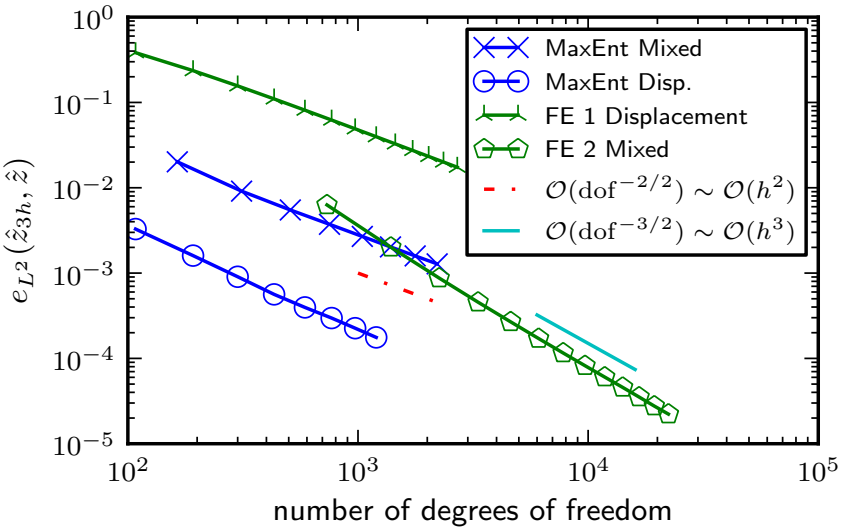

Figure 5.11: Graph showing L^2 error in $\hat{z}_{3h}$ against number of degrees of freedom using various shear-locking and shear-locking-free methods for a thick plate $\bar{t} = 0.2$.

$\sim O(h^2)$, consistent with linear interpolation/approximation. We note that comparing the purely meshless approach vs. our hybrid FE/meshless mixed approach that both convergence rates and errors are marginally worse for the latter. However, our approach still seems to be competitive with the FE 2 mixed method and significantly better than FE 1 displacement method.

In fig. 5.12 we show the convergence of z_{3h} to the analytical solution $\hat{z}_3$ in the L^2-norm against number of degrees of freedom for the proposed maximum-entropy mixed and FE 2 mixed shear-locking-free methods for a thin plate $\bar{t} = 0.001$. The maximum-entropy mixed approach has a convergence rate of $\rho = O(\mathrm{dof}^{-1}) \sim O(h^2)$ whilst the FE 2 mixed approach has a convergence rate of $\rho = O(\mathrm{dof}^{-3/2}) \sim O(h^3)$. For thin plates the proposed method appears to be superior to the FE 2 mixed formulation.

5.3.4 Fully clamped square plate with uniform pressure

Using the same domain $\bar{\Omega}_0$ as defined in eq. (5.63) we now apply fully clamped boundary conditions:

$$\boldsymbol{\theta} = z_3 = 0 \quad \forall \boldsymbol{x} \in \Gamma_0 \tag{5.67}$$

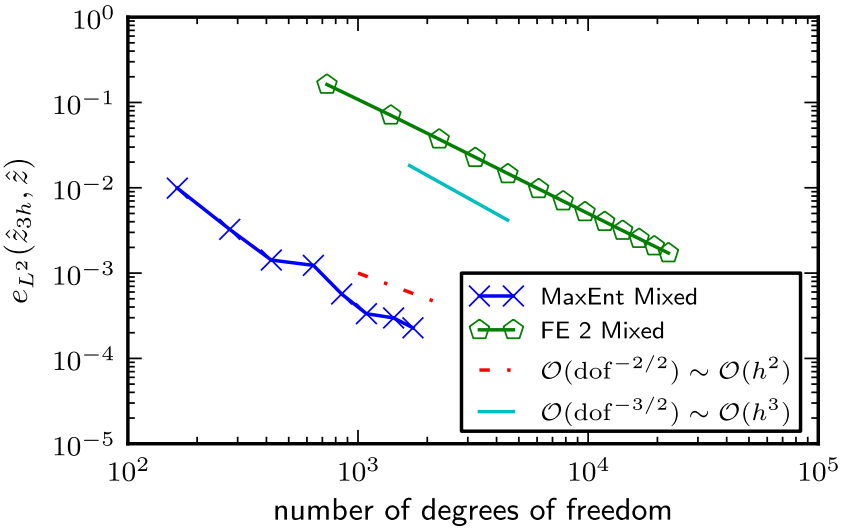

Figure 5.12: Graph showing L^2 error in $\hat{z}_{3h}$ using two locking-free methods for a thin plate $\bar{t} = 0.001$.

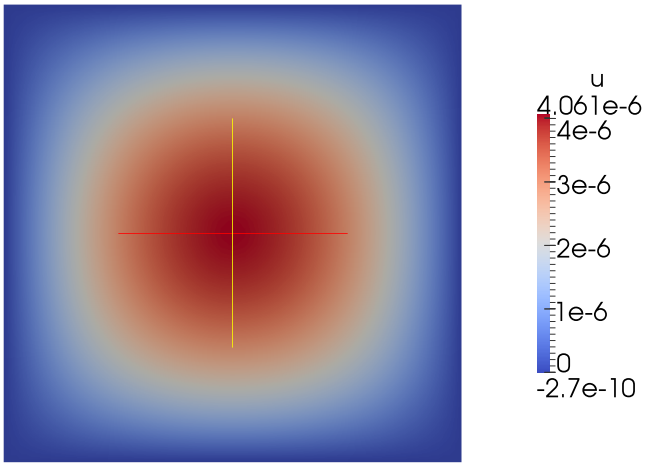

Figure 5.13: Plot of z_{3h}, MaxEnt mixed method 16×16 grid, simply-supported plate, $\bar{t} = 0.001$

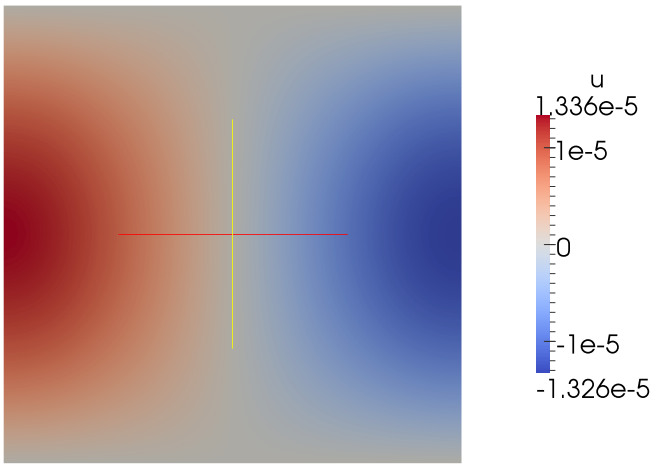

Figure 5.14: Plot of θ_{1h}, MaxEnt mixed method 16×16 grid, simply-supported plate, $\bar{t} = 0.001$

Due to the lack of analytical solution we compute a reference solution on a highly refined mesh $\mathcal{T}_h$ with $N = 70$ using the FE 2 mixed formulation. We take the Kirchhoff centre point deflection as $\hat{z}_3 = 0.126401$ according to İmrak et al. [142]. Our reference FE Reissner-Mindlin solution agrees with this value to 4 decimal places.

In fig. 5.16 we show the central deflection of the plate for the proposed method and the FE 2 mixed method alongside the reference solutions. We can see that the proposed method provides competitive results with the FE 2 mixed method.

In fig. 5.15 we show a contour plot of θ_{1h} with $\bar{t} = 0.001$. Smooth results are easily obtained with no post-processing required.

5.4 Conclusions

In this chapter we have proposed a method for the locking-free simulation of Reissner-Mindlin plates using a novel combination of maximum entropy basis functions and rotated Raviart-Thomas-Nédélec elements.

The use of maximum entropy basis functions has allowed simple and direct imposition of Dirichlet boundary conditions. This `weak' Kronecker-delta property is an inherent property of the maximum entropy approach, and we believe this affords significant advantages over the more commonly used moving-least-squares basis functions.

We comment that our approach has only required first-order consistency in the meshless

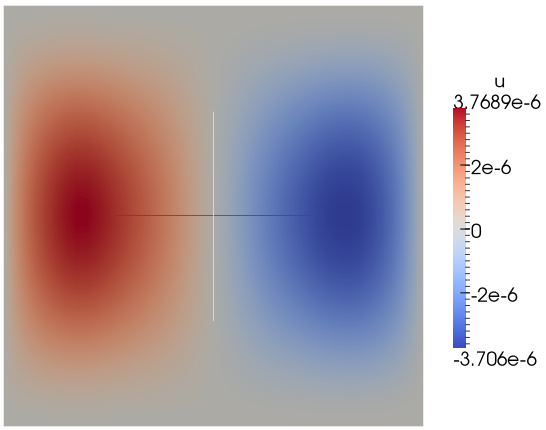

Figure 5.15: Plot of θ_{1h}, MaxEnt + *NED* mixed method 16×16 grid, clamped plate, $\bar{t} = 0.001$

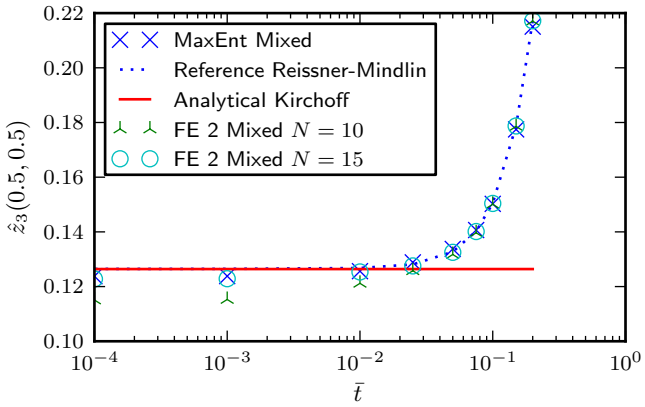

Figure 5.16: Graph showing normalised central deflection $z_3(0.5, 0.5)$ of CCCC square plate for varying $\bar{t}$. Maximum-entropy mixed: $N = 10$, $M = 16$, dofs $= 1088$. FE 2 mixed $N = 10$, dofs $= 2253$. FE 2 mixed $N = 15$, dofs $= 5323$.

basis functions, whereas approaches from other authors have typically required second-order or higher consistency. This reduces the support size of the basis functions and creates a stiffness matrix with lower bandwidth.

The approach of using a mixed variational form, although well established in the FEM, has not to our knowledge been used to solve the problem of shear-locking in the mesh-free plate literature. Through some simple test problems we have shown the efficacy of the proposed method which seems to be competitive with the quadratic FEM.

Although we have had to use an underlying mesh for the generation of a $H(\mathrm{rot}; \Omega_0)$ conforming field, we believe that this is a technological gap between meshless and FE that is already partially closed, thus opening up the possibility of making our method `truly' meshless. We support this assertion by referring to a paper by Buffa et al. [143] where $H(\mathrm{curl}, \Omega)$ conforming B-spline shape functions are constructed for the solution of isogeometric electro-magnetics problems.

Again, mimicking the approach used in many successful FE approaches such as the MITC family of elements, the elimination of the shear-strain field γ via some kind of projection or reduction operator (typically denoted Π_h or R_h respectively in the literature) may also be possible. We support this by referring to papers by Sukumar et al. and Ortiz et al. [75, 76] where, although not explicitly referred to as such, a form of projection operator is defined by volume-averaging the pressure field over elements attached to each node, eliminating the pressure field from the final stiffness matrix. We will explore this possibility in the following chapter.

6 Generalised displacement meshless methods for the shear-deformable plate problem

In this chapter we explore the use of a stabilised mixed weak form to construct a generalised displacement meshless method for the Reissner-Mindlin plate problem that is free from shear-locking.

Generalised displacement methods are a class of numerical methods including techniques such as MITC, $\bar{B}$, EAS and reduced integration which whilst being based upon an underlying mixed formulation are expressed in terms of the original problem unknowns only.

We use a stabilised mixed weak form originally introduced by Boffi and Lovadina, which is a more general version of an idea introduced by Arnold and Brezzi, where the bilinear form representing the shear energy is split using a parameter between a part calculated using only the displacement variables and a part calculated using the independent mixed shear variable. This modification has the effect of ensuring the mixed problem is coercive on the entire displacement space, and not just the kernel on which the Kirchhoff hypothesis holds.

The practical outcome of this modification is that a range of simpler and previously unavailable finite element and meshless designs suitable for the Stokes problem can be adapted for use with the Reissner-Mindlin problem. To help inform the design of our novel meshless method we examine some available designs in the finite element literature using the DOLFIN finite element framework. Two have continuous shear stresses, and two have discontinuous shear stresses. We examine the effect of the parameter α on the convergence of the method. We find that an optimal choice of α is closely related to the local discretisation size h.

To move from the stabilised mixed weak form back to a generalised mixed method where the problem is expressed in terms of displacement unknowns only we use a variation on the inf-sup stable volume averaged nodal pressure technique of Ortiz et al.. We interpret this technique as an L^2 projection operator from a high-order to a low-order space and thus it has close mathematical similarities to existing techniques. We provide a detailed al-

gorithmic and graphical overview of the procedure which was not presented in the original papers of Ortiz et al..

We then present standard benchmark problems which demonstrate the shear-locking free nature of the proposed method. We achieve convergence for the transverse displacement variable in the L^2 and H^1 norms and for the rotation variables in the L^2 norm, but not in the H^1 norm. Given the similarities between our approach and various successful finite element designs this is an unexpected result. We examine two potential causes of this problem; the selection of the parameter α, which must be related to the local discretisation size and the design and implementation of the projection operator. Even after reverting to the unprojected system the convergence problems in the rotation variables remain. This suggests that the choice of the parameter α is probably the issue. We then discuss some on-going work that may help alleviate this problem.

Note: The author of this thesis spent a two week period working with Dr. A. Ortiz at the Universidad de Chile in Santiago, Chile. Dr. A. Ortiz is one of the authors of the two papers on the volume averaged nodal pressure technique. The work undertaken with Dr. A. Ortiz relates to the application of the volume averaged nodal pressure technique to the problem of incompressible hyperelasticity. The work in this chapter on the Reissner-Mindlin plate problem is independent of this collaboration with Dr. A. Ortiz.

6.1 Introduction

In the previous chapter we demonstrated the effectiveness of using a mixed variational form to eliminate shear-locking in the Reissner-Mindlin plate problem. However, utilising the mixed variational formulation was not without cost, primarily that the number of degrees of freedom in the final system increased significantly.

Other issues also arise which are specific to our method. Because the rotated Raviart-Thomas-Nédélec elements require the use of the covariant transform between the reference element and an arbitrary element of the mesh, which is calculated from the derivatives of the element map, accuracy will decrease with heavily distorted element shapes which are typically found in large deformation problems. This problem is identical to the issues that occur in $H^1(\Omega)$ finite element methods. Ultimately, this may negate some (although not all) of the advantages of using a meshless basis for the displacement unknowns.

Another issue is that practitioners, particularly for structural mechanics applications, have been reluctant to implement and use mixed finite element methods. This is probably due to a

variety of factors; complexity of implementation and lack of available open-source codes may be some of the underlying reasons. However, schemes which are understood mathematically and designed using a mixed weak form but are only expressed in terms of the original displacement unknowns are widely used in practice. Methods of this type are often called generalised displacement methods [144].

Generalised displacement methods have three main advantages [50]; they are often easier to implement than the mixed method, they have similar or identical numbers of unknowns as in the original displacement problem, and finally the resulting linear system is typically symmetric positive definite, greatly easing the design of robust linear solvers. These advantages have led generalised displacement methods, such as enhanced assumed strains (EAS), assumed natural strains (ANS), mixed interpolation of tensorial components (MITC) and reduced integration, to becoming popular and widely used techniques in the computational structural mechanics community.

With this in mind it seems clear that the ideal meshless method for the Reissner-Mindlin problem would be a generalised displacement method. The method would be based upon a mixed weak form, inheriting the superior qualities of that approach such as being shear-locking free, and then some suitable procedure would be designed that eliminated the auxiliary unknowns relating to the shear stresses, leaving a linear system in the original displacement unknowns only. The method should use a basis for the shear stresses that does not require the use of an element map, thus retaining the advantageous properties of the meshless basis used for discretising the displacement unknowns.

The thinking behind the proposed generalised displacement meshless method for the Reissner-Mindlin plate problem is as follows. Ortiz et al. [75, 76] introduced a generalised displacement meshless method for the Stokes flow problem (or equivalently, the problem of nearly-incompressible elasticity) which works by volume-averaging the pressure across representative domains attached to each node defined by a triangulation, allowing the pressure to be written in terms of the displacement unknowns. The pressure is then eliminated from the problem, resulting in a generalised displacement method. The inf-sup condition is satisfied by the addition of extra degrees of freedom in the displacements, similar to the addition of bubble functions in the MINI finite element method. The resulting method is free from volumetric locking. Unfortuanately, when we apply the technique of Ortiz et al. directly to the Reissner-Mindlin problem the method completely fails to converge because it is unstable. This instability is caused by the violation of the kernel coercivity condition, a necessary condition for convergence and stability in any discretisation of the mixed Reissner-Mindlin problem.

The question then arises, is it possible to adapt the generalised displacement meshless method of Ortiz et al. so that it will work for the mixed Reissner-Mindlin problem? An answer lies in a small number of papers examining the adaptation of finite element designs for the Stokes problem to the Reissner-Mindlin problem. The key is recognising the mathematical difference between the Stokes problem and the Reissner-Mindlin problem within the framework of the penalised saddle point problem theory of Braess discussed in section 4.2.2. The difference is that the Stokes problem is coercive on the entire displacement space, rather than just the kernel as in the Reissner-Mindlin problem. The trick then lies in making the Reissner-Mindlin problem look more like the Stokes problem in a mathematical sense. This modification entails splitting the shear energy between a part calculated using the displacement unknowns and a part calculated using the mixed unknown using a parameter α. This modification ensures that the new Reissner-Mindlin problem is coercive on the entire displacement space, not just on the subspace on which the Kirchhoff hypothesis holds. This greatly opens up the design possibilities for stable numerical schemes.

We begin this chapter by deriving the stabilised mixed weak form from the original displacement form of the Reissner-Mindlin problem. We show that the stabilised form is essentially a blending of the advantageous properties of the displacement and the mixed weak form and that the stabilised form contains the displacement and mixed weak form as limiting cases.

Then to help inform the design of the novel meshless method we then examine some available designs suggested in the finite element literature using the DOLFIN finite element package. We present results for TRIA0220, which is based on the classic $CG_2 - DG_0$ Stokes element. We examine the effect of the parameter α on the convergence of each design. We find that an effective choice of α is closely related to the local discretisation size h.

Then we turn to the design of the proposed meshless method. No computational algorithm is given of the generalised displacement meshless method proposed in the papers of Ortiz et al. Therefore we give a full overview of the volume-averaging technique and perform some basic tests with comparison to the MINI element implemented in the DOLFIN finite element package to ensure our implementation of the procedure is correct.

We then fully develop the proposed discretisation for the Reissner-Mindlin problem using a modification of the volume-averaged pressure technique of Ortiz et al.. We call the technique the local patch projection operator, a more general term than volume-averaged pressure technique which we feel better reflects the general mathematical foundation this type of procedure is based upon.

Clearly a critical aspect of our formulation is the selection of the parameter α. For optimal

performance the parameter must be in someway related to the local discretisation size of the node set $\mathcal{N}_h$. We perform sensitivity studies to examine potential schemes for selecting α.

Whilst convergence is achieved for the transverse displacement variable z_3 in the L^2 and H^1 norms and for the rotation variable in the L^2 norms, we do not achieve convergence in the rotation variable in the H^1 norm. Because of the similarities between our approach and the stabilised MINI design this was an unexpected result. We postulate that the cause of this problem must either be to do with the selection of the parameter α or the underlying properties of the local patch projection operator. To try and narrow down the cause of the issue we perform studies with the unreduced system (ie. without the local patch projection operator). We find that the issue with convergence of the rotations in the H^1 norm still remains, suggesting that the choice of parameter α is probably the issue.

6.2 Formulation

6.2.1 Derivation of stabilised mixed weak form

In this section we will derive the stabilised mixed weak form directly from the displacement version of the Reissner-Mindlin problem. We will then explain why it is so much easier to design successful discretisations for this problem rather than for the standard mixed problem.

We begin with the following simplified form of the scaled Reissner-Mindlin plate problem:

$$a_b(\boldsymbol{\theta};\boldsymbol{\eta}) + \lambda\bar{t}^{-2}a_s(\boldsymbol{\theta}, z_3;\boldsymbol{\eta}, y_3) = g(y_3) \tag{6.1}$$

We then split the shear bilinear form $a_s(\boldsymbol{\theta}, z_3;\boldsymbol{\eta}, y_3)$ into two parts using a parameter $0 < \alpha < \bar{t}^{-2}$ [145]:

$$\begin{aligned} &a_b(\boldsymbol{\theta},\boldsymbol{\eta}) + \lambda a_s(\boldsymbol{\theta}, z_3;\boldsymbol{\eta}, y_3) \\ &= a_b(\boldsymbol{\theta},\boldsymbol{\eta}) + \lambda\alpha a_s(\boldsymbol{\theta}, z_3;\boldsymbol{\eta}, y_3) + \lambda(\bar{t}^{-2} - \alpha)a_s(\boldsymbol{\theta}, z_3;\boldsymbol{\eta}, y_3) \\ &= g(y_3) \end{aligned} \tag{6.2}$$

Now, instead of substituting the mixed shear stress variable $\boldsymbol{\gamma}$ into both parts of a_s, we substitute the following modified shear stress variable into the third term of eq. (6.2) only [146]:

$$\boldsymbol{\gamma} := \lambda(\bar{t}^{-2} - \alpha)(\nabla z_3 - \boldsymbol{\theta}) \tag{6.3}$$

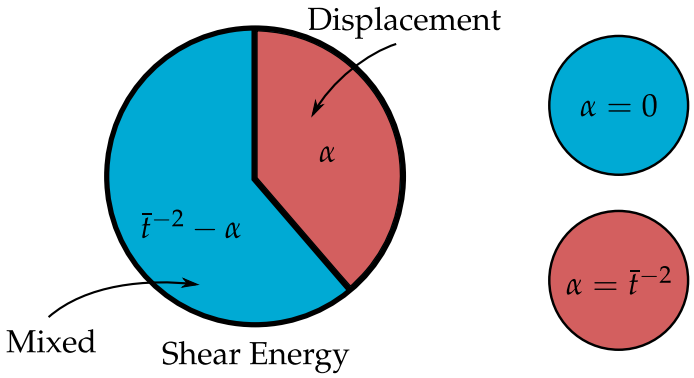

Figure 6.1: The entire shear energy contained in the shear bilinear form, represented by the entire circle, is split into two parts, one calculated from the mixed shear stress variable and one from the displacement variables. When the splitting parameter reaches the two limiting values the displacement formulation or the mixed formulation is recovered.

which gives:

$$a_b(\boldsymbol{\theta}, \boldsymbol{\eta}) + \lambda\alpha a_s(\boldsymbol{\theta}, z_3; \boldsymbol{\eta}, y_3) + (\boldsymbol{\gamma}, y_3 - \boldsymbol{\eta}) = g(y_3) \tag{6.4}$$

We then form a second equation by performing the standard Galerkin procedure using the shear stress test functions $\boldsymbol{\psi} \in S$ on eq. (6.3), resulting in the following new problem [146]:

Problem 16 (Stabilised mixed scaled Reissner-Mindlin problem)**.** *Find the transverse deflection, rotations and transverse shear stresses* $(z_3, \boldsymbol{\theta}, \boldsymbol{\gamma}) \in (\mathcal{V}_3, \mathcal{R}, S)$ *such that for all* $(y_3, \boldsymbol{\eta}, \boldsymbol{\psi}) \in (\mathcal{V}_3, \mathcal{R}, S)$*:*

$$a_b(\boldsymbol{\theta}, \boldsymbol{\eta}) + \lambda\alpha a_s(\boldsymbol{\theta}, z_3; \boldsymbol{\eta}, y_3) + (\boldsymbol{\gamma}, \nabla y_3 - \boldsymbol{\eta})_{L^2(\Omega_0)} = g(y_3) \tag{6.5a}$$

$$(\nabla z_3 - \boldsymbol{\theta}, \boldsymbol{\psi})_{L^2(\Omega_0)} - \frac{\bar{t}^2}{\lambda(1 - \alpha\bar{t}^2)}(\boldsymbol{\gamma}, \boldsymbol{\psi})_{L^2(\Omega_0)} = 0 \tag{6.5b}$$

We illustrate this shear splitting graphically in fig. 6.1.

The key difference in comparison with the standard mixed formulation eq. (5.9) in the framework of the general theory presented in section 4.2.2 is that the bilinear form a for our stabilised problem eq. (6.5):

$$a(z_3, \boldsymbol{\theta}; v_3, \boldsymbol{\eta}) := a_b(\boldsymbol{\theta}, \boldsymbol{\eta}) + \lambda\alpha a_s(\boldsymbol{\theta}, z_3; \boldsymbol{\eta}, y_3) \tag{6.6}$$

is now coercive on the *entire* space $\mathcal{X}$, not just on the subset of functions $\mathcal{Z}$ on which the Kirch-

hoff constraint holds. More specifically, in our new stabilised problem, there exists a constant[1] $\delta \geq 0$ such that:

$$a(v; v) := a_b(\boldsymbol{\theta}, \boldsymbol{\eta}) + \lambda\alpha a_s(\boldsymbol{\theta}, z_3; \boldsymbol{\eta}, y_3) \geq \delta \|v\|_{\mathcal{X}}^2 \quad \forall v \in \mathcal{X} \tag{6.7}$$

where $\mathcal{X} = \mathcal{V}_3 \times \mathcal{R} = H_0^1(\Omega) \times [H_0^1(\Omega)]^2$. This is in contrast with with the standard mixed formulation where there only exists a constant $\delta \geq 0$ such that:

$$a(v; v) := a_b(\boldsymbol{\theta}; \boldsymbol{\eta}) \geq \delta \|v\|_{\mathcal{X}}^2 \quad \forall v \in \mathcal{Z} \tag{6.8}$$

where:

$$\mathcal{Z} = \left\{ v \in \mathcal{X} \mid b(v; q) = a_s(z_3, \boldsymbol{\theta}; v_3, \boldsymbol{\eta}) = 0 \quad \forall q \in \mathcal{M} \right\} \tag{6.9}$$

is the kernel of the full space $\mathcal{X}$ on which the Kirchhoff hypothesis holds. Thus in the new stabilised Reissner-Mindlin problem eq. (6.5) part 1 of theorem 1 and theorem 3 are satisfied automatically. Thus we have a `good' problem on the condition that the inf-sup condition on b in part 2 of theorem 1 is satisfied. This is why the parameter α is referred to as a stabilisation parameter as its addition generates a mixed weak form that is stable for a far less restrictive set of conditions than for the original mixed problem.

We can express the above ideas in simpler terms; we know that the displacement form eq. (5.9) is prone to shear-locking but is always stable when discretised, whilst the standard mixed form is typically unstable when discretised, but behaves well as the small parameter $\bar{t}$ approaches zero. Therefore by splitting the shear energy between a part calculated using the standard mixed form and a part calculated using the standard displacement form, the advantageous properties of both the mixed form and the displacement form are blended together.

The new stabilised problem contains both the displacement form and the mixed form as special cases. By substituting $\alpha = \bar{t}^{-2}$ into the stabilised form eq. (6.5) we recover the original displacement form eq. (5.9). By substituting $\alpha = 0$ into the stabilised form eq. (6.5) we recover the fully mixed form previously derived in eq. (5.5).

A stabilised mixed weak form of this type was first introduced in the context of the Reissner-Mindlin plate problem by Arnold and Brezzi [146]. Their aim was to design some new simple and low-order elements for the Reissner-Mindlin problem. They introduced two element designs with discontinuous Lagrangian shear approximation of zero order $[DG_0]^2$ and two with

[1] We denote the coercivity constant δ here instead of the α suggested by Braess earlier in this thesis to avoid confusion with the stabilisation parameter α.

continuous Lagrangian shear approximation of first order $[CG_1]^2$. The developments in this paper are primarily mathematical, and thus no numerical results are presented, which explains why no actual stabilisation parameter is introduced; the parameter, which we refer to as α is implicitly set to be equal to one, which is sufficient to ensure the coercivity of the problem on the whole displacement space $\mathcal{X}$, but not the optimal performance of a numerical method.

It was in the later and more general papers by Boffi and Lovadina [145] and Lovadina [147] that recognised for the optimal performance of this stabilised mixed weak form it was important to have a stabilisation parameter α which was related to the local characteristic size of the mesh h_K. In fact, they found that a judicious choice of α will actually improve the rate of convergence. The paper of Boffi and Lovadina also recognised the similarity of the technique to the method of the augmented Lagrangian outlined in Fortin and Glowinski [148], a connection that was not made in the original paper of Arnold and Brezzi [146].

6.3 FE discretisation

In this section we will show an example discretisation of the stabilised mixed weak form using finite elements. The aim of this is to answer two questions; firstly, can the design of a stabilised finite element scheme help inform the design choices made in a novel meshless scheme, and secondly, are there any significant differences in behaviour between the finite element schemes and the meshless scheme?

As we are now talking about discretisations of the stabilised mixed weak form eq. (6.5) we introduce discrete spaces for the displacements $z_{3h} \in \mathcal{V}_{3h} \subset \mathcal{V}_3$, the rotations $\boldsymbol{\theta}_h \in \mathcal{R}_h \subset \mathcal{R}$, and the shear stresses $\boldsymbol{\gamma}_h \in S_h \subset S$ giving:

Problem 17 (Discrete stabilised mixed scaled Reissner-Mindlin problem)**.** *Find the transverse deflection, rotations and transverse shear stresses* $(z_{3h}, \boldsymbol{\theta}_h, \boldsymbol{\gamma}_h) \in (\mathcal{V}_{3h}, \mathcal{R}_h, S_h)$ *such that for all* $(y_3, \boldsymbol{\eta}, \boldsymbol{\psi}) \in (\mathcal{V}_{3h}, \mathcal{R}_h, S_h)$*:*

$$a_b(\boldsymbol{\theta}_h, \boldsymbol{\eta}) + \lambda\alpha a_s(\boldsymbol{\theta}_h, z_{3h}; \boldsymbol{\eta}, y_3) + (\boldsymbol{\gamma}_h, \nabla y_3 - \boldsymbol{\eta})_{L^2(\Omega_0)} = g(y_3) \tag{6.10a}$$

$$(\nabla z_{3h} - \boldsymbol{\theta}_h, \boldsymbol{\psi})_{L^2(\Omega_0)} - \frac{\bar{t}^2}{\lambda(1-\alpha\bar{t}^2)}(\boldsymbol{\gamma}_h, \boldsymbol{\psi})_{L^2(\Omega_0)} = 0 \tag{6.10b}$$

In fig. 6.2 we show four different finite element designs for the discrete stabilised mixed form of the Reissner-Mindlin problem in eq. (6.10). In this section we will concentrate on the element design TRIA0220. The element design studied in this section is closely related to the

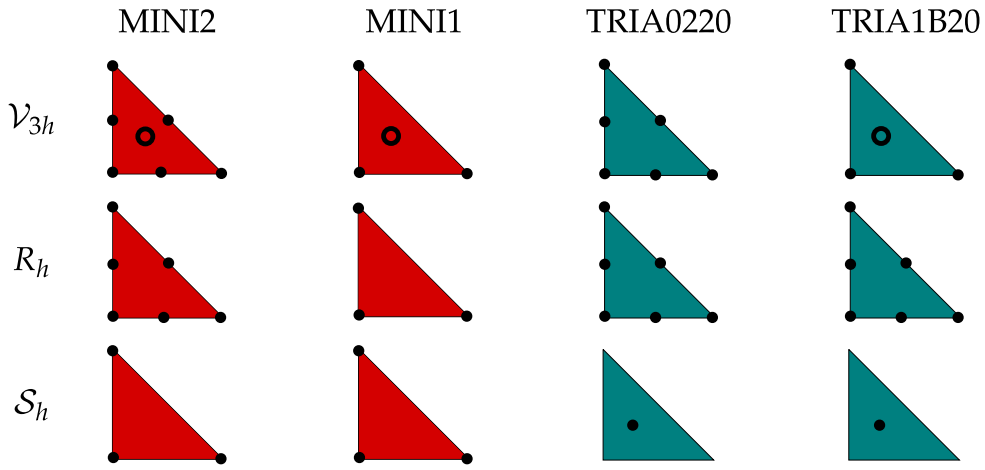

Figure 6.2: Various finite element designs available in the literature for the stabilised mixed weak form. MINI2 $(CG_2 \oplus B_3) \times [CG_2]^2 \times CG_1$ [146] and MINI1 $(CG_1 \oplus B_3) \times [CG_1]^2 \times CG_1$ [146] (red) have continuous shear stresses, whist TRIA0220 $CG_2 \times [CG_2]^2 \times DG_0$ [150] and TRIA1B20 $(CG_1 \oplus B_3) \times [CG_2]^2 \times DG_0$ [146] (green) have discontinuous stresses. The open circle represents a degree of freedom associated with the cubic bubble function space B_3 which vanishes on the element edge.

classic Stokes $[CG_2]^2$-DG_0 element, where displacements are approximated using second-order Lagrangian elements, and pressure is approximated using discontinuous zero-order Lagrangian elements. It is the `richness' of the displacement approximation space with respect to the pressure approximation space which ensures that the inf-sup condition is satisfied [149].

The TRIA0220 discretisation can be specified as follows [150]:

$$\mathcal{V}_{3h} := CG_2(\Omega_0; \mathcal{T}_h) = \left\{ y_3 \in H_0^1(\Omega_0) \mid y_3|_K \in P_2,\ \forall K \in \mathcal{T}_h \right\} \tag{6.11a}$$

$$\mathcal{R}_h := [CG_2(\Omega_0; \mathcal{T}_h)]^2 = \left\{ \boldsymbol{\eta} \in H_0^1(\Omega_0)^2 \mid \boldsymbol{\eta}|_K \in [P_2]^2,\ \forall K \in \mathcal{T}_h \right\} \tag{6.11b}$$

$$\mathcal{S}_h := [DG_0(\Omega_0; \mathcal{T}_h)]^2 = \left\{ \boldsymbol{\psi} \in L^2(\Omega_0)^2 \mid \boldsymbol{\psi}|_K \in [P_0]^2,\ \forall K \in \mathcal{T}_h \right\} \tag{6.11c}$$

In the context of Reissner-Mindlin plates and the discrete stabilised mixed weak form in eq. (6.10) the element design TRIA0220 was first suggested by Lovadina [147]. With the stabilisation parameter $\alpha = 1$, Lovadina [147] showed analytically that the method is first-order convergent in the H^1 norm for both displacement z_{3h} and rotation $\boldsymbol{\theta}_h$ variables. This is actually sub-optimal given that the space $\mathcal{V}_{3h}$ consists of quadratic functions which normally give second-order convergence in the H^1 norm, and is related to the imbalance in approximation quality between the approximation spaces $\mathcal{V}_{3h}$ and $\mathcal{S}_h$ inherited from the classical Stokes P_2-P_0 element. Interest-

ingly however, Lovadina [147] showed analytically that by making the factor α dependent on the characteristic local mesh size h_K and by setting $\alpha \sim O(h_K^{-1})$ that the order of convergence can be increased to 3/2. In an extended numerical analysis of the method, Chinosi and Lovadina [150] demonstrate that the element design actually works best for α varying as $\alpha \sim O(h_K^{-2})$ which is the dimensionally consistent choice. Clearly a `good' choice of α, which will be in some way based on the characteristic local size of the discretisation, is necessary to ensure the optimal performance of the method, although as we will see there is a reasonable amount of leeway in selecting such a value.

We have implemented TRIA0220 (and all the other element designs shown in fig. 6.2) into the DOLFIN finite element framework [127]. In algorithm 3 we show a code snippet specifying the function spaces defined in eq. (6.11), and in algorithm 5 we show a code snippet specifying the weak form in eq. (6.10). Because of the unified form language (UFL) and just-in-time compilation techniques built into the DOLFIN finite element framework changing to a different element design, such as the MINI1 element shown in fig. 6.2, is just a matter of changing the definition of the function spaces in the Python code, as shown in algorithm 4.

Algorithm 3 Python code snippet for specifying finite element function spaces for TRIA0220 element in DOLFIN

```
...
def TRIA0220(mesh):
    DG0 = FunctionSpace(mesh, "DG", 0)
    CG2 = FunctionSpace(mesh, "Lagrange", 2)

    S = MixedFunctionSpace([DG0, DG0])
    V_3 = CG2
    R = MixedFunctionSpace([CG2, CG2])

    ...
    return (V_3, R, S)
...
V_3, R, S = TRIA0220(mesh)
U = MixedFunctionSpace([V_3, R, S])
```

In fig. 6.3 we begin by examining the effect of varying the stabilisation parameter α on the convergence of the variables in various norms for a fixed disretisation and plate thickness. We reiterate the effect α has on the underlying discrete weak form; as $\alpha \to 0$ (left hand side of fig. 6.3) we tend towards the original mixed weak form eq. (5.9), which violates the kernel coercivity condition. Conversely, as $\alpha \to \bar{t}^{-2}$ (right hand side of fig. 6.3) we recover the standard displacement weak form eq. (5.5) which locks. Broadly speaking we can see that an optimal value of α lies somewhere between these two extreme points. We remark that the convergence

Algorithm 4 Python code snippet for specifying finite element function spaces for MINI1 element in DOLFIN

```
...
def MINI1(mesh):
    CG1 = FunctionSpace(mesh, "Lagrange", 2)
    B3 = FunctionSpace(mesh, "Bubble", 3)

    S = MixedFunctionSpace([CG1, CG1])
    V_3 = CG1 + B3
    R = MixedFunctionSpace([CG1, CG1])

    ...
    return (V_3, R, S)
...
V_3, R, S = MINI1(mesh)
U = MixedFunctionSpace([V_3, R, S])
```

Algorithm 5 Python code snippet for specifying stabilised mixed weak form in DOLFIN

```
z_3, theta, gamma = TrialFunctions(U)
y_3, eta, psi = TestFunctions(U)
...
E = 10920.0
kappa = 5.0/6.0
nu = 0.3
thickness = 0.001

D_c = E/(12.0*(1.0-nu**2))
G_c = E*kappa/(2.0*(1.0 + nu))

D = Constant(D_c)
# The variable G is the shear modulus \lambda
G = Constant(G_c)
t = Constant(thickness)
nu = Constant(nu)

h = CellSize(mesh)
alpha = h**-2.0

# Note: lambda is a python keyword, not a material parameter!
e = lambda u: 0.5*(grad(u) + grad(u).T)
L = lambda epsilon: D*((1.0 - nu)*epsilon + nu*tr(epsilon)*Identity(2))

a_b = D*inner(L(e(theta)), e(eta))*dx
a_s = G*alpha*inner(grad(z_3) - theta, grad(y_3) - eta)*dx

A = a_b + a_s + inner(gamma, grad(y_3) - eta)*dx + \
    inner(grad(z_3) - theta, psi)*dx + \
    - t**2.0/(G*(1.0 - alpha*t**2.0))*inner(gamma, psi)*dx
l = y_3*dx
...
```

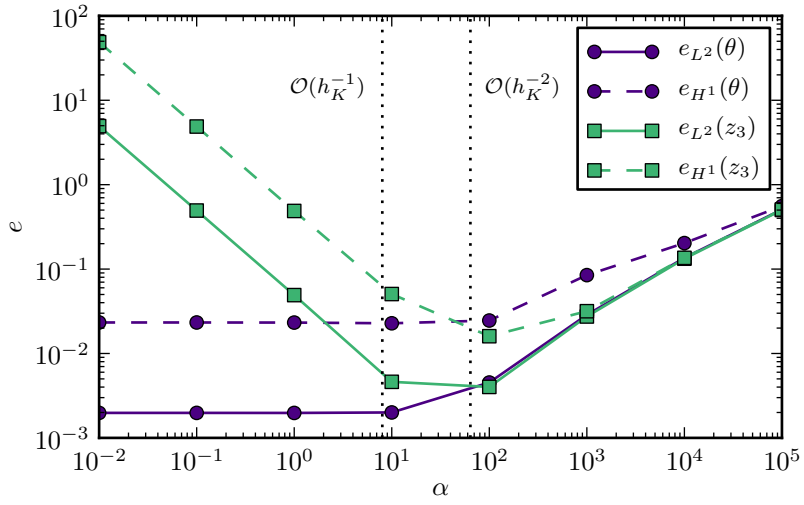

Figure 6.3: Graph showing convergence for transverse displacement and rotation variables for varying values of α. TRIA0220 element $h_K = 1/8$ on a uniform mesh. Square Domain with SSSS boundary conditions, $E = 10920$, $\nu = 0.3$, $\bar{t} = 10^{-3}$. The vertical dotted lines denote the choices $\alpha \sim \left\{O(h_K^{-1}), O(h_K^{-2})\right\}$ suggested by Chinosi and Lovadina [150].

for the rotation variable $\boldsymbol{\theta}$ is relatively insensitive to the choice of the parameter α. The choice for the transverse displacement is clearly more critical with an acceptable convergence occuring in the range $10^0 < \alpha < 10^3$ and the best convergence in the range $10^1 < \alpha < 10^2$. This range is bounded nicely by the choices $\alpha \sim \left\{O(h_K^{-1}), O(h_K^{-2})\right\}$ suggested by Chinosi and Lovadina [150] which are shown with vertical dotted lines.

We now examine how the convergence is affected for varying thickness $\bar{t}$. Clearly the ideal method would perform reasonably consistently for thick through to very thin plates. In fig. 6.4 we show convergence for varying thickness $\bar{t}$, whilst keeping α constant. We can see for thin plates $10^{-4} < \bar{t} < 10^{-1}$ that performance in the z_3 variable is essentially constant, but deteriorates slightly when the plate becomes thick $\bar{t} > 10^{-1}$. We have marked the point where $\bar{t} = h_K$, that is, the point where the plate thickness is equal to the characteristic element size. Clearly at such a point the employment of a mixed method to avoid shear-locking is unnecessary. With this in mind we employ the following modification to the parameter α which effectively turns

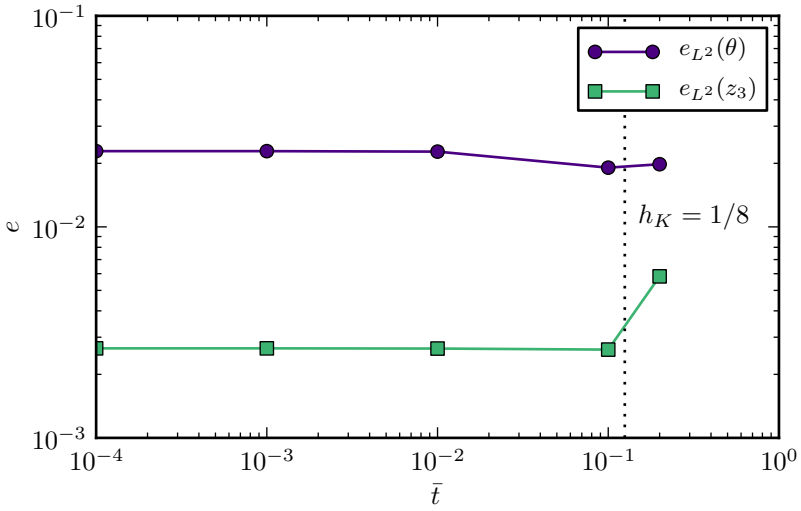

Figure 6.4: Graph showing convergence for transverse displacement and rotation variables for varying thickness $\bar{t}$ with constant $\alpha = h_K^{-2} = 64$. Note that there is a slight decrease in performance as the plate becomes thick with respect to the characteristic mesh size h_K. TRIA0220 element $h_K = 1/8$ on a uniform mesh. Square Domain with SSSS boundary conditions, $E = 10920$, $\nu = 0.3$, $\bar{t} = 10^{-3}$.

off the mixed formulation when $\bar{t} > h_K$:

$$\alpha \sim O(h_{\bar{t}}^{-2}) \tag{6.12a}$$

$$h_{\bar{t}} = \max(\bar{t}, h_K) \tag{6.12b}$$

With this modification made we repeat exactly the same experiment but with the modified form of $h_{\bar{t}}$. The results shown in fig. 6.5 suggest that the modification has been effective in suppressing the deterioration in performance for $\bar{t} > h_K$, and in fact we see slightly improved performance for $\bar{t} > h_K$.

We now examine convergence for different recipes of α. To do this we generate convergence results using the following choices for α for increasingly fine meshes:

$$\alpha = \left\{ O(h_{\bar{t}}^{-1}),\ O(h_{\bar{t}}^{-3/2}),\ O(h_{\bar{t}}^{-2}) \right\} \tag{6.13}$$

In figs. 6.6 and 6.7 we show the convergence of the transverse displacement in the L^2 and H^1 norms respectively for varying choices of the stabilisation parameter α. Convergence rates are

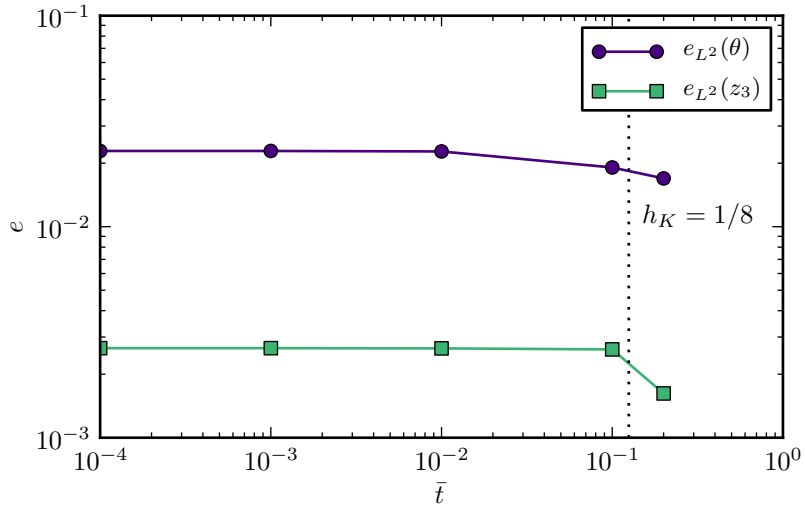

Figure 6.5: Graph showing convergence for transverse displacement and rotation variables for varying thickness $\bar{t}$ with modified variable $\alpha = h_{\bar{t}}^{-2}$. The use of the modified form of $h_{\bar{t}}$ results in a method which performs slightly *better* for thick plates. TRIA0220 element $h_K = 1/8$ on a uniform mesh. Square domain with SSSS boundary conditions, $E = 10920$, $\nu = 0.3$, $\bar{t} = 10^{-3}$.

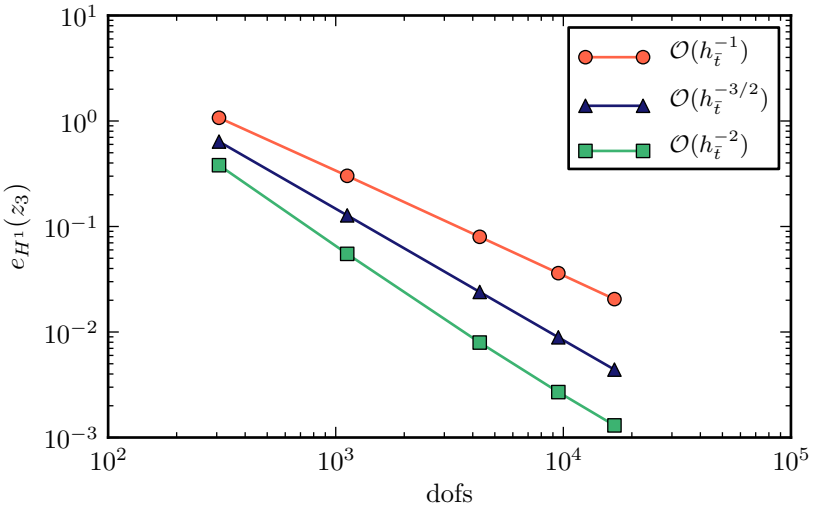

Figure 6.6: Graph showing convergence of transverse displacements in H^1 norm for varying α choices. Square domain with SSSS boundary conditions, $E = 10920$, $\nu = 0.3$, $\bar{t} = 10^{-3}$.

Table 6.1: Convergence rates for series in figs. 6.6 and 6.7. Calculated from first-order fit to curves.

α	ρ_{L^2}	ρ_{H^1}
$O(h_{\bar{t}}^{-1})$	-1.494	-1.000
$O(h_{\bar{t}}^{-3/2})$	-1.757	-1.256
$O(h_{\bar{t}}^{-2})$	-1.993	-1.379

given in table 6.1. We note that it is clearly possible to improve the convergence rate of the TRIA0220 element by judicious choice of the parameter α. The results for θ (not shown) are less sensitive to the choice of α, reinforcing the results in fig. 6.3.

We draw the following conclusions from this numerical experiment performed with the TRIA0220 element:

1. If α is too small, that is, if the coercivity of the discrete bilinear form is lost, then the convergence of z_3 deteriorates whilst θ is unaffected.

2. If α is too large, then the formulation suffers from the shear-locking effect, and the convergence of both z_3 and θ deteriorates.

3. Convergence is acheived over a sufficiently large range of α to suggest that there is a decent chance of designing a method that performs well

4. For optimal convergence, the parameter α must in some way be based upon the local discretisation size. At least for the TRIA0220 element, the choice $\alpha \sim O(h^{-2})$, which is the dimensionally consistent choice, appears to be optimal.

We will come back to these four conclusions when examining the performance of the proposed meshless method later in this chapter.

6.4 Techniques for developing generalised displacement methods

Before continuing to develop the proposed meshless method, we take a look at various ways of developing a generalised meshless displacement method, with particular emphasis on the

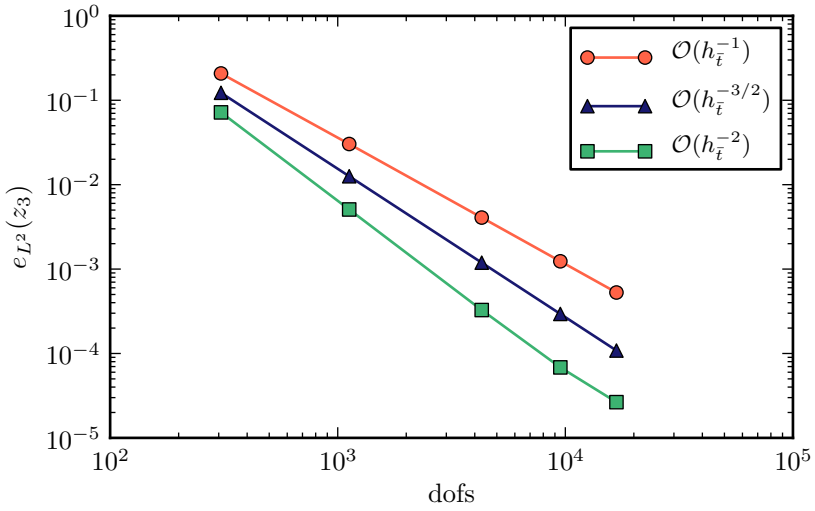

Figure 6.7: Graph showing convergence of transverse displacements in L^2 norm for varying α choices. Square domain with SSSS boundary conditions, $E = 10920$, $\nu = 0.3$, $\bar{t} = 10^{-3}$.

mathematics and implementation of the volume-averaged pressure technique of Ortiz et. al [75, 76].

For simplicity, we will use the nearly-incompressible elasticity problem, which is similar in nature to the Stokes' problem, which is in turn similar to the stabilised Reissner-Mindlin problem developed in this chapter. The discrete mixed nearly-incompressible elasticity problem with homogeneous Dirichlet boundary conditions can be stated as follows [151]:

Problem 18 (Discrete mixed nearly-incompressible elasticity problem)**.** *Given a domain $\Omega \subset \mathbb{R}^n$ containing a nearly-incompressible elastic body find the displacements and pressure $(\boldsymbol{u}_h, p_h) \in \mathcal{U}_h \times \mathcal{P}_h \subset [H_0^1(\Omega)]^2 \times L^2(\Omega)/\mathbb{R}$ such that:*

$$\mu \int_\Omega \boldsymbol{\varepsilon}(\boldsymbol{u}_h) \cdot \boldsymbol{\varepsilon}(\boldsymbol{v}) \, d\Omega + \int_\Omega p_h \operatorname{div} \boldsymbol{v} \, d\Omega = \int_\Omega \boldsymbol{f} \cdot \boldsymbol{v} \, d\Omega \qquad \forall \boldsymbol{v} \in \mathcal{U}_h \tag{6.14a}$$

$$\int_\Omega \operatorname{div} \boldsymbol{u}_h \, q \, d\Omega - \frac{1}{\lambda_e} \int_\Omega p_h q \, d\Omega = 0 \qquad \forall q \in \mathcal{P}_h \tag{6.14b}$$

where μ and λ_e are Lame's first and second constants and $\boldsymbol{\varepsilon}(\boldsymbol{v})$ is the usual small strain operator. $L^2(\Omega)/\mathbb{R}$ is the space of square-integrable functions which differ up to a constant.

This problem fits in to the penalised saddle point problem framework of Braess eq. (4.8),

with the following choices:

$$\mathcal{X} := \mathcal{U} := H_0^1(\Omega)^2, \qquad a(\boldsymbol{u}, \boldsymbol{v}) := \mu \int_\Omega \boldsymbol{\varepsilon}(\boldsymbol{u}) \cdot \boldsymbol{\varepsilon}(\boldsymbol{v}) \, d\Omega \tag{6.15a}$$

$$\mathcal{M} := \mathcal{P} := L^2(\Omega)/\mathbb{R}, \qquad b(\boldsymbol{v}, q) := \int_\Omega \operatorname{div} \boldsymbol{v} \, q \, d\Omega \tag{6.15b}$$

$$\mathcal{M}_c := L^2(\Omega)/\mathbb{R}, \qquad c(p, q) := \int_\Omega pq \, d\Omega \tag{6.15c}$$

and with the small parameter $t^2 = 1/\lambda_e$. Recall that the Lame's second parameter λ_e is defined for an isotropic material in terms of the Young's modulus E and Poisson's ratio ν as:

$$\lambda_e = \frac{\nu E}{(1+\nu)(1-2\nu)} \tag{6.16}$$

so when the body under consideration is nearly incompressible with $\nu \to 0.5$ then the small parameter will vanish $t = 1/\lambda_e \to 0$, resulting in a well-defined problem. When $1/\lambda_e = 0$ the pressure variable acts as Lagrange multipliers which enforce the incompressibility constraint.

In very general terms, without making any specific choices, the development of a generalised displacement method can be expressed mathematically as follows. We first ensure that we have chosen a $\mathcal{U}_h$ and $\mathcal{P}_h$ which satisfy the inf-sup condition. We do not need to worry about the kernel coercivity condition here because the form $a(\boldsymbol{u}, \boldsymbol{v})$ is coercive on the entire space $\mathcal{X}$, not just the kernel $\mathcal{Z}$. We then rearrange eq. (6.14b) to find p_h in terms of the displacement variable $\boldsymbol{u}_h$:

$$p_h = \lambda_e \, \Pi_h(\operatorname{div} \boldsymbol{u}_h) \tag{6.17}$$

where Π_h is a projection operator from the discrete displacement space $\mathcal{U}_h$ to the discrete pressure space $\mathcal{P}_h$:

$$\Pi_h : \mathcal{U}_h \to \mathcal{P}_h \tag{6.18}$$

Then we simply substitute our new expression for p_h back into eq. (6.14a) resulting in the following expression in terms of the original unknowns only:

$$\mu \int_\Omega \boldsymbol{\varepsilon}(\boldsymbol{u}_h) \cdot \boldsymbol{\varepsilon}(\boldsymbol{v}) \, d\Omega + \int_\Omega \Pi_h(\operatorname{div} \boldsymbol{u}_h) \operatorname{div} \boldsymbol{v} \, d\Omega = \int_\Omega \boldsymbol{f} \cdot \boldsymbol{v} \, d\Omega \quad \forall \boldsymbol{v} \in \mathcal{U}_h \tag{6.19}$$

The link between the mixed method and the generalised displacement method should now be clear; in the generalised displacement method the mixed variable (in this case, the pressure) is assumed implicitly via the projection operator Π_h, whereas in the mixed method the

mixed variable is included in the formulation explicitly. The reduction operator Π_h is a discrete modification of the usual problem variable $\boldsymbol{u}_h$, such that the generalised displacement method inherits the advantageous properties of the underlying mixed method, which most importantly in our case is the robustness with respect to the small parameter λ_e.

Of course, we haven't actually discussed how the projection operator can be implemented. It turns out that many methods can be used to construct the operation Π_h. In the following sections we will discuss some of these methods with particular regards to their applicability in meshless methods.

6.4.1 Static condensation

Static condensation, or more specifically the Schur Complement, is a projection at the linear algebra level, that is, working with the assembled matrices. The problem shown in eq. (6.14) results in a linear system with the following block matrix form:

$$\begin{bmatrix} \boldsymbol{A} & \boldsymbol{B} \\ \boldsymbol{B}^T & -\boldsymbol{C} \end{bmatrix} \begin{Bmatrix} \boldsymbol{u} \\ \boldsymbol{p} \end{Bmatrix} = \begin{Bmatrix} \boldsymbol{f} \\ \boldsymbol{0} \end{Bmatrix} \tag{6.20}$$

where the matrix $\boldsymbol{A}$, $\boldsymbol{B}$ and $\boldsymbol{C}$ are the matrices associated with the bilinear forms $a(\boldsymbol{u}_h, \boldsymbol{v})$, $b(\boldsymbol{u}_h, q)$ and $c(p_h, q)$ respectively. $\boldsymbol{f}$ is the vector associated with the operator $\langle f, v \rangle$ and the vectors $\boldsymbol{u}$ and $\boldsymbol{p}$ are the vectors of unknowns for the displacements and pressures respectively.

We can then re-write eq. (6.20) as two equations:

$$\boldsymbol{A}\boldsymbol{u} + \boldsymbol{B}\boldsymbol{p} = \boldsymbol{f} \tag{6.21a}$$

$$\boldsymbol{B}^T\boldsymbol{u} - \boldsymbol{C}\boldsymbol{p} = \boldsymbol{0} \tag{6.21b}$$

Solving eq. (6.21b) for $\boldsymbol{p}$ gives:

$$\boldsymbol{p} = \boldsymbol{C}^{-1}\boldsymbol{B}^T\boldsymbol{u} \tag{6.22}$$

Comparing eq. (6.22) to eq. (6.17) we can see that the expression $\boldsymbol{C}^{-1}\boldsymbol{B}^T$ is equivalent to the projection operator Π_h. We can then substitute eq. (6.22) back into eq. (6.21a) giving:

$$(\boldsymbol{A} + \boldsymbol{B}\boldsymbol{C}^{-1}\boldsymbol{B}^T)\boldsymbol{u} = \boldsymbol{f} \tag{6.23}$$

The matrix $\boldsymbol{B}\boldsymbol{C}^{-1}\boldsymbol{B}^T$ is called the Schur complement.

Because the above process requires the inversion of $\boldsymbol{C}$, the structure of the matrix $\boldsymbol{C}$ is critical in determining whether the static condensation procedure is practical. If $\boldsymbol{C}$ is a general sparse matrix then the inverse $\boldsymbol{C}^{-1}$ is in general *not* sparse. Recall that the matrix $\boldsymbol{C}$ is associated with the bilinear form $c(p_h, q)$:

$$c(p_h, q) := \int_\Omega p_h q \, d\Omega \tag{6.24}$$

If we construct pressure space using discontinuous Lagrangian elements $\mathcal{P}_h \subset L^2 = DG_p$ for any polynomial order p then degrees of freedom in each element are decoupled. The integration across the entire domain in eq. (6.24) then decouples into integration across element domains Ω_K:

$$c(p_h, q) := \sum_K \int_{\Omega_K} p_h q \, d\Omega \tag{6.25}$$

Each summation term in eq. (6.25) is then associated with a dense matrix $\boldsymbol{C}_K$ which results in a matrix $\boldsymbol{C}$ with the following block diagonal form:

$$\boldsymbol{C} = \begin{bmatrix} \boldsymbol{C}_1 & & & \\ & \boldsymbol{C}_2 & & \\ & & \ddots & \\ & & & \boldsymbol{C}_K \end{bmatrix} \tag{6.26}$$

The matrix $\boldsymbol{C}$ will be either diagonal for DG_0 or block diagonal for DG_p with $p \geq 1$. If the matrix $\boldsymbol{C}$ is in diagonal or block-diagonal form then the inverse $\boldsymbol{C}^{-1}$ will also be block-diagonal or diagonal and the inverse can be calculated by individually inverting each block:

$$\boldsymbol{C}^{-1} = \begin{bmatrix} \boldsymbol{C}_1^{-1} & & & \\ & \boldsymbol{C}_2^{-1} & & \\ & & \ddots & \\ & & & \boldsymbol{C}_K^{-1} \end{bmatrix} \tag{6.27}$$

With this block-diagonal form of $\boldsymbol{C}$ the static condensation procedure can be performed with minimal use of memory due to the preserved sparsity pattern and low computation time due to the cheap blockwise inversion procedure. In fig. 6.8 we show the sparsity pattern of the mixed stabilised Reissner-Mindlin system using the TRIA0220 element assembled on a two element square mesh. This procedure was implemented at the linear algebra level into the DOLFIN finite element framework using the CBC.Block package [152].

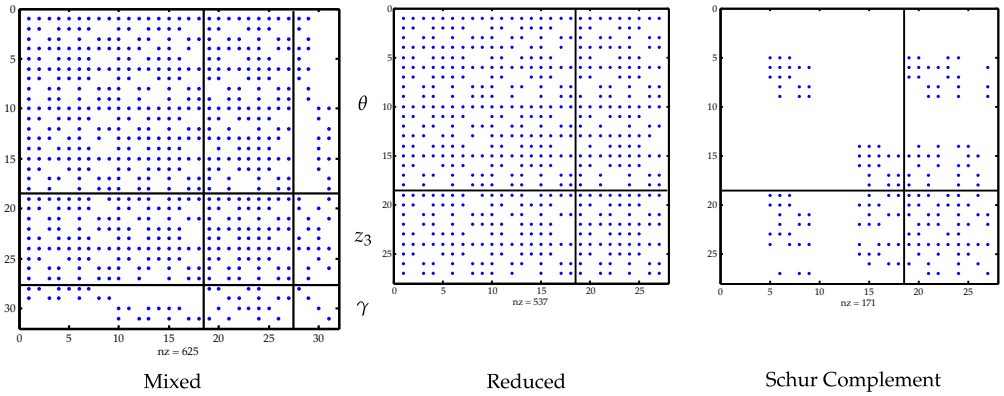

Figure 6.8: Sparsity pattern of mixed stabilised Reissner-Mindlin system, reduced system and the Schur complement, using TRIA0220 element on a two element square mesh. Note the diagonal nature of the matrix $\boldsymbol{C}$ and that the sparsity pattern of the displacement degrees of freedom is unchanged by the addition of the Schur complement.

With regards to the implementation of a generalised displacement meshless method using the static condensation procedure, the high-continuity of meshless methods means that in general we would have $\mathcal{P}_h \subset H^1(\Omega)$. Therefore the matrix $\boldsymbol{C}$ associated with the bilinear form $c(p_h, q)$ will not be in block-diagonal or diagonal form, making the inversion procedure prohibitively expensive.

6.4.2 Reduced integration

One of the earliest remedies for the problem of volumetric locking was the reduced integration method. Reduced integration is the use of a quadrature rule for the integration of the weak form of lower accuracy than required to integrate the weak form exactly. The procedure was an effective remedy for the problem of shear locking, but theoretical understanding of exactly why it worked was missing for a long time. It was considered a `trick' by many. Later, Malkus and Hughes [153] showed that in some cases the use of a reduced integration method corresponds to an implicit choice of a mixed scheme, and therefore reduced integration methods can be analysed using the mathematical framework of mixed schemes. A modern presentation of these results is given in Boffi et al. [151]. It should be noted that there is *not* a reduced integration procedure that corresponds to every mixed scheme, especially when considering meshes containing arbitrarily shaped elements [151].

6.4.3 Reduction operator

We have already discussed the use of a reduction operator in the context of the MITC element in section 5.2.4.

6.4.4 Nodal integration

Beissel and Belytschko [67] introduced the nodal integration method for the element-free Galerkin method. In nodal integration methods the bilinear form is integrated by placing integration points at the nodes only, rather than using full Gauss quadrature. In this aspect nodal integration methods are very much in the spirit of the reduced integration methods discussed in section 6.4.2. However, because of the vanishing derivatives of the basis functions at the nodal points nodal integration methods typically suffer from spurious modes. Beissel and Belytschko [67] solved this problem by adding a residual of the equilibrium equation to the bilinear form representing the mechanical energy to stabilise the method.

In a later paper J.S. Chen et al. [154] introduced the stabilised conforming nodal integration method (SCNI). In this method the spurious modes associated with the vanishing derivatives of the basis functions are stabilised by pushing the integration from the nodal positions to the local boundary using the divergence theorem. There is no longer any need to evaluate the basis functions at the nodal points, which eliminates the issue found in the method of Beissel and Belytschko [67]. The local boundary is defined by the Voronoi diagram, which is the dual of the Delaunay tessellation or mesh [154]. Each Voronoi cell defines a single smoothing domain for each node in the discretisation.

Wang and Chen [68] applied the SCNI technique to the Reissner-Mindlin problem. A single smoothing cell is used to calculate the integral in the bending bilinear form only, in the same manner as the original SCNI paper of Chen et al. [154]. The shear bilinear form is integrated using a standard nodal integration procedure in the style of the original paper of Beissel and Belytschko [67]. Although the distinction is not made clear in the paper of Wang and Chen [68], it is our view that the shear-locking problem is eliminated in this paper because of the nodal integration applied to the shear bilinear form, rather than the SCNI procedure applied to the bending bilinear form. Therefore with regards to solving the shear-locking problem the formulation of Wang and Chen [68] is very similar to a reduced integration procedure.

In a later work G. R. Liu et al. [155] considered how to apply the SCNI method to the finite element method. The resulting method is called the smoothed finite element method (SFEM). The key advance made in the SFEM [155] is that instead of there being a single smoothing cell

associated with each node, each cell in the mesh can be divided up into any number of smoothing cells. The integral within the volume of each smoothing cell is pushed to the boundary of the cell using the divergence theorem, in a similar fashion to the SCNI method. By varying the number of smoothing cells the fundamental properties of the SFEM change. When the number of smoothing cells is equal to one the element is under-integrated and suffers from spurious modes. The authors found the best results when using four smoothing cells.

The link between the SFEM (and by analogy, the SCNI method) and a mixed method was shown analytically by G.R. Liu et al. [156] by considering a three-field Hu-Washizu energy functional, which can be expressed as a mixed weak form. It is shown in [156] that when using one smoothing cell on a parallelogram element the element stiffness matrix generated by the SFEM is identical to that produced by the reduced integration procedure in the standard FEM. When an infinite number of smoothing cells are used the element stiffness matrix generated by the SFEM is identical to that produced using a full integration procedure in the standard FEM [156]. Intermediate numbers of smoothing cells sit in between these two extreme points [156].

Therefore there is a strong mathematical link between the SFEM, the use of a mixed variational formulation and the classical reduced integration procedure, so the SFEM and SCNI methods can certainly be classed as generalised displacement methods.

The ability of the SFEM to alleviate volumetric locking was explored in papers by T. T. Nguyen et al. [157] and N. Hung [158]. Both papers rely upon the SFEMs coincidence with the reduced integration method to produce SFEM schemes that are free from volumetric locking. Classical nodal integration techniques have been applied to the problem of incompressible locking in the FEM by Krysl and Zhu [159].

Bordas et al. considered a SFEM design for the Reissner-Mindlin problem in [160]. In this paper the smoothing cells are used to calculate the integral in the bending bilinear form only, similarly to the work of Wang and Chen [68] but using a varying number of smoothing cells as in [155]. The shear-locking problem is eliminated by applying the same reduction operator used in the quadrilateral MITC4 element. No smoothing is used on the shear bilinear form. Therefore with regards to solving the shear-locking problem the formulation of Bordas et al. is identical to the MITC4 element of Bathe and Dvorkin [161].

6.4.5 Volume-averaged nodal pressure technique

The volume-averaged nodal pressure technique was introduced by Ortiz et. al for two-dimensional incompressible elasticity problems in [75] and extended to three-dimensional incompressible

elasticity problems in [76]. In this paper we refer to the more general implementation of the volume-averaged nodal pressure technique in the Reissner-Mindlin problem as the local patch projection (LPP) method.

The volume-averaged nodal pressure technique works by volume-averaging the pressure across representative domains attached to each node. The representative domains are defined by a triangulation of the nodes. This allows the pressure to be written in terms of the displacement unknowns. The pressure can then be eliminated from the mixed problem, resulting in a generalised displacement method.

The volume-averaged nodal pressure procedure has similarities with both nodal integration methods and static condensation, but differs considerably in mathematical development and implementation from both. The generalised displacement method that results is derived directly from the mixed weak form of the problem in a straightforward manner. Therefore the link between the generalised displacement method and the underlying mixed method is immediately clear, unlike in reduced integration or nodal integration type procedures.

Representative nodal volumes are derived directly from the Delaunay triangulation of the nodal domain, meaning that there is no need to implement data structures to handle the Voronoi diagram as in the SCNI method of Chen et. al [154].

The inf-sup condition is satisfied by the addition of extra bubble degrees of freedom at the barycenters of the Delaunay triangulation of the nodal domain. Furthermore, the method has been shown to be numerically inf-sup stable using the procedure proposed by Chapelle and Bathe [162]. No analytical proof of inf-sup stability is currently available.

Because we will use an extension of this method in our development of a generalised displacement meshless method for the Reissner-Mindlin plate model, in conjunction with the stabilised weak form outlined in section 6.2.1, we will detail the mathematical development and computational implementation here. The presentation here differs from that in the original papers of Ortiz et al. [75, 76] which in particular lack a detailed description of the computational implementation of the procedure.

Mathematical overview

We begin with the discrete mixed nearly-incompressible elasticity problem in eq. (6.14). First of all an initial node set is specified on the domain Ω which we denote $\mathcal{N}_h^s$. Then a triangulation $\mathcal{T}_h$ of the node set $\mathcal{N}_h^s$ is generated using any suitable mesh generation method. The position of vertices of the triangulation $\mathcal{T}_h$ are therefore coincident with the node positions of the nodes

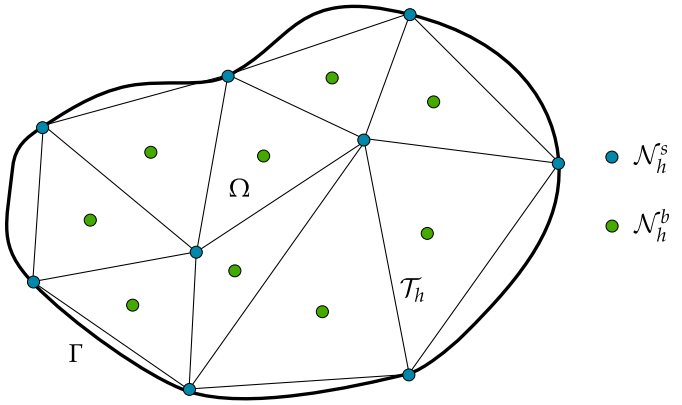

Figure 6.9: Illustration showing node set $\mathcal{N}_h$ and triangulation $\mathcal{T}_h$ on a domain Ω with boundary Γ. The nodes in the initial node set $\mathcal{N}_h^s$ are shown with blue circles. The vertices of the triangulation $\mathcal{T}_h$ are coincident with these nodes. The extra node set $\mathcal{N}_h^b$ are inserted at the barycenters of cells of the triangulation and are shown with green circles. The total node set $\mathcal{N}_h$ is the union of the initial node set $\mathcal{N}_h^s$ and the barycenter nodes $\mathcal{N}_h^b$.

in the node set $\mathcal{N}_h^s$. Based on the constructed triangulation $\mathcal{T}_h$ we then define an additional set of nodes $\mathcal{N}_h^b$ which are located at the barycenter of each cell in the triangulation $\mathcal{T}_h$. Using this new node set we define the final node set $\mathcal{N}_h$ for the problem as the union of the original node set $\mathcal{N}_h^s$ and the barycenter node set $\mathcal{N}_h^b$:

$$\mathcal{N}_h = \mathcal{N}_h^b \cup \mathcal{N}_h^s \tag{6.28}$$

We show this construction on an example domain Ω in fig. 6.9.

We then introduce the following specific choices for the discretised spaces for the displacements $\mathcal{U}_h$ and pressures $\mathcal{P}_h$. For the displacement space $\mathcal{U}_h$ we use maximum-entropy basis functions *ME* on the final node set $\mathcal{N}_h$, which includes the original node set and the barycenter node set:

$$\mathcal{U}_h := [ME(\Omega; \mathcal{N}_h, \rho)]^2 \tag{6.29}$$

where ρ is a vector containing the support radius associated with each node in $\mathcal{N}_h$. For the pressure space $\mathcal{P}_h$ we use continuous first-order Lagrangian elements CG_1 on the triangulation $\mathcal{T}_h$ of the original node set $\mathcal{N}_h$:

$$\mathcal{P}_h := CG_1(\Omega; \mathcal{T}_h) \tag{6.30}$$

We show the degrees of freedom for the displacement and pressure approximation in fig. 6.10.

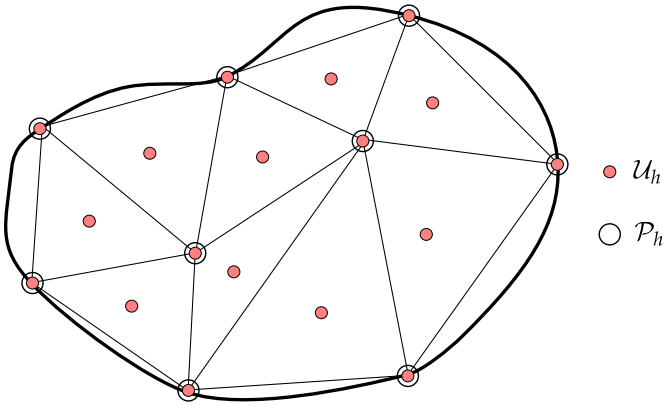

Figure 6.10: Illustration showing the degrees of freedom for the displacement space $\mathcal{U}_h$ (two per filled circle) and for the pressure space $\mathcal{P}_h$ (one per open circle)

Now we can write the approximation for the displacements $\boldsymbol{u}_h$ using the maximum-entropy meshless basis functions φ associated with the nodes in the node set $\mathcal{N}_h$ as:

$$
\begin{aligned}
\boldsymbol{u}_h(\boldsymbol{x}) &= \sum_{i=1}^{N} \boldsymbol{\varphi}_i \boldsymbol{u}_i \\
&= \begin{bmatrix} \varphi_1 & \varphi_2 & \dots & \varphi_N & 0 & 0 & \dots & 0 \\ 0 & 0 & \dots & 0 & \varphi_1 & \varphi_2 & \dots & \varphi_N \end{bmatrix} \begin{Bmatrix} u_{x1} \\ u_{x2} \\ \vdots \\ u_{xN} \\ u_{y1} \\ u_{y2} \\ \vdots \\ u_{yN} \end{Bmatrix} \\
&= \begin{bmatrix} \boldsymbol{\varphi}_{u_x} & \mathbf{0} \\ \mathbf{0} & \boldsymbol{\varphi}_{u_y} \end{bmatrix} \begin{Bmatrix} \boldsymbol{u}_x \\ \boldsymbol{u}_y \end{Bmatrix} \\
&= \boldsymbol{\Phi}_{\boldsymbol{u}} \boldsymbol{u} \quad \forall x \in \Omega
\end{aligned}
\tag{6.31}
$$

and the approximation for the pressures p_h using the first-order Lagrangian basis functions N_i

associated with the degrees of freedom at vertices of the triangulation $\mathcal{T}_h$ as:

$$\begin{aligned} p_h &= \sum_{i=1}^{M} N_i p_i \\ &= \begin{bmatrix} N_1 & N_2 & \dots & N_M \end{bmatrix} \begin{Bmatrix} p_1 \\ p_2 \\ \vdots \\ p_M \end{Bmatrix} \\ &= \boldsymbol{N}_p \boldsymbol{p} \quad \forall x \in \Omega \end{aligned} \tag{6.32}$$

The same spaces and thus basis functions are used for discretising the test spaces for the displacements $\boldsymbol{v} \in \mathcal{U}_h$ and for the pressures $q \in \mathcal{P}_h$:

$$\boldsymbol{v} = \boldsymbol{\Phi}_{\boldsymbol{u}}, \qquad q = \boldsymbol{N}_p \tag{6.33}$$

We can then substitute the basis functions defined above into the weak form of the incompressible elasticity problem eq. (6.14) giving:

$$\int_\Omega \boldsymbol{B}^T \boldsymbol{D} \boldsymbol{B} \, d\Omega \, \boldsymbol{u} + \int_\Omega \boldsymbol{B}^T \boldsymbol{m} \boldsymbol{N}_p \, d\Omega \, \boldsymbol{p} = \int_\Omega \boldsymbol{\Phi}_u^T \boldsymbol{f} \, d\Omega \tag{6.34a}$$

$$\int_\Omega \boldsymbol{N}_p^T \boldsymbol{m}^T \boldsymbol{B} \, d\Omega \, \boldsymbol{u} - \frac{1}{\lambda_e} \int_\Omega \boldsymbol{N}_p^T \boldsymbol{N}_p \, d\Omega \, \boldsymbol{p} = 0 \tag{6.34b}$$

where the $\boldsymbol{B}$ results from the small strain operator $\boldsymbol{\varepsilon}$ acting upon the basis functions for the displacements $\boldsymbol{\Phi}_{\boldsymbol{u}}$ and is defined by:

$$\boldsymbol{B} = \begin{bmatrix} \frac{\partial \boldsymbol{\varphi}_{u_x}}{\partial x_1} & 0 \\ 0 & \frac{\partial \boldsymbol{\varphi}_{u_y}}{\partial x_2} \\ \frac{\partial \boldsymbol{\varphi}_{u_x}}{\partial x_2} & \frac{\partial \boldsymbol{\varphi}_{u_y}}{\partial x_1} \end{bmatrix} \tag{6.35}$$

The $\boldsymbol{m}$ vector converts the $\boldsymbol{B}$ matrix to the divergence operator:

$$\boldsymbol{m} = \begin{Bmatrix} 1 & 1 & 0 \end{Bmatrix}^T \tag{6.36}$$

and the matrix $\boldsymbol{D}$ contains the material property μ as:

$$\boldsymbol{D} = \begin{bmatrix} 2\mu & 0 & 0 \\ 0 & 2\mu & 0 \\ 0 & 0 & \mu \end{bmatrix} \tag{6.37}$$

The volume-averaged pressure technique then develops directly from eq. (6.34b). We re-write eq. (6.34b) equation for every row a as:

$$\sum_{b=1}^{N} \int_{\Omega} \boldsymbol{N}_{pa} \boldsymbol{m}^T \boldsymbol{B}_b \, d\Omega \, \boldsymbol{u}_b - \frac{1}{\lambda_e} \sum_{b=1}^{M} \int_{\Omega} \boldsymbol{N}_{pa} \boldsymbol{N}_{pb} \, d\Omega \, p_b = 0 \tag{6.38}$$

Performing row-sum in the pressure term leads to:

$$\sum_{b=1}^{N} \int_{\Omega} \boldsymbol{N}_{pa} \boldsymbol{m}^T \boldsymbol{B}_b \, d\Omega \, \boldsymbol{u}_b - \frac{1}{\lambda_e} \sum_{a=1}^{M} \int_{\Omega} \boldsymbol{N}_{pa} \, d\Omega \, p_a = 0 \tag{6.39}$$

This row-sum procedure is a equivalent to the diagonalisation of the matrix $\boldsymbol{C}$, which is a necessary procedure for the fast inversion of $\boldsymbol{C}^{-1}$ in the static condensation procedure described in section 6.4.1. The integral across the entire domain Ω is then restricted to the domain Ω_a across the cells attached to the vertex associated with the nodal pressure degree of freedom p_a:

$$\sum_{b=1}^{N} \int_{\Omega_a} N_{pa} \boldsymbol{m}^T \boldsymbol{B}_b \, d\Omega \, \boldsymbol{u}_b - \frac{1}{\lambda_e} \sum_{a=1}^{M} \int_{\Omega_a} N_{pa} \, d\Omega \, p_a = 0 \tag{6.40}$$

We show a typical pressure degree of freedom a and the associated integration domain Ω_a in fig. 6.11. The final step is to re-arrange the previous equation giving the nodal pressure p_a in terms of the displacement unknowns u_b:

$$p_a = -\lambda_e \sum_{b=1}^{N} \left\{ \frac{\int_{\Omega_a} N_{pa} \boldsymbol{m}^T \boldsymbol{B}_b \, d\Omega}{\int_{\Omega_a} N_{pa} \, d\Omega} \right\} \boldsymbol{u}_b \tag{6.41}$$

The above quantity in the curly brackets is the average of the discrete divergence operator $\boldsymbol{m}^T \boldsymbol{B}$ across the cells attached to the particular node a.

Before continuing let's consider the form of eq. (6.41). The size of the nodal pressure is $p_a \in \mathbb{R}$

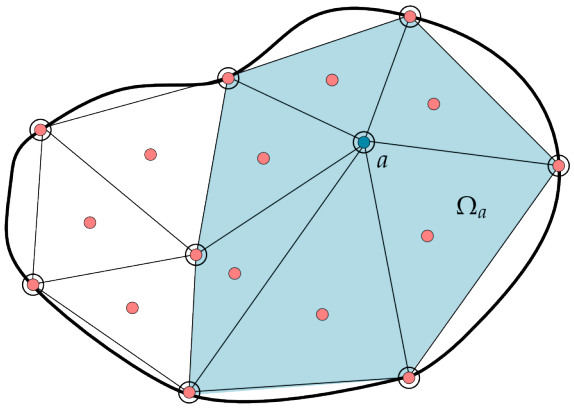

Figure 6.11: Illustration showing a pressure degree of freedom p_a and the associated integration domain Ω_a for the computation of the volume-averaged pressure

and the size of the nodal displacement vector $\boldsymbol{u}_b \in \mathbb{R}^{2\times 1}$ and therefore the size of the quantity in the curly brackets relating the two must be $\mathbb{R}^{1\times 2}$. We can therefore subsume the summation over b into a vector $\boldsymbol{q}_a \in \mathbb{R}^{1\times 2N}$ as:

$$p_a = \boldsymbol{q}_a \boldsymbol{u} \tag{6.42}$$

so we now have a relationship between the single pressure degree of freedom p_a and the displacement degrees of freedom in the vector $\boldsymbol{u}$. Then it is convenient to express all of pressure degrees of freedom $\boldsymbol{p}$ in terms of the displacement degrees of freedom vector $\boldsymbol{u}$. To do this we define a new matrix $\boldsymbol{Q} \in \mathbb{R}^{M\times 2N}$ where the rows of the matrix $\boldsymbol{Q}$ are constructed from the row vectors $\boldsymbol{q}_a$:

$$\boldsymbol{p} = \boldsymbol{Q}\boldsymbol{u} = \begin{bmatrix} \boldsymbol{q}_1 \\ \boldsymbol{q}_2 \\ \vdots \\ \boldsymbol{q}_M \end{bmatrix} \boldsymbol{u} \tag{6.43}$$

With this expression we can then eliminate the pressure unknowns $\boldsymbol{p}$ from eq. (6.34a):

$$\int_\Omega \boldsymbol{B}^T \boldsymbol{D}\boldsymbol{B}\, d\Omega\, \boldsymbol{u} + \int_\Omega \boldsymbol{B}^T \boldsymbol{m}\boldsymbol{N}_p \boldsymbol{Q}\, d\Omega\, \boldsymbol{u} = \int_\Omega \boldsymbol{\Phi}_u^T \boldsymbol{f}\, d\Omega \tag{6.44}$$

resulting in a generalised displacement method. Looking at the second integral on the left-hand side of eq. (6.44) we can see that the matrix $\boldsymbol{Q}$ is pre-multiplied by $\boldsymbol{N}_p$, the finite element basis functions associated with the pressure space $\mathcal{P}_h$. Therefore the volume-averaged pressures which satisfy the incompressibility constraint in an average sense are interpolated using the

finite element basis functions in the calculation of the bilinear form related to the volumetric energy of the solid.

Before concluding this section we will define an operator which describes the above volume-averaged nodal pressure procedure. This will be useful later when we will apply an identical procedure to the Reissner-Mindlin problem. Because of the generality of the procedure we will call the operator the local patch projection operator.

Definition 3 (Local patch projection operator)**.** *Let $v_h \in \mathcal{U}_h$ and $w_h \in \mathcal{P}_h$ where $\mathcal{U}_h$ and $\mathcal{P}_h$ with $\dim(\mathcal{U}_h) = N$ and $\dim(\mathcal{P}_h) = M$ are a meshless space and a finite element space that satisfy the inf-sup condition. The spaces are associated with degrees of freedom $\boldsymbol{v}$ and $\boldsymbol{w}$ and basis functions $\boldsymbol{\varphi}$ and $\boldsymbol{N}$ respectively such that:*

$$v_h = \boldsymbol{\varphi}\boldsymbol{v}, \qquad w_h = \boldsymbol{N}\boldsymbol{w} \tag{6.45}$$

Then the local patch projection operator $\Pi_h^p(\mathcal{L}[v_h]) : \mathcal{U}_h \rightarrow \mathcal{P}_h$ is defined by:

$$\Pi_h^p(\mathcal{L}[v_h]) = \boldsymbol{N}\boldsymbol{Q}\boldsymbol{v} \tag{6.46}$$

where $\mathcal{L}[v_h]$ is a differential operator and the matrix $\boldsymbol{Q} \in \mathbb{R}^{M\times N}$ is:

$$\boldsymbol{Q} = \begin{bmatrix} \boldsymbol{q}_1 \\ \boldsymbol{q}_2 \\ \vdots \\ \boldsymbol{q}_M \end{bmatrix} \tag{6.47}$$

with each $\boldsymbol{q}_a$ being the volume-average of the differential operator $\mathcal{L}$ acting upon the basis functions $\boldsymbol{\varphi}$ across the representative volume Ω_a attached to the degree of freedom w_a defined by:

$$\boldsymbol{q}_a = \frac{\int_{\Omega_a} N_a \mathcal{L}[\boldsymbol{\varphi}]\, d\Omega}{\int_{\Omega_a} N_a\, d\Omega} \tag{6.48}$$

Using the above definition the volume-averaged nodal pressure technique is the specific case of the local patch projection method with the following specific choice for the differential operator $\mathcal{L}$:

$$\mathcal{L}[v_h] = \operatorname{div} v_h \tag{6.49}$$

Computer implementation

We will now describe the computer implementation of the local patch projection procedure. In the original papers by Ortiz et. al [75, 76] very little description of the computer implementation is given. In this description of the LPP procedure we will use the concrete terminology of the nearly-incompressible elasticity problem with displacement $\boldsymbol{u}_h$ and pressure p_h as the unknowns, but of course the procedure applies equally to the Reissner-Mindlin problem with generalised displacements $(\boldsymbol{\theta}_h, z_{3h})$ and shear stresses $\boldsymbol{\gamma}_h$ as the unknowns that we develop later.

The local patch projection procedure can be split down into three main steps:

1. The construction of the vector $\boldsymbol{q}_a$ in eq. (6.48) for every pressure degree of freedom p_a. This involves an integration across each domain Ω_a which is the union of the cells attached to the vertex associated with the pressure degree of freedom p_a.

2. Assembly of the large sparse matrix $\boldsymbol{Q}$ eq. (6.47) which relates the displacement degrees of freedom to the nodal pressures.

3. The assembly of the stiffness matrix generated by the second integral on the left-hand side of eq. (6.44). This involves an integration in the usual manner across the entire domain Ω. The volume-averaged pressure unknowns $\boldsymbol{p} = \boldsymbol{Q}\boldsymbol{u}$ are interpolated using the finite element basis functions $\boldsymbol{N}_p$ associated with the space $\mathcal{P}_h$.

Before describing the algorithms for implementing this process we will describe the process visually. In fig. 6.12 we show a series of figures a)-g) with the same example discretisation that was developed in figs. 6.9 to 6.11. Five vertices have been labelled one through five. We are interested in the construction of the stiffness matrix resulting from the interaction between the displacement degrees of freedom located at vertices one and two which we denote $\boldsymbol{K}_{12}$:

$$\boldsymbol{K}_{12} = \int_{\Omega_1} \boldsymbol{B}_1^T \boldsymbol{D} \boldsymbol{B}_2 \, d\Omega - \int_{\Omega_2} \boldsymbol{B}_1^T \boldsymbol{m} \left\{ \sum_{c=d,e,f} N_c \mathbf{Q}_{c2} \right\} d\Omega \tag{6.50}$$

The domains Ω_1 and Ω_2 denote the two domains across which each integral is calculated, and these two domains are different ie. $\Omega_1 \neq \Omega_2$.

Ω_1 is the intersection of the supports of the basis functions associated with the nodes at vertices 1 and 2. In fig. 6.12a) we show the supports $\text{supp}(\varphi_1)$ and $\text{supp}(\varphi_2)$ as red circles surrounding nodes 1 and 2. Therefore $\Omega_1 = \text{supp}(\varphi_1) \cap \text{supp}(\varphi_2)$ is the darkly shaded red area

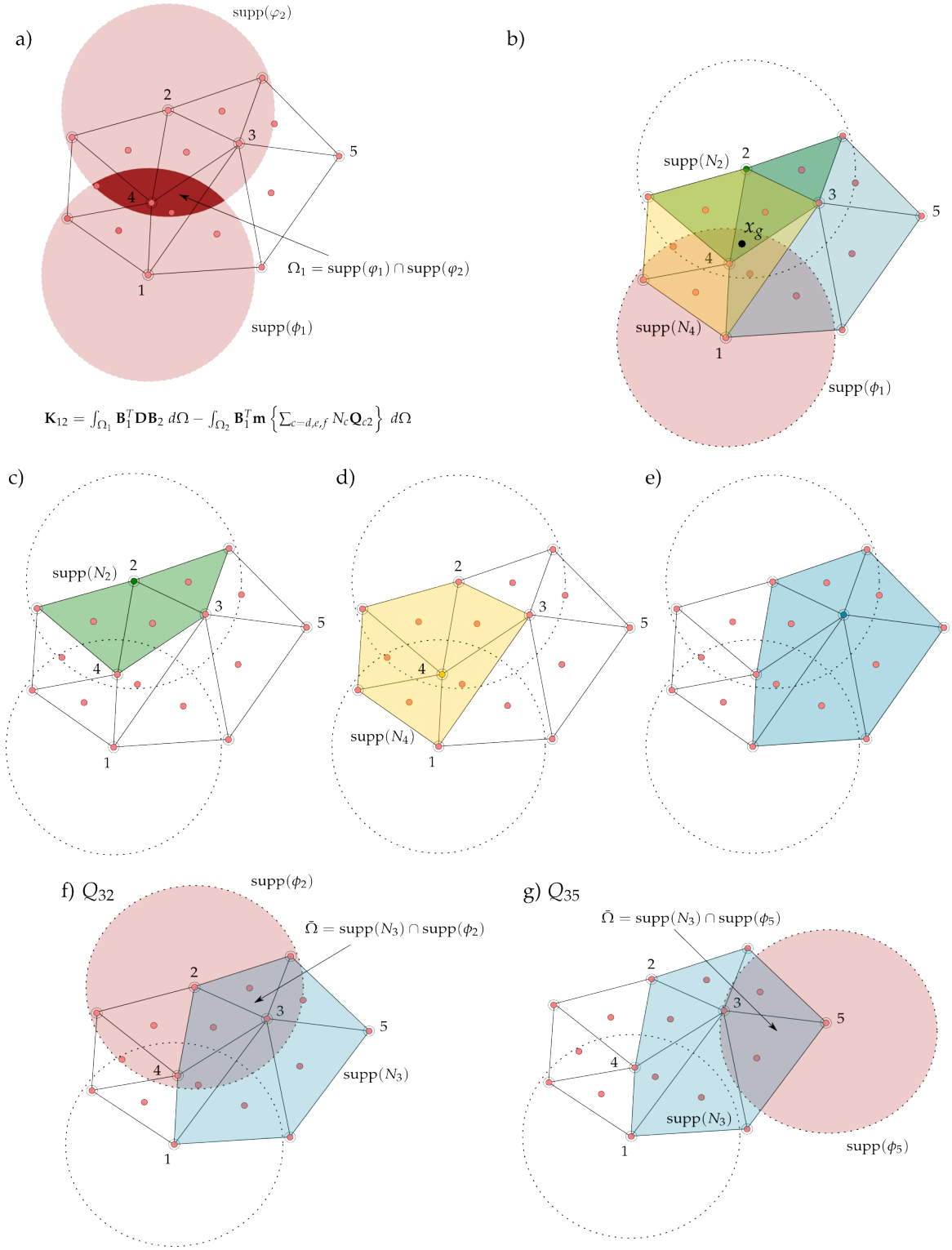

Figure 6.12: Illustration of the local patch projection procedure. See text for description of each subfigure.

in 6.12a). This is the `standard' integral domain in meshless methods relating to the intersecting supports.

Ω_2 is somewhat more complex due to the local patch-projection procedure. The support of the term $\boldsymbol{B}_1^T$ is supp(φ_1), the same as before, but the support of the functions N_c is of course defined by the triangulation $\mathcal{T}_h$ just as in the finite element method. Q_{c2} is a particular entry of the matrix $\boldsymbol{Q}$.

In fig. 6.12b we choose a specific gauss point x_g located at the black circle. At this point the basis functions N_2, N_3 and N_4 associated with the pressure degrees of freedom located at vertices two, three and four are active. Therefore the contribution from the gauss point x_g to the second integral in eq. (6.50) reads:

$$\boldsymbol{B}_1^T(x_g)\boldsymbol{m}\left\{\sum_{c=2,3,4} N_c(x_g)\boldsymbol{Q}_{c2}\right\} \tag{6.51}$$

In figs. 6.12c, 6.12d and 6.12e we show the support of the basis functions N_2, N_3 and N_4 respectively as coloured shaded areas. These shaded areas are also all shown together on fig. 6.12b.

The final term to consider in the second integral of eq. (6.50) is Q_{c2} for $c = \{2, 3, 4\}$. Remember that the $\boldsymbol{Q}$ is a matrix with rows relating to the pressure degrees of freedom and with columns relating to the displacement degrees of freedom. For example, Q_{32} relates the third node pressure degree of freedom to the second node displacement degree of freedom. In fig. 6.12f we consider the integration domain for the entry Q_{32}. The support of the pressure degree of freedom supp(N_3) is shaded light blue, whilst the support of the displacement degree of freedom supp(φ_2) is shaded light red. The integration domain $\bar{\Omega}$ is therefore the intersection of these two supports $\bar{\Omega} = \text{supp}(N_3) \cap \text{supp}(\varphi_2)$.

We can conclude from the above that:

1. In the first integral of eq. (6.50) the interaction between displacement degrees of freedom one and two is direct, as in the standard meshless method.

2. In the second integral of eq. (6.50) the interaction between displacement degrees of freedom one and two is indirect. The primary interaction is between displacement degree of freedom one and the finite element basis N_c. The interaction between displacement degree of freedom one and two occurs is at a secondary level due to the matrix entries Q_{c2} which relate the pressure degree of freedom c to the displacement degree of freedom two.

3. The assembled stiffness matrix resulting from the second integral of eq. (6.50) will have higher bandwidth than that resulting from the first integral of eq. (6.50). This is because displacement degrees of freedom which do not interact with each other in the first integral of eq. (6.50) may interact indirectly via the local patch-projection procedure in the second integral. In fig. 6.12g we show an example of this; displacement degrees of freedom one and five will not interact with each other in the first integral because $\text{supp}(\varphi_1) \cap \text{supp}(\varphi_5) = \emptyset$. However, because displacement degree of freedom one interacts with pressure degree of freedom three $\text{supp}(\varphi_1) \cap \text{supp}(N_3) \neq \emptyset$ and pressure degree of freedom three interacts with displacement degree of freedom five $\text{supp}(N_3) \cap \text{supp}(\varphi_5) \neq \emptyset$ creating an entry Q_{35} there will be a stiffness matrix entry $\boldsymbol{K}_{15}$.

We give numpy-like pseudo-code for the local-patch projection procedure in algorithms 6 and 7. These algorithms are implemented in the pymfl package for both the nearly-incompressible elasticity problem and the Reissner-Mindlin problem.

Algorithm 6 Pseudo-code for assembling $\boldsymbol{Q}$

```
Q = sparse matrix size: M by N
denominators = vector size: M by 1
for each vertex in mesh:
    for each cell attached to vertex:
        for each gauss point in cell:
            N = finite element basis function associated \
                with vertex evaluated at gauss point
            w = gauss point weight
            B = B matrix evaluated at gauss point

            numerator = w*N*B
            denominator = w*N

            dofs = displacement dof numbers
            Q[vertex, dofs] += numerator
            denominators[vertex] += denominator

for each vertex in mesh:
    Q[vertex, :] = denominators[vertex]*Q[vertex, :]
```

Verification

In this section we verify the correct implementation of the local patch-projection procedure for the nearly-incompressible elasticity problem using the leaky-lid cavity problem. The cavity

Algorithm 7 Pseudo-code for assembling $\boldsymbol{K}$

```
K = sparse matrix size: N by N
for each cell in mesh:
    for each gauss point in cell:
        N = finite element basis functions evaluated at gauss
           point
        w = gauss point weight
        B = B matrix evaluated at gauss point

        U_dofs = displacement dof numbers

        for vertex in cell:
            K_contribution = w*B.T*m*N[vertex]*Q[vertex,:]

            q_dofs = q dof numbers
            K[U_dofs, q_dofs] += K_contribution
```

problem is the standard benchmark for testing the performance of discretisations of the nearly-incompressible or Stokes' flow problem. This example was also used by Ortiz et al. in [76]. We compare the local patch-projection method with the MINI element of Arnold et al. [163] which we implement in the DOLFIN finite element package [127].

In fig. 6.13 we show the leaky-lid cavity flow problem. The domain has sides of unit-length, and a unit tangential displacement is applied along the top surface. On all the other boundaries displacement is fixed in both the x and y directions. Material properties are taken to be $E = 1$ and $\nu = 0.4999$. These properties match those found in [164].

In fig. 6.14 we compare the horizontal displacement u_x fields for the LPP MaxEnt method of Ortiz et al. [76] on an 11×11 grid of nodes + `bubble' nodes and the MINI element of Arnold et al. [163]. We can see that the LPP MaxEnt method provides a significantly smoother solution due to the high continuity of the MaxEnt basis functions. Crucially, it is clear that the smoothness of the displacement solution is unaffected by the use of finite element basis functions for the pressure space. We remark that if the LPP MaxEnt method was not free of the volumetric-locking problem the results would not match at all for $\nu = 0.4999$.

In fig. 6.15 we compare the vertical displacement u_y fields for the LPP MaxEnt method and the MINI element method. Again, we can see that the LPP MaxEnt method provides a significantly smoother solution than the MINI element method.

To give a better indication of the relative accuracy of the LPP MaxEnt method we plot the vertical displacement field u_y in fig. 6.16 extracted across the line QQ (see fig. 6.13). In addition

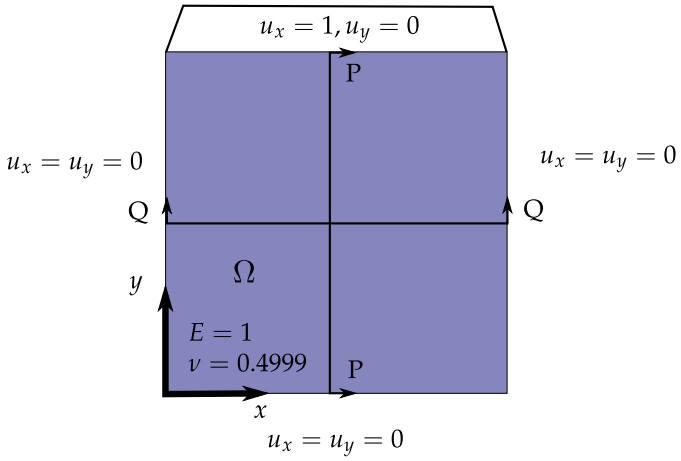

Figure 6.13: Leaky lid cavity problem. Unit horizontal displacement $u_x = 1$, $u_y = 0$ is applied to the top side, all other sides fixed $u_x = u_y = 0$.

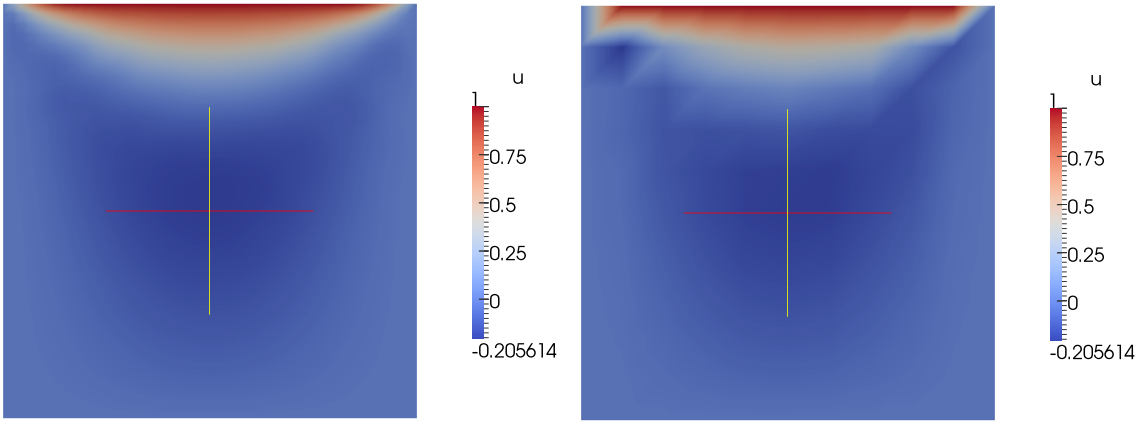

(a) LPP MaxEnt 11×11 grid + `bubble' nodes

(b) MINI element 10×10 mesh

Figure 6.14: Horizontal displacement u_x for leaky-lid cavity flow problem with LPP Maxent and MINI methods.

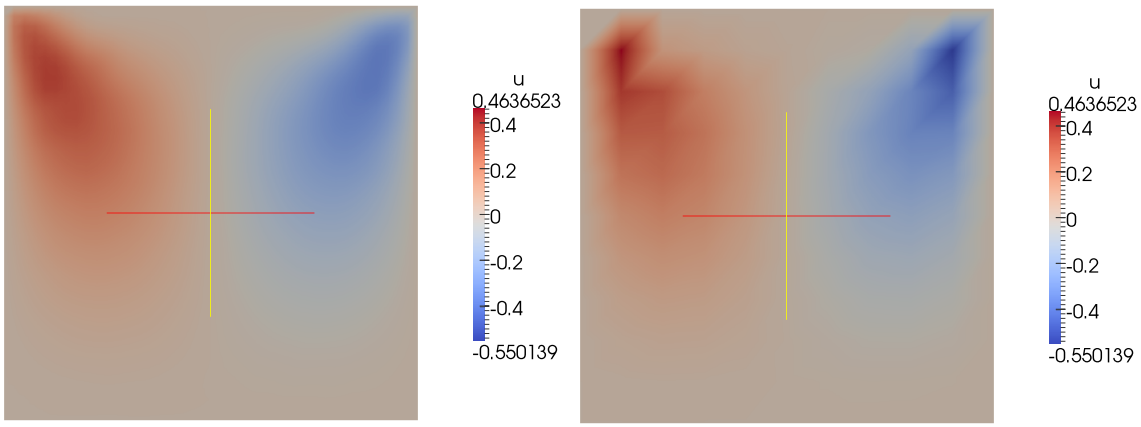

(a) LPP MaxEnt 11 × 11 grid + `bubble' nodes

(b) MINI element 10 × 10 mesh

Figure 6.15: Vertical displacement u_y for leaky-lid cavity flow problem with LPP Maxent and MINI methods.

to the LPP MaxEnt method on the coarse grid 11 × 11 we include results for the MINI element method on a very fine mesh 30 × 30 to act as a converged `reference' solution. Whilst all three methods perform well it is clear that the LPP MaxEnt method on the coarse grid can match the performance of the MINI element on the very fine mesh. In fig. 6.17 we plot the horizontal displacement u_y across the line PP (see fig. 6.13). Here the difference between the three solutions is less pronounced but the LPP MaxEnt method on the coarse grid still outperforms the MINI element on the coarse mesh. We note that the MINI element on the fine mesh results in a linear system with 6843 degrees of freedom whilst the LPP MaxEnt method on the coarse mesh has only 642 degrees of freedom.

In summary the LPP MaxEnt method is an effective way of solving the volumetric-locking problem. Excellent performance can be achieved with relatively low numbers of degrees of freedom when compared with the MINI finite element method. More results for the LPP MaxEnt method are given in Ortiz et. al [75, 76].

6.5 Meshless discretisation

We will now develop the meshless discretisation of the stabilised discrete Reissner-Mindlin problem eq. (6.10) using the local patch projection procedure in definition 3. Much of the notation that was introduced for the volume-averaged pressure procedure will be re-used here. We repeat the stabilised discrete Reissner-Mindlin problem here for convenience:

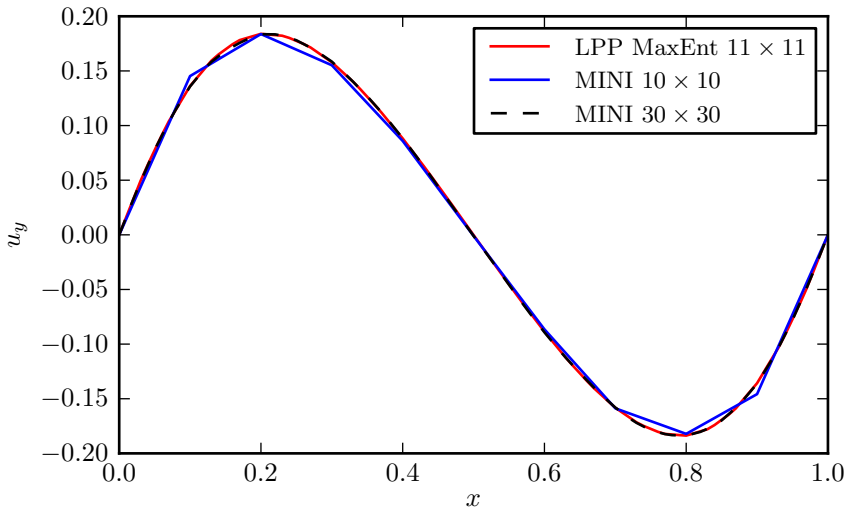

Figure 6.16: Vertical displacement u_y across line QQ.

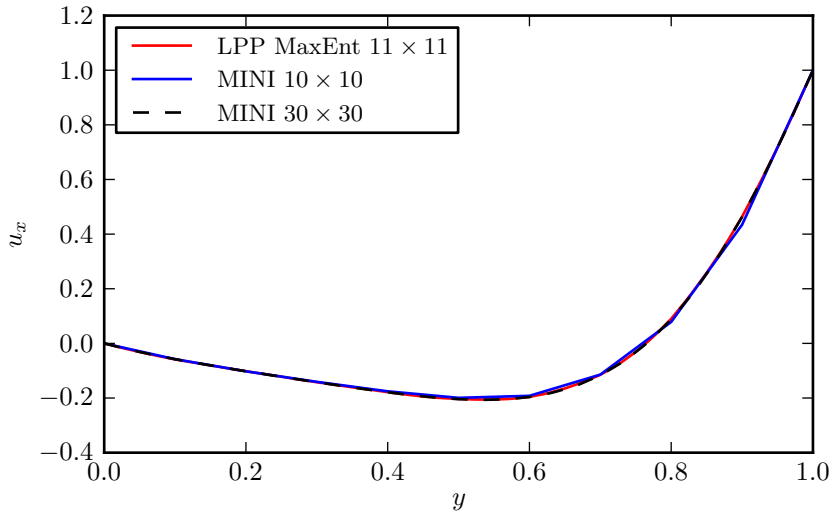

Figure 6.17: Horizontal displacement u_x across line PP.

Problem 19 (Discrete stabilised mixed scaled Reissner-Mindlin problem)**.** *Find the transverse deflection, rotations and transverse shear stresses* $(z_{3h}, \boldsymbol{\theta}_h, \boldsymbol{\gamma}_h) \in (\mathcal{V}_{3h}, \mathcal{R}_h, S_h)$ *such that for all* $(y_3, \boldsymbol{\eta}, \boldsymbol{\psi}) \in (\mathcal{V}_{3h}, \mathcal{R}_h, S_h)$*:*

$$a_b(\boldsymbol{\theta}_h, \boldsymbol{\eta}) + \lambda\alpha a_s(\boldsymbol{\theta}_h, z_{3h}; \boldsymbol{\eta}, y_3) + (\boldsymbol{\gamma}_h, \nabla y_3 - \boldsymbol{\eta})_{L^2(\Omega_0)} = g(y_3) \tag{6.52a}$$

$$(\nabla z_{3h} - \boldsymbol{\theta}_h, \boldsymbol{\psi})_{L^2(\Omega_0)} - \frac{\bar{t}^2}{\lambda(1-\alpha\bar{t}^2)}(\boldsymbol{\gamma}_h, \boldsymbol{\psi})_{L^2(\Omega_0)} = 0 \tag{6.52b}$$

We use the same node set construction with standard and `bubble' nodes $\mathcal{N}_h = \mathcal{N}_h^b \cup \mathcal{N}_h^s$ and triangulation of the standard node set $\mathcal{T}_h$ as for the incompressible elasticity problem. We then introduce the following similar specific choices of maximum-entropy basis functions for the rotation and displacement variables:

$$\mathcal{R}_h := [ME(\Omega_0; \mathcal{N}_h, \rho)]^2, \quad \mathcal{V}_{3h} = ME(\Omega_0; \mathcal{N}_h, \rho) \tag{6.53}$$

and continuous Lagrangian finite elements of first order for the shear stress variable:

$$S_h := [CG_1(\Omega_0; \mathcal{T}_h)]^2 \tag{6.54}$$

We then use the definition of the local patch-projection operator in definition 3 with the following specific choices:

$$\mathcal{U}_h := \mathcal{R}_h \times \mathcal{V}_{3h} \tag{6.55a}$$

$$\mathcal{P}_h := S_h \tag{6.55b}$$

$$\mathcal{L}[z_3 h, \theta_h] := \nabla z_{3h} - \boldsymbol{\theta}_h \tag{6.55c}$$

Using this patch projection operator, which for the Reissner-Mindlin problem takes the form:

$$\Pi_h^p : \mathcal{R}_h \times \mathcal{V}_{3h} \to S_h \tag{6.56}$$

we can re-arrange eq. (6.52b) to give an expression for the shear stress variable $\boldsymbol{\gamma}_h$ in terms of the rotations and transverse displacements:

$$\boldsymbol{\gamma_h} = \frac{\lambda(1-\alpha\bar{t}^2)}{\bar{t}^2}\Pi_h^p(\nabla z_{3h} - \boldsymbol{\theta}_h) \tag{6.57}$$

Substituting back into eq. (6.52a) to eliminate the shear stress variable gives:

$$a_b(\boldsymbol{\theta}_h, \boldsymbol{\eta}) + \lambda\alpha a_s(\boldsymbol{\theta}_h, z_{3h}; \boldsymbol{\eta}, y_3) + \frac{\lambda(1-\alpha\bar{t}^2)}{\bar{t}^2}(\Pi_h^p(\nabla z_{3h} - \boldsymbol{\theta}_h), \nabla y_3 - \boldsymbol{\eta})_{L^2(\Omega_0)} = g(y_3) \tag{6.58}$$

We will now develop the discrete equations. We can write the trial functions using the basis functions defined for the transverse displacements, rotations and shear stresses as:

$$\begin{aligned} z_{3h}(\boldsymbol{x}) &= \sum_{i=1}^{N} \varphi_i z_{3i} = \begin{bmatrix} \varphi_1 & \varphi_2 & \dots & \varphi_N \end{bmatrix} \begin{Bmatrix} z_{31} \\ z_{32} \\ \vdots \\ z_{3N} \end{Bmatrix} \\ &= \boldsymbol{\varphi}_{z_3} \boldsymbol{z}_3 \quad \forall \boldsymbol{x} \in \Omega_0 \end{aligned} \tag{6.59a}$$

$$\begin{aligned} \boldsymbol{\theta}_h(\boldsymbol{x}) &= \sum_{i=1}^{N} \boldsymbol{\varphi}_i \boldsymbol{\theta}_i \\ &= \begin{bmatrix} \varphi_1 & \varphi_2 & \dots & \varphi_N & 0 & 0 & \dots & 0 \\ 0 & 0 & \dots & 0 & \varphi_1 & \varphi_2 & \dots & \varphi_N \end{bmatrix} \begin{Bmatrix} \theta_{11} \\ \theta_{12} \\ \vdots \\ \theta_{1N} \\ \theta_{21} \\ \theta_{22} \\ \vdots \\ \theta_{2N} \end{Bmatrix} \\ &= \begin{bmatrix} \boldsymbol{\varphi}_{\theta_1} & \mathbf{0} \\ \mathbf{0} & \boldsymbol{\varphi}_{\theta_2} \end{bmatrix} \begin{Bmatrix} \boldsymbol{\theta}_1 \\ \boldsymbol{\theta}_2 \end{Bmatrix} \\ &= \boldsymbol{\Phi}_\theta \boldsymbol{\theta} \quad \forall \boldsymbol{x} \in \Omega_0 \end{aligned} \tag{6.59b}$$

$$
\begin{aligned}
\boldsymbol{\gamma}_h &= \sum_{i=1}^{M} \boldsymbol{N}_i \boldsymbol{\gamma}_i \\
&= \begin{bmatrix} N_1 & N_2 & \dots & N_M & 0 & \cdots & 0 & \\ 0 & 0 & \cdots & 0 & N_1 & N_2 & \dots & N_M \end{bmatrix} \begin{Bmatrix} \gamma_{13\,1} \\ \gamma_{13\,2} \\ \vdots \\ \gamma_{13\,M} \\ \gamma_{23\,1} \\ \gamma_{23\,2} \\ \vdots \\ \gamma_{23\,M} \end{Bmatrix} \\
&= \boldsymbol{N}_\gamma \boldsymbol{\gamma} \quad \forall x \in \Omega_0
\end{aligned}
\tag{6.59c}
$$

We define our trial functions using the same basis as the test functions:

$$
y_{3h} = \boldsymbol{\varphi}_{z3}, \qquad \boldsymbol{\eta}_h = \boldsymbol{\Phi}_\theta, \qquad \boldsymbol{\psi}_h = \boldsymbol{N}_\gamma \tag{6.60}
$$

allowing us to re-write eq. (6.58) as:

$$
\begin{aligned}
&\int_{\Omega_0} \boldsymbol{B}_b^T \boldsymbol{D}_b \boldsymbol{B}_b \, d\Omega \, \boldsymbol{\theta} + \lambda\alpha \int_{\Omega_0} \boldsymbol{B}_s^T \boldsymbol{B}_s \, d\Omega \begin{Bmatrix} \boldsymbol{\theta} \\ \boldsymbol{z}_3 \end{Bmatrix} + \\
&\frac{\lambda(1-\alpha\bar{t}^2)}{\bar{t}^2} \int_{\Omega_0} \boldsymbol{B}_s^T \boldsymbol{N}_\gamma \boldsymbol{Q} \, d\Omega \begin{Bmatrix} \boldsymbol{\theta} \\ \boldsymbol{z}_3 \end{Bmatrix} = \int_{\Omega_0} \boldsymbol{\varphi}_{z_3} g \, d\Omega
\end{aligned}
\tag{6.61}
$$

where the $\boldsymbol{B}_b \in \mathbb{R}^{3\times 3N}$ and $\boldsymbol{B}_s \in \mathbb{R}^{2\times 3N}$ are matrices containing component-wise derivatives of the shape function vectors:

$$
\boldsymbol{B}_b = \begin{bmatrix} \frac{\partial \varphi_{\theta 1}}{\partial x_1} & \boldsymbol{0} \\ \boldsymbol{0} & \frac{\partial \varphi_{\theta 2}}{\partial x_2} \\ \frac{\partial \varphi_{\theta 1}}{\partial x_2} & \frac{\partial \varphi_{\theta 2}}{\partial x_1} \end{bmatrix} \tag{6.62}
$$

$$
\boldsymbol{B}_s = \begin{bmatrix} -\boldsymbol{\varphi}_{\theta x} & \boldsymbol{0} & \frac{\partial \varphi_{z3}}{\partial x_1} \\ \boldsymbol{0} & -\boldsymbol{\varphi}_{\theta y} & \frac{\partial \varphi_{z3}}{\partial x_2} \end{bmatrix} \tag{6.63}
$$

$\boldsymbol{D}_b \in \mathbb{R}^{3\times3}$ is the matrix containing the bending material properties of the plate:

$$\boldsymbol{D}_b = D\begin{bmatrix} 1 & \nu & 0 \\ \nu & 1 & 0 \\ 0 & 0 & \frac{1-\nu}{2} \end{bmatrix} \tag{6.64}$$

The $\boldsymbol{Q} \in \mathbb{R}^{2M\times3N}$ matrix is generated by the local patch-projection procedure outlined in definition 3. More specifically, the matrix $\boldsymbol{Q}$ is:

$$\boldsymbol{Q} = \begin{bmatrix} \boldsymbol{q}_1 \\ \boldsymbol{q}_2 \\ \vdots \\ \boldsymbol{q}_M \end{bmatrix} \tag{6.65}$$

where the individual entries $\boldsymbol{q}_a \in \mathbb{R}^{2\times3M}$ are now *matrices* instead of vectors defined by the following equation:

$$\boldsymbol{q}_a = \frac{\int_{\Omega_a} \boldsymbol{N}_a \boldsymbol{B}_s \, d\Omega}{\int_{\Omega_a} \boldsymbol{N}_a \, d\Omega} \tag{6.66}$$

The division by an integral of a matrix looks a little peculiar in this extension of the local-patch projection to the shear-stress which is a vectorial quantity. To make the exact mathematics clear, we re-write the above equation as:

$$\boldsymbol{q}_a = \left[\int_{\Omega_a} \boldsymbol{N}_a \, d\Omega\right]^{-1} \int_{\Omega_a} \boldsymbol{N}_a \boldsymbol{B}_s \, d\Omega \tag{6.67}$$

The matrix $\int_{\Omega_a} \boldsymbol{N}_a \, d\Omega \in \mathbb{R}^{2\times2}$ will be diagonal so its inverse is simply the inverse of each diagonal entry. We have implemented the above formulation into the pymfl package.

6.6 Results

In this section we examine two test problems, a simply-supported plate with uniform pressure which we studied in the previous chapter, and a new problem we refer to as the Chinosi clamped plate problem. This problem has a special load function which gives closed form polynomial displacement solutions.

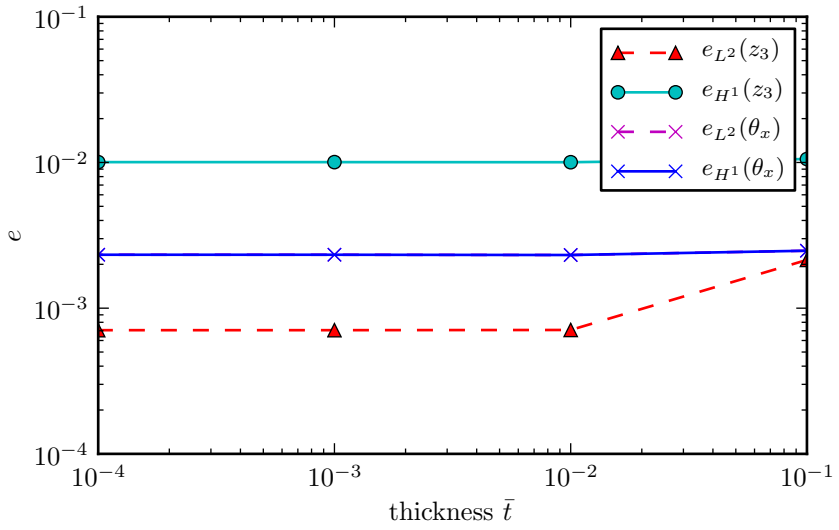

Figure 6.18: Graph showing for a fixed discretisation of 8 × 8 grid + `bubble' nodes The LPP MaxEnt method's performance is largely insensitive to changing values of $\bar{t}$ and is therefore free from the effects of shear-locking. LPP MaxEnt method for simply-supported plate problem. Note: Series for $e_{L^2}(\theta_1)$ and $e_{H^1}(\theta_1)$ coincide.

6.6.1 Simply supported plate with uniform pressure

We examine the convergence of a simply supported plate with uniform pressure. This is the same problem we used to examine the performance of the MaxEnt + NED scheme in section 5.3. The boundary conditions are shown in fig. 5.5a.

We begin by examining whether the scheme is indeed free from the negative effects of shear-locking. It is also important that for a given discretisation the performance of the method for varying thickness parameter α is broadly similar; if we have to choose a particular α for a particular $\bar{t}$ then clearly we do not have a reliable method. To determine this we take a fixed discretisation with 8 divisions (ie. 9 nodes per side) and set $\alpha = 32.0$. We then examine the convergence of the method by varying $\bar{t}$ over the range $10^{-4} \leq \bar{t} \leq 10^{-1}$. The results are shown in fig. 6.18. We can see that the errors $e_{H^1}(z_3)$, $e_{L^2}(\theta_1)$ and $e_{H^1}(\theta_1)$ are insensitive to changing $\bar{t}$. There is a very minor deterioration in performance in the error $e_{H^1}(z_3)$ for $\bar{t} \geq 10^{-2}$. This deterioration is the same as that for the TRIA0220 element when $\bar{t} > h_K$. A similar modification to eq. (6.12) can be made for the proposed LPP MaxEnt formulation which essentially turns off the mixed formulation at a certain point when it is no longer required (results not shown). This improves the performance for thick plates. We conclude that as the convergence for fixed α is largely independent of the thickness we can perform further studies using one value of $\bar{t}$ only.

We know from our experiments with the TRIA0220 finite element method that choosing α to be constant does not give the optimal rate of convergence for increasingly fine discretisations. Furthermore we know that as $\alpha \to 0$ the convergence deteriorates as we recover the fully mixed formulation, which suffers from spurious modes. Conversely as $\alpha \to \bar{t}^{-2}$ the convergence deteriorates due to the shear-locking problem. Thus an optimal value of α depends on some characteristic discretisation length and lies somewhere inbetween these two extreme points $0 \leq \alpha \leq \bar{t}^{-2}$.

To examine the effect of α on the performance of the method we perform a sensitivity study on the convergence behaviour of the method against the stabilisation parameter and discretisation size. The methodology is as follows; we take a sequence of uniform discretisations with degrees of freedom varying between $2.2 \leq \log(\dim U) \leq 3.7$ and run for each discretisation a set of simulations with the stabilisation parameter varying between $-2 < \log(\alpha) < 4$, resulting in 65 individual simulations. The plate thickness is kept fixed at $\bar{t} = 10^{-3}$.

Before discussing the results we give a description of the presentation of the sensitivity study in fig. 6.19. Along the x-axis is the number of degrees of freedom $\log(\dim U)$ and along the y-axis is the stabilisation parameter $\log(\alpha)$ and in this case along the z-axis (contours) is the L^2 error in the transverse displacement z_3 $\log(e_{L^2}(z_3))$. Dark red areas show areas of poor convergence ranging through to dark blue areas which show good convergence. Each gradation in colour between these two extreme points represents half an order of magnitude of convergence. The small black circles represent a data point from one of the 65 individual experiments. Between these data points the results are interpolated using the matplotlib Delaunay triangulation module. Between each data point for a discretisation series (lines of data points parallel with y-axis) there is half an order of magnitude difference for the stabilisation parameter α.

In fig. 6.19 we show the sensitivity study for the L^2 error in the transverse displacements z_3. Roughly speaking, for each discretisation series (lines of data points parallel with y-axis) we can see that there if α is selected as being either too small or too large the method fails to converge due to the occurrence of spurious modes or shear-locking, respectively. If we were to keep α fixed (lines parallel with x-axis) whilst refining the discretisation we would not remain near the optimal convergence line. The optimal choice of α is then set by the optimal convergence line which passes through the lowest point of error for each discretisation series.

For each discretisation series there seems to be around an order of magnitude leeway for the selection of a good α. For example, for the third discretisation series with $\log(\dim U) = 2.8$ we can achieve convergence in the range $-3.0 \leq \log(e_{L^2}(z_3) \leq -3.5$ using $1 \lesssim \log(\alpha) \lesssim 2.3$. This is encouraging in that it suggests that the convergence of the proposed method is not so sensitive

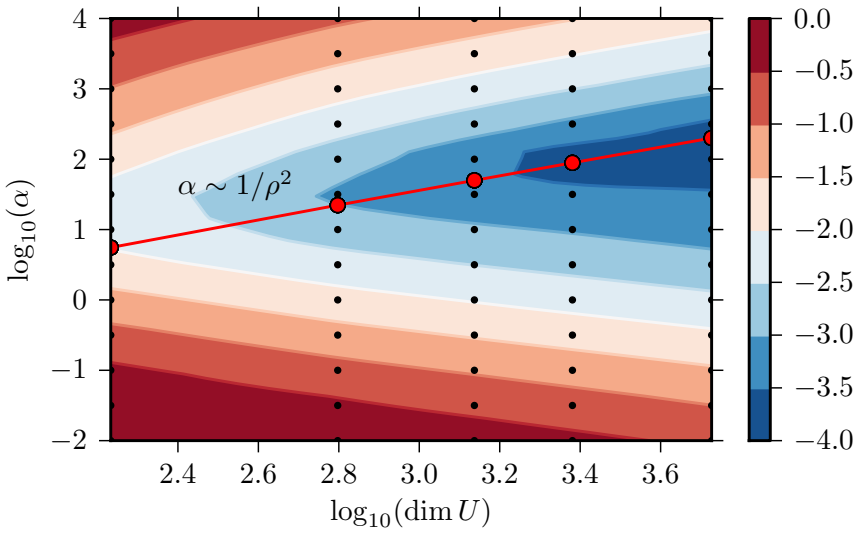

Figure 6.19: Contour plot showing sensitivity of $e_{L^2}(z_3)$ with respect to stabilisation parameter α and number of degrees of freedom $\dim(U)$. Simply-supported plate problem. LPP MaxEnt.

to the choice of α that it will be impossible to come up with a reliable scheme.

We recall that as $0 \leq \alpha < \bar{t}^{-2}$ and that the dimensionally consistent choice is then a measure of the local discretisation length to the power of minus two. We take the support radius as the natural measurement of the local discretisation length and for all of the simulations we take $\rho = \text{const}$. In fig. 6.19 we plot the values $\rho = \text{const}$ for each discretisation series as red circles and then join these points together with a red line. We can see the choice of $\alpha \sim 1/\rho^2$ tracks the optimal convergence line reasonably well, suggesting that like the finite element method, the dimensionally consistent choice based on the local discretisation length is a sound one.

Of course, we have only examined the sensitivity of the L^2 error in the transverse displacement variable z_3, which does not alone demonstrate that we have a good scheme with $\alpha \sim \rho^{-2}$. We will now examine the sensitivity of the other error measures. In all of the following sensitivity studies the x-axis and y-axis ranges are the same as in fig. 6.19. The red line showing $\alpha \sim 1/\rho^2$ remains providing a point of reference for comparison. The colours have been re-scaled, but each gradation in colour still represents a half-order of magnitude of convergence.

In fig. 6.20 we show the sensitivity study for the H^1 error in the transverse displacements z_3. We can see that the optimal convergence line now sits roughly one-half order of magnitude above the red reference line. However, the red reference line still manages to match the best

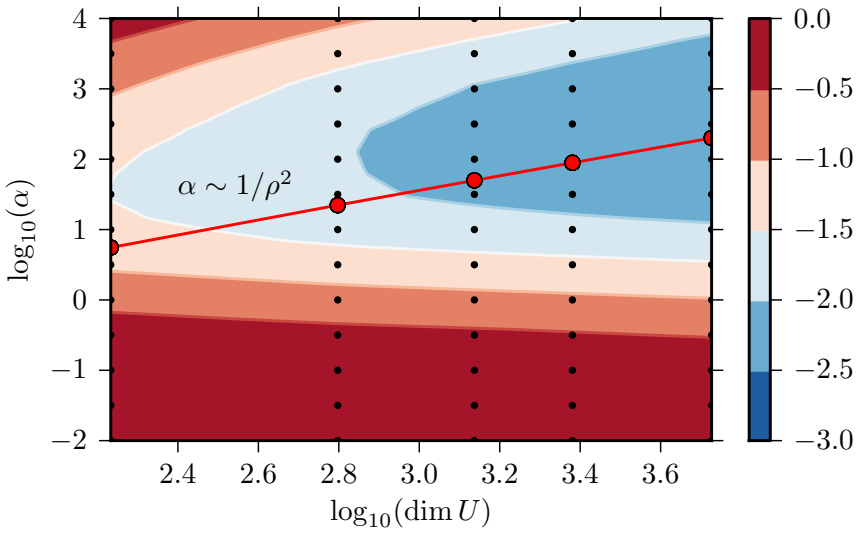

Figure 6.20: Contour plot showing sensitivity of $e_{H^1}(z_3)$ with respect to stabilisation parameter α and number of degrees of freedom $\dim(U)$. Simply-supported plate problem. LPP MaxEnt.

error for a given discretisation series within one-half order of magnitude, except for the coarsest discretisation series. The leeway for selecting a good α in the $e_{H^1}(z_3)$ error measure seems wider than that for the $e_{L^2}(z_3)$ error measure.

In fig. 6.21 we show the sensitivity study for the L^2 error in the rotation variable θ_1. The optimal convergence line matches well with the red reference line. The red reference line manages to match the best error for a given discretisation within one-half order of magnitude for all discretisation series. Again, the leeway for selecting a good α in the $e_{H^1}(\theta_1)$ error measure seems wider than that for the $e_{L^2}(z_3)$ error measure.

In fig. 6.22 we show the sensitivity study for the H^1 error in the rotation variable θ_1. Here we can see that the optimal convergence line lies in the range $-1.5 \leq e_{H^1}(\theta_1) \leq -2.0$ for every convergence series, meaning that we do not achieve lower convergence as the discretisation is refined. Consequently, it is easy to see from this sensitivity study that it is impossible to achieve convergence in the H^1 norm for the rotation variable with any fixed choice of α.

Now that we have ascertained that $\alpha \sim \rho^{-2}$ is a roughly optimal choice (except, of course, in the error measure $e_{H^1}(\theta_1)$) we perform a traditional convergence study using $\alpha \sim \rho^{-2}$. We show the results in fig. 6.23. We can see that we achieve convergence for the transverse displacement variable z_3 in both the L^2 and H^1 norm. However, for the rotation variable θ we achieve a

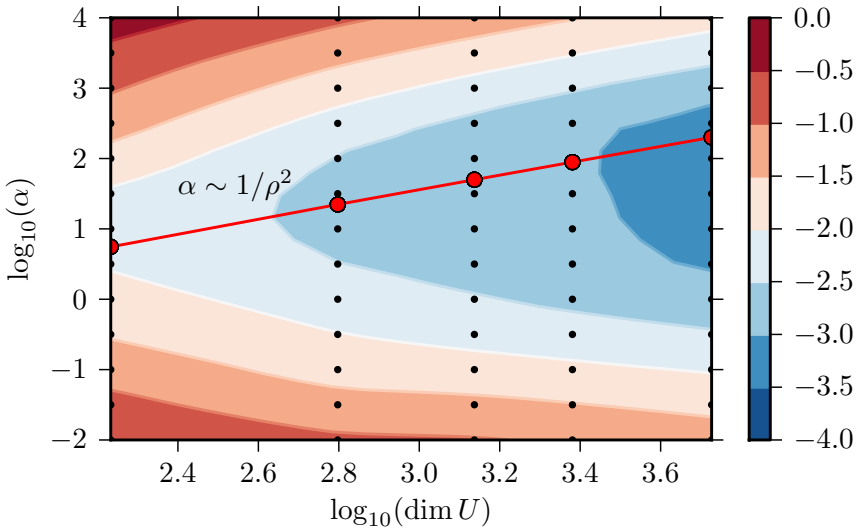

Figure 6.21: Contour plot showing sensitivity of $e_{L^2}(\theta_1)$ with respect to stabilisation parameter α and number of degrees of freedom $\dim(U)$. Simply-supported plate problem. LPP MaxEnt.

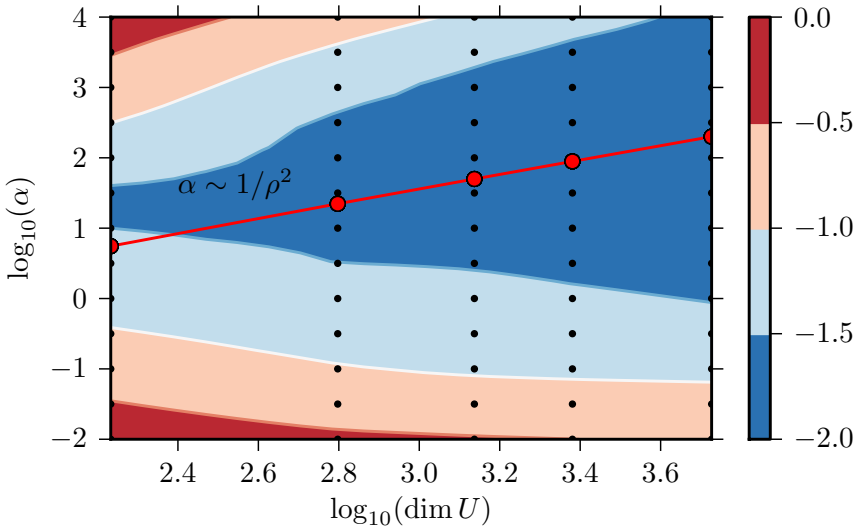

Figure 6.22: Contour plot showing sensitivity of $e_{H^1}(\theta_1)$ with respect to stabilisation parameter α and number of degrees of freedom $\dim(U)$. Simply-supported plate problem. LPP MaxEnt.

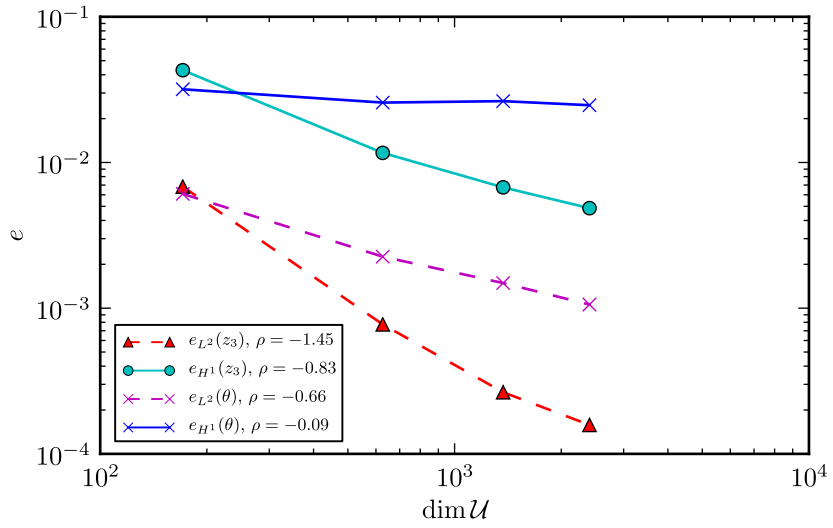

Figure 6.23: Plot showing convergence of proposed LPP MaxEnt method for simply-supported plate problem.

significantly reduced rate of convergence in the L^2 norm, and almost no convergence in the H^1 norm. This negative result confirms the results shown in the sensitivity study fig. 6.22. We have not found any of the finite element designs discussed previously to exhibit this lack of convergence.

In figs. 6.24 and 6.25 we show plots of the transverse displacement and rotation for a thick plate $\bar{t} = 0.1$ using the LPP MaxEnt method on a 10×10 grid of nodes + `bubble' nodes. We can see that we retain the high continuity solution typical of meshless basis functions despite using an underlying mesh to discretise the shear stresses. The central displacement of the plate is given as $z_{3h}(0.5, 0.5) = 4.2727 \times 10^{-6}$ which closely matches the analytical solution $z_3(0.5, 0.5) = 4.2728 \times 10^{-6}$.

In figs. 6.26 and 6.27 we show plots of the transverse displacement and rotation for a thin plate $\bar{t} = 0.001$ using the LPP MaxEnt method on a 10×10 grid of nodes + `bubble' nodes. Again, we can see that we retain the high continuity solution typical of meshless basis functions despite using an underlying mesh to discretise the shear stresses. The central displacement of the plate is given as $z_{3h}(0.5, 0.5) = 4.0624 \times 10^{-6}$ which closely matches the analytical solution $z_3(0.5, 0.5) = 4.06237 \times 10^{-6}$.

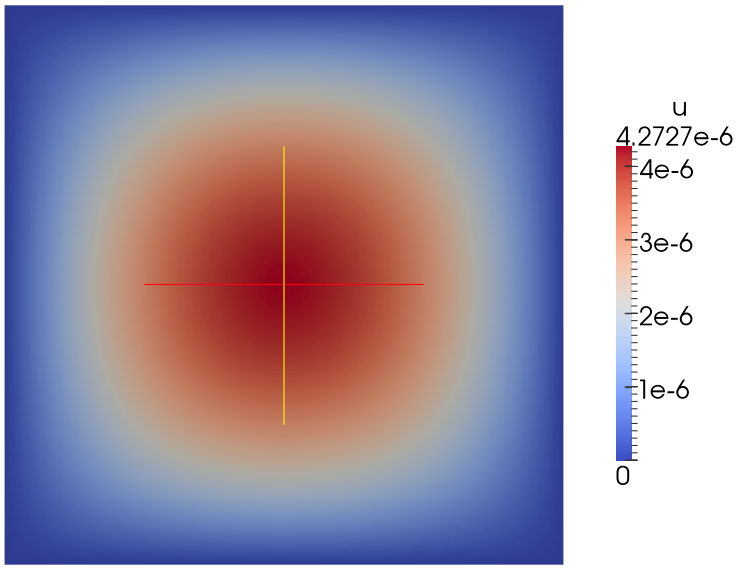

Figure 6.24: Plot of z_{3h}, LPP MaxEnt method. 10×10 grid + `bubble' nodes, simply-supported plate, $\bar{t} = 0.1$.

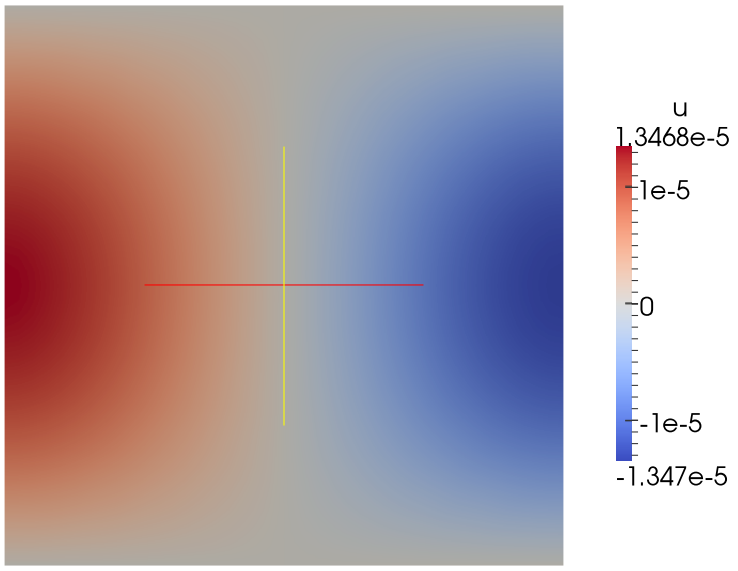

Figure 6.25: Plot of θ_{1h}, LPP MaxEnt method. 10×10 grid + `bubble' nodes, simply-supported plate, $\bar{t} = 0.1$.

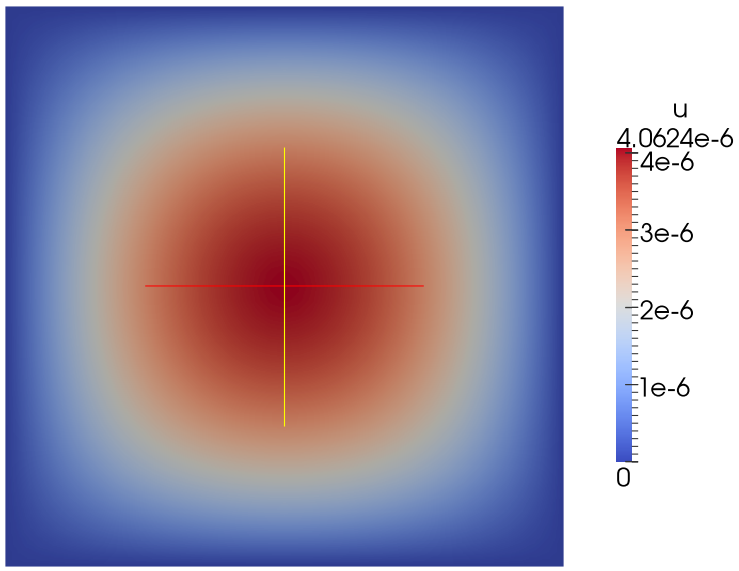

Figure 6.26: Plot of z_{3h}, LPP MaxEnt method. 10×10 grid + `bubble' nodes, simply-supported plate, $\bar{t} = 0.001$.

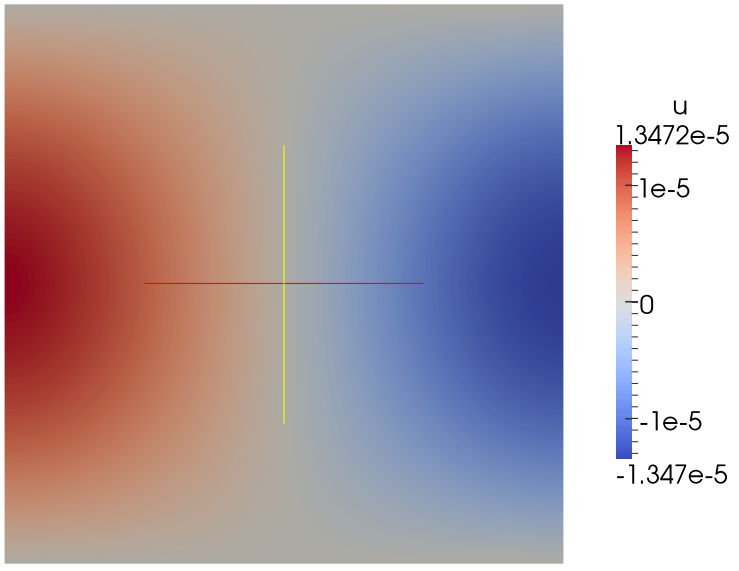

Figure 6.27: Plot of θ_{1h}, LPP MaxEnt method. 10×10 grid + `bubble' nodes, simply-supported plate, $\bar{t} = 0.001$.

6.6.2 Chinosi fully clamped square plate

To make sure that there is not a specific issue with simulating the SSSS plate problem with the proposed LPP MaxEnt method we will now examine the Chinosi plate problem. This problem is set on a square domain with hard clamped boundary conditions and the following transverse loading function:

$$\begin{aligned} f(x_1, x_2) = \frac{E}{12(1-\nu^2)}[&12x_2(x_2-1)(5x_1^2-5x_1+1)(2x_2^2(x_2-1)^2 \\ &+ x_1(x_1-1)(5x_2^2-5x_2+1)) \\ &+ 12x_1(x_1-1)(5x_2^2-5x_2+1)(2x_1^2(x_1-1)^2 \\ &+ x_2(x_2-1)(5x_1^2-5x_1+1))] \end{aligned} \tag{6.68}$$

giving the following closed-form analytical solutions:

$$\theta_1(x_1, x_2) = x_2^3(x_2-1)^3x_1^2(x_1-1)^2(2x_1-1) \tag{6.69a}$$

$$\theta_2(x_1, x_2) = x_1^3(x_1-1)^3x_2^2(x_2-1)^2(2x_2-1) \tag{6.69b}$$

$$\begin{aligned} z_3(x_1, x_2) = &\frac{1}{3}x_1^3(x_1-1)^3x_2^3(x_2-1)^3 \\ &- \frac{2t^2}{5(1-\nu)}[x_2^3(x_2-1)^3x_1(x_1-1)(5x_1^2-5x_1+1) \\ &+ x_1^3(x_1-1)^3x_2(x_2-1)(5x_2^2-5x_2+1)] \end{aligned} \tag{6.69c}$$

In figs. 6.28 and 6.29 we show the plots of the transverse displacement and rotation for a thin plate $\bar{t} = 0.001$. The central displacement of the plate is given as $z_{3h}(0.5, 0.5) = 8.1242 \times 10^{-5}$ which closely matches the analytical solution $z_3(0.5, 0.5) = 8.1381 \times 10^{-5}$.

In fig. 6.30 we show the convergence behaviour for the proposed LPP MaxEnt method for the Chinosi problem. The trends are the same as for the simply-supported plate, namely that we do not achieve convergence in the H^1 norm for the rotation variable. We conclude that this is a general issue with the proposed LPP MaxEnt method in its current form.

6.7 Evaluation

In this section we will evaluate the results obtained with the proposed LPP MaxEnt method using the behaviour of the TRIA0220 finite element discussed in section 6.3 as a basis for com-

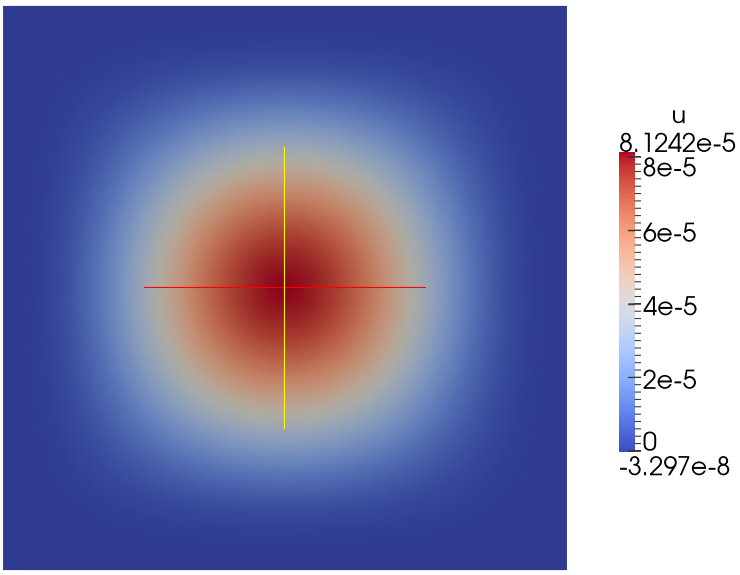

Figure 6.28: Plot of z_{3h}, LPP MaxEnt method. 10×10 grid + `bubble' nodes, Chinosi clamped plate, $\bar{t} = 0.001$.

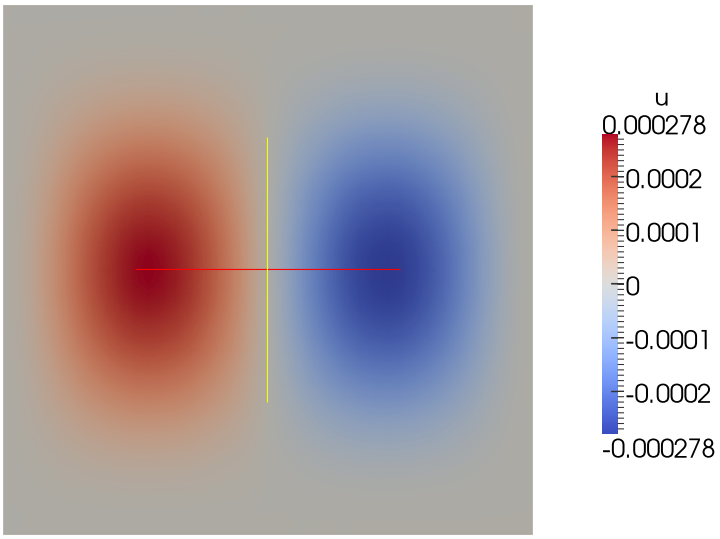

Figure 6.29: Plot of θ_{1h}, LPP MaxEnt method. 10×10 grid + `bubble' nodes, Chinosi clamped plate, $\bar{t} = 0.001$.

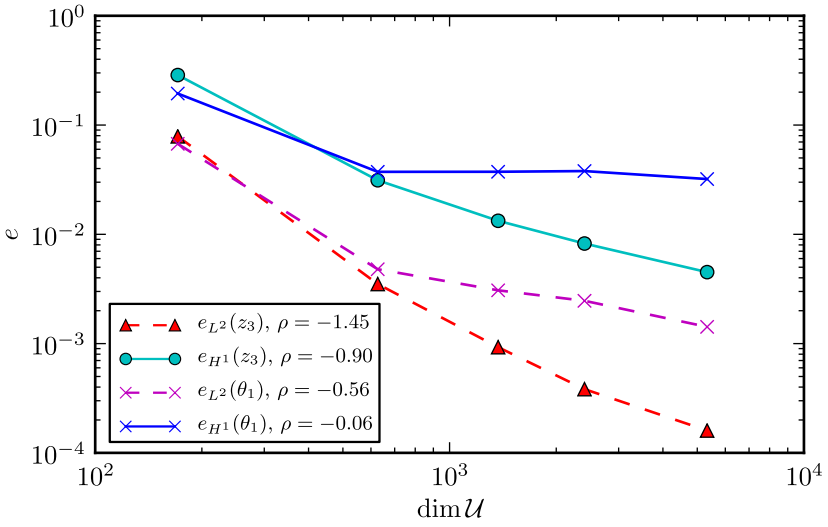

Figure 6.30: Plot showing convergence of proposed LPP MaxEnt method for Chinosi clamped plate problem. Note: The convergence rates calculations exclude the first data point of each series.

parison. We will then attempt to narrow down the cause of the failure to converge in the H^1 norm for the rotation variable θ.

On page 183 we gave a list of conclusions for the numerical experiments performed with the TRIA0220 element. The following conclusions, which we draw from the numerical experiments performed with the LPP MaxEnt method, differ in some notable ways with those for the TRIA0220 finite element scheme:

1. If α is too small, the coercivity of the discrete bilinear form is lost, and the convergence of both z_3 and θ deteriorates. In contrast, for the TRIA0220 scheme only the convergence of z_3 deteriorates if α is too small.

2. If α is too large, the formulation suffers from the shear-locking effect, and the convergence of both z_3 and θ deteriorates. This is identical to the behaviour of the TRIA0220 scheme.

3. Convergence is achieved over a large range of α, similarly to the TRIA0220 scheme, except of course in the H^1 norm for the rotation variable.

4. For optimal convergence, the parameter α must be based upon the local discretisation size. The choice of $\alpha \sim O(\rho^{-2})$ seems roughly optimal, which is the dimensionally consistent choice. However, convergence cannot be achieved using any fixed α for the rotation variable in the H^1 norm.

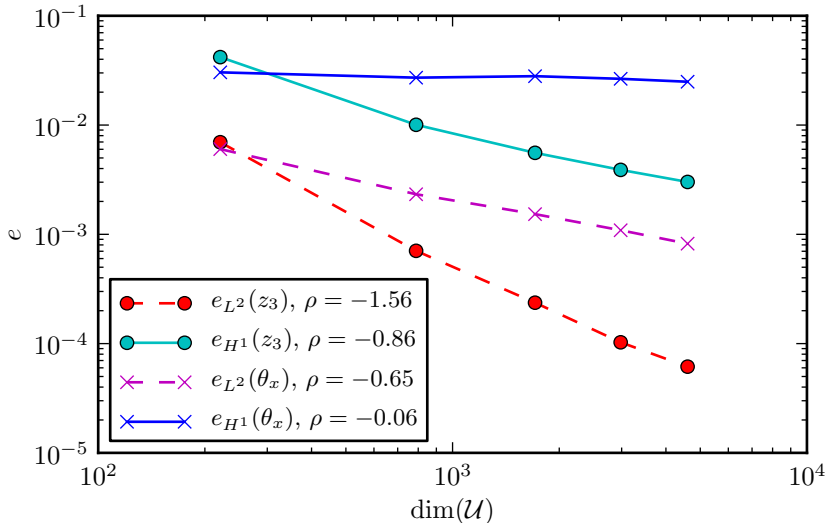

Figure 6.31: Plot showing convergence of unprojected MaxEnt method for the simply-supported plate problem.

The main difference between the performance of the LPP MaxEnt method and TRIA0220 is therefore the convergence behaviour of the rotation variable θ. For the LPP Maxent method the loss of coercivity of the discrete bilinear form negatively effects the convergence of both z_3 and θ, rather than just z_3 for TRIA0220. Furthermore, the rate of convergence of θ in the L^2 norm is reduced over the rate of convergence of z_3 in the L^2 norm, with $\rho = -0.56$ vs $\rho = -1.45$. With such a low rate of convergence in the L^2 norm it is perhaps no surprise that convergence cannot be achieved in the H^1 norm.

The question then arises, which aspect of the method is causing the poor convergence performance in the rotation variable? We postulate that the LPP procedure could be causing the deteriorated convergence perhaps due to the mass-lumping procedure, which is a variational `crime' [165]. To test this we perform simulations without using the LPP procedure. We solve eq. (6.52) using the same choices for the displacements $\mathcal{V}_{3h}$ and $\mathcal{R}_h$ as in eq. (6.53) and shear stresses S_h as in eq. (6.54). This results in a full saddle point system with explicit solution of the shear stress unknowns $\boldsymbol{\gamma}$. We show the convergence of the method without the LPP procedure for the SSSS plate problem in fig. 6.31. We can see that even without the LPP procedure the rotation variable still fails to converge in the H^1 norm. Therefore we can rule out the possibility that the LPP procedure is causing the problem.

We have also done a variety of numerical experiments with the MINI1 element. The design of the MINI1 element is shown in fig. 6.2. The MINI1 element is similar to our LPP Max-

Ent method in that it uses first-order complete basis functions for all problem unknowns displacements, rotations and shear stresses. The inf-sup condition is satisfied using an additional bubble function in the transverse displacement space whilst in the LPP MaxEnt we use an additional meshless node inserted at the barycenter of each cell. The kernel coercivity condition is guaranteed using the stabilised mixed weak form, similarly to our method. In our numerical experiments we have not encountered any issues with achieving convergence using the MINI1 element in any relevant norm and variable (results not shown).

We conclude this section by stating that there is a clearly an issue when using a meshless basis function together with this particular stabilisation approach. Our sensitivity studies have shown that it is impossible to achieve convergence in the H^1 norm for the rotation variable θ using a fixed value of α on a uniform discretisation. By performing numerical experiments using the un-projected stabilised system we have ruled out the LPP procedure as the potential cause of the problem. Furthermore numerical experiments performed using the MINI1 finite element design demonstrate that it is possible to use first-order basis functions and still achieve convergence. It seems that other methods are required to ensure the kernel coercive condition is met in meshless methods. We will discuss ongoing work towards this in the next section.

6.8 Conclusions

In this chapter we have explored the possibility of developing a generalised mixed method for the Reissner-Mindlin plate problem using a stabilised mixed weak form. The stabilised mixed weak form has been used to ensure the kernel coercivity condition is satisfied automatically. This change opens up previously unavailable discretisation designs that are more suited to the Stokes problem than the Reissner-Mindlin problem.

To develop the proposed method we generalised the volume-averaged nodal displacement procedure of Ortiz et al. to the Reissner-Mindlin problem. We gave the volume-averaged nodal displacement procedure a more general mathematical framework and we call the resulting method the local patch-projection procedure. We have given a full mathematical and algorithmic overview of the construction of the LPP method and verified the correct implementation using the leaky-lid cavity flow problem as a benchmark.

In numerical testing of the proposed LPP MaxEnt method we have achieved convergence in the L^2 and H^1 norms for the transverse displacement variable z_3 and in the L^2 norm for the rotations θ. However, we have failed to achieve convergence in the H^1 norm of the rotation variable.

By examining the MINI1 finite element method we have ruled out the cause being the use of only first-order complete basis functions. Furthermore we have eliminated the cause being the LPP procedure by numerical experiments with the unprojected mixed system. Therefore we conclude that the probable cause of this convergence failure is an incompatibility between the use of the meshless basis functions and the proposed stabilisation procedure.

We believe the way forward is to design a generalised displacement method that naturally satisfies the discrete kernel coercivity condition without the addition of stabilisation. In our collaboration with A. Ortiz at the Universidad de Chile we have been examining the application of the LPP method to incompressible hyperelastic problems. The discrete linearised problem for each solution step of the non-linear incompressible hyper-elasticity problem also does not uniformly satisfy the kernel coercivity condition [166]. We believe that new insight into this problem will help us re-examine the kernel coercivity issue in the proposed LPP MaxEnt method for the Reissner-Mindlin plate problem leading to an improved generalised displacement method.

7 Conclusions and future work

7.1 Introduction

In this final chapter we provide conclusions along with recommendations for possible directions for future work. These conclusions are based upon the meshless numerical techniques developed in chapters 4 to 6 of this thesis.

7.2 General conclusions

The main objective of the research presented in this thesis was the development of novel meshless numerical methods for the simulation of shear-deformable beam and plate structures that are free from the adverse effects of shear-locking. The approach taken, for the first time in a meshless framework, has been to move from the displacement weak form to the mixed weak form where the shear stresses are treated as an independent variational quantity in the weak form. Numerous authors have demonstrated in the finite element literature that this approach produces the most robust and general techniques.

In chapter 4 we presented a new method for the Timoshenko beam problem based upon a mixed variational form. We approximate the shear stresses on an underlying mesh. In the case of the $ME - DG_0$ method using scheme D1 (see fig. 4.2(a)) we demonstrate that the proposed method converges to the well-known $CG_1 - DG_0$ Timoshenko beam finite element in the local or Delaunay limit. The $CG_1 - DG_0$ finite element is uniformly LBB stable. Because no transform is used between the reference and global elements of the underlying mesh the robustness of the meshless approximation field is retained, and the implementation of the method is greatly simplified and computational time will be reduced over using two meshless basis functions. Our method achieves convergence rates of $\rho \sim -2.5$ in the L^2 norm using first-order consistent Maximum-Entropy basis functions for the clamped-clamped beam problem. This compares well with the SCNI method of Wang and Chen who achieve a convergence rate of $\rho \sim -2.8$ but using a second-order consistent basis function. Recently we have extended local patch-

projection technique presented in chapter 6 to the scheme D1 presented in chapter 4, resulting in a generalised displacement method for the Timoshenko beam problem. This work will be presented in an upcoming journal paper.

In chapter 5 we presented a new method for the Reissner-Mindlin plate problem based upon a mixed variational form. We identify the correct function space setting for the shear stresses as the Sobolev space of functions with square integrable rotation. We use rotated Raviart–Thomas-Nédélec elements to discretise the shear-stresses along with maximum-entropy basis functions to discretise the displacements. This technique has close similarities to the well known mixed interpolation of tensorial component (MITC) family of finite elements. We present various standard benchmark problems that demonstrate the shear-locking free nature of the proposed method.

In chapter 6 we explored the use of a stabilised mixed weak form of the Reissner-Mindlin problem to construct a generalised displacement meshless method that is free from shear-locking. The use of stabilisation is a necessary step to ensure that the kernel coercivity condition is uniformly satisfied and allows the adaptation of numerical methods originally intended for the solution of the Stokes problem. Generalised displacement methods are a class of numerical methods that whilst being based upon an underlying mixed formulation are expressed in terms of the original displacement unknowns only. We implement the inf-sup stable volume-averaged pressure technique originally proposed by Ortiz et al. [75, 76]. We develop a generalisation of this technique which we call the local patch-projection (LPP) technique and apply our formalised version to eliminate the shear stresses from the stabilised mixed weak form. The resulting linear problem is expressed in terms of the displacement unknowns only. We present various standard benchmark problems which show that whilst the proposed LPP MaxEnt method is free from shear-locking and converges in the L^2 norm for the transverse displacement and rotation variables and the H^1 norm for the transverse displacement variable, we fail to obtain convergence in the H^1 norm for the rotations. Sensitivity studies show that it is not possible to achieve convergence for any constant choice of the stabilisation parameter on a fixed and uniform grid of meshless nodes. By examining the unprojected (fully mixed) system we eliminate the LPP procedure being the cause of the problem. By examining the MINI1 finite element design we rule out the use of the first-order consistent basis function being the problem. We therefore conclude that the likely cause of convergence failure is an incompatibility between the use of this stabilised mixed weak form and the use of meshless basis functions.

We take this moment to emphasise that some authors working in the field of meshless methods for the thin-structural theories have often failed to show all relevant convergence results.

Some authors have only reported pointwise-type convergence results, for example, the displacement at the centre of a clamped plate, or a comparison across a line with a super-imposed analytical solution. Such graphs can be misleading in implying convergence when infact there is sub-optimal convergence or no convergence at all. They give little indication for how convergence changes with respect to the small parameter. In this regard we consider the testing methodology in this thesis to be of a higher standard than that typically found in the meshless literature and we would encourage other authors to test using a similar methodology to fully expose any shortcomings in the methods that they propose.

7.3 Future work

The work presented in this thesis might be extended in the following ways. These extensions are ordered from the relatively achievable through to more long-term developments which would constitute significantly new areas of research.

1. Solve the outstanding issue relating to the stabilised mixed weak form and the use of meshless basis functions. In collaboration with Dr. A Ortiz we are currently investigating the kernel coercivity problem in the incompressible hyper-elasticity problem and we believe that the outcomes of this work could help solve the kernel coercivity issue in the current LPP MaxEnt method for the Reissner-Mindlin plate problem, resulting in a method without the current issues.

2. Extend the definition of the local patch-projection operator to allow the use of meshless basis functions for the auxiliary (pressure or stress) variable function space. It would be interesting to see whether the additional computational expense of using a meshless basis leads to any appreciable improvement in accuracy over the cheaper mesh-based procedures used in this thesis.

3. Extend the improved LPP MaxEnt method to the shell problem. This will involve the application of two projections resulting in a method that is free from the effects of both shear-locking and membrane-locking.

4. Explore the possibility of approximating the shell mid-surface using meshless shape functions. Because of their high continuity meshless basis functions are an ideal candidate for approximating the shell mid-surface from a smooth CAD geometry. Mesh-based tech-

niques can struggle with this. This could be an interesting cross disciplinary project with academics working in the field of computational geometry.

5. Develop analytical tools for to examine the stability of meshless methods based on mixed weak forms. Whilst we have used the kernel coercivity and LBB conditions as general guidelines for the design of the mixed meshless methods in this thesis, it would certainly be more satisfying to have a direct analytical proof that the methods are stable. To our knowledge there is currently no work on extending well-known analytical methods such as the macro-element technique from finite element to meshless methods.

6. Explore the development of enriched mixed and generalised displacement partition of unity methods. Because of the generality of the mixed approach used in this thesis it is a promising strategy for the development of new methods that are free from locking and use more complex basis functions and enrichments. For example, a family of enriched MITC finite elements with modified reduction operators to eliminate shear-locking would be a significant advance in finite element technology.

Bibliography

1. Melenk, J. M. & Babuska, I. The Partition of Unity Finite Element Method: Basic theory and Applications. *Computer Methods in Applied Mechanics and Engineering* **139,** 289–314 (1996).
2. Nguyen, V. P., Rabczuk, T., Bordas, S. & Duflot, M. Meshless methods: A review and computer implementation aspects. *Mathematics and Computers in Simulation* **79,** 763–813 (2008).
3. Fries, T. & Matthies, H. Classification and Overview of Meshfree Methods. *Informatikbericht* **2003** (2003).
4. Liu, G. R. *Mesh free methods, moving beyond the finite element method* (CRC, 2009).
5. Liu, G. & Gu, Y. *An Introduction to Meshfree Methods and Their Programming* 1st ed. (Springer, 2005).
6. Lucy, L. B. A numerical approach to the testing of the fission hypothesis. *The Astronomical Journal* **82,** 1013 (1977).
7. Gingold, R. A. & Monaghan, J. J. Smoothed particle hydrodynamics - Theory and application to non-spherical stars. *Monthly Notices of the Royal Astronomical Society* **181,** 375–389 (1977).
8. Johnson, G. R., Stryk, R. A. & Beissel, S. R. SPH for high velocity impact computations. *Computer methods in applied mechanics and engineering* **139,** 347–373 (1996).
9. Bonet, J. & Kulasegaram, S. Correction and stabilization of smooth particle hydrodynamics methods with applications in metal forming simulations. *International Journal for Numerical Methods in Engineering* **47,** 1189–1214 (2000).
10. Swegle, J. W., Hicks, D. L. & Attaway, S. W. Smoothed particle hydrodynamics stability analysis. *Journal of Computational Physics* **116,** 123–134 (1995).

11. Belytschko, T., Guo, Y., Liu, W. K. & Xiao, S. P. A unified stability analysis of meshless particle methods. *International Journal for Numerical Methods in Engineering* **48,** 1359–1400 (2000).

12. Liu, W. K., Jun, S., Zhang, Y. F., *et al.* Reproducing kernel particle methods. *International Journal for Numerical Methods in Fluids* **20,** 1081–1106 (1995).

13. Lancaster, P. & Salkauskas, K. Surfaces Generated by Moving Least Squares Methods. *Mathematics of Computation* **37,** 158, 141 (1981).

14. Liu, G. G.-R. & Liu, M. B. *Smoothed Particle Hydrodynamics: A Meshfree Particle Method* (World Scientific, 2003).

15. Nayroles, B., Touzot, G. & Villon, P. Generalizing the finite element method: diffuse approximation and diffuse elements. *Computational mechanics* **10,** 307–318 (1992).

16. Belytschko, T., Lu, Y. Y., Gu, L., *et al.* Element-free Galerkin methods. *International Journal for Numerical Methods in Engineering* **37,** 229–256 (1994).

17. Krysl, P. & Belytschko, T. Analysis of thin plates by the element-free Galerkin method. *Computational Mechanics* **17,** 26–35 (1995).

18. Krysl, P. & Belytschko, T. Analysis of thin shells by the Element-Free Galerkin method. *International Journal of Solids and Structures* **33,** 3057–3080 (1996).

19. Belytschko, T., Lu, Y., Gu, L. & Tabbara, M. Element-free Galerkin methods for static and dynamic fracture. *International Journal of Solids and Structures* **32,** 2547–2570 (1995).

20. Liu, G. R. & Gu, Y. T. A point interpolation method for two-dimensional solids. *International Journal for Numerical Methods in Engineering* **50,** 937–951 (2001).

21. Arroyo, M. & Ortiz, M. Local maximum-entropy approximation schemes: a seamless bridge between finite elements and meshfree methods. *International Journal of Numerical Methods in Engineering* **65,** 2167–2202 (2006).

22. Wang, J. G. & Liu, G. R. A point interpolation meshless method based on radial basis functions. *Int. J. Numer. Meth. Eng* **54,** 1623–1648 (2002).

23. Gu, L. Moving kriging interpolation and element-free Galerkin method. *International Journal for Numerical Methods in Engineering* **56,** 1–11 (2003).

24. Atluri, S. N. & Zhu, T. A new Meshless Local Petrov-Galerkin (MLPG) approach in computational mechanics. *Computational Mechanics* **22,** 117–127 (1998).

25. Strouboulis, T., Copps, K. & Babuska, I. The generalized finite element method. *Computer Methods in Applied Mechanics and Engineering* **190,** 4081–4193 (2001).

26. Belytschko, T., Moës, N., Usui, S. & Parimi, C. Arbitrary discontinuities in finite elements. *International Journal for Numerical Methods in Engineering* **50,** 993–1013 (2001).

27. Oden, J. T., Duarte, C. A. M. & Zienkiewicz, O. C. A new cloud-based hp finite element method. *Computer Methods in Applied Mechanics and Engineering* **153,** 117–126 (1998).

28. Griebel, M. & Schweitzer, M. A. A particle-partition of unity method for the solution of elliptic, parabolic, and hyperbolic PDEs. *SIAM Journal on Scientific Computing* **22,** 853–890 (2001).

29. Shepard, D. in *Proceedings of the 1968 23rd ACM National Conference* (ACM, 1968), 517–524. doi:10.1145/800186.810616.

30. Oh, H.-S. & Jeong, J. W. Almost everywhere partition of unity to deal with essential boundary conditions in meshless methods. *Computer Methods in Applied Mechanics and Engineering* **198,** 3299–3312 (2009).

31. Oh, H.-S., Jae, W. J. & Won, T. H. The generalized product partition of unity for the meshless methods. *Journal of Computational Physics* **229,** 1600–1620 (2010).

32. Reddy, J. *Theory and Analysis of Elastic Plates and Shells* 2nd ed. (CRC Press, 2006).

33. Zhang, S. *A linear shell theory based on variational principles* PhD thesis (The Pennsylvania State University, 2001).

34. Love, A. E. H. The small free vibrations and deformation of a thin elastic shell. *Philosophical Transactions of the Royal Society of London. A* **179,** 491–546 (1888).

35. Kirchhoff, G. Über das Gleichgewicht und die Bewegung einer elastischen Scheibe. *Journal für die reine und angewandte Mathematik* **1850,** 51–88 (1850).

36. Reissner, E. On the theory of bending of elastic plates. *Journal of Mathematical Physics* **23,** 184 (1944).

37. Reissner, E. The effect of transverse shear deformation on the bending of elastic plates. *Journal of Applied Mechanics* **12,** A69 (1945).

38. Mindlin, R. D. Influence of rotatory inertia and shear on flexural motions of isotropic elastic plates. *Journal of Applied Mechanics,* A31 (1951).

39. Reddy, J. A refined nonlinear theory of plates with transverse shear deformation. *International Journal of Solids and Structures* **20,** 881–896 (1984).

40. Chapelle, D. & Bathe, K. *The Finite Element Analysis of Shells - Fundamentals* 2nd (Springer, 2010).

41. Zienkiewicz, O. C., Taylor, R. L. & Too, J. M. Reduced integration technique in general analysis of plates and shells. *International Journal for Numerical Methods in Engineering* **3,** 275–290 (1971).

42. Dvorkin, E. N. & Bathe, K. A continuum mechanics based four-node shell element for general non-linear analysis. *Engineering Computations* **1,** 77–88 (1984).

43. Bathe, K., Brezzi, F. & Cho, S. W. The MITC7 and MITC9 Plate bending elements. *Computers & Structures* **32,** 797–814 (1989).

44. Lee, P. & Bathe, K. Development of MITC isotropic triangular shell finite elements. *Computers & Structures* **82,** 945–962 (2004).

45. Wilson, E. L., Taylor, R. L., Doherty, W. P. & Ghaboussi, J. Incompatible displacement models. *Numerical and Computer Methods in Structural Mechanics* **43** (1973).

46. Simo, J. C. & Rifai, M. S. A class of mixed assumed strain methods and the method of incompatible modes. *International Journal for Numerical Methods in Engineering* **29,** 1595–1638 (1990).

47. Bletzinger, K., Bischoff, M. & Ramm, E. A unified approach for shear-locking-free triangular and rectangular shell finite elements. *Computers & Structures* **75,** 321–334 (2000).

48. Koschnick, F., Bischoff, M., Camprubí, N. & Bletzinger, K. The discrete strain gap method and membrane locking. *Computer Methods in Applied Mechanics and Engineering* **194,** 2444–2463 (2005).

49. Falk, R. S. Locking-free finite elements for the Reissner-Mindlin plate. *Math. Comp* **69,** 911–928 (2000).

50. Arnold, D. N. Mixed finite element methods for elliptic problems. *Computer Methods in Applied Mechanics and Engineeering,* 281–300 (1990).

51. Babuška, I. The finite element method with Lagrangian multipliers. *Numerische Mathematik* **20,** 179–192 (1973).

52. Brezzi, F. On the existence, uniqueness and approximation of saddle-point problems arising from Lagrangian multipliers. *RAIRO Anal. Numer* **8,** 129–151 (1974).

53. Brezzi, F. & Bathe, K.-J. A discourse on the stability conditions for mixed finite element formulations. *Computer Methods in Applied Mechanics and Engineering* **82,** 27–57 (1990).

54. Tiago, C. & Leitão, V. M. A. in *Advances in Meshfree Techniques* (eds Leitão, V. M. A., Alves, C. J. S. & Duarte, C. A.) *Computational Methods in Applied Sciences* 5, 123–145 (Springer Netherlands, 2007).

55. Liew, K., Zhao, X. & Ferreira, A. J. A review of meshless methods for laminated and functionally graded plates and shells. *Composite Structures* **93,** 2031–2041 (2011).

56. Kanok-Nukulchai, W., Barry, W., Saran-Yasoontorn, K. & Bouillard, P. H. On elimination of shear locking in the element-free Galerkin method. *International Journal for Numerical Methods in Engineering* **52,** 705–725 (2001).

57. Garcia, O., Fancello, E. A., de Barcellos, C. S. & Duarte, C. A. *hp*-Clouds in Mindlin's thick plate model. *International Journal for Numerical Methods in Engineering* **47,** 1381–1400 (2000).

58. De T. R. Mendonça, P., de Barcellos, C. S. & Duarte, A. Investigations on the *hp*-Cloud Method by solving Timoshenko beam problems. *Computational Mechanics* **25,** 286–295 (2000).

59. Choi, Y. & Kim, S. Bending analysis of Mindlin-Reissner plates by the element free Galerkin method with penalty technique. *Journal of Mechanical Science and Technology* **17,** 64–76 (2003).

60. Benson, D., Bazilevs, Y., Hsu, M. & Hughes, T. Isogeometric shell analysis: The Reissner-Mindlin shell. *Computer Methods in Applied Mechanics and Engineering* **199,** 276–289 (2010).

61. Donning, B. M. & Liu, W. K. Meshless methods for shear-deformable beams and plates. *Computer Methods in Applied Mechanics and Engineering* **152,** 47–71 (1998).

62. Bui, T. Q., Nguyen, M. N. & Zhang, C. A meshfree model without shear-locking for free vibration analysis of first-order shear deformable plates. *Engineering Structures* **33,** 3364–3380 (2011).

63. Bui, T., Nguyen, M. & Zhang, C. Buckling analysis of Reissner–Mindlin plates subjected to in-plane edge loads using a shear-locking-free and meshfree method. *Engineering Analysis with Boundary Elements* **35,** 1038–1053 (2011).

64. Leitão, V., Alves, C. & Duarte, C. A. *Advances in Meshfree Techniques* 1st ed. (Springer, 2007).

65. Liu, W., Li, S. & Belytschko, T. Moving least-square reproducing kernel methods (I) Methodology and convergence. *Computer Methods in Applied Mechanics and Engineering* **143,** 113–154 (1997).

66. Beirão da Veiga, L., Buffa, A., Lovadina, C., Martinelli, M. & Sangalli, G. An isogeometric method for the Reissner–Mindlin plate bending problem. *Computer Methods in Applied Mechanics and Engineering* **209–212,** 45–53 (2012).

67. Beissel, S. & Belytschko, T. Nodal integration of the element-free Galerkin method. *Computer Methods in Applied Mechanics and Engineering* **139,** 49–74 (1996).

68. Wang, D. & Chen, J. Locking-free stabilized conforming nodal integration for meshfree Mindlin-Reissner plate formulation. *Computer Methods in Applied Mechanics and Engineering* **193,** 1065–1083 (2004).

69. Cho, J. & Atluri, S. Analysis of shear flexible beams, using the meshless local Petrov-Galerkin method, based on a locking-free formulation. *Engineering Computations* **18,** 215–240 (2001).

70. Vidal, Y., Villon, P. & Huerta, A. Locking in the incompressible limit: pseudo-divergence-free element free Galerkin. *Communications in Numerical Methods in Engineering* **19,** 725–735 (2003).

71. González, D., Cueto, E. & Doblaré, M. Volumetric locking in natural neighbour Galerkin methods. *International Journal for Numerical Methods in Engineering* **61,** 611–632 (2004).

72. Simo, J., Taylor, R. & Pister, K. Variational and projection methods for the volume constraint in finite deformation elasto-plasticity. *Computer Methods in Applied Mechanics and Engineering* **51,** 177–208 (1985).

73. Recio, D. P., Jorge, R. M. & Dinis, L. M. S. Locking and hourglass phenomena in an element-free Galerkin context: the B-bar method with stabilization and an enhanced strain method. *International Journal for Numerical Methods in Engineering* **68,** 1329–1357 (2006).

74. Sorić, J. & Jarak, T. Mixed meshless formulation for analysis of shell-like structures. *Computer Methods in Applied Mechanics and Engineering* **199,** 1153–1164 (2010).

75. Ortiz, A., Puso, M. & Sukumar, N. Maximum-entropy meshfree method for compressible and near-incompressible elasticity. *Computer Methods in Applied Mechanics and Engineering* **199,** 1859–1871 (2010).

76. Ortiz, A., Puso, M. & Sukumar, N. Maximum-entropy meshfree method for incompressible media problems. *Finite Elements in Analysis and Design* **47,** 572–585 (2011).

77. Hale, J. & Baiz, P. A locking-free meshfree method for the simulation of shear-deformable plates based on a mixed variational formulation. *Computer Methods in Applied Mechanics and Engineering* **241–244,** 311–322 (2012).

84. Allaire, G. *Numerical Analysis and Optimization: An Introduction to Mathematical Modelling and Numerical Simulation* (OUP Oxford, 2007).

85. Fernández-Méndez, S. & Huerta, A. Imposing essential boundary conditions in meshfree methods. *Computer Methods in Applied Mechanics and Engineering* **193,** 1257–1275 (2004).

86. Fish, J. & Belytschko, T. *A First Course in Finite Elements* Pap/Cdr (John Wiley & Sons, 2007).

87. Cai, Y. & Zhu, H. A PU-based meshless Shepard interpolation method satisfying delta property. *Engineering Analysis with Boundary Elements* **34,** 9–16 (2010).

88. Kaljevic, I. & Saigal, S. An improved element free Galerkin formulation. *International Journal for Numerical Methods in Engineering* **40,** 2953–2974 (1997).

89. Most, T. & Bucher, C. New concepts for moving least squares: An interpolating non-singular weighting function and weighted nodal least squares. *Engineering Analysis with Boundary Elements* **32,** 461–470 (2008).

90. Most, T. & Bucher, C. A Moving Least Squares weighting function for the Element-free Galerkin Method which almost fulfills essential boundary conditions. *Structural Engineering and Mechanics* **21,** 315–332 (2005).

91. Belytschko, T., Krongauz, Y., Fleming, M., Organ, D. & Liu, W. K. S. Smoothing and accelerated computations in the element free Galerkin method. *J. Comput. Appl. Math.* **74,** 111–126 (1996).

92. Shannon, C. E. A mathematical theory of communication. *The Bell Systems Technical Journal* **27,** 379–423 (1948).

93. Jaynes, E. T. Information theory and statistical mechanics. II. *Physical Review* **108,** 171–190 (1957).

94. Frank, S. A. Measurement scale in maximum entropy models of species abundance. *Journal of Evolutionary Biology* **24,** 485–496 (2011).

95. Ratnaparkhi, A. Learning to parse natural language with maximum entropy models. *Machine Learning* **34,** 151–175 (1999).

96. Jaynes, E. in *Proceedings of the Maximum Entropy Formalism Conference* (Massachusetts Institute of Technology, 1979).

97. Sukumar, N. Construction of polygonal interpolants: a maximum entropy approach. *International Journal for Numerical Methods in Engineering* **61,** 2159–2181 (2004).

98. Sukumar, N. Maximum Entropy Approximation. *AIP Conference Proceedings* **803,** 337–344 (2005).

99. Sukumar, N. & Wright, R. W. Overview and construction of meshfree basis functions: from moving least squares to entropy approximants. *International Journal of Numerical Methods in Engineering* **70,** 181–205 (2007).

100. Boyd, S. & Vandenberghe, L. *Convex Optimization* (Cambridge University Press, 2004).

101. Sukumar, N. & Wets, R. J. Deriving the Continuity of Maximum-Entropy Basis Functions via Variational Analysis. *SIAM Journal on Optimization* **18,** 914–925 (2007).

102. Cyron, C. J., Arroyo, M. & Ortiz, M. Smooth, second order, non-negative meshfree approximants selected by maximum entropy. *International Journal of Numerical Methods in Engineering* **79,** 1605–1632 (2009).

103. González, D., Cueto, E. & Doblaré, M. A higher order method based on local maximum entropy approximation. *International Journal for Numerical Methods in Engineering* **83,** 741–764 (2010).

104. Rosolen, A., Millán, D. & Arroyo, M. On the optimum support size in meshfree methods: A variational adaptivity approach with maximum-entropy approximants. *International Journal for Numerical Methods in Engineering* **82,** 868–895 (2010).

105. Millán, D., Rosolen, A. & Arroyo, M. Thin shell analysis from scattered points with maximum-entropy approximants. *International Journal for Numerical Methods in Engineering* **85,** 723–751 (2011).

106. Yaw, L. L., Sukumar, N. & Kunnath, S. K. Meshfree co-rotational formulation for two-dimensional continua. *International Journal for Numerical Methods in Engineering* **79,** 979–1003 (2009).

107. Fasshauer, G. E. *Meshfree approximation methods with Matlab* (World Scientific Pub Co Inc, 2007).

108. Hardy, R. L. Multiquadric equations of topology and other irregular surfaces. *J. Geophys. Res* **76,** 1905–1915 (1971).

109. Wendland, H. Meshless Galerkin methods using radial basis functions. *Mathematics of Computation* **68,** 1521–1532 (1999).

110. Bochner, S. Monotone Funktionen, Stieltjes Integrale und Harmonische Analyse. *Ann. of Maths* **42,** 647–656 (1933).

111. Iske, A. Radial basis functions: basics, advanced topics and meshfree methods for transport problems. *Universitae Politecnico di Torino,* 247 (2003).

112. Liu, G. *Mesh Free Methods: Moving Beyond the Finite Element Method* 1st ed. (CRC Press, 2002).

113. Powell, M. J. D. The theory of radial basis function approximation in 1990. *Advances in numerical analysis* **2,** 105–210 (1992).

114. Liu, G. R. A G space theory and a weakened weak (W^2)form for a unified formulation of compatible and incompatible methods: Part I theory. *International Journal for Numerical Methods in Engineering* **81,** 1093–1126 (2010).

115. Liu, G. R. A G space theory and a weakened weak (W^2) form for a unified formulation of compatible and incompatible methods: Part II applications to solid mechanics problems. *International Journal for Numerical Methods in Engineering* **81,** 1127–1156 (2010).

116. Wendland, H. Piecewise polynomial, positive definite and compactly supported radial functions of minimal degree. *Advances in Computational Mathematics* **4,** 389–396 (1995).

117. Buhmann, M. D. A new class of radial basis functions with compact support. *Mathematics of Computation* **70,** 307–318 (2000).

118. Wu, Z. Compactly supported positive definite radial functions. *Advances in Computational Mathematics* **4,** 283–292 (1995).

119. Itoh, T., Kitagawa, T. & Nakata, S. Implicit surface reconstruction of 3D objects: Preconditioned iterative methods for the CSRBF-type linear systems. *Electronics and Communications in Japan (Part III: Fundamental Electronic Science)* **89,** 11–20 (2006).

120. Babuška, I. The finite element method with Lagrangian multipliers. *Numerische Mathematik* **20,** 179–192 (1973).

121. Zhu, T. & Atluri, S. N. A modified collocation method and a penalty formulation for enforcing the essential boundary conditions in the element free Galerkin method. *Computational Mechanics* **21,** 211–222 (1998).

122. Nitsche, J. in *Abhandlungen aus dem Mathematischen Seminar der Universität Hamburg* **36** (1971), 9–15.

123. Belytschko, T., Organ, D. & Krongauz, Y. A coupled finite element-element-free Galerkin method. *Computational Mechanics* **17,** 186–195 (1995).

124. Huerta, A. & Fernández-Méndez, S. Enrichment and coupling of the finite element and meshless methods. *International Journal for Numerical Methods in Engineering* **48,** 1615–1636 (2000).

125. Wagner, G. J. & Liu, W. K. Hierarchical enrichment for bridging scales and mesh-free boundary conditions. *International Journal for Numerical Methods in Engineering* **50,** 507–524 (2001).

126. Abrahams, D. *Boost Python C++ library* 2011--.

127. Logg, A. & Wells, G. N. DOLFIN: Automated finite element computing. *ACM Transactions on Mathematical Software (TOMS)* **37,** 20 (2010).

128. Kirby, R. C. Algorithm 839: FIAT, a new paradigm for computing finite element basis functions. *ACM Transactions on Mathematical Software* **30,** 502–516 (2004).

129. Jones, E., Oliphant, T., Peterson, P., *et al. SciPy: Open source scientific tools for Python* 2001--.

130. Häggblad, B. & Bathe, K. J. Specifications of boundary conditions for Reissner/Mindlin plate bending finite elements. *International Journal for Numerical Methods in Engineering* **30,** 981–1011 (1990).

131. Arnold, D. N. & Falk, R. S. The boundary layer for the Reissner-Mindlin plate model. *SIAM Journal on Mathematical Analysis* **21,** 281–312 (1990).

132. Argyris, J. H., Fried, I. & Scharpf, D. W. The TUBA family of plate elements for the matrix displacement method. *The Aeronautical Journal of the Royal Aeronautical Society* **72,** 701–709 (1968).

133. Hardesty, S. S. *Optimization of shell structure acoustics* PhD thesis (Rice University, 2010).

134. Arnold, D. N. Discretization by finite elements of a model parameter dependent problem. *Numerische Mathematik* **37,** 405–421 (1981).

135. Braess, D. Stability of saddle point problems with penalty. *ESAIM: Mathematical Modelling and Numerical Analysis - Modélisation Mathématique et Analyse Numérique* **30** (1996).

136. Raviart, P. A. & Thomas, J. M. in *Mathematical Aspects of Finite Element Methods* (eds Galligani, I. & Magenes, E.) 292–315 (Springer Berlin Heidelberg, 1977).

137. Nedelec, J. C. Mixed finite elements in $\mathbb{R}^3$. *Numerische Mathematik* **35,** 315–341 (1980).

138. Braess, D. *Finite Elements: Theory, Fast Solvers, and Applications in Solid Mechanics* 3rd ed. (Cambridge University Press, 2007).

139. Ledger, P. D., Morgan, K. & Hassan, O. Electromagnetic scattering simulation using an $H(\mathrm{curl})$ conforming *hp* finite element method in three dimensions. *International Journal for Numerical Methods in Fluids* **53,** 1267–1296 (2007).

140. Ciarlet, P. G. *The Finite Element Method for Elliptic Problems* 2nd (SIAM: Society for Industrial and Applied Mathematics, 2002).

141. Karniadakis, G. & Sherwin, S. J. *Spectral/hp Element Methods For Computational Fluid Dynamics* (Oxford University Press, 2005).

142. İmrak, C. E. & Gerdemeli, İ. An Exact Solution for the Deflection of a Clamped Rectangular Plate under Uniform Load. *Applied Mathematical Sciences* **1,** 2129–2137 (2007).

143. Buffa, A., Sangalli, G. & Vázquez, R. Isogeometric analysis in electromagnetics: B-splines approximation. *Computer Methods in Applied Mechanics and Engineering* **199,** 1143–1152 (2010).

144. Babuška, I. & Osborn, J. E. Generalized Finite Element Methods: Their Performance and Their Relation to Mixed Methods. *SIAM Journal on Numerical Analysis* **20,** 510–536 (1983).

145. Boffi, D. & Lovadina, C. Analysis of new augmented Lagrangian formulations for mixed finite element schemes. *Numerische Mathematik* **75,** 405–419 (1997).

146. Arnold, D. & Brezzi, F. Some new elements for the Reissner-Mindlin plate model. *Boundary value problems for partial differential equations and applications,* 287–292 (1993).

147. Lovadina, C. A New Class of Mixed Finite Element Methods for Reissner-Mindlin Plates. *SIAM Journal on Numerical Analysis* **33,** 2457–2467 (1996).

148. Fortin, M. & Glowinski, R. *Augmented Lagrangian Methods: Applications to the Numerical Solution of Boundary-Value Problems* (Elsevier, 1983).

149. Fortin, M. & Brezzi, F. *Mixed and Hybrid Finite Element Methods* (Springer-Verlag Berlin and Heidelberg GmbH & Co. K, 1991).

150. Chinosi, C. & Lovadina, C. Numerical analysis of some mixed finite element methods for Reissner-Mindlin plates. *Computational Mechanics* **16,** 36–44 (1995).

151. Boffi, D., Brezzi, F. & Fortin, M. in *Mixed Finite Elements, Compatibility Conditions, and Applications* (eds Boffi, D. & Gastaldi, L.) *Lecture Notes in Mathematics* 1939, 45–100 (Springer Berlin Heidelberg, 2008).

152. Mardal, K.-A. & Haga, J. B. in *Automated Solution of Differential Equations by the Finite Element Method* (eds Logg, A., Mardal, K.-A. & Wells, G.) *Lecture Notes in Computational Science and Engineering* 84, 643–655 (Springer Berlin Heidelberg, 2012).

153. Malkus, D. S. & Hughes, T. J. R. Mixed finite element methods -- Reduced and selective integration techniques: A unification of concepts. *Computer Methods in Applied Mechanics and Engineering* **15,** 63–81 (1978).

154. Chen, J.-S., Wu, C.-T., Yoon, S. & You, Y. A stabilized conforming nodal integration for Galerkin mesh-free methods. *International Journal for Numerical Methods in Engineering* **50,** 435–466 (2001).

155. Liu, G. R., Dai, K. Y. & Nguyen, T. T. A Smoothed Finite Element Method for Mechanics Problems. *Computational Mechanics* **39,** 859–877 (2007).

156. Liu, G. R., Nguyen, T. T., Dai, K. Y. & Lam, K. Y. Theoretical aspects of the smoothed finite element method (SFEM). *International Journal for Numerical Methods in Engineering* **71,** 902–930 (2007).

157. Nguyen, T. T., Liu, G. R., Dai, K. Y. & Lam, K. Y. Selective smoothed finite element method. *Tsinghua Science & Technology* **12,** 497–508 (2007).

158. Hung, N.-X., Bordas, S. P. A. & Hung, N.-D. Addressing volumetric locking and instabilities by selective integration in smoothed finite elements. *Communications in Numerical Methods in Engineering* **25,** 19–34 (2009).

159. Krysl, P. & Zhu, B. Locking-free continuum displacement finite elements with nodal integration. *International Journal for Numerical Methods in Engineering* **76,** 1020–1043 (2008).

160. Nguyen-Xuan, H., Rabczuk, T., Bordas, S. & Debongnie, J. A smoothed finite element method for plate analysis. *Computer Methods in Applied Mechanics and Engineering* **197,** 1184–1203 (2008).

161. Bathe, K. J. & Dvorkin, E. N. A four-node plate bending element based on Mindlin/Reissner plate theory and a mixed interpolation. *International Journal for Numerical Methods in Engineering* **21,** 367–383 (1985).

162. Chapelle, D. & Bathe, K. The inf-sup test. *Computers & Structures* **47,** 537–545 (1993).

163. Arnold, D., Brezzi, F. & Fortin, M. A stable finite element for the Stokes equations. *Calcolo* **21,** 337–344 (1984).

164. Nakshatrala, K. B., Masud, A. & Hjelmstad, K. D. On finite element formulations for nearly incompressible linear elasticity. *Computational Mechanics* **41,** 547–561 (2008).

165. Strang, G. Piecewise polynomials and the finite element method. *Bull. Amer. Math. Soc* **79,** 1128–1137 (1973).

166. Auricchio, F., Beirão da Veiga, L., Lovadina, C. & Reali, A. A stability study of some mixed finite elements for large deformation elasticity problems. *Computer Methods in Applied Mechanics and Engineering* **194,** 1075–1092 (2005).